

ABSTRACT

Title of Dissertation: RAPID HEATING AND CHEMICAL
SPECIATION CHARACTERIZATION FOR
COMBUSTION PERFORMANCE
ANALYSIS OF METALLIZED,
NANOSCALE THERMITES AND PVDF
BOUND SOLID PROPELLANT
COMPOSITIONS

Miles Christian Rehwoldt, Doctor of
Philosophy, 2021

Dissertation directed by: Professor Michael R. Zachariah, Department of
Chemistry and Biochemistry

Energetic materials research focuses on performance analysis of cost-effective solid materials which safely, precisely, and efficiently transitions stored chemical potential energy to kinetic energy at a rate throttled through chemical or architectural means. Heterogenous compositions of metal fuels and solid materials with a high storage capacity of condensed oxidizing elements, such as oxygen and/or fluorine, is a class of energetic material of interest given its relatively high reaction enthalpies and adiabatic flame temperatures. In the wake of the earliest instances of metal fuels being used as a high energy additive during World War II, characterizing the reaction mechanisms of micron and nanoparticle aluminum fuels with various oxidizer sources has been a primary subject of research within the solid energetics community.

The advent of nanotechnologies within the past two decades brought with it the promise of a prospective revolution within the energetics community to expand the utility and characterization of metallized energetic materials in solid propellants and pyrotechnics. Significant prior research has mapped reactivity advantages, as well as the many short comings of aluminum-based nanoscale energetic formulations. Examples of short comings include difficulties of materials processing, relative increase in native oxide shell thickness, and particle aggregate sintering before primary reaction. The less than flaw-less promises of nanoscale aluminum fuels have thus become the impetus for the development of novel architectural solutions and material formulations to eliminate drawbacks of nanomaterial energetics while maintaining and improving the benefits.

This dissertation focuses on further understanding reaction mechanisms and overall combustion behavior of nanoscale solid energetic composite materials and their potential future applications. My research branches out from the heavy research involved in binary, aluminum centric systems by developing generalized intuition of reaction and combustion behaviors through modeling efforts and coupling time-of-flight mass spectrometry to rapid heating techniques and novel modes of product sampling. The studies emphasize reaction mechanisms and microwave sensitivities of under-utilized compositions using metal fuels such as titanium, generalize the understanding of the interaction of fluoropolymer binders with metal fuels and oxidizer particles, and characterize how multi-scale architectural structure-function relations of materials effect ignition properties and energy release rates.

RAPID HEATING AND CHEMICAL SPECIATION CHARACTERIZATION
FOR COMBUSTION PERFORMANCE ANALYSIS OF METALLIZED,
NANOSCALE THERMITES AND PVDF BOUND SOLID PROPELLANT
COMPOSITIONS

by

Miles Christian Rehwoldt

Dissertation submitted to the Faculty of the Graduate School of the
University of Maryland, College Park, in partial fulfillment
of the requirements for the degree of
Doctor of Philosophy
2021

Advisory Committee:

Dr. Michael R. Zachariah, Co-Chair, Advisor
Dr. Efrain Rodriguez, Co-Chair
Dr. Dongxia Liu
Dr. Liangbing Hu
Dr. Peter B. Sunderland, Dean's Representative

© Copyright by
Miles Christian Rehwoldt
2021

Dedication

To my wife, Kim, for your unconditional love, guidance, and steadfast confidence in me. To my parents for their love and support throughout all my years of schooling, especially in times of hardship. To my extended family and friends for encouraging me to reach my goals and to never settle for less than my best.

Acknowledgements

I express my sincere gratitude to everyone involved, either directly or indirectly, who aided in making this dissertation possible. I especially want to thank my dissertation advisor, Dr. Michael Zachariah, for his attentive, unwavering support both professionally and financially which has made this journey a truly worthwhile growing experience. This work would not have been possible without support from the Airforce Office of Scientific Research and DTRA MSEE Consortium.

My time in the Zachariah Group has been an amalgamate of my own work and contributions from my lab mates, both past and present, whose insights and collaborations have greatly impacted my success over the past 5 years. I would specifically like to thank Dr. Jeffery DeLisio for helping me start on this journey by setting me up with the necessary skills and laboratory intuition for success in this lab, and Dr. Dylan Kline who has been both an effective intra-lab collaborator and reliable friend. It has been a true pleasure working with Dr. Haiyang Wang, Feiyu Xu, Dr. Yong Yang, Dr. Phillip Guerieri, Yujie Wang, Dr. Haihan Chen, Zaira Alibay, Prithwish Biswas, Pankaj Ghildiyal, Dr. Tao Wu, and Dr. Xizheng Wang. Our discussions and assistance have been invaluable for establishing a positive work environment and integral in the development of collaborative works. Additionally, I would like to recognize my out-of-lab collaborators which includes Dr. Raymond R. Unocic of Oak Ridge National Laboratory, Dr. Dongxia Liu et al. of University of Maryland, College Park, Dr. William Erikson et al. of Sandia National Laboratories, and Dr. Michael Zdilla of Temple University. Although many projects did not or have not yet resulted

in a publication, the findings gained from these experienced are recognized in this document as motivation for further works.

Finally, I would like to acknowledge my advisory committee, Dr. Liangbing Hu, Dr. Efrain Rodriguez, Dr. Dongxia Liu, and Dr. Peter B. Sunderland for taking the time and effort to help see this process through.

Table of Contents

Dedication	ii
Acknowledgements	iii
Table of Contents	v
List of Tables	ix
List of Figures	x
List of Abbreviations	xviii
Chapter 1: Introduction	1
1.1 Basics of Solid Energetic Materials	1
1.2 Historical Developments of Solid Energetics	3
1.3 Solid Propellants	5
1.4 Metallized Heterogenous Energetic Composites	7
1.5 Nanoscale Energetic Materials	9
1.6 Observed Mechanisms of Nanoscale Thermites	13
1.7 Observed Pitfalls in the Application of Heterogenous Nanoscale Composites	14
1.8 Mechanisms of Nano-Al Particle Oxidation and Thermite Ignition	17
1.9 Fluoropolymer-based MICs for Propellant Systems	19
1.10 Architectural Controls of Energetic Materials	22
1.11 Novel Microstructures for Energetic Particle Compositions	24
1.12 Rapid Prototyping of Energetic Materials (Additive Manufacturing)	28
1.13 Dissertation Research Objectives	32
1.14 Chapter Prefaces	35
Chapter 2: Diagnostics and Instrumentation	40
2.1 Rapid Thermometry of Materials (Temperature-Jump)	40
2.1.1 <i>Methods and Motivation of Temperature-Jump Thermometry</i>	40
2.1.2 <i>Conducting and Analyzing the T-Jump Experiment</i>	42
2.1.3 <i>Measuring the Activation Energy of Ignition</i>	45
2.2 Rapid Chemical Speciation (T-Jump/Time-of-Flight Spectrometry)	46
2.2.1 <i>Linear Time-of-Flight Mass Spectrometry</i>	46
2.2.2 <i>Conducting and Analyzing the TOFMS Experiment</i>	47
2.2.3 <i>Temperature-Jump Time-of-Flight Mass Spectrometry Method</i>	50
2.2.4 <i>Measuring Activation Energy of Species Release</i>	53
2.3 Rapid Chemical Speciation: Molecular Beam Mass Spectrometry	54
2.3.1 <i>Methods and Motivation of Molecular Beam Mass Spectrometry</i>	54
2.3.2 <i>Formation and Characteristics of the Molecular Beam</i>	56
2.4 Instrumental Build: T-Jump Nano	59
2.4.1 <i>Introduction and Project Purpose</i>	59
2.4.2 <i>T-Jump Nano Operation and Design</i>	61
2.4.3 <i>T-Jump Nano Printed Circuit Board and Housing</i>	66
Chapter 3: Probing the Reaction Mechanism of Nanoscale Titanium/Potassium Perchlorate Pyrotechnic Powder	68
3.1 Introduction	69
3.2 Materials/Sample Preparation and Characterization	71
3.2.1 <i>Materials Preparation</i>	71

3.2.2 Titanium Nanoparticle Characterization.....	72
3.3 Rapid Heating Experiments	73
3.3.1 Temperature Jump (T-Jump)/Linear Time-of-Flight Mass Spectrometry .	73
3.3.2 TEM Heating.....	75
3.3.3 Ignition Characterization	76
3.4 Results and Discussion	79
3.4.1 Oxide Layer Characterization	79
3.4.2 Rapid Heating ($\sim 10^5$ K/s) Mass Spectrum Characterization.....	81
3.4.3 Rapid Heating ($\sim 10^5$ K/s) Ignition Characterization.....	87
3.4.4 Pre-Ignition: Oxide Layer Interaction with $KClO_4$	93
3.5 Conclusions.....	96
Chapter 4: Ignition and combustion analysis of direct write fabricated aluminum/metal oxide/PVDF films	97
4.1 Introduction.....	98
4.2 Methods/Experimental	100
4.2.1 Materials.....	100
4.2.2 Film fabrication	101
4.2.3 Characterization	104
4.3 Results and Discussion	107
4.3.1 Fabrication of Al/MO/PVDF films	107
4.3.2 Film combustion.....	111
4.3.3 T-Jump/TOFMS analysis of Al/MO/PVDF films	118
4.4 Conclusions.....	123
Chapter 5: High Temperature Interactions of Metal Oxides and a PVDF Binder....	125
5.1 Introduction.....	126
5.2 Experimental Methods	128
5.2.1 Materials.....	128
5.2.2 Thin Film Sample Preparation	129
5.2.3 Nanoparticle and Composite Characterization.....	130
5.2.4 Heating Experiments.....	132
5.2.4.1 Thermogravimetric Analysis-Differential Scanning Calorimetry (TGA- DSC).....	132
5.2.4.2 T-Jump/Linear Time of Flight Mass Spectrometry.....	132
5.3 Results and Discussion	134
5.3.1 Slow Heating Thermochemical Analysis	134
5.3.2 Rapid Heating Time-of-Flight Mass Spectrometry.....	139
5.4 Conclusion	145
Chapter 6: Numerically Evaluating Energetic Composite Flame Propagation with Thermally Conductive, High Aspect Ratio Fillers	147
6.1 Introduction.....	148
6.2 Modeling Structure	151
6.2.1 Thermal Transportation and Chemistry	151
6.2.2 Physical Layout.....	153
6.2.3 Model Analysis and Parameters	155
6.3 Results.....	157
6.3.1 Role of Rod Aspect Ratio in Combustion Performance	157

6.3.1.1	<i>Flame Propagation and Energy Release Rates</i>	159
6.3.1.2	<i>Pre-Heating of the Flame Front</i>	161
6.3.2	<i>Role of Rod Thermal Conductivity in Flame Propagation</i>	163
6.4	<i>Conclusion</i>	166
Chapter 7:	<i>Spatially focused microwave ignition of metallized energetic materials</i>	167
7.1	<i>Introduction</i>	167
7.2	<i>Methods/Experimental</i>	171
7.2.1	<i>Mie Theory Calculations</i>	171
7.2.2	<i>Materials</i>	171
7.2.3	<i>Film fabrication</i>	173
7.2.4	<i>Burn rate characterization</i>	176
7.2.5	<i>Focused microwave ignition</i>	176
7.3	<i>Results and Discussion</i>	178
7.3.1	<i>Microwave absorption of metals and material selection</i>	178
7.3.2	<i>Microwave sensitivity of metal powders</i>	184
7.3.3	<i>Microwave sensitivity of metallized propellants</i>	186
7.3.4	<i>Controlled-environment combustion characteristics of metallized propellants</i>	189
7.3.5	<i>Architecting of a microwave-initiated solid propellant</i>	191
7.4	<i>Conclusions</i>	194
Chapter 8:	<i>Summary and Future Works</i>	195
8.1	<i>Conclusion Summary</i>	195
8.2	<i>In situ TEM Heating of Select Perovskite Particles</i>	199
8.2.1	<i>Introduction</i>	199
8.2.2	<i>Experimental Instrumentation, Materials and Approach</i>	201
8.2.3	<i>Results and Discussion</i>	206
8.2.4	<i>Conclusions</i>	215
8.3	<i>MBMS Characterization of Energetic Films</i>	216
8.3.1	<i>Introduction</i>	216
8.3.2	<i>Materials and Experimental Approach</i>	219
8.3.3	<i>Results and Discussion</i>	222
8.3.4	<i>Conclusions</i>	232
8.4	<i>The Role of Isotope Labeling in Thermite Systems</i>	233
8.4.1	<i>T-Jump/TOFMS Analysis of Isotope Labeled Nanoscale CuO</i>	235
8.4.2	<i>Future Mechanistic Studies</i>	239
Supplemental Information	242
Chapter 2	<i>Supplemental Figures</i>	242
Chapter 3	<i>Supplemental Figures</i>	243
Chapter 4	<i>Supplemental Figures</i>	245
Chapter 5	<i>Supplemental Figures</i>	247
Chapter 6	<i>Numerical Methods</i>	248
Chapter 7	<i>Supplemental Figures</i>	255
Appendices	257
Appendix A:	<i>Specifications and Maintenance of the T-Jump/TOFMS System</i> ..	257
Appendix B:	<i>Solution-Based Additive Manufacturing with Hyrel 3D System</i> ..	262
B.1	<i>Hardware and Instrument Parameters</i>	262

<i>B.2 Frequently used Architecture and Gcode Scripts</i>	273
Appendix C: Matlab Scripts for T-Jump/TOFMS	284
Appendix D: Arduino Script Example for T-Jump Nano	291
Appendix E: 2D Flame Front Model MATLAB Script.....	292
List of References	304

List of Tables

Table 3.1: Highlighted physical properties of aluminum and titanium species.....	70
Table 3.2: T-Jump activation energies.	88
Table 4.1: Energetic precursor formulations.....	102
Table 4.2: Film mechanical and morphological properties.	104
Table 4.3: Film energy release comparison when compared to Al/PVDF.	117
Table 7.1: Energetic precursor formulations.....	174
Table 7.2: Complex dielectric constant and complex magnetic constants used in calculations to estimate the intensity fraction absorbed and the maximum temperature.	181
Table 7.3: Free-standing burn velocities in air and argon environments and ability to be ignited with microwaves.	188

List of Figures

Figure 1.1: Historical developments and use of heterogenous solid energetic materials from early man’s use of wood fueled fires, the recorded formulation of gun powder, to man’s ventures to the stars. Original “Rockets Red Glare” artwork by Abraham Hunter ©2016. Image sources: Nasa.gov, Wikimedia commons.	4
Figure 1.2: A comparison of specific combustion enthalpies of energetic metals with O ₂ in relation to modern explosives with the relative abundance of reactive metals displayed. ²⁹	8
Figure 1.3: Reducing heterogenous energetic components enhances reactivity due to reduced diffusion length scales and specific surface area, s. Monomolecular energetics have fuel and oxidizer “pre-packaged” at the molecular scale.....	11
Figure 1.4: Modeling and experimentation of the coalescence of aluminum nanoparticles under rapid heating conditions. Rapid sintering is a primary factor in the reduction burn rates compared to theoretical single particle burn rates. Adapted with permission from the stated references. ^{40,45}	17
Figure 1.5: Comparison of exothermicity (per gram of metal) and relative volatility of products formed from the oxidation/fluorination of energetic metals.....	20
Figure 1.6: Polymer bound energetic composite architectures: Mesoparticles (3D), Thin films (2D), Fibers (1D). ^{37,96}	28
Figure 1.7: Sub-divisions of most common methods for macroscopic additive manufacturing of energetic materials. ⁹⁷	31
Figure 2.1: Routine setup of the T-Jump experiment conducted in a sealed chamber of differing atmosphere. Key heating, timing, and monitoring components are depicted.	43
Figure 2.2: Ti/CuO thermite T-Jump ignition in argon illustrating the a) temperature profile and light intensity as a function of time where the b) ignition point can be determined through frame by frame analysis of synchronized high-speed videography.....	44
Figure 2.3: T-Jump analysis of the a) ignition temperature of Ti/KClO ₄ energetic composition as a function of heating rate(β) for which the b) activation energy of ignition maybe calculated using the relation given by the Flynn–Wall–Ozawa isoconversion method.	45
Figure 2.4: Schematic of the a) TOF ionization, acceleration, and detection of gas species which have a b) voltage/signal profiles which are actuated by a trigger source	47
Figure 2.5: Box schematic of the Time-of-Flight electronics wiring setup which includes the triggering device, oscilloscope, and power supply for all necessary components.	49
Figure 2.6: Coupling of the a) TOFMS system with the T-Jump technique using the b) customized T-Jump probe.	51
Figure 2.7: Time resolved a) full mass spectrum and b) single species detection profile as a function of temperature from the heating of KClO ₄ submicron particles (T-Jump/TOFMS).....	53
Figure 2.8: Experimental setup and Molecular Beam Mass Spectrometer schematic of flame sampling during combustion.	56

Figure 2.9: Schematic of the T-Jump nano (Autodesk Eagle 8.4.2.) apparatus including the high heating rate wire, solid-state relay, and oscilloscope.....	62
Figure 2.10: Initial solderless breadboard prototype of the T-Jump nano. The breadboard in the top left includes a monostable multivibrator and solid-state relay that would actuate a high-voltage pulse to resistively heat a wire. This multivibrator would be modulated with a signal sent by the Arduino Uno (top right) which is controlled with triggers wired in on the breadboard below it.....	63
Figure 2.11: Arduino output waveforms: repeated (green) and single shot (blue)....	64
Figure 2.12: Theoretical output signals for heating and Arduino control (BNC outputs)	66
Figure 2.13: Diagram of custom printed circuit board to serve as a shield for Arduino Uno (Rev3). Printed circuit board is manufactured by OSH Park.....	67
Figure 2.14: a) PCB of T-Jump Nano circuit mounted to Arduino board and b) PCB aluminum enclosure with output switches, BNC connectors, and heating relay.....	67
Figure 3.1: Maximum combustion enthalpies of stoichiometric mixtures ($\phi=1$)	71
Figure 3.2: SEM characterized spray-dried micron-sized KClO_4 particles with b) a rough particle size distribution (200 particle sample size)	72
Figure 3.3: TEM characterized titanium nanoparticles from US Research Nanomaterials, Inc.	73
Figure 3.4: SEM of nTi/ KClO_4 powder coated on platinum T-Jump wires	74
Figure 3.5: Average active Titanium content determined by TGA-DSC of titanium nanoparticles heated in oxygen at 10 °C/min.....	77
Figure 3.6: X-ray diffraction pattern of a) Titanium nanoparticles as received, b) simulant TiO_2 nanoparticles, c) Spray Dry KClO_4 particles, and d) TKP combustion products heated to 750°C (TGA).....	78
Figure 3.7: XPS analysis of titanium nanoparticles and TiO_2 -anatase nanoparticles with peak fits.....	80
Figure 3.8: a) KClO_4 T-Jump averaged spectrum over 10ms collection time (used only for species identification purposes) and b) KClO_4 oxygen release as a function of heating rate (Release temperatures determined by averaging 3-4 repeated measurements).	82
Figure 3.9: Arrhenius plots of KClO_4 oxygen release and ignition of relevant mixtures. See Table 3.2 for activation energies.....	83
Figure 3.10: TGA-DSC of Spray Dried KClO_4 depicting the onset of a) crystalline phase transition (orthorhombic-cubic) at 300°C, b) melting at 590°C followed immediately by c) decomposition to KCl at 610°C, and finally d) KCl melting at 770°C.....	84
Figure 3.11: a) nTi/ KClO_4 ignition species averaged mass spectrum over 10ms collection time and b) nTi T-Jump averaged mass spectrum over 10ms collection time	85
Figure 3.12: nTi/ KClO_4 T-Jump ignition in vacuum (top) and argon (bottom) at $\sim 3 \times 10^5$ K/s visually depicting the constraining effect of ignition in a pressurized environment.	87
Figure 3.13: Pressure dependence of nTi/ KClO_4 ignition in O_2 and Ar.....	89

Figure 3.14: In situ heating of a (a) single TKP aggregate at room temperature with micron sized KClO_4 superimposed onto nanosized titanium particles. Subsequent (b) heating of the aggregate up to 850 K (580 °C) results in KClO_4 decomposition (c) leaving the remaining reactant/product particles coated in KCl.	91
Figure 3.15: Rapid Heating TEM of titanium nanoparticles with minimal sintering	92
Figure 3.16: TKP primary reaction mechanism summary; the sudden release of oxygen from the enveloping KClO_4 melt reacts with the preserved nanostructure of the titanium particles. Oxygen reacts with the oxide layer, enhances oxygen diffusion, and then reacts with the titanium core.	93
Figure 3.17: Catalytic effect of TiO_2 on KClO_4 decomposition (TGA analysis in argon).	94
Figure 3.18: TGA analysis in argon between simulat mixture, TKP, and bare oxidizer; oxygen decomposition of TKP and simulat mixture occur at roughly the same temperature.	95
Figure 4.1: TEM of as received aluminum and metal oxide nanoparticles	101
Figure 4.2: SEM images of a) Al/PVDF single layer film cross-section, and b)-c) 5-layer film morphology and combustion sample prep	103
Figure 4.3: a) Al/MO/PVDF T-jump wire coating b) ignited via rapid joule heating (T-Jump)	106
Figure 4.4: SEM cross-section of 5-layer ($\approx 14 \mu\text{m}/\text{layer}$) 3D printed a) Al/PVDF, b) Al/ Bi_2O_3 /PVDF, c) Al/CuO/PVDF, and d) Al/ Fe_2O_3 /PVDF Films	108
Figure 4.5: Shear rate-controlled viscosity measurements as a function of shear rate for the most viscous (red) and least viscous (blue) DMF based precursor inks	110
Figure 4.6: Stress-Strain curves of a single layer of the various film composites...	111
Figure 4.7: SEM images of the cross-section of a) Al/ Bi_2O_3 /PVDF, b) Al/CuO/PVDF, and c) Al/ Fe_2O_3 /PVDF at 67 wt. % particle loading	111
Figure 4.8: a) Snap shots of steady flame propagation of Al/CuO/PVDF with 50 wt. % particle loading accompanied by b) representative linear distance over time plots of each composition. Averaged flame speed results are consolidated in a c) comparative bar graph.	112
Figure 4.9: Characteristic film combustion (right to left) behavior of a) Al/PVDF, b) Al/ Bi_2O_3 /PVDF 50 wt. % particle loading, c) Al/CuO/PVDF 50 wt. % particle loading, d) Al/ Fe_2O_3 /PVDF 50 wt. % particle loading, e) Al/ Bi_2O_3 /PVDF 67 wt. % particle loading, and f) Al/CuO/PVDF 67 wt. % particle loading.....	112
Figure 4.10: Combustion products analysis (SEM, EDS, XRD) of a) Al/PVDF, b) Al/ Bi_2O_3 /PVDF, c) Al/CuO/PVDF, and d) Al/ Fe_2O_3 /PVDF films ignited in an argon atmosphere	114
Figure 4.11: Illustration of the proposed mechanism for the observed burning behavior of Al/MO/PVDF films	115
Figure 4.12: Snap shots of spatiotemporal temperature measurements made by color camera pyrometry on a) Al/PVDF, b) Al/ Bi_2O_3 /PVDF (50 wt.% particles), c) Al/ Bi_2O_3 /PVDF (67 wt.% particles), d) Al/ Fe_2O_3 /PVDF (50 wt.% particles), e) Al/CuO/PVDF (50 wt.% particles), and f) Al/CuO/PVDF (67 wt.% particles) films burning from right to left.	116

Figure 4.13: Ignition of the various Al/MO/PVDF composites in argon and vacuum environments.....	119
Figure 4.14: Ignition temperature of metal oxide specified powdered thermite relative to the ignition temperature of thermite integrated into Al/PVDF composites in argon and vacuum.	119
Figure 4.15: Normalized HF signal intensity of the various Al/MO/PVDF composites subject to T-Jump/TOFMS	120
Figure 4.16: T-Jump/TOFMS Mass spectra of Al/MO/PVDF composites averaged over 10 ms.....	121
Figure 4.17: T-Jump/TOFMS Mass spectra of MO/PVDF composites averaged over 10 ms.....	122
Figure 5.1: TEM depictions of aggregates of the metal oxide particles used in this study.....	131
Figure 5.2: SEM cross-sections of all metal oxide/PVDF thin film compositions illustrating metal oxides encapsulated within the PVDF matrix.	132
Figure 5.3: TGA-DSC of select metal oxide/PVDF thin films under an argon environment, heated at 10 °C/min.....	134
Figure 5.4: Temperature dependent XRD analysis of condensed phase TGA-DSC heated products of metal oxide/PVDF thin films: a) CuO/PVDF, b) Bi ₂ O ₃ /PVDF, c) TiO ₂ /PVDF, d) MgO/PVDF, e) Al ₂ O ₃ /PVDF, f) SiO ₂ /PVDF.....	136
Figure 5.5: Averaged mass spectrum over a 10 ms collection period of rapidly heated Pt wires which are thinly coated with the selected metal oxide/PVDF compositions. The most notable mass species are label.....	140
Figure 5.6: Time-dependent full mass spectra of rapidly heated PVDF ($\approx 3 \times 10^5$ K/s) over 3 ms depicting onset HF release 200 μ s prior to the detection of the large pyrolysis species.	141
Figure 5.7: T-Jump/TOFMS measured relative HF release maximum (HF ratio) of metal oxide/PVDF compositions as a function of release temperature.	142
Figure 5.8: Initialization of the proposed interactions between the studied metal oxides and PVDF where those on the top layer release far more HF gas and react with decomposing PVDF at early temperatures compared to neat PVDF decomposition.	144
Figure 6.1: Spectrum of thermal conductivities typically used in polymer composites with tunable thermal properties	149
Figure 6.2: Relative thermal diffusivity (<i>afar</i>) mapping with respect to volume fraction for a) simple homogeneously mixed, uniform distribution, and b) distribution of rod of variable aspect ratios as well as an example of c) the heterogeneity scaling of solid energetic constituents relative to δ	155
Figure 6.3: a) Flame front snapshot and b) time resolved behavior of the accumulated area of the pre-heated zone, total burned material, and burned energetic material for the case of AR=55, Vol.%=20, t=480 μ s (left to right propagation).	158
Figure 6.4: Effect of aspect ratio and vol.% of rods with a fixed thermal conductivity on a) the change in total area burned, b) energy released over the allotted burn time, and c) the extent of pre-heating during flame propagation.....	159

Figure 6.5: Effect of thermal conductivity and vol.% of rods with an aspect ratio (AR=45) on a) the change in total area burned, b) energy released over the allotted burn time, and c) the extent of pre-heating during flame propagation.	164
Figure 6.6: Thermal mapping of energetic material propagation integrating rods with varied thermal conductivities within an invariant AR=45 rod mapping of 20 vol.% at $t=325 \mu\text{s}$ (Propagation from left to right).....	165
Figure 7.1: Transmission electron microscopy images of the as-received (a) nano-Aluminum (Novacentrix) and (b) nano-Titanium (US Research Materials). Images taken with a FEI Tecnai12	172
Figure 7.2: Scanning electron microscopy images of the cross-section for as-received (a) 3-4.5 μm diameter Al micron particles (Alfa Aesar) and (b) 10-14 μm diameter Al micron particles (Alfa Aesar). Images taken with a FEI NNS450	173
Figure 7.3: Scanning electron microscopy images of the cross-section for (a-b) Al/PVDF and (c-d) Ti/PVDF films. Each printed sample is 4 layers thick. Images taken with FEI NNS450.....	175
Figure 7.4: (a) Needle-based microwave ignition experiment at 2.45 GHz. Peak power of the entire system is $\approx 15\text{W}$. (b) Simulations of the electric field at the tip of the needle for a frequency of 2.45 GHz (using Ansys HFSS and an auto-generated mesh).....	177
Figure 7.5: (a) Calculated fraction of microwave (2.45 GHz) intensity absorbed for bare and core-shell Al and Ti nanoparticles in a 25 μm diameter cylinder as a function of depth and (b) the estimated maximum temperature after being exposed to a microwave input of 15 W for 0.5 s. Physical properties used in calculation are provided in Table 7.2.	181
Figure 7.6: (a) Ignition of nano-Ti powder in air (50nm diameter) using microwave needle apparatus imaged using a high-speed camera. $t=0$ defined as starting time for power supplied to the applicator. Dashed white line indicates position of needle. (b) Simulation of the experiments in (a) showing the near field electric field on the ground plane performed using Ansys HFSS and an auto-generated mesh.	184
Figure 7.7: Ignition of Ti/PVDF (65 wt.% Ti) film in air using microwave needle apparatus imaged using a high-speed camera. $t=0$ defined as starting time for power supplied to the applicator. Dashed white line indicates position of needle.	188
Figure 7.8: Distance vs. time data used to estimates for the propagation rate of Table 7.3 compositions in air and argon	190
Figure 7.9: (a) Depiction of the architecture for a layered Al/PVDF, Ti/PVDF propellant that can be initiated with microwaves where layers 1-4 are Al/PVDF ($\Phi=1$) and layer 5 is Ti/PVDF (65 wt.% Ti) ($\approx 35 \mu\text{m}$ thick). (b) SEM/EDS image of layered film cross-section as outlined in a. (c) EDS line scan results for line drawn in b. ...	192
Figure 7.10: Microwave needle ignition of a layered Al/PVDF, Ti/PVDF propellant where layers 1-4 are Al/PVDF ($\Phi=1$) and layer 5 is Ti/PVDF (65 wt.% Ti). (a) Al/PVDF region does not ignite when exposed to microwave radiation and (b) Ti/PVDF layered region ignites and propagates into Al/PVDF region.	193

Figure 8.1: Protochips Atmospheric System for TEM: a) Scroll pump, b) Gas manifold, c) Holder, d) Leak check station, e) Software, f) Power Supply, g) E-Chip calibration file, and h) FEI Titan TEM-STEM.	201
Figure 8.2: TEM images taken at UCR of LaCoO ₃ particles which highlight the morphological mixture of particles.	204
Figure 8.3: Initial TEM images of perovskite nanoparticles and first attempt at EELS scans highlighting the need for pre-heating of material to 300 °C.	206
Figure 8.4: LaCoO ₃ nanoparticle aggregate imaging a) prior to and c) after heating with b)-d) EELS mapping illustrating the splattering of cobalt atoms around the substrate puncture.	207
Figure 8.5: a)-c) TEM image and EELS mapping of La _{0.6} Sr _{0.4} FeO ₃ prior to heating with a d)-f) core-shell type structure forming upon reaching 1000 °C.	208
Figure 8.6: Heating protocols for La _{0.6} Sr _{0.4} CoO ₃ , LaCoO ₃ , and LaCrO ₃ samples. .	209
Figure 8.7: TEM imaging and EELS elemental mapping of La _{0.6} Sr _{0.4} CoO ₃ a)-d) before and e)-h) after the proscribed heat protocol under 760 Torr nitrogen gas.	210
Figure 8.8: TEM imaging and EELS elemental mapping of LaCoO ₃ a)-d) before and e)-h) after the proscribed heat protocol under 760 Torr nitrogen gas.	211
Figure 8.9: TEM imaging and EELS elemental mapping of LaCrO ₃ before and after the proscribed heat protocol under 760 Torr nitrogen gas.	212
Figure 8.10: Heating protocol for simulating chemical looping experiments with cycling of H ₂ /Ar and O ₂ environments	213
Figure 8.11: Quartz tube/camera setup within the vacuum environment of the sampling region of the MBMS	222
Figure 8.12: Al/PVDF combustion mass spectra in a) Vacuum (~10 ⁻⁶ Torr) for T-Jump/TOFMS ignition product sampling and b) 1 atm N ₂ for MBMS combustion product sampling.	223
Figure 8.13: a) Al/PVDF combustion average mass spectra in N ₂ with additives: b) 20 wt.% I ₂ and c) 5 wt.% SiO ₂	225
Figure 8.14: Species over time of HF and AlF ₃ detected as products from the combustion of Al/PVDF, Al/PVDF/SiO ₂ , and Al/PVDF/I ₂ in 1 atm N ₂	227
Figure 8.15: Spatial mapping of the temperature distribution of the flame from the combustion of Al/PVDF-based energetic films within the quartz tube of the MBMS.	228
Figure 8.16: Mean spatial flame temperature and corresponding light intensity from Al/PVDF composite combustion.	229
Figure 8.17: a) Evolution of acetylene and CO ₂ product species of Al/PVDF combustion in air compared with the b) time scale of the combustion event.	231
Figure 8.18: Average mass spectrum of a) commercial CuO and b) water washed Cu ¹⁸ O.	235
Figure 8.19: Time resolved mass spectrum analysis for Cu ¹⁸ O with respect to a) O ₂ isotopes and b) water and carbon dioxide isotopes.	236
Figure 8.20: Air Sensitive Sample Holder (ASSH) with a s) sheath and cap design with b) 3D printed collar for puncturing of the aluminum foil seal. ¹³⁰	237
Figure 8.21: a) Cumulative mass spectrum and b) time resolved O ₂ isotope speciation from T-Jump/TOFMS of Cu ¹⁸ O nanopowder prepared using air-free and water-free methods.	238

Figure 8.22: Time resolved speciation of a) major ^{18}O containing molecules (water, carbon dioxide, oxygen gas) and b) all carbon dioxide isotope species.	238
Figure S2.1: KClO_4 particles coated on T-Jump Pt wire with particles prepared by the a) aerosol spray pyrolysis method and by b) ball milling. Ball milling results in particles which are harder to coat on the $76\mu\text{m}$ Pt wire.....	242
Figure S2.2: Example of the mass-time calibration for TOF collected in 2019.....	243
Figure S3.1: EDS of homogenously mixed nTi/ KClO_4 powder composite.	243
Figure S3.2: Protochips In Situ microscopy TEM heating probe.....	244
Figure S3.3: Post combustion products collected on carbon tape depicting titanium oxide formation with KCl first being vaporized by the heat of reaction then condensing on the surface of the titanium oxide.	244
Figure S3.4: Aluminum and Titanium nanoparticles immersed in water for 3 days (Titanium remains unreacted).	244
Figure S3.5: Comparison of a) room temperature TKP aggregate with a b) TKP aggregate which has been heat past the melting point of KCl and TEM elemental mapping performed.	245
Figure S4.1: Quartz tube argon chamber for simultaneous film combustion and high-speed videography.	245
Figure S4.2: Combustion of Al/PVDF in a) argon and b) air captured at 3000 FPS and c) tracked using Image J to obtain flame speeds.....	245
Figure S4.3: EDS homogeneity analysis of the cross-section of films with various metal oxides and particle loadings.....	246
Figure S4.4: SEM images of the top surface of Al/ Fe_2O_3 /PVDF films at a)-b) 50 wt. % particle loading and c)-d) 67 wt. % particle loading.	246
Figure S4.5: Comparison of a) Al/ Bi_2O_3 , b) Al/ CuO , c) Al/ Fe_2O_3 thermite ignition to d) Al/ Bi_2O_3 /PVDF, e) Al/ CuO /PVDF, f) Al/ Fe_2O_3 /PVDF film ignition in argon. ..	247
Figure S5.1: Time-dependent full mass spectra of rapidly heated CuO /PVDF ($\approx 3 \times 10^5$ K/s) over 3 ms depicting onset CO_2 prior to HF release and subsequent release of larger pyrolysis species.	247
Figure S5.2: CuO /PVDF a) TGA profile and b) resulting rate of mass loss as function of CuO mass.	248
Figure S6.1: a) Grid of relevant temperature nodes for position index p,q at the $(n+1)^{\text{th}}$ time step with b) visualization of the implicit finite difference method using adjacent temperature nodes in the previous time step.	249
Figure S6.2: Thermal resistance approach for defining effective thermal conductivity at the boundary of discrete thermal conductivity distribution.	251
Figure S6.3: Thermal mapping of energetic material propagation incorporating rods of constant thermal conductivity ($k=k_0 10^4$) with varied aspect ratios at 30 vol.% at $t=325\mu\text{s}$ (Propagation from left to right).....	254
Figure S6.4: Truncated fluctuations of the extent of pre-heating as a function of time during flame propagation.....	254

Figure S7.1: Images from microwave heating and ignition experiments for nano-titanium as performed in a glass tube with an inert Argon environment. Right image shows small heating point immediately around the microwave source.....	255
Figure S7.2: Ti-PVDF argon environment post combustion products.	256
Figure B.1: Photo-polymerization process of UV curable materials.....	270
Figure B.2: Dual rectangular print design	274
Figure B.3: Dual Printing Head, Dual rectangular print design	277
Figure B.4: Print design for printing on glass coverslips	279
Figure B.5: Print design for printing of viscous, high particle loading inks on glass coverslips	282

List of Abbreviations

ASP	Aerosol Spray Pyrolysis
ASSH	Air Sensitive Sample Holder
nAl	Aluminum Nanoparticles
AN	Ammonium Nitrate
AP	Ammonium Perchlorate
ALD	Atomic Layer Deposition
HMX	Cyclotetramethylenetetranitramine
RDX	Cyclotrimethylenetrinitramine
DSC	Differential Scanning Calorimetry
DLP	Digital Light Processing
DIW	Direct Ink Writing
E-gun	Electron Gun
ESD	Electrostatic Discharge
FPS	Frames Per Second
FFF	Fused Filament Fabrication
GAP	Glycidyl azide
Viton A	Hexafluoropropylene/vinylidene fluoride
CL-20	Hexanitrohexaazaisowurtzitane
HTPB	Hydroxyl-terminated polybutadiene
MIC	Metastable Intermolecular Composite
MCP	Microchannel Plate
MEMS	Microelectromechanical Systems

MBMS	Molecular Beam Mass Spectrometer
NIST	National Institute of Standards and Technology
NC	Nitrocellulose
TNT	Trinitrotoluene
PTFE	(Poly)tetrafluoroethylene
PVDF	(Poly)vinylidene Fluoride
PI	Proportional-Integral
PID	Proportional-Integral-Derivative
RTOFMS	Reflectron Time-of Flight Mass Spectrometry
SEM	Scanning Electron Microscopy
SLA	Stereolithography
T-Jump	Temperature Jump
THV	Tetrafluoroethylene/hexafluoropropylene/vinylidene fluoride
TGA	Thermogravimetric Analysis
TOFMS	Time-of-Flight Mass Spectrometer
nTi	Titanium Nanoparticles
TKP	Titanium/Potassium Perchlorate
TEM	Transmission Electron Microscopy
XRD	X-ray Diffraction
XPS	X-ray Photoelectron Spectroscopy

Chapter 1: Introduction

The discovery of novel materials and improved engineering controls for enhanced combustion performance has been instrumental to our existence on this planet. They are a means of generating heat, light, and gases for industry, transportation, cooking, climate control, and advancements in warfare.¹ Combustible materials come in all phases (*i.e.* gas, liquid, solid) with mechanisms for combustion being either self-contained (*i.e.* monomolecular propellants/explosives) or heterogenous, in which multiphase processes take place. In particular, the evolution of solid energetic materials through history is marked by the desire for controllable, reliable access to chemically stored potential energy to be converted to kinetic energy.¹ Research efforts focusing on the utility of solid energetic materials focus on several characteristics, which include heat of combustion (amount of energy produced from combustion reaction), sensitivity to external stimuli (*e.g.* impact, shock, electrostatic, thermal), brisance (shattering capability), detonation velocity, power (work energy per time), material quality, and material stability² (ability of energetic material to remain unaltered under adverse conditions or after long periods of storage).^{3,4} Furthermore, characterization of combustion performance is often standardized based on ignition delay times,⁵ duration of combustion, flame front morphology (*e.g.* height, intensity, area, etc.), velocity, and interactions with the environment.^{4,6,7}

1.1 Basics of Solid Energetic Materials

Solid energetic materials are categorized into “propellants”, “explosives”, and “pyrotechnics” with general applications in space technology,⁸ ordinance, fireworks,

automobile airbags,⁹ mining, initiators, and deconstruction.^{3,6,10,11} The difference in these categorizations is the rate at which the non-linear reactions proceed after they ignite. Compositions ignite when the exothermicity of a reaction exceeds the energy dissipation rate to establish a self-sustained chemical reaction at a nominal temperature point, known as the “ignition temperature”.^{1,3,5,12,13} Explosives are defined as a material which detonates, characterized by a high pressure shock wave (*i.e.* rapid change in pressure) moving at supersonic speeds through the explosive medium. The reaction rate is determined by the velocity of the shock wave ($\geq 10^3$ m/s) and not the rate of heat transfer.^{1,3,6} Both propellants and pyrotechnics are heterogenous compositions of fuel and oxidizer, which are non-explosive with burning described as a deflagration event. Deflagration is characterized by a relatively slow reaction taking place on the surface of the energetic material and proceeds into the grain via heat transfer mechanisms (10^3 - 10^2 m/s).^{1,3,6,10,11} In general, explosive materials may also deflagrate in which the transition point from deflagration to detonation in both monomolecular and composite energetics has been an important topic of research.^{3,14} Propellants generate gas to provide lower pressures over a longer time period to effectively provide and sustain pressure (thrust) in propelling objects.^{3,6} Solid propellants have advantages, such as safety, storage stability (30+ years), resistance to unintended detonation, simplicity, adequate functionality, and high mass flow rates, which make solid propellants preferable in small missiles for instantaneous readiness.^{9-11,15} The Saint Robert’s law ($r_b = a \cdot P^n$) is widely used for solid propellant characterization to calculate a fit of burning rate, r_b , as a function of pressure, P , and determine its pressure exponent, n , which ultimately sets its viability for applicational usage.¹⁶ Comparatively,

pyrotechnics have many of the same characteristics as propellants but evolve large amounts of heat and generate negligible gaseous products.^{3,6}

1.2 Historical Developments of Solid Energetics

Developments and advancements of solid energetic materials of all types draw a direct relationship between basic research and technology in the realm of warfare, where advancements give an impetus to further research.³ Flame and incendiary devices are the oldest form of organic material chemical weapons dating back to as early as the caveman's use of flames and burning coals for cooking and fending off animals and rivals.³ Basic incendiaries have proven to be effective in their potential for destruction, as exemplified by the use of fireballs of resinous wood and straw in the Greco-Roman Classical Era to the indiscriminate deployment of thermite bombs over early 20th century European cities and Napalm in the jungles of Vietnam.³ Energetic materials have gone through many technological developments and adaptations beyond simple incendiary devices and has had a major influence over the course of history as we know it.^{3,17}

The debut of the earliest forms of recreational fireworks for great displays of lights, color, noise, and smoke in China during the Song dynasty would eventually lead to the development of pyrotechnics for illuminating ravaged fields of battle (*e.g.* star shell flare) and colored smoke signaling devices (*e.g.* M18 smoke grenades) for air to ground identification.³ The discovery of black powder (*i.e.* KNO_3 , also known as saltpeter, sulfur, and charcoal) by the Chinese, Arabs, and Hindus (formulas recorded by the English monk Roger Bacon in 1249) began the history of explosives as a primary means to transition chemical energy to mechanical work.^{3,9,15,17} Further European

developments of black powder with differing equivalence ratios (relative ratio of composite fuel mass to oxidizer mass compared to the stoichiometric ratio)^{1,18} led to its ubiquitous utility in blasting, mining, and propulsion in early 14th century developments of guns and ballistics technology. One notable example is the British Congreve rocket; adapted from crude, black powder fueled Indian bamboo rockets and immortalized by Francis Scott Key’s “rocket’s red glare” description in the writing of the Star Spangled Banner during the siege of Fort McHenry in the War of 1812.^{3,17,19}

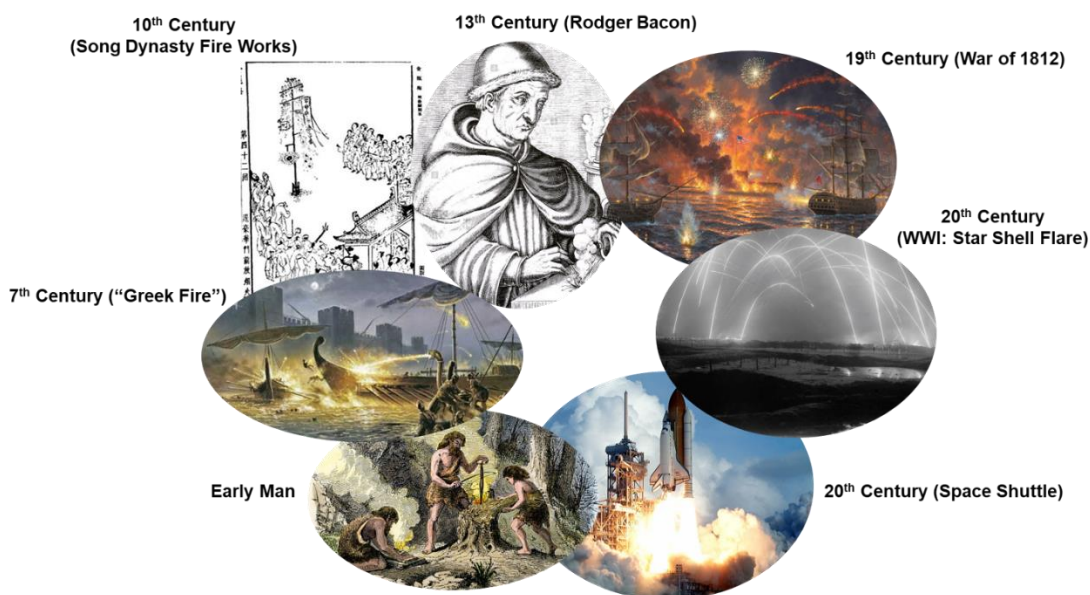


Figure 1.1: Historical developments and use of heterogenous solid energetic materials from early man’s use of wood fueled fires, the recorded formulation of gun powder, to man’s ventures to the stars. *Original “Rockets Red Glare” artwork by Abraham Hunter ©2016.* Image sources: Nasa.gov, Wikimedia commons.

In 1833, the synthesis of nitrostarch (*i.e.* starch in nitric acid) by French chemist Henri Braconnot launched the development of modern, more powerful smokeless monomolecular propellants, detonators, and high explosive technology after 350+ years of black powder use.^{3,20} The heterogenous energetic composite of black powder would be phased out by increasingly more powerful single component nitroamine

explosives with utilizations and adaptations developed for differing applications depending on various thermal stabilities, mechanical properties, and sensitivities to external stimuli.^{6,21} The power of high explosive technology was put on display during World War I & II with volleys of artillery shells and aerial bombs tipped with Trinitrotoluene (TNT), which was developed in 1863 by Germany's J. Willibrand but not exploited for its explosive characteristics until 1904.³ Likewise, Henning developed cyclotrimethylenetrinitramine (RDX or cyclonite) in 1899 Germany. RDX was initially used for medical purposes but ultimately became the most viable and utilized successor of TNT for its superior brisance and use underwater for torpedo applications.³ Endeavors for even higher enthalpy molecular architectures with the potential for even larger energy output resulted in the synthesis of currently used high explosives such as hexanitrohexaazaisowurtzitane (CL-20), cyclotetramethylenetetranitramine (HMX), and many other nitroamine explosives.^{3,6,21}

1.3 Solid Propellants

Although high explosive materials generate large amounts of gas over a short period of time, they alone are largely unsuitable for propellant applications. This is due to the exceedingly large pressures generated, lack of mechanical strength, high shock and impact sensitivity, lack of thermal stability, and low temperature phase changes which compromise mechanical integrity.^{6,21} Therefore, heterogeneous solid propellants with greater mechanical integrity and reliability were established as the backbone for space exploration through instrumented or manned spacecraft.¹¹ Traditional solid rocket propellants are prepared through liquid or semi-liquid methods for fabrication of homogenous mixtures of a gas producing solid oxidizer powder embedded within

an organic polymeric fuel, which also acts as a plastic binder.^{3,9,11,22,23} Effective binders for solid propellant applications need to be a high caloric material, compatible with high-energy ingredients, and allows for high-solid loadings to be thoroughly mixed for enhanced interfacing of the fuel and oxidizer.^{7,11} Typically, this is the case for non-toxic polymers which are minimally hygroscopic with low glass transition temperatures and have a narrow molecular weight distribution for low viscosity precursor mixing.^{7,11} While a variety of both energetic (*e.g.* glycidyl azide (GAP), nitrocellulose (NC)^{24,25}) and non-energetic (*e.g.* epoxy-, nitrocellulose-, and fluorine- containing polymers^{3,9,11}) binders have been employed and extensively studied, no binder type has been as effective as the inexpensive polyurethane binder hydroxyl-terminated polybutadiene (HTPB).¹⁵ HTPB has been used for over half a century owing to its superior mechanical and aging properties,⁹ suitable chemical stability and degradation behavior for enhanced reaction kinetics, and ability to mechanically withstand larger variations in temperature.^{6,7,11}

Conventional HTPB solid propellants typically have up to 80 wt.% of oxidizer with traditional propellants using ammonium perchlorate (AP) as the primary oxidizer.^{9,15,23} AP was first synthesized by German chemist E. Mitscherlich in 1832 and can act as both an oxidizer and low-grade explosive. AP has been extensively studied and primarily used in most solid rocket motors for its thermal stability, high oxygen content, and ability to generate corrosive gases.²⁶ The chlorine-based corrosive gases etch through the native aluminum oxide shell to produce fast burning rates and large energy outputs.^{3,9,11,22,23} Understanding the deflagration behavior of these materials and probing the diffusional and kinetic processes between additional

energetic components of heterogenous systems has become the forefront of energetic materials research in exploring combustion propagation limits.^{16,20}

1.4 Metallized Heterogenous Energetic Composites

Due to the fundamental thermodynamic limitations of organic CHNO chemistry, fine metal powders with high reaction enthalpies are used within contemporary heterogenous solid energetic systems. Even the most modern molecularly engineered single component high explosives, such as CL-20, are near the limitations of potential energy that may be stored in such chemical bonds.^{3,27,28} Aluminum is one of the more commonly utilized metal powders in solid propellant systems, powder ignitors, and modern incendiary devices. This is due to its large abundance in the Earth's crust^{29,30}, relative stability, low ignition threshold, and high specific energy density as a result of oxygen oxidation compared to the enthalpy of detonation of high explosives (31 kJ/g vs. 6.2 kJ/g).^{3,18,20,31} In general, the choice of metal powder is dependent on cost and specific kinetics/reaction mechanisms of powdered metal fuels with oxygen producing far more exothermic interactions than monomolecular explosives and thus reach higher temperatures of reaction.³² A comparison of the specific heats of combustion for materials of primary focus within the energetic community are shown in Figure 1.2.

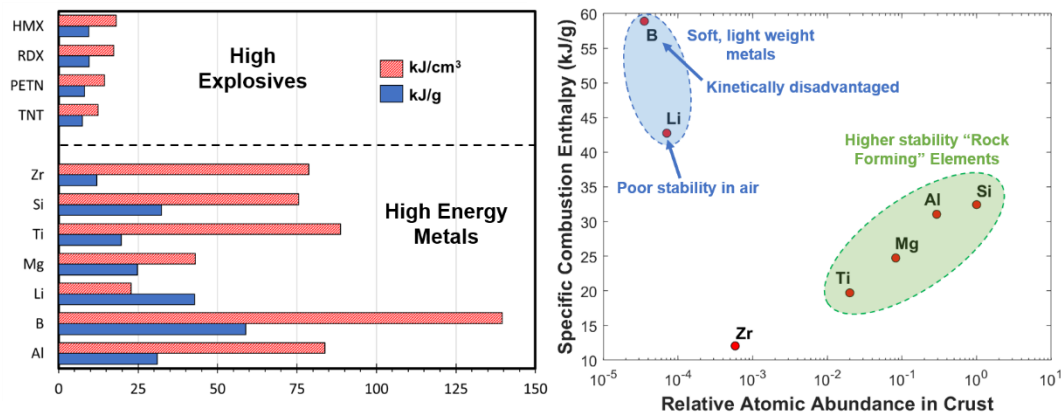
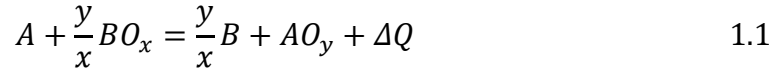


Figure 1.2: A comparison of specific combustion enthalpies of energetic metals with O_2 in relation to modern explosives with the relative abundance of reactive metals displayed.²⁹

Aluminized explosives were first proposed by R. Escales of Germany in 1899 with the creation of “Ammonal”. This mixture of ammonium nitrate, charcoal, and aluminum was utilized in incendiary artillery shells, rifle bullets, and grenades to set fire to buildings, supply dumps, and enemy observation balloons by both factions of World War I (1914-1917).³ Such energetic compositions are typically categorized as either “reactive materials”, “metastable intermolecular composites” (MICs), or pyrotechnics. Heterogenous powdered mixtures of metal fuels (*e.g.* Al, Ti, Mg, Si, B) and oxidizers in the form of metal oxides or metal salts as a source of condensed oxygen (*e.g.* CuO , MoO_3 , Fe_2O_3 , Bi_2O_3 , I_2O_5 , $KClO_4$, NH_4ClO_4 , etc.) are colloquially referred to as “thermites” and fall under the subcategory of pyrotechnics.^{23,31,33} These high combustion enthalpy reactions are based on the formation of a more thermodynamically stable oxide (*e.g.* Al_2O_3 , TiO_2 , MgO , SiO_2 , B_2O_3) that typically contains a single metal oxide. The addition of multiple oxidizers can lead to unexpected results and incomplete combustion due to the potential for unintended alloying reactions.³⁴ A generalized thermite reaction between reactants is represented by the

basic chemical notation of metals (A, B), metal oxides (BO_x, AO_y), and energy release (ΔQ) in eq. 1.1:



Traditional thermites are attractive as a cheap, environmentally benign local high heat source for applications in welding rail road ties³⁵ and destruction or transformation of a substrate material.^{6,20,24,36} A spur of military research endeavors began focusing on the usage of metallized systems after the discovery that the extremely effective German bombs of World War II were infused with aluminum powder.³ During the early years of the space race with the Soviet Union following WWII (1939-1945), theoretical research showed that the specific impulse (*i.e.* the ability of the propellant to accelerate a payload vehicle) and total energy density of propellants could be increased by integrating reactive metal powders (*e.g.* Al, Mg, B) of various size distributions.^{8,31,37,38} Additionally, the inclusion of reactive metal powders minimize combustion instabilities by providing condensed phase particles, which can attenuate oscillatory behavior in a rocket motor.³⁷ Thus, industrial formulations and casting of solid rocket motors are fueled by widely used HTPB bound conventional propellants, which integrate micron sized (15-30 μm) aluminum particle fuel along with the standard ammonium perchlorate oxidizer.^{8,38,39}

1.5 Nanoscale Energetic Materials

Analysis of the combustion behavior of traditional AP/HTPB/Al systems utilizing particle sizes in the range of 10-100 μm showed the formation of large aluminum droplets with long ignition delays. Such droplets burn slowly and relatively

far from the propellant surface, reducing heat feedback and performance.⁴⁰⁻⁴² These type of experiments demonstrated how the thermodynamic benefits of metals and traditional thermite compositions are often offset by their slow kinetics derived from diffusion length scale limitations.^{27,36,43} The rapidity of monomolecular explosive reactions is a result of the close proximity of nascent molecular fuel and oxidizer decomposition products of the energetic molecule ($\sim 10^{-10}$ m).^{27,34} Research over the last 20+ years has shown that the reactivity of high energy metallized heterogenous composites can be improved by shrinking the diffusion length scales between fuel and oxidizer down to the nanoscale (Figure 1.3).^{6,27,31,36} Solid fuels and oxidizers at the nanoscale have higher surface energies and have shown to reduce melting and decomposition temperatures, even though it is generally accepted that there is no significant thermodynamic advantage of the nanoscale.⁴¹ However, the intimate interfacial contact and larger specific surface area ($10\text{-}50\text{+ m}^2/\text{g}$) between spherical or irregularly shaped components⁴⁴ play a critical role in combustion performance and energy release rates.^{6,8,15,20,25,36} The replacement of micron aluminum with readily available aluminum nanoparticles (nAl) has shown to reduce Al ignition delay and ignition temperature (≈ 2300 K to < 1000 K),⁴⁵⁻⁴⁷ and ultimately lead to particles burning closer to the surface of propellant compositions for continuous heat feedback and faster steady burning rates.^{8,36,39-41}

Energetic compositions where one or more components are sub-micron, but colloquially and arbitrarily less than 100 nm, are referred to as “nanoenergetics”.^{20,27,35,36} Nanoscale MICs are generally divided into two categories: powdered forms and multilayer laminates.^{6,48} Components of powdered nanoscale

MICs are synthesized by a variety of techniques based on their chemistry and composites prepared by arrested reactive milling^{49,50}, physical mixing through ultrasound agitation, or sol-gel methods. Techniques for nanoparticle synthesis include, but not limited to, the following: electrical explosion (metals), high-temperature combustion method (metal nitrides), aerosol spray pyrolysis (alloys, metal oxides), plasma arc vapor-phase synthesis (metal nitrides), and laser techniques.^{6,18,24,25} Multilayer reactive laminate films with nanoscale layer thicknesses are typically synthesized via bottom-up vapor deposition methods, which make them beneficial for precise deposition for microscopic “smart” energetic devices.^{6,20,48,51}

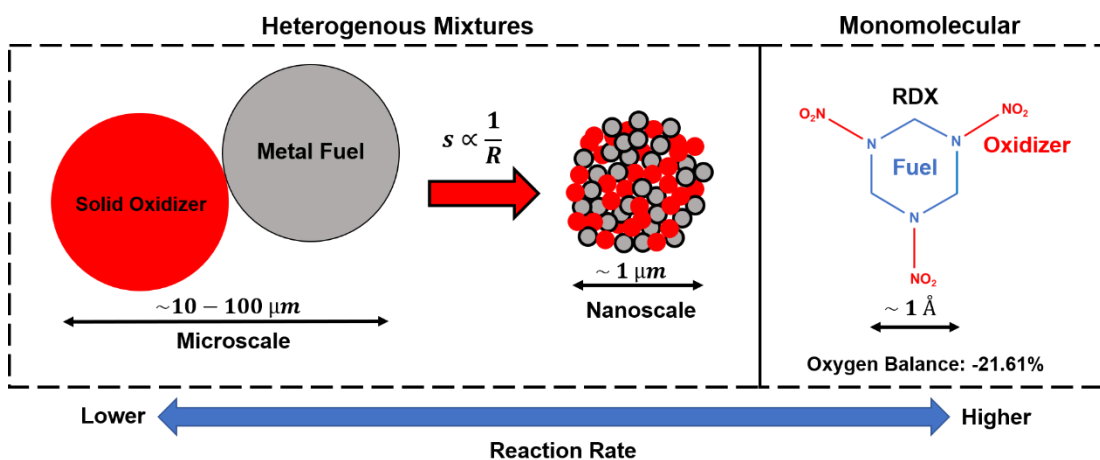


Figure 1.3: Reducing heterogenous energetic components enhances reactivity due to reduced diffusion length scales and specific surface area, s . Monomolecular energetics have fuel and oxidizer “pre-packaged” at the molecular scale.

In contrast to traditionally used monomolecular explosives¹⁸ which usually yield extremely high detonation velocity but low energy density⁶ and no stoichiometric control (typically characterized by molecular oxygen balance), MICs can be adjusted for particle size distribution,^{6,31} choice of fuel and oxidizer,^{6,31} equivalence ratio,^{1,6,31} material geometry and preparation,^{34,52} and reactant packing.^{6,31} Each of these

parameters allows for tuning of energy density, reactivity, ignition temperature, combustion performance, and gas generation of nanoenergetics.^{31,33,35} Both oxidizers and metal fuel particle size govern ignition onset temperature, burn rate, and dynamic pressure of the reaction with variations in the thermal response of the oxidizer upon heating (*i.e.* melting, decomposition to sub-oxides, sublimation, or mechanistic sequences thereof) playing a critical role in determining the degree of their utility and tunability.^{31,53} Preparation of hybrid nano-energetic composites consisting of elementary constituents of both MICs and traditional explosives has shown even the ability to tune the transition from deflagration to detonation and adjust performance through material density and ratio of MICs to explosives, making them suitable replacements of primary explosives.⁵⁴

The length scale and performance tunability of high energy density nanoscale MICs make them appropriate systems for tunable generators of biocidal-agents (*e.g.* SiF_x , Ag, I_2),^{18,20,55} actuation applications in initiators/detonators,^{20,36} and in single-use, solid state, miniaturized microelectromechanical systems (MEMS) for solid propellant thruster arrays.^{6,15,24,56} Adequateness of use in these applications is guaranteed by uniform combustion of gas generating nano-thermite propellants (*e.g.* Al/CuO, Al/MoO₃, Al/Bi₂O₃)³⁵ where most conventional solid propellants (*e.g.* AP/HTPB) and nano-energetics with metal salt oxidizers (*e.g.* AP, AN) are not suitable due to ignition inconsistencies, hygroscopic nature, lack of sensitivity, encapsulation inadequacies, environmental concerns, and lack of safety.^{15,20,23,24,56}

1.6 Observed Mechanisms of Nanoscale Thermites

Divulging the relevant ignition mechanisms of nanoscale metallized energetics for applications under various environmental conditions can be complex. Oxidation mechanisms and vigor of oxidation correlates strongly with the mode of transport (*i.e.* condensed phase or gas phase) and degree of mobility of the oxidizing agent.⁵⁷ The mode of oxygen transport from metal oxide sources is not strictly gas phase or condensed phase driven in general cases. Thermite oxidation mechanisms are often a combination of transport mechanisms where the reliance of either mechanism to achieve ignition can be discerned by varying the concentration of free oxygen.^{12,34,53} The lower bound of ignition temperatures in aluminum thermites has been determined to be limited by aluminum diffusion. Condense phase dominated MICs are driven by oxygen ion conductivity (*e.g.* Bi₂O₃, perovskites)^{13,53,58} and show no significant change in ignition temperatures^{23,57} as a function of ambient O₂ pressure. This behavior is contrasted by gas phase dominant reactions whose ignition temperature, under atmospheric conditions, correlates well with the release of oxygen gas from solid oxidizer sources (*e.g.* Al/CuO, Al/Fe₂O₃, Al/KClO₄, Al/I₂O₅)^{23,53} and experience a comparative increase in ignition temperatures with lowered O₂ pressure.¹² Measurements of the global reactivity of various nano-aluminum thermites demonstrate a thermally driven, narrow distribution (effectively constant) of critical reaction rates at the point of ignition.¹² The critical reaction rate is independent of the ambient environment, oxidizer choice, overall reaction enthalpy, or mode of oxygen transport.^{12,13,58} Various differences in ignition temperature between materials are a reflection of a critical oxygen ion conductivity¹³ or concentration of gaseous oxygen¹²

necessary for reaching the critical oxygen impingement rate for thermal runaway. Kinetics for the critical reaction rate can be described by an exponential Arrhenius model where the temperatures for sufficient oxygen mobility are determined by material activation energies of oxygen lattice diffusion and/or oxidizer decomposition.^{12,13,23}

1.7 Observed Pitfalls in the Application of Heterogenous Nanoscale Composites

Despite the addition of light, reactive metals and their hydrides theoretically producing higher specific impulses and stability during combustion of solid propellants, their experimental inclusion often leads to a reduction in combustion efficiency.^{2,11} Gas generation of low average molecular weight molecules at high temperature during propellant combustion is critical to both propellants and nanoenergetic materials for achieving a high specific impulse.^{6,11,15,35} The combustion of metallized propellants is said to result in “two-phase flow”. Deflagration generates a significant amount of condensed phase particulates being ejected behind the main exhaust plume in addition to gas phase species, reducing its efficiency.^{11,35,43,56} It is for this reason that low gas generating thermite mixtures are not directly used as a propellant, unlike organic explosives and propellant mixtures.²⁴ Heat generating thermite-based propellants typically include gas-generating work substances in the form of an energetic binder, like NC, or even low molecular weight oxidizers (*e.g.* AP)⁵⁹ and explosive constituents such as RDX or HMX⁶⁰, even though transient gasification/pressurization rates are enhanced by high temperature nano-aluminum thermite combustion (*e.g.* Al/CuO < Al/Bi₂O₃ < Al/I₂O₅ < Al-Bi(OH)₃ < Al/KClO₄ < Al/NH₄ClO₄).^{6,15,23,24,35}

The perceived advantages of nanoscale MICs are often overshadowed by their intrinsic drawbacks which limit their wide utilization in propellant systems.¹⁸ Fabrication of nanoscale MICs are more costly³³ than their micron sized counterparts, and their increased specific surface area make compositions increasingly hazardous to handle due to their ability to aerosolize and enhanced sensitivity to external stimuli (*e.g.* friction, impact electrostatic discharge (ESD)).^{8,20,36} Thin, passivating oxide shells (2-6nm) are common among nearly all metals and can be characterized via X-ray Photoelectron Spectroscopy (XPS) and Transmission Electron Microscopy (TEM).^{39,61} This oxide layer becomes a significant volume/weight fraction of the total core-shell metal particle composition at the nanoscale.⁶² While micron aluminum contains 95 wt.%+ active content, nano-aluminum particles contain 65-80 wt.% active Al content which eventually leads to reduced specific impulse potential and combustion performance efficiency.^{8,36,45,47,62} The thin oxide shell may hinder further oxidation at standard conditions, but aluminum powders are easily susceptible to oxidation by water. Aluminum's susceptibility to water effectively limits the application of nanoscale aluminum in humid conditions and in mixtures with highly hygroscopic oxidizers due to poor long term stability.^{20,23,36,39} Moreover, the incorporation of high surface area nanoparticles within propellant precursor formulations gradually changes rheological properties (Einstein formula)⁸ and makes it more difficult to process and uniformly mix nanocomponents within polymer binders.^{20,27,33,36} Some studies have shown that while the addition of Al nanoparticles at low mass loadings (<20 wt.%) within a polymer binder may slightly increase material tensile strength, further increases in particle loading lead to detrimental deterioration of mechanical integrity.⁶³

Mechanical integrity is an incredibly critical feature for propellants where even a tiny crack in a burn grain could create local pressure peaks and cause erratic propulsion or even rupture the rocket mortar tube.³

One of the most important observed disadvantages of using nanoparticle fuels is the shockingly minimal gain in enhanced burning rates of submicron material compared to theoretical expectations (Figure 1.4).²⁷ Burning of larger particles in the range of 30-100 μm follow the d^2 -law (diffusion-limited burning) and transition to kinetically controlled burning (d -law) for particle sizes of $\approx 10\mu\text{m}$. However, particle burning times at the nanoscale largely deviates from the kinetically controlled trend and becomes nearly independent of particle size ($\sim d^{0.3}$).^{40,45} TEM research focusing on morphological properties of nano-aluminum has shown that the high surface energy of individual nanoparticles leads to heavy agglomerations via Van der Waals interactions which are thermodynamically driven to coalesce (sinter) during high temperature applications.^{39,40,57,64} If the timescale for sintering is faster or comparable to the oxidation reaction timescale, then aggregates of nanoscale primary particles will coalesce prior to combustion and result in burning times corresponding to that of particles with larger characteristic length scales.^{20,36,45,64}

In situ TEM heating experiments of aluminum nanoparticles at heating rates comparable to combustion ($\sim 10^6$ K/s) demonstrated that $\approx 80\%$ of the nanoparticle surface area is lost as a result of sintering.^{45,64} Moreover, these same experiments showed that the sintering time (≈ 50 ns) of nano-aluminum is competitive with the reaction time (≈ 10 μs). This indicates that aluminum particles should sinter long before the main combustion event.^{5,45,57,64} This behavior is made apparent by the observation

that the reactivity of powered aluminum MICs has been shown to be more strongly correlated with the size of the oxidizer particles as opposed to the size of aluminum particles.³¹

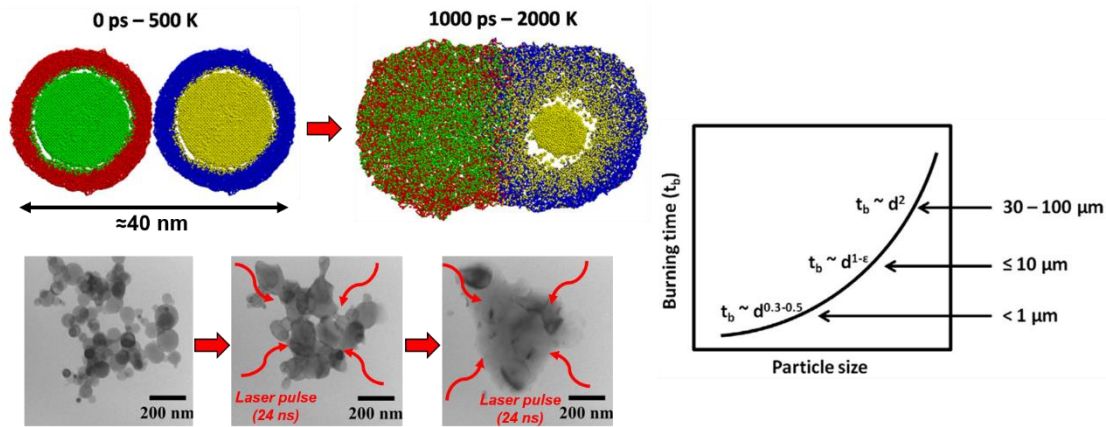


Figure 1.4: Modeling and experimentation of the coalescence of aluminum nanoparticles under rapid heating conditions. Rapid sintering is a primary factor in the reduction burn rates compared to theoretical single particle burn rates. Adapted with permission from the stated references.^{40,45}

1.8 Mechanisms of Nano-Al Particle Oxidation and Thermite Ignition

Several mechanistic based studies have previously been undertaken to better understand aluminum nanoparticle oxidization under various heating conditions to optimize the benefits of nanoscale aluminum-based MICs while reducing their drawbacks. Much of this research is motivated by preliminary research highlighting two mechanistic pathways for aluminum nanoparticle ignition for which there remains much debate rooted in the microstructural interactions between the Al core and the alumina shell upon heating.^{31,61}

The melt dispersion mechanism states that, under rapid heating conditions (10^6+ K/s), the high stress on the oxide shell from the expansion of the aluminum core as it melts results in a sudden rupture of the oxide shell and high velocity insertion of

molten aluminum clusters.^{8,45,64,65} No direct experimental observations or computational works have suggested an explosive rupture of the alumina shell.^{45,61} The vast majority of both experimental and computational studies observe the diffusion mechanism of aluminum oxidation. A combination of nano-cracks^{61,62} generated from polymorphic phase transitions^{34,46,47} of the alumina shell and an induced electric field established between the alumina shell and aluminum core⁴⁵ drives aluminum ion diffusion through the permeable sub-oxide shell until encountering oppositely diffusing external oxygen.⁵⁷

Diffusive reaction behavior was supported early on through studies relying on slow heating (1-50 K/min) methods of characterization in the form of thermogravimetric analysis (TGA),^{46,47} in situ hot stage x-ray diffraction (XRD),⁶¹ and in situ TEM.^{61,62} These techniques analyzed and monitored the evolution and morphology of alumina shell polymorphs. Experiments using high heating rates pushed the theoretical line between the proposed regimes of influence of the diffusion mechanism and melt dispersion mechanism through T-Jump ignition delay experiments ($\sim 10^6$ K/s)^{5,31} and in situ TEM laser heating experiments ($\sim 10^8$ K/s).^{57,64} Both experiments showed no evidence of aluminum particle spallation and even demonstrated that the ignition time delay of nano-aluminum correlated well with oxide shell thickness, suggesting a diffusion mechanism even at ultra-high heating rates.

The phenomenon of “reactive sintering” is highlighted in similar in situ TEM studies of overall nano-aluminum thermite reaction mechanisms. In the areas of intimately mixed fuel and oxidizer, an initial low temperature condensed phase reaction produces heat near the Tammann temperature (*i.e.* half the melting temperature)^{34,53} to

further sinter and draw in surrounding particles to the reacting interface and facilitate the reaction to completion.^{34,57} Gas generating oxidizers such as CuO and Fe₂O₃ do liberate oxygen on their own when rapidly heated to decomposition, but leave much of the oxygen trapped in their sub-oxides in the absence of significant local heat generation.^{23,57} Thus, observations of reactive sintering are seen as visual evidence of a two-step combustion mechanism where an initial fast reactive sintering step precedes a more drawn out burn of the remaining fuel by O₂ liberated by the heat released by the reactive sintering step.⁵⁷ This perspective emphasizes the importance of uniform, homogenous mixing of nanosized components for efficient, uniform burning.¹⁵

1.9 Fluoropolymer-based MICs for Propellant Systems

Contemporary energetic materials research focuses on the use of solid fluorinated oxidizers and binders which may alleviate the issue of two-phase flow due to the combination of high heats of formation of metal fluorides and their associated low boiling points compared to metal oxide formation.^{32,33,43,66} Fluorine is the most electronegative element in which the heat of reaction of aluminum with fluorine gas (F₂) is higher than that of aluminum oxidation by oxygen gas (O₂) (55.7 kJ/g vs. 31 kJ/g).^{10,32,33,43} MICs using fluorine containing oxidizers follow suit, having lower onset temperatures and higher theoretical energy densities over their oxygen based counterparts per mole of fuel consumed.^{6,33,43} Metal fluoride product species (*e.g.* BF₃, SiF₄, AlF₃, TiF₃/TiF₄) are much more volatile than metal oxides at standard conditions and make it possible to generate more gas phase products at relatively similar adiabatic flame temperatures.^{10,43,66}

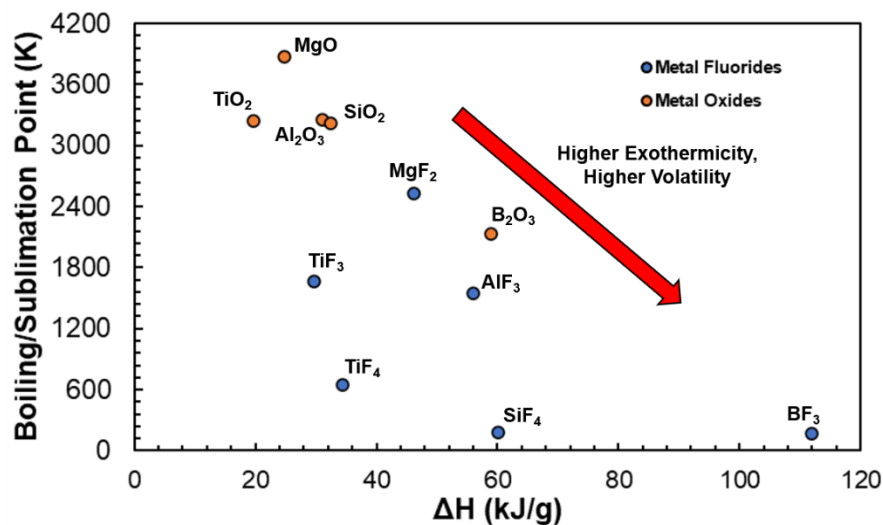


Figure 1.5: Comparison of exothermicity (per gram of metal) and relative volatility of products formed from the oxidation/fluorination of energetic metals

Sources of condensed phase fluorine can be in the form of stable metal fluorides (*e.g.* CuF₂, CoF₂, BiF₃ and NiF₂) which may be mechanically mixed or milled into fine powders.^{43,50} Relatively stable forms of condensed phase fluorine are more commonly sourced from fluorine containing polymers which may be used in a powdered form or fabricated to act as both an oxidizer and a binder for mechanical integrity.¹⁰ The hydrophobicity of fluoropolymers even provides support for long-term storage, transportation, and underwater utilization of MICs.⁶ Although the use of fluorine containing binders has been known to be an acidic oxidizer^{33,67} as early as 1965, their use in nanoparticle thermite systems has only seen a large growth in research within the last two decades as a result of the prospects of enhanced particle dispersion and increased surface contact with the fluoropolymer.^{8,11,31}

Fluorinated polymers considered for solid propellant systems have a general monomer formula of the type C_wH_xF_yO_z. The most researched fluoropolymers used in aluminum and magnesium systems are typically polytetrafluoroethylene (PTFE or

Teflon, 75 wt.% F), tetrafluoroethylene-hexafluoropropylene-vinylidene fluoride (THV, 73 wt.% F), hexafluoropropylene and vinylidene fluoride (Viton A, 66 wt.% F), and polyvinylidene fluoride (PVDF, 59 wt.% F).^{10,11,20,33} Aside from solid propellant applications, established applications of energetic metal-fluoropolymer composites include the use of Al/Teflon in explosives and Mg-Teflon-Viton (MTV) pyrotechnic compositions for infrared decoy flares, signals, ignitors, and tracers rounds.^{33,68,69} Choosing a fluoropolymer for a specific application depends on the individual thermochemistry, mechanical properties, fluorine content, and solubility in precursor solutions.¹⁰ In particular, PVDF has a low melting point and the highest solubility in compatible organic solvents such as dimethylformamide (DMF) which make it attractive for use in contemporary additive manufacturing methods despite the relatively low fluorine content.⁷⁰

Fluoropolymers such as these are especially attractive in aluminized systems as the fluorine content reacts with both the metal fuel and its native oxide layer (Al_2O_3). Reactions with oxide layer provide localized heat release which facilitates the exposure of fresh aluminum for further reaction.^{10,67,71} The reaction of nano-aluminum integrated with various fluoropolymer types has been extensively researched and has revealed a pre-ignition reaction (PIR) between the fluoropolymers and the aluminum oxide layer which is facilitated by the hydroxyl groups on the surface of the oxide shell. The exothermic PIR results in decreased onset temperature of polymer decomposition by over 100 K and ultimately regulates the burning rates of the main reaction between fluoropolymer decomposition products and the aluminum core through either gas-phase^{10,33,63,67} or condensed phase mechanisms.^{6,10,33,67,72} Furthermore, combustion

performance and flame temperature of metal-fluoropolymer systems in oxygen containing atmospheres is enhanced compared to inert atmospheres as carbon soot generated from fluoropolymer decomposition and residual Al are oxidized.^{63,70}

1.10 Architectural Controls of Energetic Materials

The primary focus of scientific developments and enhancements of energetic materials for the last 150 years has been the synthesis of novel molecules and substances.^{20,54} Owing to thermodynamic limitations and increased sensitivity of such molecular engineered materials, contemporary research in energetic materials instead focuses on the modification and preparation of existing materials.²⁰ The most critical modification to existing materials for enhanced combustion performance and progressivity has proven to be control of the burning surface and burn rate through architectural manipulations.^{19,70}

The earliest material approaches to modifying the performance of explosives came from the invention of dynamite by Alfred Nobel in the stabilization nitroglycerine into different porous nanomaterials, and the discovery of the shape charge effect by American scientist Charles E. Munroe in 1888 to focus explosive energy over a limited area.⁵⁴ Many of the issues pertaining to explosives applications was with respect to their handling and stability. Early modifications to desensitize neat explosives, such as RDX and PETN, used superficial methods to combine them with oils, waxes, or even other explosives.³ Later developments at Los Alamos Scientific Laboratory in 1952 even combined HTPB and fluoropolymers, such as Viton A, to yield plastic-bonded explosives (*e.g.* PB-RDX, C4, Formex) for improved mechanical strength, thermostability, safety, and higher energy density.^{3,6,73,74} More current research on this

front deviates from simple mixtures and instead looks at creating novel cocrystals of two existing explosives (*e.g.* CL-20 and HMX, CL-20 and TNT) to obtain a unique crystal structure with equally unique, potentially improved, physiochemical properties compared to either of its co-formers.^{4,16,75,76}

Similar modifications to solid propellant systems sought to control the combustion rate to enhance projectile thrust and velocity. Early examples include the use of “brown powder” (*i.e.* substitution of partially pyrolyzed rye straw for carbon in traditional black powder) and 7-perforated progressive geometry which secured Commodore George Dewey an overwhelming victory against the Spanish naval fleet in 1898 at the battle of Manila.^{3,17,19} The development of nanotechnology for energetic materials is motivated by the perceived architectural enhancements that it may provide. Nano-structured materials have existed and used in human practices for many centuries (*e.g.* the Lycurgus Cup, church windows, etc.) before the deliberate manufacturing of nanoscale materials.³⁶

Global burn rates for propellant and pyrotechnic MICs have been adjusted through microstructure and macrostructure architectures which enhance reactivity and gas generation, or promote certain modes of heat transfer.⁵⁷ Nano-thermites alone have demonstrated the importance of material preparation and combustion conditions with flame velocities ranging between a few millimeters per second to several thousand meters per second.³¹ Global burn rates are maximized with confinement where there exists an inverse relationship between packing density and reaction propagation rates, regardless of particle size.^{6,34,52,56} The rapid combustion of loose, low density nano-thermite powder is dominated by the convection of hot gases and ballistic advection of

condensed phase, molten particles²⁰ through voided space.^{6,52,54,77} Progressively denser compositions regress in flame propagation speeds and transitions from convection and advection dominated heat transfer to conductive heat transfer as ballistic modes of heat transfer are made more difficult in denser, less internally porous materials.^{6,54,56}

More complex architectures for solid energetics are often motivated or fundamentally reinforced by modeled simulations which probe how various degrees of system heterogeneity (*i.e.* global vs. local distribution) in reaction mixtures influence combustion processes with respect to kinetics of the chemical reaction and how material properties (*e.g.* thermal conductivity, melt flow) affect heat flow.⁷⁸⁻⁸⁰ These models take the perspective of either two interacting particle types (*i.e.* fuel and oxidizer)⁸¹ for kinetics analysis or from an ensemble perspective. Ensemble perspectives typically use cellular models to describe micro-heterogenous combustion waves to further understand how flame behavior evolves from quasi-homogenous (*i.e.* constant velocity behavior) to so called “discrete combustion waves” and their connection to material length scales (*i.e.* flame thickness vs. particle size, particle density, melt flow).^{78,79,82}

1.11 Novel Microstructures for Energetic Particle Compositions

Although the use and various compactions of nanoscale metal particles and oxidizers may be considered an architectural enhancement, more sophisticated material preparation is sought to both diminish the drawbacks of nanoscale MICs and architecturally tune burn rates. The general research goal of the energetic materials community has been to develop precision energetic substances for “smart materials” with high performance, safety, reliability, and minimal environmental impact.⁵⁴

Architectural microstructure of energetic materials is expanded beyond simple scale downs of particle length scales and packing through modern technological advances which permit the ability to create and assemble new types of structures and morphologies (*i.e.* core-shell structures, reactive nanowires, directly-assembled particles and laminates, multi-length scale synergetic mixtures, and crystal structure manipulations).^{31,83,84}

Architectural modifications of individual particle microstructures through molecular deposition or aerosol spray synthesis techniques are the most prevalent methods in producing materials for studying structure-function relationships. One such microstructure is core-shell structured energetic materials which play an important role in altering energetic and mechanical properties of thermites, explosives, and solid oxidizers as a result of the superior interfacial contact between core and shell materials.^{6,85} Physically mixed nano-thermites compositions, as mentioned in Sections 1.5-1.7, struggle with friction, impact, and electrostatic discharge sensitivities and are limited in the degree of physical mixing due to particle aggregations. Sub-micron core-shell MICs can be fabricated by either reducing, replacing, or completely eliminating the passivating native oxide shell of the metal fuel and thus further reducing diffusive barriers and length scales.^{6,36,86} Core-Shell MICs mix constituents at the particle level and can help eliminate some of the issues of aggregation. Additionally, replacing of the passivating oxide layer with a fluoropolymer, solid oxidizer, or explosive material through precision atomic layer deposition (ALD)⁶ has demonstrated the ability to functionalize the shell material to control reaction rates and combustion efficiency, alter ignition behavior and energy density, improve long term stability (*e.g.*

encapsulating MICs requiring hygroscopic oxidizers),^{23,39} and reduce sensitivities.^{6,23,31,85,86}

Precisely controlling composition and shell thickness is critical for all the different material combinations of core-shell microstructures to achieve a tunable balance between increased energy output, desired pressurization rates, enhancements in thermal stability, and reduction in sensitivities.^{6,23} Despite the high degree of precision over microstructural architecture in the fabrication of core-shell materials, ALD methods often are limited in the types of materials which can be deposited, take a long time to optimize deposition parameters, and are relatively costly to implement for large scale production.⁶ Moreover, there exist pervasive technical problems in effectively passivating the surface of metal particles without reducing the active metal content.³⁶

Aerosol methods such as aerosol spray pyrolysis (ASP),^{23,58} evaporation induced self-assembly,²⁶ and electrospray deposition^{67,87} have potential for scale up while offering the ability to synthesize slightly less precise sub-micron core-shell particles, simply decorate,^{88,89} or encapsulate intimately assembled mixtures within a polymer matrix or recrystallized oxidizer shell.^{25,26,90} The atomization of precursor droplets effectively generates thousands of microscale mixed microreactors which can be subject to electric fields and elevated temperatures in facilitating chemical processes.²⁶ Aerosol methods can assemble synergetic compositions of soluble oxidizers or explosives embedded in porous structures to limit crystal growth (*e.g.* impregnated porous silica),^{36,90,91} or synthesize size restricted neat or doped oxidizers. The synthesis of doped perovskite oxidizers^{13,58} and alloyed metal fuels (*e.g.* High

Entropy Alloys (HEAs), Al-Li, Al-Mg),⁹²⁻⁹⁴ in itself represent materials with an even higher degree of microstructure tunability. These materials have demonstrated the ability to tune the ignition temperature, activation energy, chemical kinetics, and specific impulse of MICs as microscopic properties within the crystal structure (*i.e.* average bond energy, electronegativity, oxygen vacancy concentration, ion-conductivity, melting/boiling points, etc.) are systematically varied.

The aerosol technique of electrospray deposition (ESD), in particular, is compatible with many polymer containing, conductive precursors for use as a facile means for nanoparticle assembly within monodispersed micron sized droplets which dry before deposition onto a substrate.^{20,24,25,63} This technique has demonstrated a bottom up approach for direct control of packaging sub-micron particles into narrow size distributions of micron scale structures held together by a low loading of polymeric binder scaffolding (1-10 wt.%).^{25,40,90} Particles of this type are referred to as “mesoparticles” and may have their size and morphology changed depending on the solvent type, polymer concentration, solids loading, and strength of the applied electric field for atomization of the liquid precursor.^{6,20,25,63} Mesoparticle fabrication stabilizes and intimately assembles primary particles consisting of sub-micron metal fuels and oxidizers, droplet-size controlled soluble oxidizers (*e.g.* AP, KClO₄),⁴¹ high specific area catalysts with complex architectures⁹¹ (*e.g.* mesoporous silica, CuO, Fe₂O₃), gas generating explosives,⁶ or other niche additives.^{40,41,55} The primary motivation for fabricating mesoparticles lies in its intrinsic characteristics of simultaneously being micron sized while having a porous microstructure giving it the equivalent specific surface area as an ensemble of individual nanoparticles.^{25,40,90} The micron size gives

mesoparticles the advantage of ease of processing within propellant precursors while still maintaining reactivity enhancements of nanoscale materials for faster propellant combustion rates and larger specific impulses.^{37,41,90} Furthermore, using low temperature, gas generating energetic polymers (*e.g.* NC) and explosive additives (*e.g.* TNT, RDX, AP) enhances dispersion of nanoparticles prior to primary ignition and contributes to convective heat transfer.^{6,26,40,41,60} Optimal composition mixtures reduce aggregation and prevent sintering of nanoparticles^{39,57} at the onset of combustion, resulting in improved reactivity,⁴¹ short burn times, higher pressurization rates,²⁵ and smaller (submicron) product particles compared to physically mixed MICs.^{24,25,40,90}

1.12 Rapid Prototyping of Energetic Materials (Additive Manufacturing)

Electrospray deposition is a unique method of aerosol fabrication as it is capable of fabricating various propellant architectures. These architectures include 2D thin film nanocomposites^{67,95} and 1D nanofiber mats (electrospinning)⁹⁶ in addition to the 3D mesoparticle architectures (Figure 1.6).^{6,87,97}

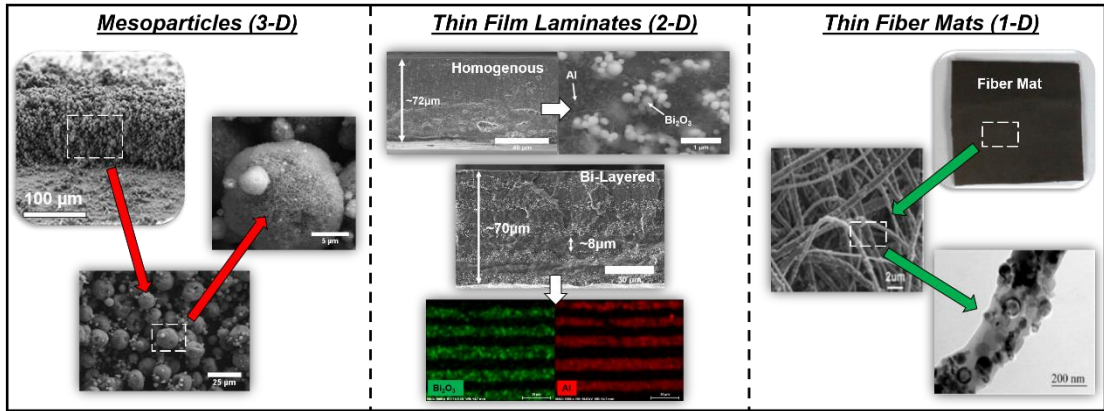


Figure 1.6: Polymer bound energetic composite architectures: Mesoparticles (3D), Thin films (2D), Fibers (1D).^{37,96}

In general, each architectural type is obtained by adjusting the precursor solvent type, polymer type, polymer concentration, and solids loading.⁴⁰ The porous, high specific area nanofiber mats, alone, allow for improved processing and dispersion of high viscosity precursors while dramatically increasing combustion propagation velocity with decreasing fiber diameter (≈ 60 cm/s vs. ≈ 10 cm/s).^{10,70,96,98} Each architecture type is built up along a single dimension which make it possible to fabricate a single material which combines two or more architecture types of potentially differing equivalence ratios in a layer by layer laminate structure.

As mentioned in Section 1.7, the aggregation of nanoscale energetic components eventually leads to degradation of both reactive and mechanical properties at high mass loading.⁹⁵ This point remains true for electro-sprayed thin films but is alleviated when either thin, high-strength energetic nanofibers^{98,99} or dense layers of neat polymer binder⁹⁵ are interspaced between dense layers of high mass loading of nanoenergetic material. Both material schemes are observed to have increased burning rates with decreasing layer separation and reinforce mechanical strength with respect to fracture toughness, impact behavior, wear corrosion, and tensile strength.^{70,95,98} Additionally, γ -phase and α -phase PVDF polymer binders are polarizable by the large electric field to form piezoelectric β -phase PVDF.^{10,20,36} This may be an unintended molecular architectural manipulation but ultimately allows these materials to be utilized for novel engineering controls. Modeling and experimental efforts have been made to acquire β -phase PVDF¹⁰⁰ whose orientation relative to Al nanoparticles has shown to result in superior reactivity with both the alumina shell and Al core.¹⁰

Electrospray's control of both microscopic and macroscopic patterning, porosity, and geometry classifies it as an additive manufacturing (AM) technique. Additive manufacturing, or 3D printing, is a broad set of fabrication techniques and technologies for cost effective rapid prototyping of complex, high resolution structures based on digital model files.^{6,20,97,101} Breakthroughs in additive manufacturing technologies over the last decade have allowed 3D printing to be successfully applied to diverse fields, including the energetics community.^{20,97,101} Traditional casting methods of propellant systems are restrictive in the types of architectures which can be achieved as well as the quality of the finished product. Additive manufacturing of reactive systems expands component mixing capabilities (*e.g.* in situ active thermite mixing for graded material)¹⁰² as well as control over macroscale and microscale architectures. Such architectures may tune the degree of enhancements of heat transfer modes and provide a spectrum of propellant thrust profiles.^{20,84,97,103,104} One such example is the recent development of repeatably manufactured and successfully fired 30 mm caliber rounds with complex bore shapes.^{19,20,36}

Reactive materials additive manufacturing can be roughly divided into two types; those with 2D planar structures or those which are manufactured as volumetric structures.^{20,101} Techniques range in complexity from solvent-based blade casting, spin coating, electrodynamic deposition, and direct ink writing to solvent-free aerosol jet printing, vapor deposition (physical/chemical), fused filament fabrication (FFF), and photopolymerization through precision ultra violet (UV) laser stereolithography (SLA) or digital light processing (DLP).^{20,97,101,105} The specific choice of an additive manufacturing method typically comes down to material compatibility, applicable

ranges of precursor viscosity, architectural precision, mechanical integrity, and cost of potential scale up. Robotically directed layer-by-layer extrusion¹⁰⁵ where liquid phase materials/suspensions solidify upon deposition, either by thermally assisted fused filament fabrication^{105,106} or direct ink writing (DIW), is the most ubiquitous form of additive manufacturing due to its simplicity and relatively low cost for an individual user (Figure 1.7).^{6,20,97,101,104} While fused filament fabrication has been used to manufacture and tailor the performance of Al/PVDF energetic systems^{107–110}, wet AM processes are safer and more compatible with energetic materials utilizing a wide range of high-performance polymers and dispersed phases of materials.^{18,84,105,108}

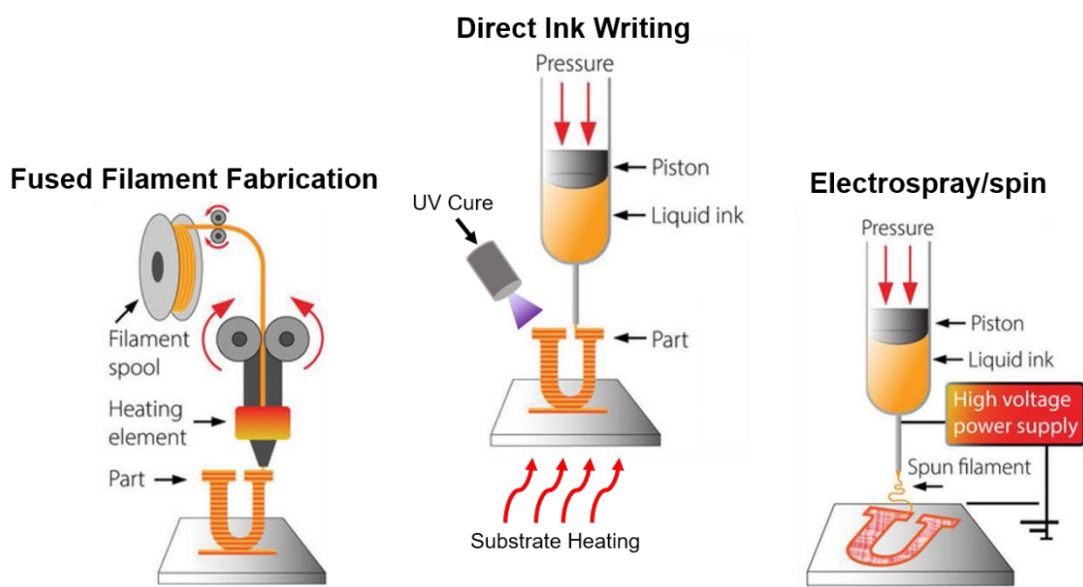


Figure 1.7: Sub-divisions of most common methods for macroscopic additive manufacturing of energetic materials.⁹⁷

Propellant compositions fabricated through DIW may either be entirely solvent-based or combine a mixture of DLP photopolymerization and chemical curing to produce materials which are mechanical isotropic (Figure 1.7).^{20,97,105,111} The latter is generally preferred as solvent-based processes intrinsically produce potentially toxic

fumes upon solvent evaporation and leave behind relatively porous product materials.^{20,72,77,97,112} However, since propellants incorporating nanometal fuels reflect much of the incoming UV light, solvent-based precursors are preferable for metallized high mass loading prints which may be aided by anti-clogging ultra-sonic vibration.^{20,97,113} Many of the thin films produced by solvent-based DIW processes are similar to those manufactured by electrospray as they may use the same precursor formulations. DIW, however, can be a much faster process while allowing for much greater control over specific patterning with precursor inks at much higher particle loadings and product materials which are denser.^{70,114} With no mechanism to control or limit crystal growth, most DIW fabricated materials do not use solid materials which are soluble within the precursor solvent, thus barring any practical use of high oxygen containing perchlorate oxidizers.⁷⁰ Moreover, the solvent-based process eliminates the use of mesoparticles or nanofibers with higher degrees of microstructure. Mixing of nanoscale materials for DIW still remains a potential challenge.

1.13 Dissertation Research Objectives

The studies undertaken in this dissertation look to build upon the knowledge of some of the prior works mentioned in this introductory section and explore avenues to push the limits in the understanding of fundamental processes which may have been overlooked or not well studied. The ability to experimentally emulate and probe the behavior of underutilized reactive systems subject to rapid heating conditions is a core feature of this dissertation. Thermogravimetric/Differential scanning calorimetry (TGA/DSC) testing has been the most common technique to characterize thermal properties, phase transitions, and exothermicities of both explosives and heterogenous

reactive materials in various chemical environments (*e.g.* air, oxygen, nitrogen, helium, argon, etc.).^{6,115} Slow heating rates (1-50 °C/min) of TGA/DSC allow for precise observations and activation energy measurements of crystallinity changes and decomposition behavior prior to a perceived thermal initiation event.^{6,91} However, heating rates within self-sustained reaction events exceed 10⁵ °C/s with mechanisms for reaction proceeding far from equilibrium.^{6,10,53,58} Commercial thermal analysis techniques using slow heating TGA/DSC largely fail to set the appropriate conditions for properly analyzing rapid chemical processes which may have mass transfer constraints.^{53,57,115} Thus, many chemical mechanisms corresponding to combustion events at high heating rates require diagnostics which emulate combustion behavior within various environments.^{6,10,67}

Heating rates in the range of 10⁵-10⁸ °C/s have been achieved in previously published works using Temperature-Jump (T-jump) rapid wire heating^{57,67,115} or in situ TEM rapid heating (*i.e.* Protochips rapid heat stage, laser heating), and combustion behavior captured and characterized with high-speed color camera pyrometry.^{57,63,64,67,116} The coupling of T-Jump for ignition with Linear Time-of-Flight mass spectrometry (T-Jump/TOFMS), in particular, has been a core diagnostic tool in the Zachariah Research Group for over a decade as a means to probe the chemical evolution and activation energies of reactive materials and their components when subject to rapid platinum wire heating (T-Jump).^{67,91,115} However, there exists a lack of mechanistic studies at high heating rates where the kinetics, and relationships between ignition conditions and performance of heterogeneous reactive material systems are still not well understood.^{27,31,34,53,115} The large majority of studies have focused on

aluminum based MICs and their pre-ignition and post-ignition morphological properties and chemical speciation.^{34,57,64,67} MICs with fuels of differing thermochemical properties such as silicon (Si), titanium (Ti), zirconium (Zr), and magnesium (Mg) have not been well investigated by the same types of studies aluminum has been subject to.^{8,55} Furthermore, while much extensive work has been carried out on the decomposition kinetics of single solid oxidizers and fluoropolymer interactions with nanoscale Al fuel, little to no studies have investigated how alternative nanoscale fuels and solid oxidizers fundamentally interact with the polymer binder within tertiary reactive systems during combustion.^{7,8,115}

One of the main objectives of this work is to investigate the reaction mechanisms of superficially studied aluminum and titanium nano-thermite MICs, and further probe fluoropolymer interactions with solid oxidizers/native oxide shells using rapid heating diagnostic tools. My experimental and theoretical research efforts not only probe architectural and thermochemical based synergetic relationships of multicomponent nanoscale systems (*e.g.* laminate structures, carbon fibers, mesoporous silica)^{10,20,99,106} but look to understand how these energetic systems and their microstructures may couple and respond to actuated external stimulus (*i.e.* laser, microwaves, static fields, mechanical strain, acoustics, etc.) for controllable throttling of ignition behavior and combustion burn rates.^{9,36,117}

One of the many challenges in the energetics community, as mentioned in Section 1.12, is moving from nanopowdered systems to high thermite loading, architecturally complex objects with the potential for industrial scale up and strengthening through additive manufacturing.^{54,106,112,118} Solvent-based DIW methods

were used in this research to provide flexibility in pattern design, and the range of viscosities and material constituents which may be used for producing relatively dense materials with reduced anisotropy between consecutive layers compared to electrospray fabrication.^{70,105,112} Although solvent-based wet processes for depositing polymer thin films exhibit some limitations regarding fabrication of multilayers and control over thin film spatial composition, DIW additive manufactured⁷ thermite laminates can be used for architectural throttling and mechanical strengthening of nanoenergetic materials with appropriate choice of laminate constituents and engineering controls for optimized solvent evaporation.¹⁰⁵

1.14 Chapter Prefaces

Throughout this dissertation, each chapter will describe specific experimental approaches whose objective is to add to the general goal of probing chemistry at metal/ceramic/polymer interfaces of metallized energetic nanocomposites when far from chemical/thermal equilibrium. This knowledge will ultimately be used to tailor the throttling of ignition behavior and combustion burn rates of energetic systems for a desired application.

Chapter 2 presents itself as a chapter which primarily focuses on the diagnostic tools, both old and new, used throughout each of the chapters and goes into more detail about the importance, background, and functionality of each measurement technique. More specifically, this chapter attempts to answer the following questions: How do we emulate rapid heating of steady-state combustion of energetic materials and measure ignition properties? How can one acquire thermochemical data at rapid heating rates?

What were some attempts at improving these methods to increase their reach of scientific relevance?

The collaborative study with Sandia National Labs to investigate the reaction mechanism of the nanoscale dry powder pyrotechnic powder, Ti/KClO₄, is the topic of focus of chapter 3. This chapter highlights this highly exothermic mixture as the first study of mine which looks at the use of an underutilized metal fuel and how its interaction with the strong metal salt oxidizer, when subject to rapid heating conditions, may be potentially unique based on the composition and thermal response of the nanoscale metal fuel. In situ TEM heating is conducted to help answer questions regarding both the reaction mechanisms as well as the progression of nanostructure morphology, if any. Would titanium nano fuel be susceptible to the same stability concerns as aluminum when combined with a hygroscopic oxidizer? Do nano titanium particles sinter and lose their nanostructure prior to primary reaction? Additionally, this chapter acts as a continuation of chapter 2 in demonstrating the extent to which the technique of temperature jump/time-of-flight mass spectrometry can be utilized to reveal the behavior of rapidly progressing thermochemical processes of energetic and non-energetic compositions in various ambient environments.

Chapter 4 combines the methods learned in chapter 3 in the study of determining the effect of packing aluminum-based nano-thermites into previously studied aluminum/PVDF propellant films. How does integrating aluminum thermites effect local energy density and energy release rates, flame speed, flame temperature, gasification, mechanical integrity, and ignition behavior? What is the difference in performance between dry thermite powders and how do they behave once bound by a

PVDF binder? Does the tertiary system help reduce apparent sintering behavior? Is it even useful to do this? Much of these questions are addressed using T-Jump/TOFMS but also heavily relies on color camera pyrometry for mapping spatiotemporal measurements of the respective flame fronts and the estimation of energy release rates.

Several assumptions are made in chapter 4 regarding the energetic formulation of the Al/MO/PVDF films as the aluminum fuel may react with both the metal oxide and the PVDF binder oxidizers. For simplicity, the stoichiometry of the formulations assumed the metal/metal oxide and metal/PVDF reaction were mutually exclusive with minimal consideration of the metal oxide/PVDF reaction. Chapter 5 builds on this aspect and focuses solely on the metal oxide/PVDF interaction when subject to high heating rates. This topic has previously been studied by research almost exclusively focusing on the aluminum oxide shell interaction with PVDF as it relates to the role of released HF gas in the facilitation of the overall reaction with the metal core. Chapter 5 generalizes the interaction and subjects several energetic material relevant metal oxides, either as a primary oxidizer or native shell oxide of alternative metal fuels, to T-jump/TOFMS characterization.

Although the chapter 6 and chapter 7 still focus on PVDF bound energetic systems, the studies explored in these chapters examine synergetic relationships between materials and material architectures which aid in the rate of energy transfer throughout the systems to tune and actuate their capabilities. Chapter 6 highlights intra-material coupling and distribution of energy while chapter 7 investigates the ability of added materials to respond to external stimuli for remote actuation purposes.

Chapter 6 assess how randomly distributed/oriented high conductivity rods of various aspect ratio can effectively facilitate the proliferation of energy throughout the material to enhance overall burn rates. Such a study was approached from a flame front model point of view to effectively control the various parameters which are normally difficult to control. Dense, porous free energetic materials are considered to answer some fundamental questions pertaining to the flow of heat using highly conductive, relatively inert materials as a vector for primary heat transfer: to what extent can highly conductive, non-energetic additives enhance the burn rates and energy release rates? At what point does adding more volume percentage of material hinder propagation? What aspect ratio enhances the flame behavior the best and why? Does increasing the thermal conductivity of the additive relative to the energetic material indefinitely result in appreciable gains in energy release rates?

The ability to control the reaction rate and even ignite an energetic material remotely without traditional surface joule heating methods is an incredibly useful and sought out capability. Past studies have analyzed volumetric heating with the use of microwaves which are absorbed by a microwave sensitive material or couple to ionized products of an already propagating flame front. However, microwaves have not had much success in effectively coupling to unignited aluminumized energetic systems even with the use of microwave absorbing carbon-based additives. Chapter 7 investigates this behavior further by considering alternative metal fuels as a potential energetic microwave sensitive additive and how their core-shell morphology and chemical composition may lead to successful material ignition. Furthermore, microscale architectures are fabricated through additive manufacturing to combine

materials which may be highly sensitive to microwaves to those which are not to supplement microwave absorbing deficiencies of superior propellant systems.

The final chapter of this dissertation covers overall conclusions of this dissertation and highlights projects of note where much lab time was devoted but did not end up in a publication due to an unsatisfactory result or collaborations which did not continue. Topics here include molecular beam mass spectrometry for atmospheric sampling of rapidly heat materials, in situ TEM studies of oxygen mobility in doped perovskites for tunable oxygen transfer rates, and novel isotope labeling methods for T-jump/TOFMS in reaction mechanism tracking. Much of the completed work gives impetus for future works in the improvement of novel diagnostic techniques which capture transient thermochemical behavior of increasing complex energetic material systems.

Chapter 2: Diagnostics and Instrumentation

2.1 Rapid Thermometry of Materials (Temperature-Jump)

2.1.1 Methods and Motivation of Temperature-Jump Thermometry

Thermogravimetry and Differential Scanning Calorimetry (TGA/DSC) is a powerful, standardized tool for thermal analysis of materials. It can be viewed as a sophisticated, high resolution scale which can sense heat fluxes from a platinum thermocouple.¹¹⁹ It has been the key instrument for many of the most basic research studies across several different fields of research for which many material properties such as material melting and boiling point temperatures, heat capacity, exothermicity, and chemical kinetics can be quantified.¹¹⁹ The thermal behavior of energetic composites through the perspective of TGA/DSC can give one the ability to heat a small sample to temperatures as high as 1600 °C and obtain high resolution quantitative thermochemical data.^{67,91,120–123} However, energetic materials are primarily researched for their inherent ability to undergo thermal runaway after being supplied with enough initial energy to reach the ignition temperature. Thermal runaway, by definition, can only occur when reaction rates and the rate at which kinetic energy is generated within the system is much larger than the rate at which kinetic energy is lost from the system. Additionally, an energetic material must be able to transport enough of its nascent chemically liberated kinetic energy to spatial regions which have yet to ignite for the reaction to be sustained. Such a reaction must reach a sufficiently high adiabatic flame temperature over a sufficiently small distance which allows a high enough diffusive heat flux for unburned material to reach the ignition temperature before the flame is

quenched.^{79,124–127} The characteristic thermal gradient of the flame front corresponds to a heating rate between 10^5 - 10^6 °C/s, much larger than the 25°C/min heating rate of the TGA/DSC.

To analyze how materials behavior under rapid heating conditions, the Temperature-Jump (T-Jump) system was developed. The basic premise of this experimental technique is to mimic the heating rate delivered by a flame front by initiating the reaction at the characteristic heating rate of 10^5 - 10^6 °C/s. The T-Jump assembly consists of a wire flash heating approach where a 76 μ m diameter platinum wire (OMEGA Engineering Inc.) is prepared by soldering 6–12 mm wire between two electrical feedthrough copper leads of a vacuum flange. The flange assembly of the T-Jump was incorporated to allow one the ability to use a well-sealed, isolated chamber to conduct flash ignition experiments of energetic materials in atmospheres of differing pressures (10^{-3} - 10^3 Torr) and gas species. Solid material suspended in an inert, volatile solvent, in the form of powder in hexane or composite precursor solution, may be deposited onto the wire with a micropipette or other suitable coating technique such that there exists a thin homogeneous layer of sample (<10 μ m, 5-50 μ g). If one is coating powder, it is best to use powder which is submicron (<1 μ m) for effective, intimate coating on the wire surface. Larger features can make coating the wire difficult and result in anisotropic heating of the sample. Figure S2.1, in the supplemental section of chapter 2, serves as an example of the difference in platinum wire coating for particles of the same chemical composition but drastically differing particle size. Samples to be coated may also be dissolved in a solvent and coated such that the dissolved sample recrystallizes on the wire upon the quick evaporation (\approx 3-10 s) of the

pipetted droplet. Generally, the sample need not be energetic if the T-Jump technique is coupled to another diagnostic system.

2.1.2 Conducting and Analyzing the T-Jump Experiment

Flash heating is implemented by utilizing a triggering square wave pulse generator (Stanford Research Systems, Inc. Model DG535 Four Channel Digital Delay/Pulse Generator) and a DC power supply which is connected to a heating actuator/modulator. When triggered by the trigger box, the actuator delivers up to 10 A of current when supplied with a single voltage pulse (4-14 V) with a predetermined pulse time (1-9 ms) across the platinum wire. The raw data of the current and the voltage outputs from the actuator are monitored using a Teledyne LeCroy 600 MHz oscilloscope with two channels connecting a Teledyne LeCroy CP030A 30 A 50 MHz current probe and a BNC cable placed in parallel with the platinum wire circuit. The voltage of the DC power supply (10-21 V) is adjusted for each pulse time length for optimized heating such that the platinum wire is as hot as possible, “white hot”, without breaking the wire.

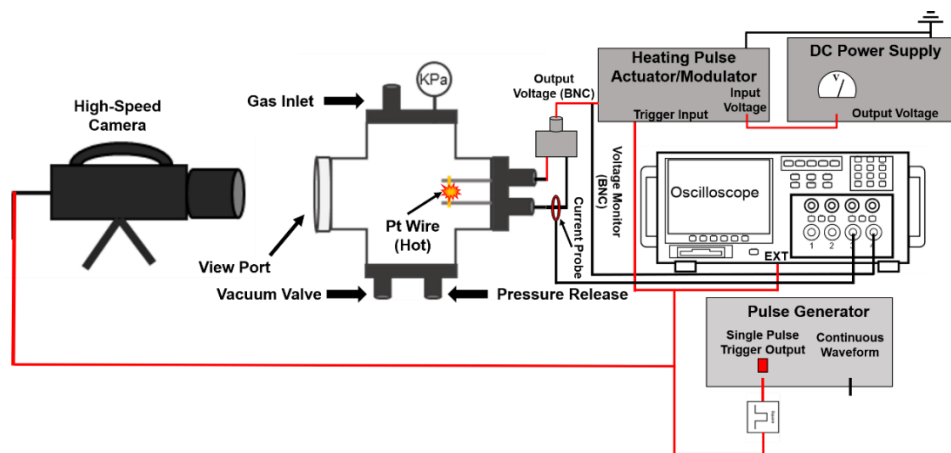


Figure 2.1: Routine setup of the T-Jump experiment conducted in a sealed chamber of differing atmosphere. Key heating, timing, and monitoring components are depicted.

When flashed, the platinum wire acts as the probe by which fast response thermometry of the wire can be acquired. Temperature readings obtained through the calibrated relationship between the temperature of the Pt wire and its resistance from the Callendar–Van Dusen equation show the wire reaching temperatures as high as ~ 1400 K.^{67,120,128–130} If one uses a 3 ms heating pulse, this corresponds to a heating rate of roughly $\sim 4 \times 10^5$ K/s, when starting from room temperature. The key assumption of this technique is that the temperature of a sufficiently small amount of coated sample is approximately the temperature of the wire, thus replicating the heating rates expected in a combustion event.¹²⁰

Synchronizing the triggering mechanism of the heating to the acquisition of high-speed videography (10^5 FPS) allows one to visually analyze the time at which an ignition event occurs relative to the start of heating. Throughout all studies using this technique, the ignition temperature is defined by the sudden increase in light intensity originating from the thermal runaway of the reacting sample.¹²⁰ The raw data of the voltage and current across the platinum wire are processed through a Matlab code

(Supplemental) utilizing the Callendar–Van Dusen equation in order to generate a plot of the average wire temperature as a function of time with a 0.1 ms resolution and an instrument base uncertainty of ± 25 °C. Despite the temporal resolution, the behavior of the temperature plot is smooth enough such that interpolations of the data points may be made to form a continuum of values. With this information, one may measure the ignition temperature of an energetic material by comparing the time of ignition, found through videography, to the temperature of the wire at the time of the observed ignition event. This analysis is also aided using two Matlab scripts, one (Appendix: C-0) which corrects for the contact resistance of the heated wire circuit, and the other (Appendix: C-1) which reports the temperature of the wire at a given time with a finite difference estimate of the heating rate at the point of ignition. The heat rate is calculated at the point of ignition with the time resolution limited to the frame rate of the high-speed camera. The analytical and visual results of the ignition behavior are shown in Figure 2.2. Other than monitoring the maximum temperature reached, it should be noted that the temperature of the wire after the ignition event is no longer analytically useful.

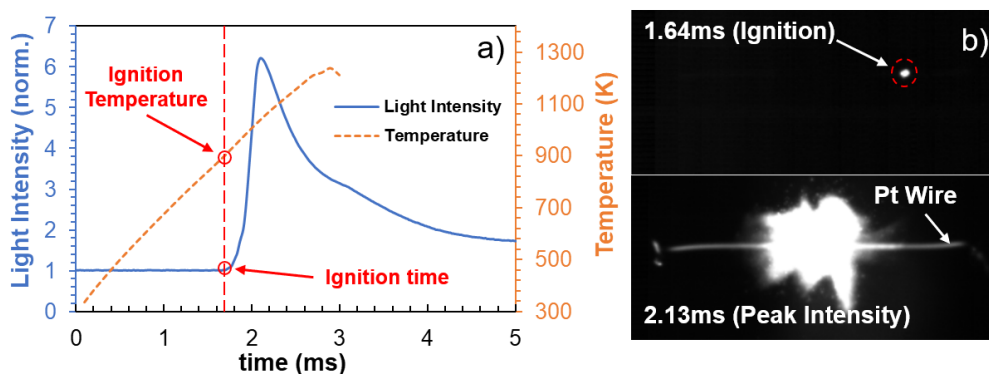


Figure 2.2: Ti/CuO thermite T-Jump ignition in argon illustrating the a) temperature profile and light intensity as a function of time where the b) ignition point can be determined through frame-by-frame analysis of synchronized high-speed videography.

2.1.3 Measuring the Activation Energy of Ignition

Considering the specific range of heating rates is 10^5 - 10^6 °C/s, the choice of heating pulse time may seem a bit arbitrary given the constant maximum wire benchmark temperature of ≈ 1400 K. One may use any pulse time between 1-9 ms and achieve a heating rate within the desired range. The convention used in the Zachariah lab is that measurements between differing sample type will use the same heating pulse time (3 ms) in order to better compare them. However, the T-jump analysis of materials is not limited to simply the observation of the ignition temperature of an energetic system. Utilizing differing pulse times/heating rates results in a behavior where the observed temperature of ignition appears to increase as the heating rate increases.^{115,120} It has been shown that that one may use the temperature of ignition as a function heating rate data in order to extract an effective global activation energy, E_a , of the ignition event using the using the Arrhenius kinetic model approach of the Flynn–Wall–Ozawa isoconversion method.^{115,131–134} An example of this analysis is shown in Figure 2.3 where multiple measurements of the ignition temperature are made for the same heating pulse time over five pulse times corresponding to evenly spaced heating rates, β .

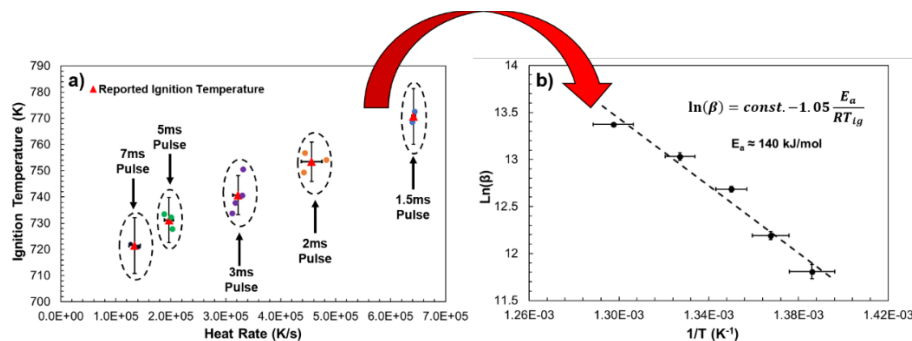


Figure 2.3: T-Jump analysis of the a) ignition temperature of Ti/KClO₄ energetic composition as a function of heating rate(β) for which the b) activation energy of ignition maybe calculated using the relation given by the Flynn–Wall–Ozawa isoconversion method.

The activation energy analysis of this type is conducted by treating the average ignition temperature for each heating rate regime (heating pulse time) as being the reported ignition temperature. The reported ignition temperature is then used to plot Figure 2.2b and extract the activation energy the ignition event.

2.2 Rapid Chemical Speciation (T-Jump/Time-of-Flight Spectrometry)

2.2.1 Linear Time-of-Flight Mass Spectrometry

Temperature-Jump Time-of-Flight Mass Spectrometry (T-Jump/TOFMS) is a chemical species detection instrument which couples linear time-of-flight mass spectrometry with the rapid heating technique of T-Jump flash heating. By itself, the linear time-of-flight mass spectrometer (Jordan TOF Products Inc.) is an instrument which is capable of sampling and detecting gas phase species at a rate of 1 full mass spectrum per 0.1 ms using an 18 mm Z-Gap microchannel plate (MCP). To obtain a full mass spectrum, the sample of gaseous species must be separated into tightly consolidated regions according to the mass of the species. The tighter the bunching of like masses, the better resolution of the spectrum when detected by the MCP. The degree of resolution should be in a state such that the mass spectrum can clearly resolve peaks which are 1 mass unit apart, although a resolution of 0.5 mass units is ideal. A basic schematic of the linear time-of-flight setup and operation is shown in Figure 2.4 where a more descriptive diagram maybe found on the Jordan TOF Products Inc. webpage.

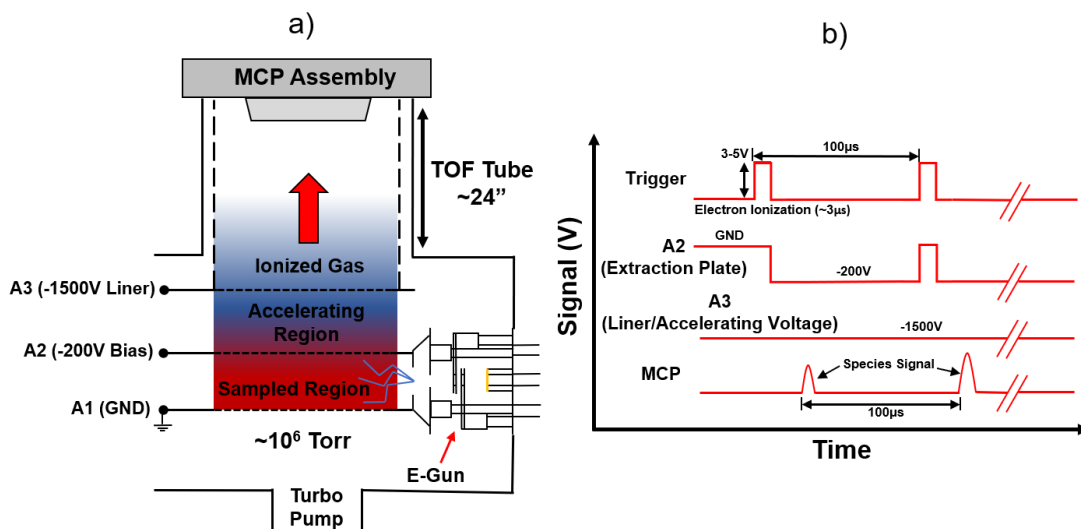


Figure 2.4: Schematic of the a) TOF ionization, acceleration, and detection of gas species which have a b) voltage/signal profiles which are actuated by a trigger source

To form the spectrum in the first place, the gas species must enter a sampling region defined by two plates with established voltages, one set at ground and the other capable of being voltage biased temporally. Gas species which have diffused into the sampling region are subject to ionization as a result of a current of bombarding 70 eV electrons emanating from an electron gun source. Although the level of electron energy utilized is enough to obtain optimal signal-noise ratios, the electron energy is also enough to fragment the parent species into a signal profile containing the parent species along with its fragmentation species. Many known species have their electron ionization fragmentation patterns documented (NIST Web Book) and thus presents a means to refine the identification process of a parent species which may have the same mass as another species.

2.2.2 Conducting and Analyzing the TOFMS Experiment

The same triggering mechanism which initiates the T-Jump experiment also triggers the extraction plate and electron gun power supply with a continuous TTL

square wave. After a dwell time of $\approx 3 \mu\text{s}$ for electron ionization, the A2 biasing plate extracts positively charged ions into the accelerating region between A2 and A3 plates, as illustrated in Figure 2.4.¹³⁵ A liner at the same voltage as A3 is established within the TOF tube in order to create and shield a field free region which maybe traversed at constant velocity. Lighter species will be accelerated to a higher velocity than heavier species and will therefore separate themselves from the initial packet of ions as the species traverse the length of the flight tube. In this way, the length of the flight tube is linked to the resolution of the MCP species signal. The longer the flight tube, the more time species will have to separate into consolidated regions which impact the MCP detector at different times depending on their mass. Generally, lighter masses will have higher resolved mass speaks since they move faster and are able to separate themselves quicker than the higher mass species. The raw data of MCP signal voltages as a function of time are output to the same oscilloscope mentioned in section 2.1.2 and collected over a pre-determined time length of 10 ms or 100 full spectra. Since the electron gun and extraction plate are triggered multiple times with 100 μs intervals, multiple spectra are collected with the same species being observed at periodic absolute time values. This periodic behavior is broken up into intervals defined by the 100 μs for each spectrum collection time and thus each spectrum, as a whole, corresponds to an absolute time value in increments of 0.1 ms. In this manner, one may track the evolution of the spectrum, and therefore a single species, with a resolution of 0.1 ms until reaching the total data collection time allotted (10 ms). A simple box schematic of the wiring of the system outside of Figure 2.4 is shown in Figure 2.5 which includes trigger, monitoring, and pulsing systems used.

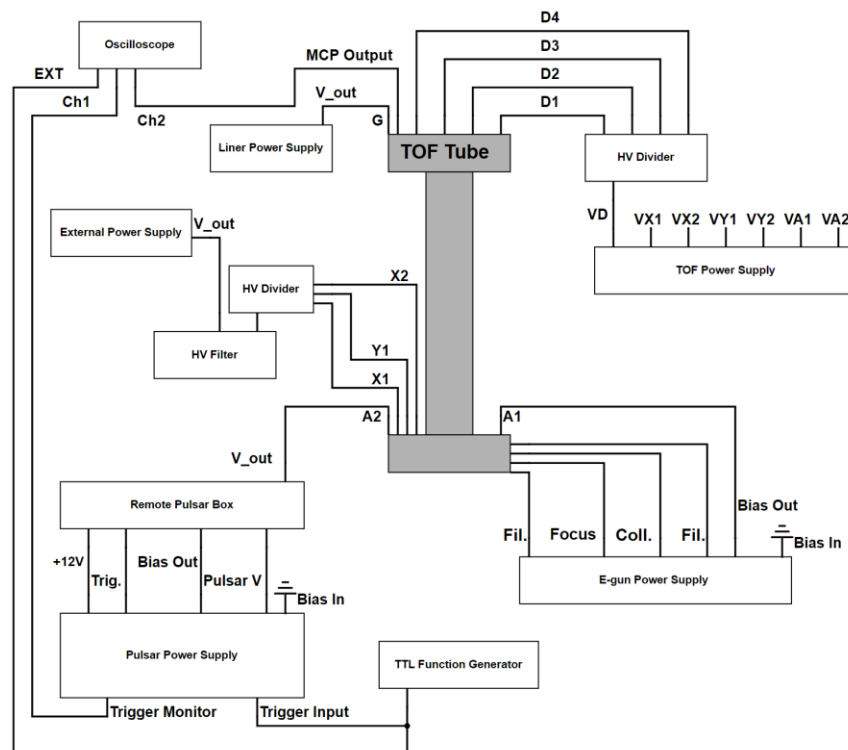


Figure 2.5: Box schematic of the Time-of-Flight electronics wiring setup which includes the triggering device, oscilloscope, and power supply for all necessary components.

The transient details of the spectrum intensity over time are managed by a Matlab script (Appendix C) which takes the raw data directly from the oscilloscope (times and MCP signals), processes the data through a mass-time calibration, and outputs the mass spectra as the signal intensity as a function of mass/ion-charge ratio. The time-mass calibration is constructed by sampling species of known mass and noting the time elapsed after the falling edge of the trigger signal before being detected within a single spectrum. This measurement is done until enough known species are sampled which outlines a smooth calibration curve which spans mass values of $m/z=1$ to $m/z=260$. Species which are easiest to use for calibration include noble gases (Ar, Ne, Kr, Xe), air, SF₆, and sublimating iodine.¹³⁶ Theoretically, the calibration should

be one which is quadratic since the species should follow a trajectory which is consistent with kinematic motion which has a constant acceleration (constant electrostatic force between two charged plates) in two regions, constant velocity (field-free) in one region, and a time of 0 for $\frac{m}{z} = 0$. Therefore, the general form of the calibration curve should take the form of $\frac{m}{z} = at^2 + bt + c$, where the values of a, b, c are determined by the parameters of the fitted quadratic determined from calibration measurements. The exact detection time of each ion depends on the electric field in the accelerating region which is directly proportional to the set voltage of the plates. An example of such a calibration curve is shown in Figure S2.2.

2.2.3 Temperature-Jump Time-of-Flight Mass Spectrometry Method

The samples of primary interest include solid energetic materials and their individual constituents, if belonging to a heterogenous composition. In order to observe gas phase reaction intermediates and products evolve from an energetic reaction on combustion time scales, it is useful to couple Time-of-Flight mass spectrometry to the T-Jump technique discussed in section 2.1.2 The previously discussed resolution of the TOFMS (0.1 ms) and total collection time (10 ms) makes coupling T-Jump to TOFMS ideal given the characteristic time scales of a nano-thermite combustion event being roughly $\approx 1-2$ ms in length (Figure 2.2). T-Jump is coupled to TOFMS by using a custom-made T-Jump probe which consists of a vacuum sealing flange and electrical feedthroughs, but also the ability to extend and contract. How the probe couples to the main components of the TOFMS system is illustrated in Figure 2.6 which was previously made by a former member of the Zachariah Group.¹³⁷

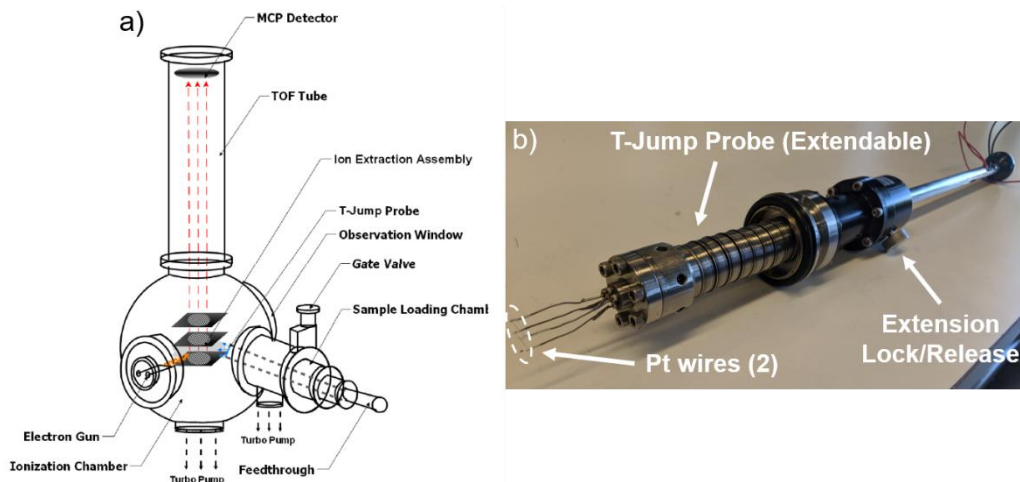


Figure 2.6: Coupling of the a) TOFMS system with the T-Jump technique using the b) customized T-Jump probe.

The retracted rod-like T-Jump probe is prepared with the coated 76 μm Pt wire and inserted into a roughing chamber. The roughing chamber is pumped down to 10^{-2} - 10^{-1} Torr using a mechanical pump and remains at that pressure range for 5-10 minutes. After this process, a gate valve separating the roughing chamber from the mechanical pump is closed and another gate valve separating the roughing chamber from the main TOF ionization chamber ($\sim 10^{-7}$ Torr) is immediately opened. The pressure should equilibrate to $\sim 10^{-6}$ - 10^{-5} Torr, a safe pressure for usage of the electron gun and other high voltage elements within the TOF chamber. The T-jump probe is then extended to close-proximity (≈ 1 -2 in.) of the TOF voltage plates for effective sampling of the ignition species upon heating. As in the pure T-Jump setup shown in Figure 2.1, a viewport directly opposite the T-Jump probe is integrated within the TOF chamber to allow for capturing of high-speed videography and the capability to inspect instrument parts for potential maintenance issues. The proximity of the violent ignition events to the sensitive TOF voltage plates and electronics may cause there to be issues in terms

of plates shorting and burning out easily replaceable electronic components or more permanent corruption of voltage plate insulation. Issues pertaining to these possibilities are linked to how violent the energetic reaction is and its ability to produce many transient ions, and the amount of material utilized. Therefore, it is best to coat the platinum wires as lightly as possible when dealing with violently reacting materials in order to maintain the functionality and integrity of the TOFMS instrument. This problem is largely not a factor when dealing with endothermic reactions, but small amounts are still needed for more accurate temperature measurements. More on the specifics of how to maintain the instrument and things to consider when troubleshooting is noted in the Appendix A.

Since the premise of TOFMS relies on an environment which is essentially free from collisions with other gas molecules, the TOF tube and sampling regions, shown in Figure 2.4, must be under high vacuum in order to lengthen the mean free path ($\lambda_{mf} \sim \frac{1}{p}$) for nascent gas species to be sampled correctly. This means that all experiments coupling T-Jump and TOFMS must be conducted under vacuum, which has been shown to affect the behavior and morphology of the ignition event when compared to pressurized environments.^{72,120} Regardless, the technique of T-Jump/TOFMS gives one the ability to simultaneously monitor the temperature of ignition between samples, capture high-speed videography, and collect time resolved speciation of the entire heating process from start to finish. Since T-Jump and TOFMS utilize the same triggering mechanism, the two setups in Figure 2.5 and Figure 2.1 can be seamlessly incorporated with channels 1,2,3,4 of the oscilloscope representing the pulsar voltage timing signal, the MCP detector signal, the voltage across the platinum

wire, and the measured current flowing through the platinum wire, respectively. As such, T-Jump/TOFMS is not exclusively used for energetic compositions since now there is an added diagnostic technique to “see” the unseen from the rapid heating of oxidizer components such as nanoscale metal oxides (CuO , Fe_2O_3 , Bi_2O_3) or submicron strong oxidizing salts (Ammonium Perchlorate, KClO_4). Knowing the reaction pathway for oxidization is an important task which this instrument was designed for and presents a quantitative method to tweeze out individual component contributions to overall energetic reactions. Figure 2.7 is an example from a published paper of mine given as an example of the type of quantitative data obtained from the technique of T-Jump/TOFMS.

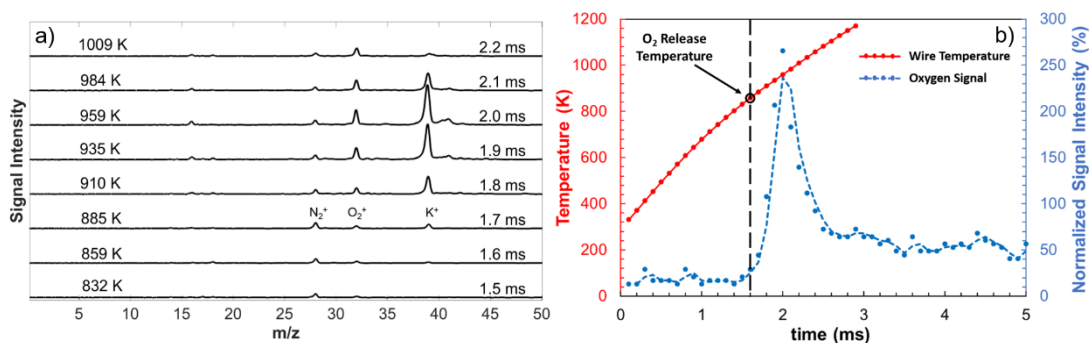


Figure 2.7: Time resolved a) full mass spectrum and b) single species detection profile as a function of temperature from the heating of KClO_4 submicron particles (T-Jump/TOFMS)

2.2.4 Measuring Activation Energy of Species Release

In the same way that the pure T-Jump technique data in Figure 2.3 can be processed using the Flynn–Wall–Ozawa isoconversion method to obtain an activation energy for ignition, an activation energy of species release, such as oxygen release, can be measured.¹¹⁵ The same Matlab script (Appendix: C-1) used to report the ignition temperature and heating rate can be used to report the temperature of initial species

detection and the heating rate at that point in time with a characteristic time step of 0.1 ms. These measurements may be used to develop a kinetics approach to understanding the energy landscape of energetic compositions and revealing reaction pathways involving non-energetic additive constituents and/or the oxidation pathways of oxidizer components which lead to ignition.

2.3 Rapid Chemical Speciation: Molecular Beam Mass Spectrometry

2.3.1 Methods and Motivation of Molecular Beam Mass Spectrometry

Although T-Jump/TOFMS mass spectrometry is an extremely powerful tool in analyzing the transient behavior of chemical species under rapid heating conditions, it can only be conducted under high vacuum conditions with small amounts of material ($\approx 10 \mu\text{g}$). Samples to be rapidly heated from the T-Jump Pt wires are intimately integrated within the system ionization chamber with no way of decoupling them and getting comparable results. Larger amounts of energetic material being sampled will either compromise the T-Jump/TOFMS electronics or lead to deviations from the temperature gathered from Pt wire thermometry.

Molecular beam mass spectrometry (MBMS) presents a method of conducting chemical speciation through time-of-flight mass spectrometry of energetic systems by decoupling the ionization chamber from the region where the energetic reaction takes place. MBMS decoupling of the sample from the ionization region allows one the capability to probe gas phase products from a flame using relatively large sample types (films, liquids, powders) at elevated pressures of differing ambient carrier gases.¹³⁰ Since the T-Jump/TOFMS system is performed in vacuum, gas phase interactions are

limited with very few collision interactions between species. Elevated pressures allow for an environment rich in molecular collisions and interactions where various reaction products, not seen in vacuum, can be detected during the full duration of film propagation (≈ 1 second), allowing the reaction to be studied in a wide range of practical application conditions. Given the duration of a full combustion event of several milligrams of material, roughly 3.5 seconds worth of time resolved data can be captured utilizing the 600 MHz Teledyne LeCroy Oscilloscope at a sampling rate of 1-3 full mass spectra per millisecond (1-3 kHz). Additionally, MBMS utilizes an altered form of the TOF tube called Reflectron Time-of-Flight (RF-TOF). RF-TOF effectively doubles the flight distance of ions and enhances the resolution of their detection by integrating a voltage lens array which directs incident ions back towards the 40 mm diameter MCP (larger detection area) located adjacent to the ionization chamber.¹³⁸ Adjustments the voltage lens can be made which enhance signal resolution and the shape of the signal envelope of the incident mass species. A more technical drawing of this system is provided by Jordan TOF Products Inc. The choice of a RF-TOF over a quadrupole mass spectrometer is based on the need for detecting a transient event, thus the need to sweep the entire mass spectrum in an enhanced time-resolved manner (≈ 10 kHz). The specifications of the build required additional customized parts for which the build of the MBMS was undertaken, completed, and documented by a former lab member of the Zachariah Research Group, Jeff Delisio.¹³⁰ The way in which the sampling region is separated from the ionization region and the method of molecular beam sampling is illustrated by the MBMS schematic in Figure 2.8. Energetic materials are ignited via wire joule heating within a controlled atmosphere and the species of the

transient combustion are sampled through a small orifice, ionized from electron impact, and detected through RETOF.

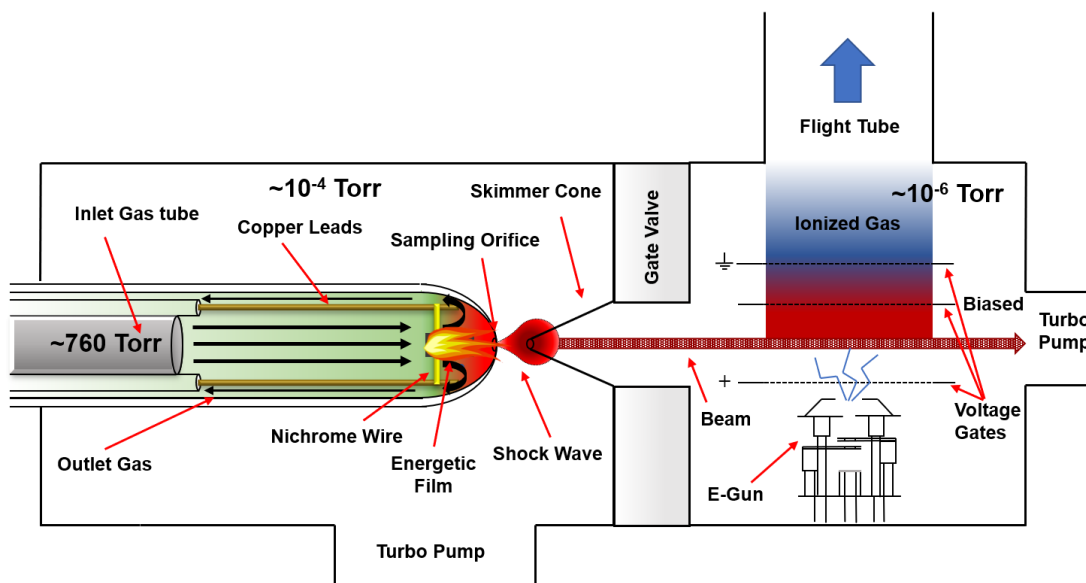


Figure 2.8: Experimental setup and Molecular Beam Mass Spectrometer schematic of flame sampling during combustion.

2.3.2 Formation and Characteristics of the Molecular Beam

The premise of molecular beam mass spectrometry relies on the phenomenon of creating a molecular beam. The molecular beam has been defined as “a ‘train’ of molecules with some degree of correlated motion, despite the absence of any overall hydrodynamic flow”.¹³⁹ The formation of such a beam is only possible through a differential pumping approach within a choked flow system using the assumption of isentropic flow ($\Delta S=0$) which expands gas from a region of relatively high pressure to one of much lower pressure while creating a supersonic free-jet of molecules.^{138–141} Hot gaseous products within a carrier gas, with no directed motion, funnel through a sampling orifice at the end a quartz tube from which the resulting shock wave is probed and further collimated by a skimmer cone into a refined beam with little directional

deviations among gas molecules, as shown in Figure 2.8.^{140,141} The energy of the isentropic flow system must be conserved during the transition and can be represented as the sum of the directional kinetic energy and the enthalpy, as equation 2.1 shows.

$$c_p T_o + \frac{v_o^2}{2} = c_p T_1 + \frac{v_1^2}{2} \quad (2.1)$$

In the system of interest, $v_o = 0$ since the gas which diffuses through orifice is largely stagnate with no directed motion. The act of rapid expansion through the transition from the high-pressure continuum region (reaction event) to the collisionless low-pressure region (ionization region), through the small orifice (100-200 μm), constitutes isentropic free-jet expansion.¹³⁹⁻¹⁴² Thus, the work needed to expand gas within the lower pressure environment must originate from the internal energy of the system. How much internal energy is converted depends on the change in the temperature of the gas as it transitions from the high pressure to low pressure regions corresponding to the relationship between pressure, P, and temperature, T, during an adiabatic process (equation 2.2).

$$\frac{T_1}{T_o} = \left(\frac{P_1}{P_o}\right)^{\frac{\gamma-1}{\gamma}} \quad (\gamma \equiv \text{adiabatic index}) \quad (2.2)$$

One can see from equation 2.2, that a system with a nitrogen ($\gamma \approx 1.4$) carrier gas which starts at room temperature with a pressure difference ratio of 10^{-7} (10^3 Torr to 10^{-4} Torr) results in a final beam temperature of roughly 1.5 K. Other experiments also report the drastic decrease in molecular beam temperatures as low as 1K.^{140,142} The ultra-cold molecular beam is a corner stone feature of MBMS sampling in which the creation of the beam not only efficiently transports the sampled molecules to the ionization chamber, but also freezes the gas molecules to no longer react, enabling the

preservation of the sample during transit.¹⁴² Given the degree of temperature decrease from the transition from high to low pressure regions through the choked flow orifice, nearly all the thermal energy of the system has converted to kinetic energy for which one can define the Mach number as it relates to the supersonic speeds reached as result.^{140,142,143} Combining equations 2.1 and 2.2 while dividing the beam velocity by the speed of sound gives an expression shown in equation 2.3 which relates the Mach number, Ma , to the initial pressure drop ratio across the choke point¹⁴¹.

$$Ma = \frac{v}{v_s} = \sqrt{\left(\frac{2}{\gamma - 1}\right) \left(\left(\frac{P_o}{P_1}\right)^{\frac{\gamma-1}{\gamma}} - 1 \right)} \quad (2.3)$$

As equation 2.3 infers, one would need a pressure difference ratio of at least 2 for the supersonic ($Ma > 1$) nature to be obtained and the molecular beam formed.^{140,141} Figure 2.8 represents the specific instrument setup which routinely establishes a pressure difference ratio of 10^{-7} between the sampling region and the atmospheric conditions within the quartz tube, inferring the emergence of the supersonic molecular beam. This pressure differential theoretically corresponds to a beam speed of roughly Mach 20 in a nitrogen ($\gamma \approx 1.4$) gas carrier, and Mach 40 in an argon ($\gamma \approx 1.6$) gas carrier.¹⁴⁰ Differential pumping utilizing a molecular pump and turbo pump adds an additional difference of 10^{-2} Torr established across the skimmer cone separating the ionization chamber from the sampling region. The gate valve behind the skimmer cone in Figure 2.8 is only opened once the appropriate pressure in the sampling region has been reached.

The skimmer cone orifice was designed with a diameter of 100 μm so that the molecular beam flow through the skimmer cone can be optimized such that there exists

a large MBMS signal to noise ratio and the ionization chamber pressure can be maintained between 10^{-5} Torr and 10^{-6} Torr.¹³⁰ The structure of the shockwave relative to the position of the skimmer cone has been previously documented and visualized by studies using sketches and Schlieren photography.^{139,140} For optimal species sampling and optimized MBMS signal intensity, it is paramount that the skimmer cone be aligned well with the sampling orifice of the quartz tube and placed within the isentropic center streamline region of the shockwave structure at a separation distance of roughly ≈ 1 cm.^{139,141} This separation puts the entrance of the skimmer cone just before the Mach Disk of the shockwave structure.^{139,141} The alignment process can be difficult but made easy when aided with the use of a 3D stage manipulator which allows one to move the sampling orifice into place while monitoring the live signal of a carrier gas displayed on the oscilloscope. The quartz tube is then locked into place once the maximum signal for molecular beam sampling has been found. The results of preliminary MBMS experiments are discussed in chapter 8 and will highlight limitations and expanded utilities of MBMS beyond what has been noted in this chapter.

2.4 Instrumental Build: T-Jump Nano

2.4.1 Introduction and Project Purpose

As mentioned in section 2.2.1, the cornerstone instrument in the Zachariah Group is the Temperature Jump (T-Jump) Time of Flight Mass Spectrometer (TOFMS). In summary, the main feature of this instrument is that it couples and synchronizes mass spectrometry with the rapid heating of a fast response platinum wire thermometer coated with a small amount of sample. As it stood, a single synchronizing

function generator acts as both a single and continuous triggering mechanism. In normal operation, a 1-10 KHz TTL square wave, with a width of roughly 5 μ s, triggers an oscilloscope to start recording data, an electron gun pulsar power supply to vary ejection of ions, and the heating of a platinum/Nichrome wire. Data collection occurs over a 10 ms where 10-100 total spectra are collected. In order to achieve this type of data collection, both the oscilloscope and electron gun pulsar source must see a continuous trigger signal corresponding to each spectra/ionization time period. However, heating of the wire over a period of 1-100 ms requires only a single heating pulse with a variable width and amplitude. As a result, the current setup must utilize a separate heating pulsar box powered by a variable power supply which takes the continuous trigger input and outputs a single heating pulse with a calibrated width and amplitude.

The purpose of this project is to modernize the current setup while physically consolidating all the major control components, increasing versatility of control, and enhancing ease of availability and mobility for this type of system to be utilized for other instrument setups requiring synchronization and various heating schemes, such as laser heating.

While there isn't anything necessarily wrong with the current setup, most of the components are bulky and lack portability. The system requires a function generator, heating pulsar box, oscilloscope, and power supply. All these components, in total, require considerable desk space and are also interchangeably used for different experiments in the lab, making setup and break down of the instrumentation quite time consuming. The current heating scheme is also fairly one dimensional by only allowing

a single heating pulse. Previously, there was no way of being able to take the continuous trigger input voltage and output a continuous square wave with a variable width and amplitude for heating purposes. This capability alone would broaden the studies I could undertake with the T-Jump/TOFMS system and other experiments requiring such behavior.

2.4.2 T-Jump Nano Operation and Design

The project design and construction were undertaken by me and Dylan J. Kline. This project was called the T-Jump Nano. The design relies on the versatile capabilities of a programmable Arduino Uno microcontroller in place of a function generator. This switch instantly downsizes the current function generator while enhancing control capabilities with a modernized and simplified interface. For this specific design, a programmed Arduino Uno was coupled to the circuit board to have three BNC output types: a programmable continuous waveform, a programmable single shot, and a modulated heating waveform which could be either single shot or continuous. Switches are implemented complementary to the programmed Arduino Uno action within the circuit scheme for all waveforms to be output simultaneously. This allows for the capability of triggering an oscilloscope, or any other electrical component, while capturing the data which may come as a result of the single shot output.

The base circuit design for creating a device with these functions was adopted by a circuit scheme put together by an ex-lab member of the Zachariah Group, Dr.

Jeffrey DeLisio.¹³⁰ Elements of the base design are depicted in the modified circuit diagram shown in Figure 2.9.

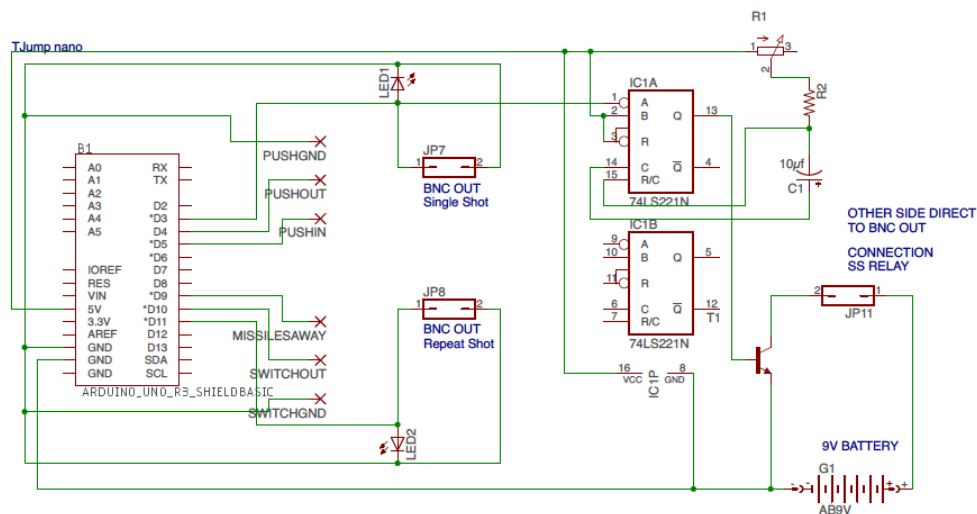


Figure 2.9: Schematic of the T-Jump nano (Autodesk Eagle 8.4.2.) apparatus including the high heating rate wire, solid-state relay, and oscilloscope.

The base design was adapted to integrate the Arduino Uno microcontroller as the brains to operate the backbone of the instrument in the monostable multivibrator. The low voltage/current mechanical relay was replaced with a relatively high voltage/current solid-state relay for flexibility in utilized current and voltage while ensuring longevity of instrument components. Indicator LEDs were also integrated for troubleshooting purposes and presentation. Although the label for the input waveform for the monostable multivibrator (Pin1) has a parallel BNC monitor output labelled “BNC OUT Single Shot”, the waveform can be any customizable waveform created in the Arduino Uno software which can be a single pulse or a series of pulses of varying time widths. A push switch initiates the waveform delivered by the Arduino Uno and will run until completion. The “BNC OUT Repeat Shot” monitors the continuous waveform which is needed for the TOFMS configuration. This waveform is activated

via a flip switch and is independent of the “BNC OUT Single Shot” waveform, meaning that it may have a unique customization simultaneously. The prototype of this design is depicted in Figure 2.10.

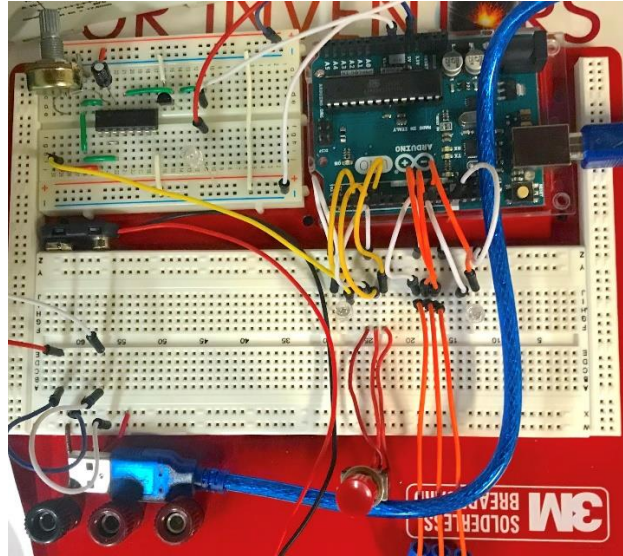


Figure 2.10: Initial solderless breadboard prototype of the T-Jump nano. The breadboard in the top left includes a monostable multivibrator and solid-state relay that would actuate a high-voltage pulse to resistively heat a wire. This multivibrator would be modulated with a signal sent by the Arduino Uno (top right) which is controlled with triggers wired in on the breadboard below it.

Initial experiments to test the functionality of the Arduino Uno and its execution of the trigger’s code produced two simultaneous pulses like those in Figure 2.11.

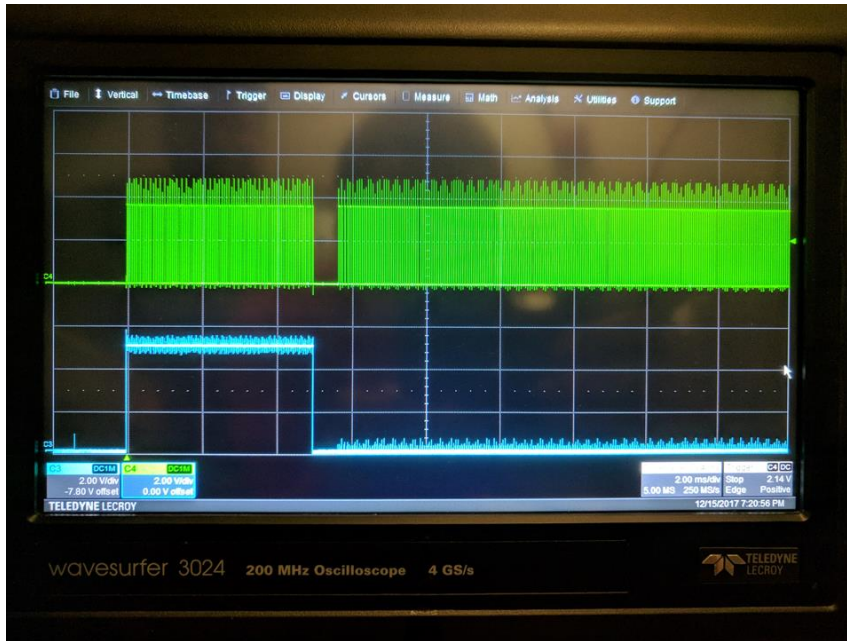


Figure 2.11: Arduino output waveforms: repeated (green) and single shot (blue).

As one can see, the device properly executes the implemented 5 ms, single shot pulse (blue) that would be used to trigger the resistive heating of a wire. At the same time, the other segment of the circuit board continuously produces 20 μ s pulses (green) until collection by the oscilloscope stops or the trigger is deactivated. When examining the pulses closely, there appeared to be a response resembling those seen in proportional-integral (PI) or proportional-integral-derivative (PID) control schemes. Zoomed images of the initial setpoint change (from LOW to HIGH) was reflected by the output of the device through a sharp step change accompanied by oscillations as the device attempts to control the output voltage internally. This noise to signal ratio is well within the acceptable range for its desired utility.

When the single shot pulse ends, there appears to be a gap of ≈ 150 -200 μ s that can be readily explained by the code shown in Appendix D. In the section of the code executed from lines 46-64, the code turns the Pulse Width Modulation (PWM) pin 3 to

low, which has been benchmarked as lasting 6-10 μs , and then the code prints a serial output to indicate the amount of time the single shot pulse was on. This series of actions accounts for the remaining time. In operational conditions, the prototype code shown would eliminate the serial printing since it could be measured much more easily on the oscilloscope directly and the `digitalWrite()` command could be substituted for direct port calls that are benchmarked at $\approx 0.4 \mu\text{s}$. It is important to note, however, that the typical application of this device calls for 100 μs pulses and thus the significance of the gap in the collection by the oscilloscope would be 1-2 samples at maximum.

The heating aspect of this circuit utilizes a re-triggerable monostable vibrator chip (SN74LS221N) which is powered by the Arduino Uno 5 V pin and activated by the programmed Arduino waveform input. The chip takes the input waveform and elongates the pulse width using timing components in the form of a capacitor and potentiometer as shown in Figure 2.9. The width of the output waveform is related to the discharge time of the capacitor by the relation $\tau = 0.7RC$. Having the resistor be a potentiometer allows one to have relative control over the width of the output waveform. This added component does nothing but modulate the input waveform. In order to gain control over both the output waveform width and amplitude, an amplifying BJT transistor is powered by a 9V battery and actuated by the output of the monostable vibrator chip at the BJT base (Pin 13). This action controls a solid-state relay which is connected in series to a separate circuit loop which initiates heating of the already existing T-Jump probe by a variable power supply. In this way the heating behavior of the wire can be programmed directly by the Arduino Uno and executed by the monostable vibrator in a variety of ways which can be simultaneously measured by

a continuously triggered oscilloscope for a select number of data segments. A summary of the result is shown in Figure 2.12.

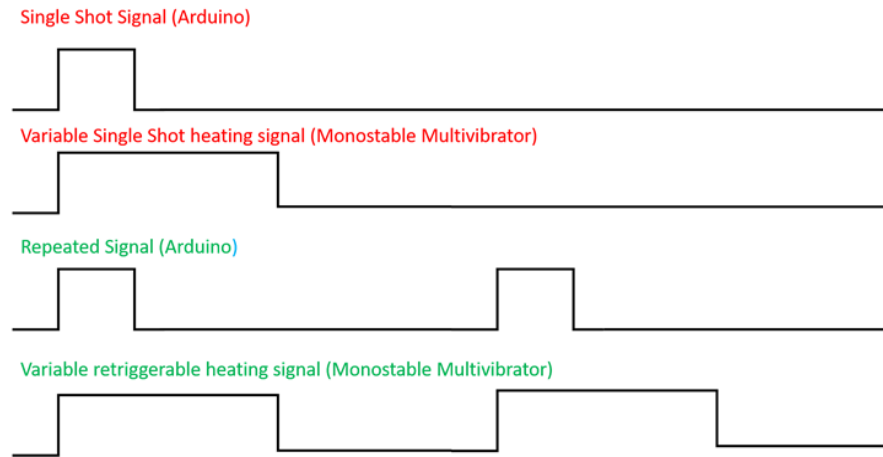


Figure 2.12: Theoretical output signals for heating and Arduino control (BNC outputs)

2.4.3 T-Jump Nano Printed Circuit Board and Housing

The circuitry of this build was designed so that the corresponding circuit board would attach directly to the Arduino Uno as an Arduino shield. This eliminates the use of the bulkier heating pulse box and function generator and replaces them with a roughly 4in² board with a 2-inch height. Combined with the solid-state relay and BNC connects, this corresponds to a build which can easily fit inside a small enclosure that is several times smaller than the combined real estate taken up by its predecessors. Although the Arduino Uno does need a computer to initially program it, this responsibility is simply taken up by the oscilloscope which itself is a Windows computer acting as a consolidated power source and programming interface. Below, Figure 2.13 and Figure 2.14 illustrate the final PCB layout, Arduino shield, and the fabricated aluminum enclosure.

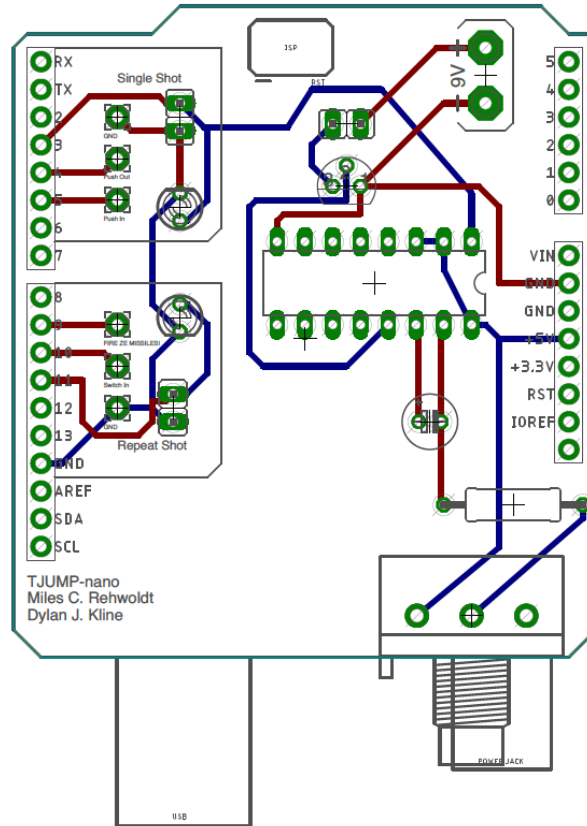


Figure 2.13: Diagram of custom printed circuit board to serve as a shield for Arduino Uno (Rev3). Printed circuit board is manufactured by OSH Park.

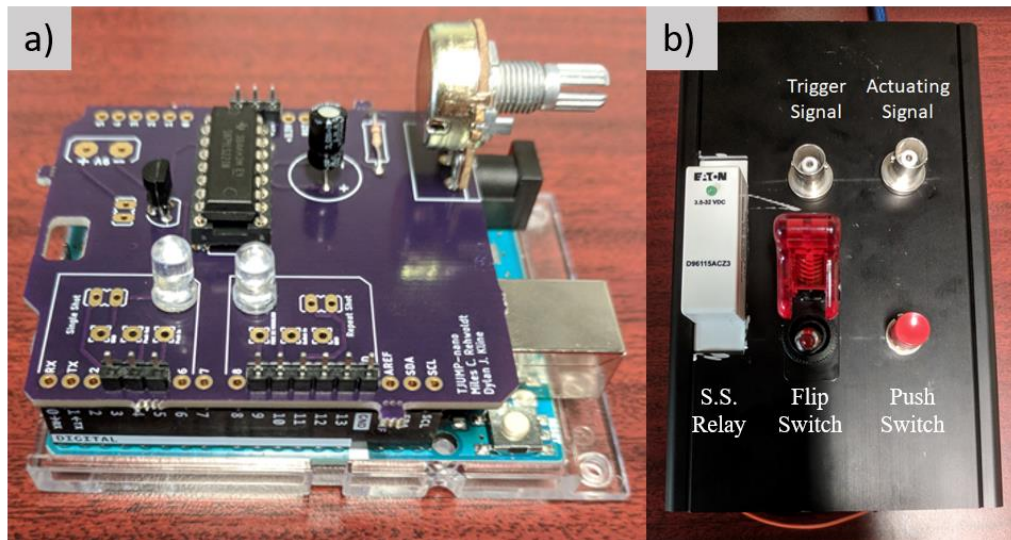


Figure 2.14: a) PCB of T-Jump Nano circuit mounted to Arduino board and b) PCB aluminum enclosure with output switches, BNC connectors, and heating relay.

Chapter 3: Probing the Reaction Mechanism of Nanoscale Titanium/Potassium Perchlorate Pyrotechnic Powder*

Summary:

The reaction mechanism and ignition characteristics of the pyrotechnic composite of titanium nanoparticles and micron-sized potassium perchlorate was investigated under rapid heating conditions ($\sim 5 \times 10^5$ K/s) by temperature jump (T-Jump) time-of-flight mass spectrometry. X-ray photoelectron spectroscopy surface analysis and transmission electron microscopy (TEM) characterization of titanium nanoparticles show a reactive oxide layer (~ 6 nm) composed of amorphous TiO_2 and roughly 20% crystalline TiN and titanium oxynitride. The T-Jump and thermogravimetric analysis reveals the oxide layer to be responsible for catalysis of oxygen release from KClO_4 , resulting in ignition temperatures as low as 720 K in atmospheric pressure argon. Fast and slow in situ heating TEM corroborate the findings of oxygen atmosphere ignition characteristics, which illustrate KClO_4 melting and coating of titanium nanoparticles immediately before oxidizer decomposition and titanium oxidation. Unlike aluminum, which has been shown to have a rapid loss of surface area before combustion as a result of sintering, Ti retained its high surface area. A combination of a reactive shell and the preservation of titanium nanostructure under rapid heating may lead to enhanced oxygen diffusion and increased potential for transient energy release.

* The results presented in this chapter have been previously published and are reprinted with permission from: Miles C. Rehwoldt, Yong Yang, Haiyang Wang, Scott Holdren, and Michael R. Zachariah, *The Journal of Physical Chemistry C*, 2018 122 (20), 10792-10800. Copyright 2018 American Chemical Society.

3.1 Introduction

Nanoscale metal particles such as aluminum, boron, zirconium, magnesium, and titanium have been the focus of recent research regarding their potential as fuels in energetic composites. The combination of relatively high combustion enthalpies and reduced reaction length scales make nanoscale metallized energetic systems particularly interesting for their potential for transient, high yield energy release.^{27,37,130,144–147}

Although the favorable thermodynamics of such systems are well known, their kinetics are relatively slow and specific reaction mechanics largely unknown. The nature of such reaction mechanics depends heavily on the individual and collective characteristics of the fuel and oxidizer under the rapid heating conditions indicative of combustion.²⁷ Although there have been several mechanistic studies of this type involving aluminum nanoparticles due to its relatively low cost and high energy density, there have been few such studies that have investigated titanium nanoparticles (nTi) as a viable alternative fuel source.¹²⁸ As a fuel with strong oxidizers, titanium can boast of a higher theoretically normalized combustion enthalpy per unit volume compared to aluminum and typical organic monopropellants such as cyclotrimethylenetrinitramine (RDX) and 2,4,6-trinitrotoluene (TNT).^{27,130} Significant differences in physical and thermal characteristics between aluminum, titanium, and their respective metal oxides make such an investigation enticing when considering their possible consequences on ignition mechanics (Table 3.1).

Table 3.1: Highlighted physical properties of aluminum and titanium species.

Material	Melting Point (K)	Thermal Expansion Coefficient ($10^{-6} K^{-1}$) (298 K)	Density (g/cm^3) (298K)
Al	933	23.1	2.70
Al ₂ O ₃	2345	8.4	3.98
Ti	1941	8.6	4.50
TiO ₂	2116	8.4	4.23

This article investigates the reaction mechanism of titanium nanoparticles (nTi) with the commonly used, strong pyrotechnic oxidizer potassium perchlorate (KClO₄) under rapid heating conditions.^{53,144,145,148,149} This class of energetic mixture is commonly used in energetic components such as thermal igniters and/or mechanical actuators, taking advantage of a superior combustion enthalpy compared to more traditional thermites, which use metal oxide oxidizers (Figure 3.1). Titanium/potassium perchlorate (TKP) mixtures were previously studied in a mechanistic manner at slow heating conditions by Sandia National Laboratories as a part of their mission to gain intuition and the “ability to predict and model pyrotechnic ignition thresholds”.¹⁵⁰ This investigation expands upon the findings from the Sandia work by subjecting the nanoscale energetic composite to controlled high heating rates while simultaneously monitoring gas phase species using time-of-flight mass spectrometry (TOFMS).

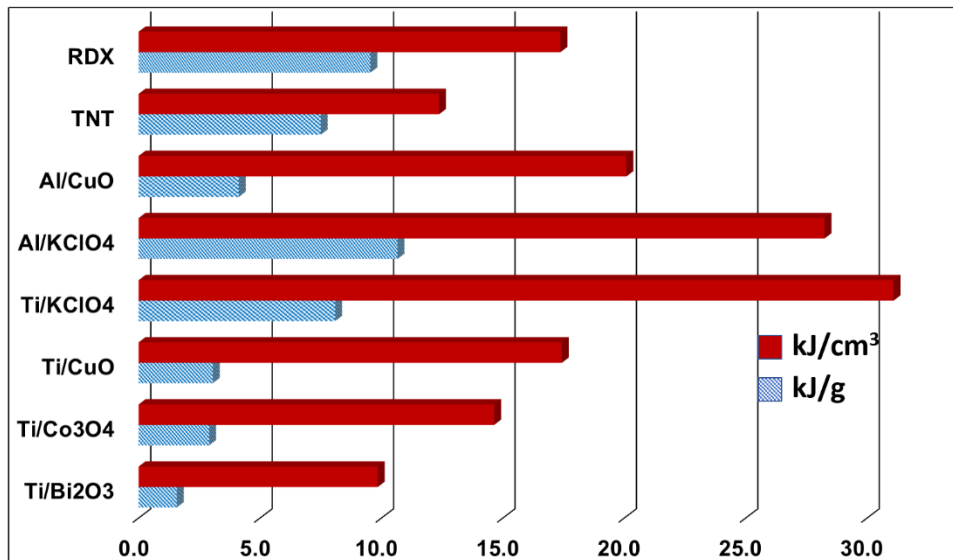


Figure 3.1: Maximum combustion enthalpies of stoichiometric mixtures ($\phi=1$)

3.2 Materials/Sample Preparation and Characterization

3.2.1 Materials Preparation

Titanium nanoparticles (30–50 nm) were purchased from US Research Nanomaterials, Inc. and anatase TiO₂ nanoparticles (<50 nm) were purchased from Sigma Aldrich. Micron-sized KClO₄ (~500 nm mean diameter) particles were synthesized via Aerosol Spray Pyrolysis operating at 423 K by first dissolving roughly 2 g of larger-sized particles purchased from Sigma Aldrich (99.5%) in 200 mL of deionized water.^{146,148,151} Particle sizes and composition were characterized by transmission electron microscopy (TEM, JEM-2100, JEOL Ltd.), scanning electron microscopy (SEM, Hitachi, SU-70 FEG-SEM), X-ray diffraction crystallography (XRD), and X-ray photoelectron spectroscopy (XPS, Kratos AXIS 165 spectrometer). Utilizing images from TEM and SEM, specifics of the particle sizes can be analyzed using the Nano Measurer 1.2.5 software (Figure 3.2 and Figure 3.3).

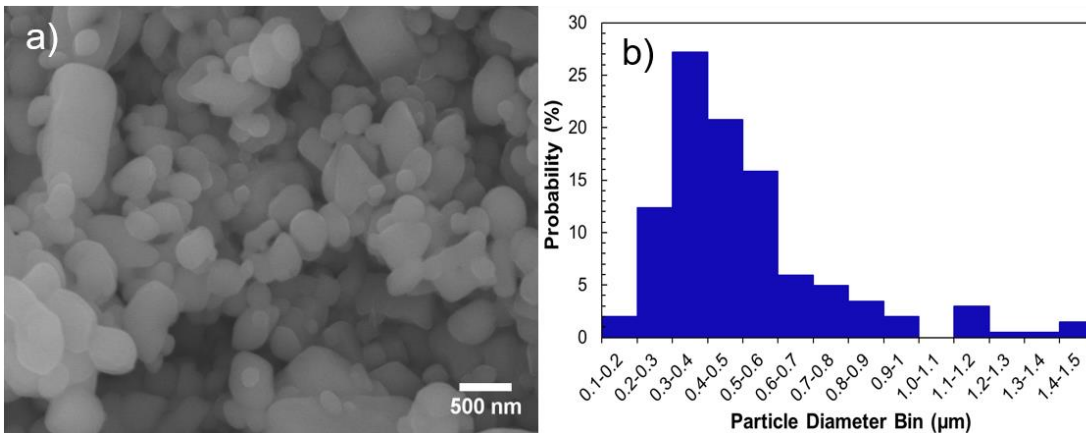


Figure 3.2: SEM characterized spray-dried micron-sized KClO_4 particles with b) a rough particle size distribution (200 particle sample size)

3.2.2 Titanium Nanoparticle Characterization

The as received titanium nanoparticles are quoted to have an average size of 40 nm with a specific area of $50 \text{ m}^2/\text{g}$ from the manufacturer but appear to have many particles which are slightly larger (50-150nm), indicating a wide size distribution. As is the case with many reactive metals, there exists a thin oxide layer on the surface of the titanium nanoparticles once exposed to air.^{57,130,152} The oxide layer both hinders further reactions with ambient oxygen and reduces the amount of reactive material available per unit mass of titanium. Probing of the titanium nanoparticles and their oxide layer was conducted via a combination of XRD, XPS, and TEM analysis, with initial imaging showing most particle oxide layers being around 6 nm or less, as seen in Figure 3.3.

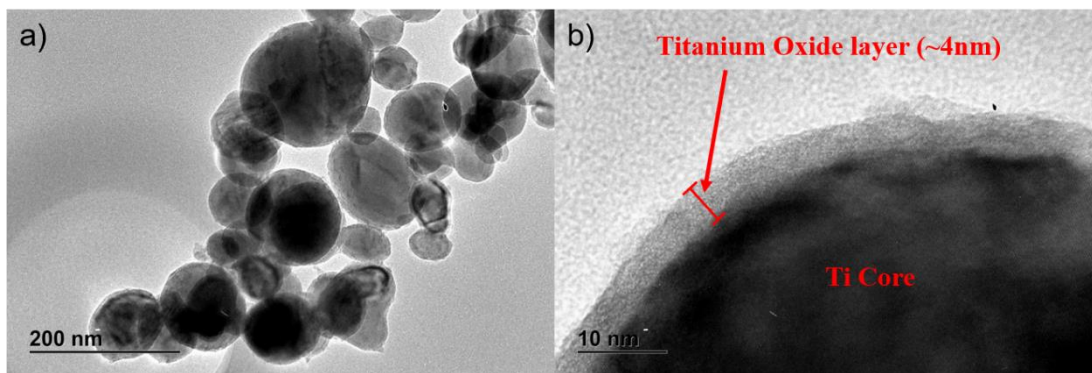


Figure 3.3: TEM characterized titanium nanoparticles from US Research Nanomaterials, Inc.

3.3 Rapid Heating Experiments

3.3.1 Temperature Jump (T-Jump)/Linear Time-of-Flight Mass Spectrometry

Ignition of physically mixed TKP at ultrahigh heating rates was conducted via temperature jump time-of-flight mass spectrometry (T-Jump/TOFMS).^{53,67,128,129,148} The apparatus illustrated in Figure 2.6a couples a linear time-of-flight mass spectrometer with a T-Jump probe, which is directly loaded into the ionization chamber of the linear mass spectrometer. The T-Jump probe is an extendable device, which consists of electrical feedthroughs and a vacuum sealing flange separating the high-vacuum environment of the TOFMS chamber ($\sim 10^{-6}$ Torr) from atmospheric conditions.

Before each experimental run, the T-Jump probe is prepared by soldering 6–12 mm of 76 μm diameter platinum wire (OMEGA Engineering Inc.) between the copper leads of the electrical feedthroughs. The nanopowder samples, 10 mg or less, which have been dispersed in hexane and sonicated (30–45 min) are deposited on the wire with a micropipette such that there exists a thin homogeneous layer of sample ($< 10 \mu\text{m}$) (10–40 μg) (Figure 3.4 and Figure S3.1).¹⁴⁸

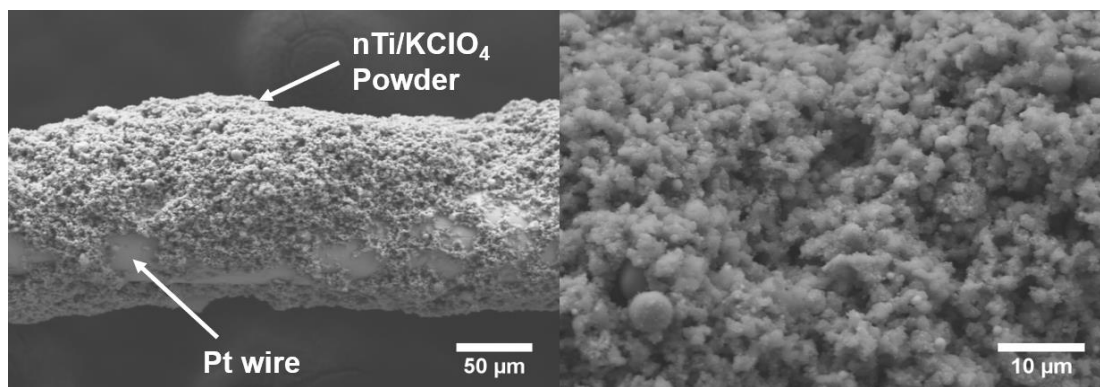


Figure 3.4: SEM of nTi/KClO₄ powder coated on platinum T-Jump wires

Once loaded into the TOFMS chamber, the platinum wire is resistively heated by a direct current voltage supply, which delivers a 1.5–9 ms pulsed square wave signal. The platinum wire acts as the probe by which fast response thermometry of the wire can be acquired. Temperature readings obtained through the calibrated relationship between the temperature of the Pt wire and its resistance from the Callendar–Van Dusen equation show the wire reaching temperatures as high as ~1400 K at heating rates as rapid as $\sim 10^6$ K/s. In this manner, the temperature of a sufficiently small amount of coated sample is approximately the temperature of the wire, whereas the heating rate replicates the heating rates expected in a combustion event.^{27,115,128,129} In all the cases, the heating rate is varied by maximizing the temperature of the wire while varying the voltage pulse time. Measurements were repeated at least three times at each heating pulse and heating rates measured at the point of species detection. The T-Jump measurements in the mass spectrometer and in argon were conducted using 1.5, 2, 3, 5, and 9 ms heating pulses, with the current reaching as high as 10 A when supplied with voltages in the range of 4–14 V (depending on pulse time).

Synchronized resistive heating mass spectrometry is obtained by utilizing a single trigger signal, which communicates simultaneous wire heating and collection of

time-resolved mass spectra due to the sample being heated. Gas phase species produced as a result of sample heating are ionized by a 70-eV electron gun ionization source, which is pulsed at 10 kHz, acquiring 0.1 ms/spectrum. A synchronized Teledyne LeCroy 600 MHz oscilloscope collects the raw data of mass spectra, voltage, and current readings. Current readings measured by a Teledyne LeCroy CP030A 30 A 50 MHz current probe are combined with the measured voltage to experimentally determine resistance, resulting in a time-resolved temperature profile once processed in Matlab.

3.3.2 TEM Heating

In situ microscopy of rapid sample heating was carried out by employing a Protochips TEM heating probe, which is depicted in Figure S3.2. The software allows for programmable heating of the probe TEM grid, which can reach temperatures as high as 1600 K at heating rates as fast as $\sim 6 \times 10^6$ K/s. The heating parameters of the probe, described in detail by Dr. Jeffrey DeLisio, mimic the heating conducted in T-Jump/TOFMS experiments, making this instrument ideal for comparable microscopic analysis of relevant samples at combustion time scales.¹³⁰ For these experiments, the Protochips TEM heating probe was programmed to heat to 1470 K at a heating rate of 4×10^5 K/s and held for 1 ms. Intermediate TEM heating rates were also utilized to capture in situ behavior of the energetic mixture at critical temperature values observed from the thermogravimetric analysis (TGA) analysis. The TKP sample was deposited onto a TEM heating grid, heated at a rate of roughly 100 K/s, and held at temperatures of 773, 853, 1023, and 1073 K.

3.3.3 Ignition Characterization

Thermal characterization of KClO_4 and its interactions with Ti at elevated temperatures were conducted using a TGA–DSC analysis. All the samples (1–3 mg) were heated to 1470 K at a heating rate of 25 K/min under an argon flow of 100 mL/min. Although this method utilizes much slower heating rates, it was employed to clearly resolve and identify any significant interactions, which may be of importance in the reaction mechanism of TKP at higher heating rates. Before mixing, preliminary thermogravimetry and differential scanning calorimetry (TGA–DSC) tests were conducted on titanium nanopowder to determine its active titanium content using a SDT Q600 from TA Instruments. Roughly 1 mg of titanium powder was loaded into an alumina crucible inside the instrument and heated to 1470 K at a heating rate of 25 K/min under an oxygen flow of 100 mL/min. Calculations utilizing a series of four separate measurements taken from the data sets illustrated in Figure 3.5 report the average active titanium mass content to be ~70%.

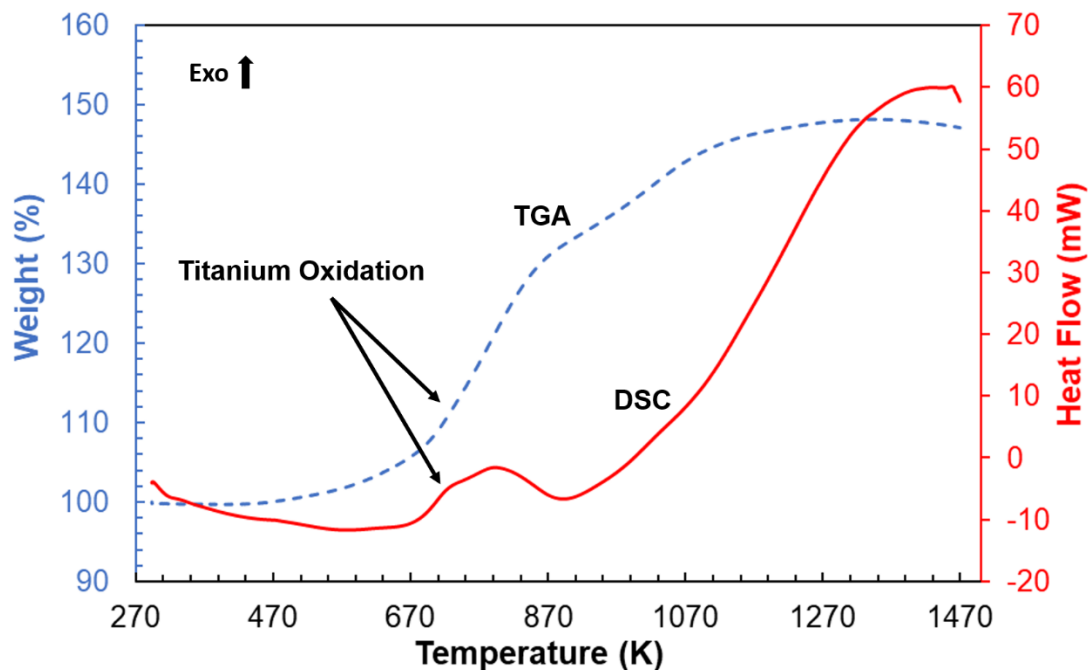


Figure 3.5: Average active Titanium content determined by TGA-DSC of titanium nanoparticles heated in oxygen at 10 °C/min.

Physically mixed TKP was prepared stoichiometrically with the percentage of active titanium (70%) taken to be the pre-XPS assumption of a fully TiO_2 oxide layer. As the results will show, the existence of TiN in the oxide layer adds a chemical species which can be further oxidized to form TiO_2 . Since the TGA-measured reactive mass content remains invariant with respect to the findings of XPS, the percentage of active titanium is smaller than in the case of a 100% TiO_2 oxide layer but still contains reactive TiN content. However, even if 20% of the chemical species of the oxide layer is composed of TiN and titanium oxynitride (TiON), this only corresponds to a 3–4% decrease in the estimated active mass percentage of titanium. Thus, the following single-step exothermic reaction assumption was the foundation of the TKP reactant mixture composition.¹⁵⁰



Elemental mapping analysis and XRD of TKP combustion products confirm this assumption to be valid for both slow and fast heating (Figure 3.6d and Figure S3.3).

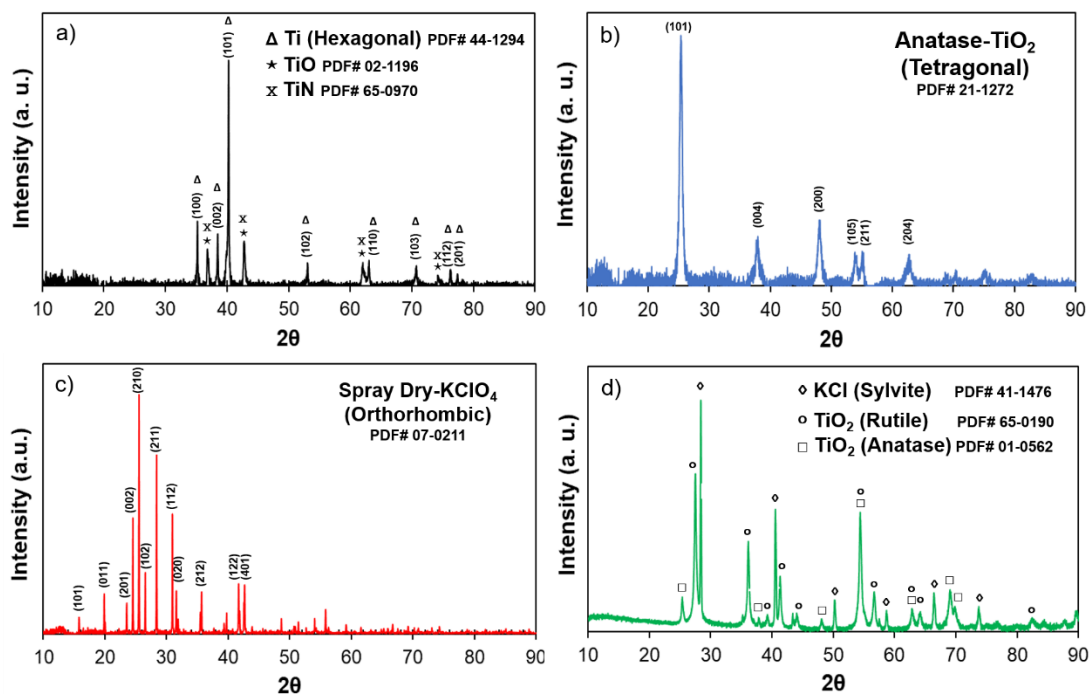


Figure 3.6: X-ray diffraction pattern of a) Titanium nanoparticles as received, b) simulant TiO₂ nanoparticles, c) Spray Dry KClO₄ particles, and d) TKP combustion products heated to 750°C (TGA)

Spray-dried KClO₄ particles, 51 wt %, are first dispersed in hexane and sonicated for 30 min. Titanium nanoparticles, 49 wt %, are then added and sonicated for another 30 min. The energetic composite is deposited onto the platinum T-Jump wires and ignited using various voltage pulse widths. Ignition was carried out in vacuum, oxygen, and argon environments, with a separate T-Jump-only chamber used for the latter two. The gas phase species of ignition can be monitored in the vacuum environment of the TOFMS but not in the atmospheric pressure environments due to

operational limitations of the TOFMS. In this study, ignition is defined as the point of first light of the heated sample above the visible thermal emission of the wire itself. Light emissions from the ignition event are captured through the chamber viewports using a synchronized Vision Research Phantom V12.1 highspeed camera running at 80 000 frames per second (FPS) at 10 μ s exposure.

3.4 Results and Discussion

3.4.1 Oxide Layer Characterization

The XRD measurements of the as-received titanium nanoparticles show both the hexagonal lattice structure of titanium and the composition of the oxide layer (Figure 3.6a). Interestingly, none of the nontitanium metal peaks correspond to any of the phases of TiO_2 , but match the patterns for titanium nitride (TiN) and titanium(II) oxide (TiO). The overlapping diffraction patterns of these two species make it difficult to distinguish between the two.

Further analysis of titanium particle surface composition was conducted using high-resolution XPS, with the results shown in Figure 3.7. Samples for analysis included as-received titanium nanoparticles at room temperature, titanium nanoparticles heated to 650 K inside the high-vacuum XPS environment, and anatase TiO_2 nanoparticles. Along with carbon-based surface contaminants, the XPS analysis of anatase TiO_2 particles reports an atomic percentage of titanium, which has roughly a 1:2 ratio with oxygen (Figure 3.7a). The atomic quantification measurements, along with O 1s and Ti 2p peak positioning, confirms the chemical composition to be TiO_2 for the control sample. All the relevant XPS peaks in Figure 3.7 are the given chemical

labels based on the NIST XPS database and literature using C 1s 284.8 eV calibrated XPS.¹⁵³

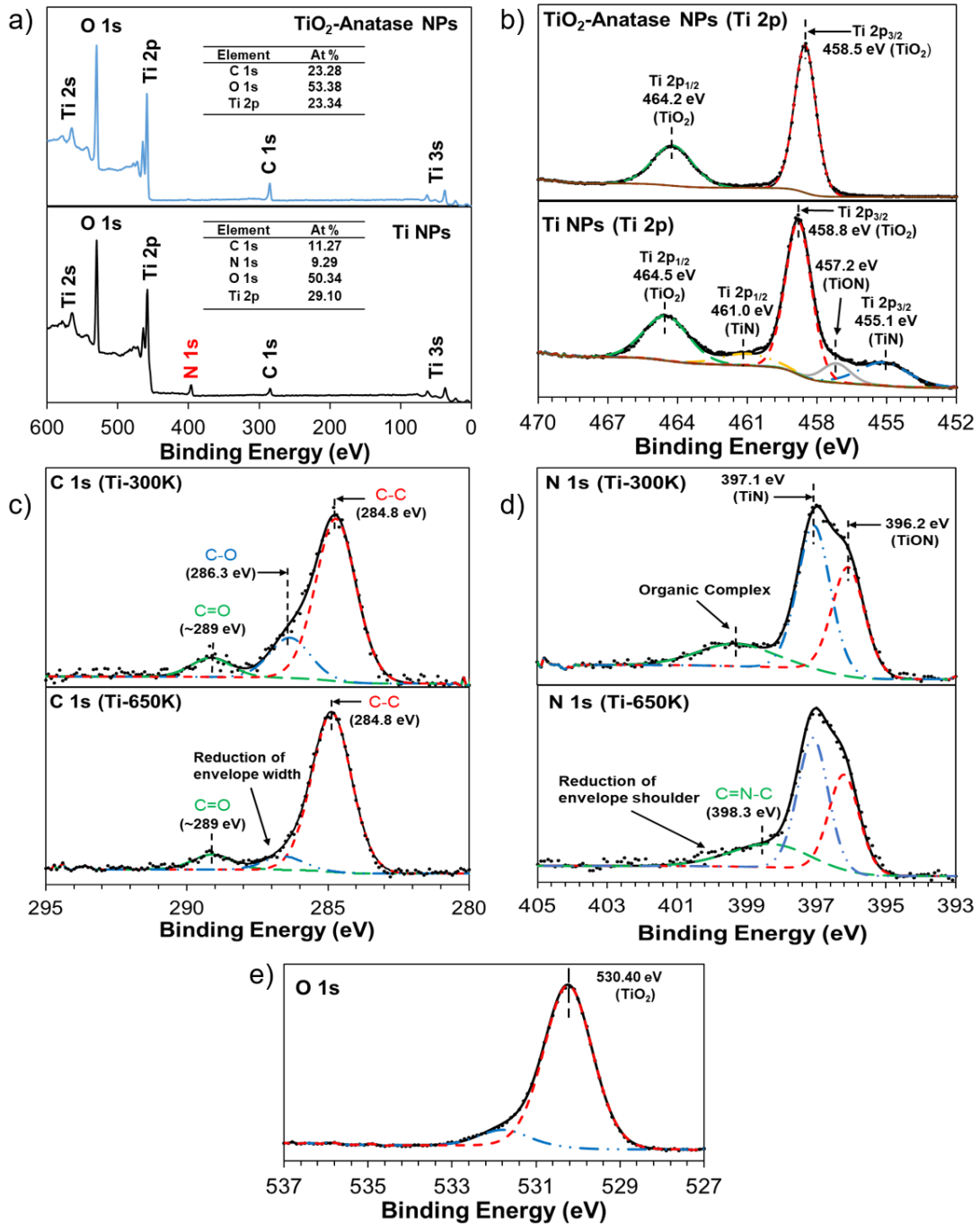


Figure 3.7: XPS analysis of titanium nanoparticles and TiO₂-anatase nanoparticles with peak fits

Just as with anatase TiO₂, the O 1s and Ti 2p peak positions of the titanium nanoparticle oxide layer are indicative of the TiO₂ oxidation state of titanium (Figure 3.7b–e).¹⁵³ With the lack of TiO₂ corresponding XRD peaks, it was concluded that TiO₂ exists in the oxide layer in an amorphous state. The atomic percentages report a titanium-to-oxygen ratio that is slightly smaller than 1:2, but also includes a significant amount of nitrogen not seen in the anatase TiO₂ sample (Figure 3.7a). This nitrogen content detected with XPS agrees with the XRD analysis that observed TiN as an additional component in the Ti nanoparticles.^{154,155} Additionally, it was observed the existence of an accompanying N 1s and Ti 2p broadening for which peak fit positions correspond to titanium oxynitride (TiON) making up a small percentage of the oxide layer (Figure 3.7b–d).^{153,154} In total, the XPS-based quantification of nitrogen estimates the species composition of the oxide layer to be as much as 20% TiN and TiON, with amorphous TiO₂ roughly making up the remaining 80%.

3.4.2 Rapid Heating ($\sim 10^5$ K/s) Mass Spectrum Characterization

The T-Jump/TOFMS measurements of micron-sized KClO₄ were conducted and the results are shown in Figure 3.8.

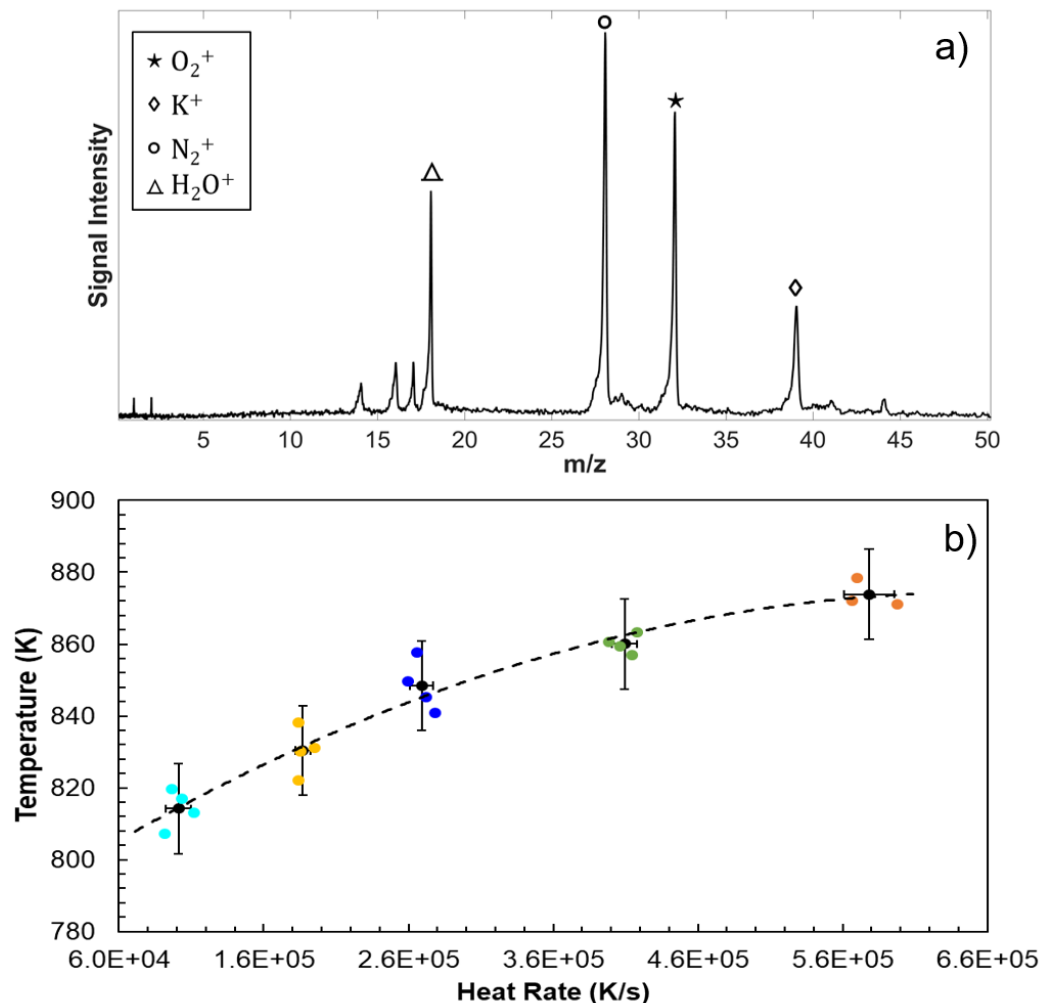


Figure 3.8: a) $KClO_4$ T-Jump averaged spectrum over 10ms collection time (used only for species identification purposes) and b) $KClO_4$ oxygen release as a function of heating rate (Release temperatures determined by averaging 3-4 repeated measurements).

The transient mass spectra shown in Figure 2.7a clearly illustrates potassium ions and molecular oxygen being the primary detected species above the background. The full mass spectrum averaged over 10 ms is shown in Figure 3.8a with the temperature of first detection of potassium/oxygen ions as a function of heating rate shown in Figure 3.8b. The temperatures of oxygen release from $KClO_4$ decomposition was experimentally determined by analyzing oxygen ($m/z = 32$) as a function of time

and noting the time where the signal rises above the background in Figure 2.7b. By varying the heating rate, β , the activation energy, E_a , for oxygen release can be obtained using the Arrhenius kinetic model approach of the Flynn–Wall–Ozawa isoconversion method applied in Figure 3.9 (Table 3.2).^{115,148}

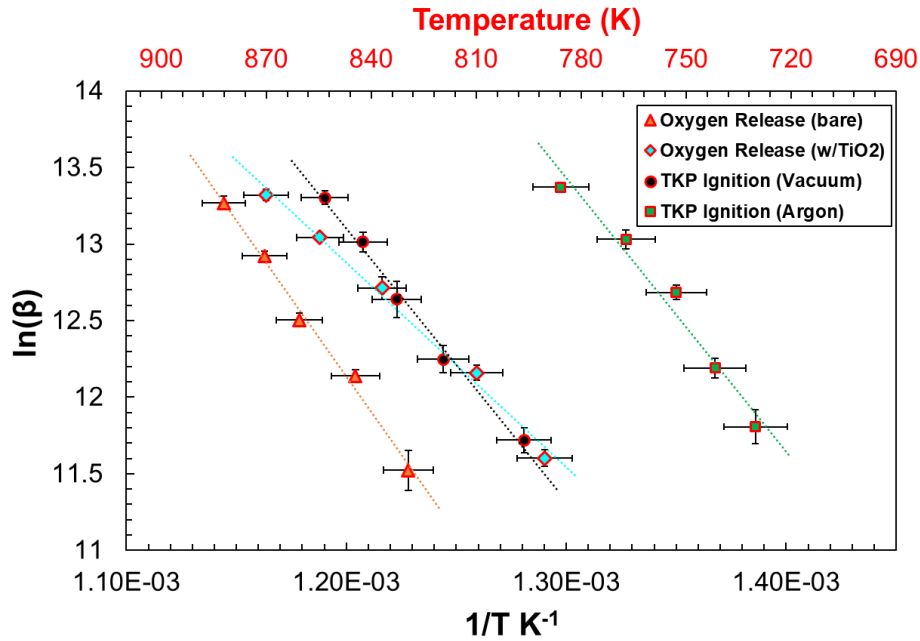


Figure 3.9: Arrhenius plots of KClO_4 oxygen release and ignition of relevant mixtures. See Table 3.2 for activation energies.

Generally, determination of the time of oxygen release is limited by the rate at which a full spectrum is acquired (0.1 ms). This can make identifying the point of oxygen release ambiguous, especially at higher heating rates. It is estimated that the extent of uncertainty in this measurement can be in the range of 10– 30 K. The largest contribution to this error stems from the intrinsic uncertainty in the current and voltage measurements. This uncertainty is typically larger than the statistical uncertainty of a collection of repeated measurements but can be reduced by considering the standard deviation of the mean from those same repeated measurements. It should be noted that compared to the findings from work by others at Sandia National Laboratories at slow

heating conditions, there appears to be only one oxygen release event that can be resolved at high heating rates.¹⁵⁰

At slow heating rates of KClO_4 in the TGA, one can identify the 20 K interval in Figure 3.10, where exothermic decomposition immediately follows the melting endotherm.^{144,149,156–158}

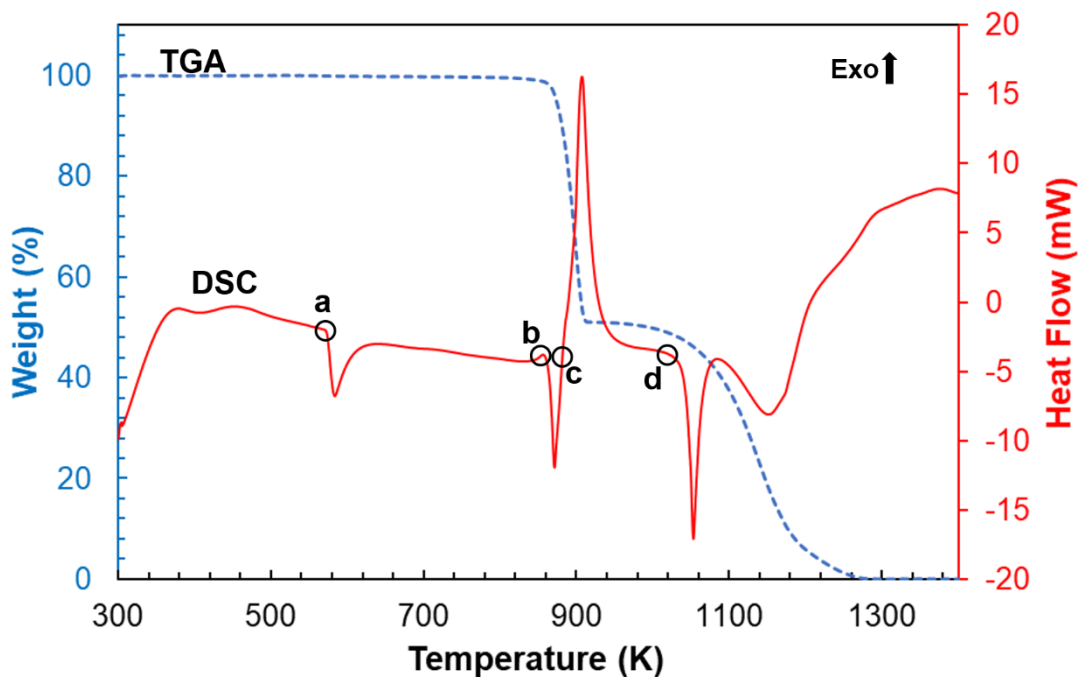


Figure 3.10: TGA-DSC of Spray Dried KClO_4 depicting the onset of a) crystalline phase transition (orthorhombic-cubic) at 300°C, b) melting at 590°C followed immediately by c) decomposition to KCl at 610°C, and finally d) KCl melting at 770°C

In comparison, the release of oxygen under rapid heating occurs at temperatures below the TGA–DSC observed melting temperature of KClO_4 (~ 870 K). Previously conducted T-Jump studies investigating the oxygen release of metal oxides demonstrate the same behavior of oxygen release occurring at lower temperatures for significantly higher heating rates.¹¹⁵ The heightened activation energy of oxygen release compared to the metal oxides mentioned in literature may suggest a heightened

degree of sensitivity to a sudden release of oxygen, enhancing its ignition capabilities for combustion with titanium. It should also be noted that smaller KClO_4 particles will cause observed melting to occur at slightly lower temperatures compared to as-received larger particles.¹⁵⁸

Outside of oxygen detection, mass spectrum analysis of TKP reveals the presence of H_2 , Cl-O products, CO_2 formation, and other fragmentation complexities. As the mass spectrum shows in Figure 3.11a, the H_2 peak ($m/z = 2$) is unexpectedly large.

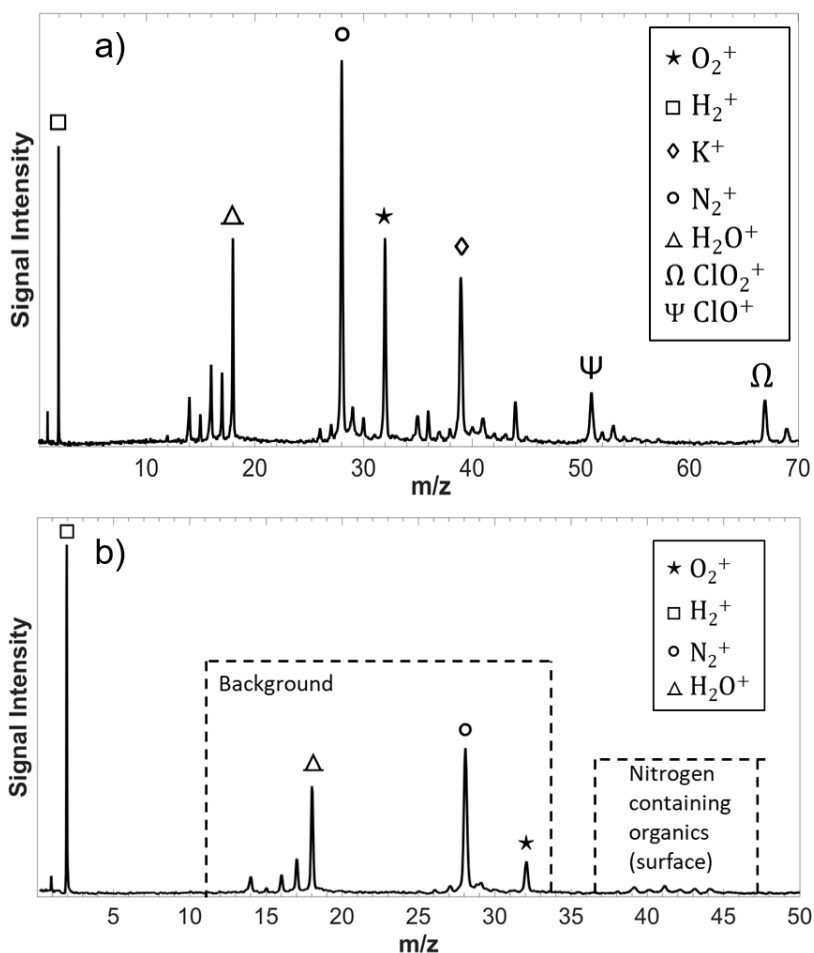


Figure 3.11: a) $n\text{Ti}/\text{KClO}_4$ ignition species averaged mass spectrum over 10ms collection time and b) $n\text{Ti}$ T-Jump averaged mass spectrum over 10ms collection time

Whereas the presence of H₂ in the mass spectrum of KClO₄ can be attributed to the ionization fragmentation of water vapor originating from background atmosphere, the increased H₂ is a consequence of added titanium nanoparticles and its behavior under rapid heating. The T-Jump mass spectrometry of titanium nanoparticles shown in Figure 3.11b alone reveals that these particles release a relatively large amount of H₂ after rapid heating. Similar observations of H₂ release from rapidly heated aluminum nanoparticles were documented in the Zachariah group as being an indication of a reaction with surface water. The proposed mechanism suggests that upon heating to the aluminum melting point, aluminum diffuses outward and reacts with water adsorbed to the alumina shell, producing H₂.¹²⁸ Though this may be a viable mechanism in the case of aluminum, there are a couple of observations that make this an incompatible mechanism for the case of titanium. Unlike aluminum, titanium does not react readily with liquid water (Figure S3.4) and does not have a low enough melting point for metal diffusion to take place within the temperatures achieved (Table 3.1). Though it may be possible for water to react with surface TiN to form TiO₂, H₂, and NH₃, there is no evidence from mass spectrometry indicating the abrupt emergence of ammonia ($m/z = 17$) above the background as strongly as hydrogen gas. Given the vacuum conditions ($\sim 10^{-6}$ Torr) of the mass spectrometer and their absence from the O 1s high-resolution XPS in Figure 3.7e, the majority of water and hydroxyl radicals must desorb from the surface either at room temperature or far below the ignition temperature of TKP, thus rendering water as a negligible factor in the ignition mechanism of TKP under vacuum conditions.

High-resolution XPS measurements of titanium nanoparticles illuminates a surface that is laden with carbon-based contaminants for which the existence of TiN has been shown to have surface nitrogen organic complexes.¹⁵⁹ In situ XPS heating of titanium particles shows a reduction in both the broadening of the N 1s peak and the contribution of carbon contaminants to the total carbon XPS signal (Figure 3.7c). Reinforced by mass spectrometry, the carbon-based oxynitride contaminants decompose upon heating and are further fragmented by the electron gun ionizer of the mass spectrometer resulting in the large H₂ peak seen from Figure 3.11.

3.4.3 Rapid Heating ($\sim 10^5$ K/s) Ignition Characterization

As mentioned previously, ignition studies of stoichiometric mixtures of TKP was conducted in vacuum ($\sim 10^{-6}$ Torr), argon (~ 835 Torr), and various pressures of oxygen with video snapshots of combustion intensity shown in Figure 3.12. Determining the ignition temperature is a much clearer process, given the capture rate of the ignition event using 80,000 FPS videography, which allows for ~ 10 μ s resolution, and 10 times that of the mass spectra acquisition rates.

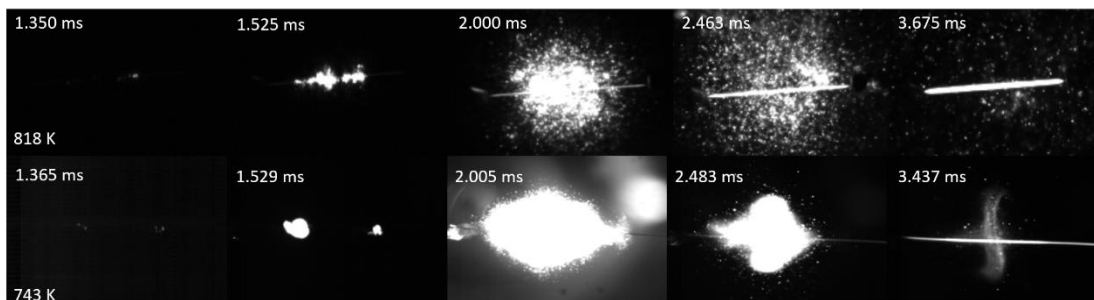


Figure 3.12: nTi/KClO₄ T-Jump ignition in vacuum (top) and argon (bottom) at $\sim 3 \times 10^5$ K/s visually depicting the constraining effect of ignition in a pressurized environment.

Analysis of ignition in each environment reveals the dependence of ignition temperature on the heating rate depicted in Figure 3.9. Further data processing determined activation energies of ignition listed in Table 3.2.

Table 3.2: T-Jump activation energies.

Material	Event type	Environment	Pressure (Torr)	E_a (kJ/mol) (± 10)
KClO ₄	O ₂ Release	vacuum	4×10^{-6}	160
nTi/KClO ₄	Ignition	vacuum	4×10^{-6}	140
nTi/KClO ₄	Ignition	argon	835	140
nTiO ₂ /KClO ₄	O ₂ Release	vacuum	4×10^{-6}	105

The results summarized in Table 3.2 characterize the ignition activation energy as determined from Arrhenius plots in Figure 3.9 as being independent of external pressure. Figure 3.9 consolidates the resulting ignition data found from T-Jump experiments in argon and vacuum and plots the corresponding data for oxygen release of the pure oxidizer for comparison. In the case of the two ignition environments analyzed thus far, the ignition temperatures all occur at least 50 K below the oxygen release temperature of the pure oxidizer for a given heating rate. This finding suggests that either the reaction mechanism is dominated by a purely condensed phase reaction before the temperature of oxygen release in KClO₄ or the release of oxygen is catalyzed by interactions not yet considered.^{12,53,129,150,160}

Past studies aiming to differentiate the effects of free and bound oxygen on ignition in aluminum-based thermite systems evaluated the ignition dependence on oxygen environments of various pressures.¹² For example, the reaction of aluminum nanoparticles with bismuth oxide has been accepted as being one that is dominated by a condensed phase reaction between aluminum and the highly mobile oxygen ions

within the crystal lattice of the metal oxide.³⁴ The results of the study conducted by Zhou et al. confirmed this notion by observing the independence of ignition temperature with added free oxygen concentration.^{12,13,57} This investigation utilized the same approach to test the possibility of a condensed phase dominant reaction mechanism.

With ignition of neat titanium nanoparticles in varied oxygen environments acting as a reference, the ignition of TKP was conducted at a heating rate of $\sim 2 \times 10^5$ K/s, and the results are shown in Figure 3.13. The results conclude that the reaction is not dominated by a condensed phase interaction. Figure 3.13 demonstrates the gaseous dependence of ignition temperature for which both bare titanium and TKP become increasingly sensitive to the availability of gaseous oxygen at lower pressures, indicating an ignition dependence on gas phase interactions.

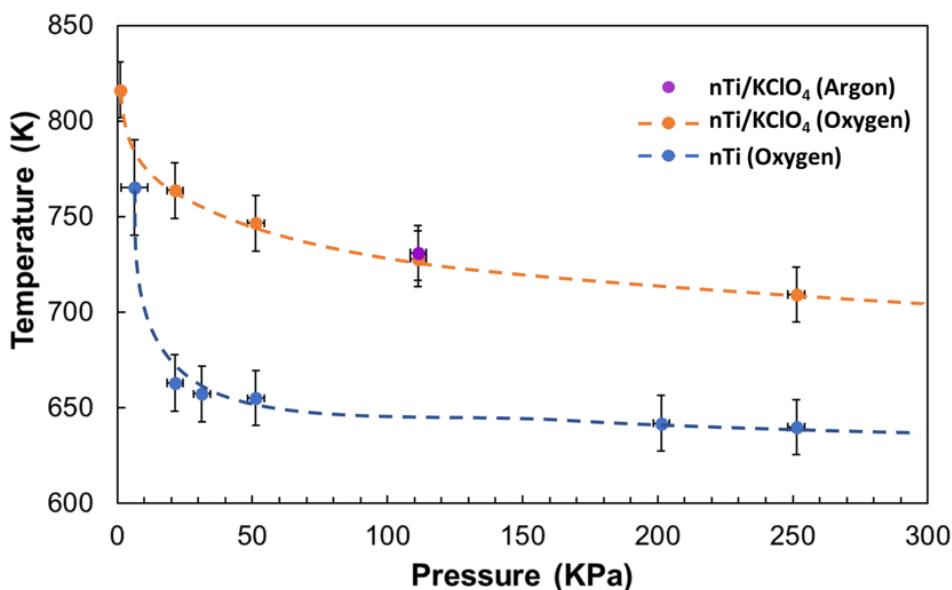


Figure 3.13: Pressure dependence of nTi/KClO₄ ignition in O₂ and Ar.

In Figure 3.13, whereas a higher ignition temperature for pure titanium results from the lack of oxygen as the pressure approaches 0, a higher ignition temperature of TKP in vacuum is due to the nascent oxygen rapidly escaping the reaction zone. Figure 3.12 illustrates this behavior where ignition in vacuum appears to have a less restrained behavior compared to ignition in argon, resulting in isotropic dispersion of hot particles. At elevated pressures, the diffusivity of nascent oxygen from the oxidizer decreases, increasing its likelihood of being in close proximity with the titanium fuel. This “caging” effect of external argon pressure concentrates reactant species closer to the wire, increasing the reaction energy release density and lowering the temperature necessary for a runaway exothermic reaction (ignition). The feature of Figure 3.13 that appears most discernible is that the ignition temperature of TKP at elevated oxygen pressure is higher than that of pure titanium by more than 80 K. This suggests a mechanism that is actively retarding the reaction rate of gaseous oxygen with titanium. As shown in Figure 3.13, the superimposed ignition temperature of TKP in argon suggests that though the ignition temperature does depend on whether the system is in a pressurized environment, the ignition behavior does not appear to be affected by the species of the pressurizing gas. This reinforces the hypothesis of a process that effectively insulates the titanium particles from the ambient environment before reacting with oxygen supplied by the oxidizer (~750 K). Although this study concluded that there is not a dominant condensed phase reaction, this does not necessarily mean that a parallel condensed phase interaction path does not occur.^{12,57}

In situ TEM heating at ~100 K/s was carried out to further investigate the mechanism within the TKP system which retards oxygen mobility to the titanium core,

delaying ignition. Images shown in Figure 3.14 were taken of a single aggregate before, during, and after heating.

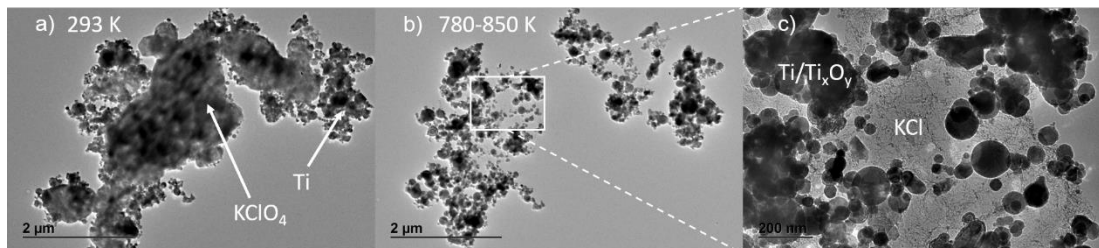


Figure 3.14: In situ heating of a (a) single TKP aggregate at room temperature with micron sized KClO_4 superimposed onto nanosized titanium particles. Subsequent (b) heating of the aggregate up to 850 K (580 °C) results in KClO_4 decomposition (c) leaving the remaining reactant/product particles coated in KCl.

In Figure 3.14a, an aggregate of the TKP mixture is depicted with the larger KClO_4 particles encompassing most of the titanium nanoparticles. Heating of the aggregate resulted in real-time observations of KClO_4 melting, followed by immediate decomposition with the apparent extinction of relatively smaller KClO_4 particles occurring at temperatures as low as 780 K (Figure 3.14b). Closer examination of the aggregate post-heating (Figure 3.14c) reveals what appears to be a thin layer of KCl product residue coating the residual titanium particles, providing evidence for a mechanism that conceals titanium nanoparticles from external oxidation before reacting with oxidizer released oxygen. Further heating to 1073 K, past the melting point of KCl, illustrates a definitive melting event where the expansion of the KCl melt wets and further cloaks the once resolvable titanium/titanium oxide particles. TEM elemental X-ray mapping (EDS) in Figure S3.5 confirms the existence of chlorine, titanium, and oxygen within these coalesced structures.

Additionally, Figure 3.14 and Figure 3.15 depict the agglomerates of titanium nanoparticles whose morphology appears to be minimally affected by the prescribed

rapid heating. Unlike aluminum particles, the nanostructure of titanium particles is preserved under high temperature rapid heating, with the titanium core remaining immobile.^{37,40}

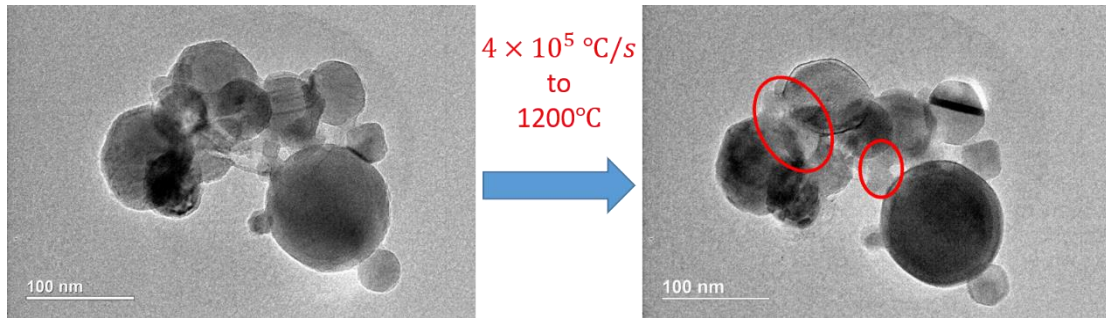


Figure 3.15: Rapid Heating TEM of titanium nanoparticles with minimal sintering

Consequently, titanium nanoparticles maintain their potential for enhanced reactivity, which could potentially lead to reduced ignition temperatures compared to commonly studied aluminum nanoparticles.¹² Gaseous oxygen would thus need to diffuse through the titanium oxide layer to react with the titanium core. The oxidation kinetics study of nano-titanium particles conducted by Muravyev et al. affirms the enhanced reactivity of nano-titanium particles and supports the model of oxygen diffusion through the oxide layer.¹⁶¹ Compared to the findings from Muravyev et al., results from this study for the ignition behavior and TGA characterization of nano-titanium particles in an oxygen environment, shown in Figure 3.13 and Figure 3.10, correspond to particles whose ignition temperature (~ 650 K), oxidation onset, and metal content (70 wt %) are more similar to what the Muravyev et al. study finds for their porous titanium particles.¹⁶¹ As such, the oxidation mechanism and behavior of the titanium particles at relatively high and slow heating rates may align with what their study finds for the oxidation trends of the porous titanium particles.

Diffusion of oxygen to the titanium core may also be further facilitated by the added complexity of a reactive oxide shell for which TiN is oxidized by nascent oxygen.¹⁵³ Evidence for this is drawn from the absence of TiN in the XRD pattern of TKP combustion products (Figure 3.6d). These findings are also corroborated with the conclusions made in a previous study conducted by Zong et al., which investigated the burning time of titanium nanoparticles synthesized via laser ablation as a function of particle size.¹⁴⁷ The burning time was found to be a linearly increasing function of particle diameter, suggesting a ballistic oxygen diffusion within a kinetically limited shrinking core mechanism. The overall proposed mechanism for the TKP reaction is summarized and illustrated more clearly in Figure 3.16.

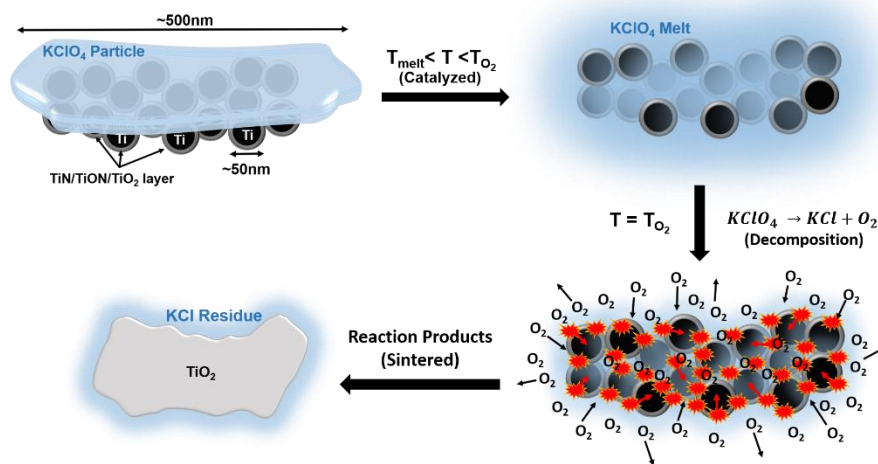


Figure 3.16: TKP primary reaction mechanism summary; the sudden release of oxygen from the enveloping $KClO_4$ melt reacts with the preserved nanostructure of the titanium particles. Oxygen reacts with the oxide layer, enhances oxygen diffusion, and then reacts with the titanium core.

3.4.4 Pre-Ignition: Oxide Layer Interaction with $KClO_4$

Considering the observations thus far, the interaction of the oxide layer with potassium perchlorate was investigated using TiO_2 nanoparticles with TGA–DSC

analysis. To simulate this interaction, various weight percentages of anatase TiO₂ nanoparticles (nTiO₂) (<50 nm) were physically mixed with spray dried KClO₄. The results from this analysis, shown in Figure 3.17, clearly illustrates a catalytic behavior of TiO₂, where the melting and oxygen decomposition temperature of KClO₄ shift to lower temperatures as the weight percentage of TiO₂ increases. This behavior has been investigated previously by repeated studies conducted several years ago, which characterized and modeled the catalytic behavior as one that is electronic in nature and related to the semiconductor properties of TiO₂.^{156,160,162}

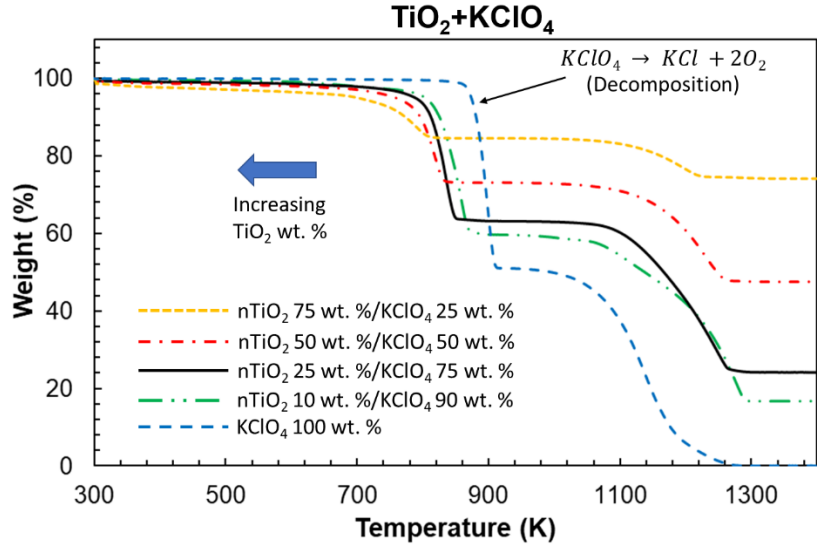


Figure 3.17: Catalytic effect of TiO₂ on KClO₄ decomposition (TGA analysis in argon).

Based on active titanium content and stoichiometry of a typical mixture of TKP, it was estimated that the weight percentage contributed by the oxide layer is roughly 15 wt %. This equates to a TiO₂ content of roughly 20 wt % when mixed only with KClO₄. The TGA analysis of the stoichiometric TKP and the simulant mixture shows oxygen release weight loss occurring at roughly the same time. This

phenomenologically confirms the validity of using this weight percentage of TiO₂ to simulate its interaction with the oxidizer as shown in Figure 3.18.

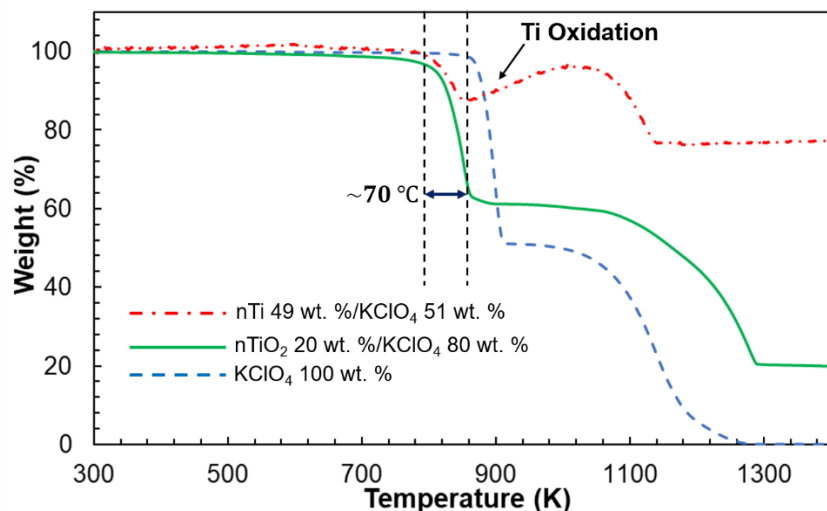


Figure 3.18: TGA analysis in argon between simulant mixture, TKP, and bare oxidizer; oxygen decomposition of TKP and simulant mixture occur at roughly the same temperature.

The T-Jump/TOFMS measurements of the simulant mixture (nTiO₂ (20 wt %)/KClO₄ (80 wt %)) shown in Figure 3.9 once again demonstrate this catalytic behavior, with oxygen release occurring ~40–50 K before oxygen release from the bare oxidizer. The Arrhenius plot of oxygen release for the simulant mixture in Figure 3.9 gives a corresponding activation energy, shown in Table 3.2, which is ~55 kJ/mol smaller than the activation energy for pure KClO₄ oxygen release, and roughly consistent with the ~42 kJ/mol drop in oxygen release activation energy found by Collins et al. under slower heating conditions.¹⁶⁰ Catalysis of oxygen release reconciles the previous findings, which suggested that ignition occurs before the oxygen release from the oxidizer. The ignition temperature displayed in Figure 3.9 closely follows the catalyzed oxidizer oxygen release for each respective heating rate, reinforcing the notion of a gas phase dominant reaction mechanism.

3.5 Conclusions

This article reports on the efforts to probe the mechanism by which passivated titanium nanoparticles reacts with micron-sized potassium perchlorate particles. The roughly 6 nm particle shell composed of TiO_2 , TiON , and crystalline TiN plays a role in the gas phase dominant reaction mechanism of TKP. As in situ heating TEM observations and TGA measurements demonstrate, the oxide surface acts as a point of catalysis for which KClO_4 melts, encapsulates the titanium nanoparticles, subsequently decomposes to release oxygen, and reacts with both the oxide layer and titanium core. Along with oxide layer catalyzed oxygen release and facilitated oxygen diffusion, lack of pre-ignition sintering could be a factor for lower ignition temperature of TKP compared to mixtures incorporating widely utilized aluminum fuels. From an application standpoint, titanium nanoparticles could thus be a second-best option in place of, or complimentary to, aluminum nanoparticles in terms of characteristic specific combustion enthalpy and its intrinsic ability to avoid pre-ignition sintering. To obtain concrete conclusions on this manner, a more rigorous comparative study with aluminum with respect to niche applications would need to be undertaken.

Chapter 4: Ignition and combustion analysis of direct write fabricated aluminum/metal oxide/PVDF films †

Summary:

Metallized energetic composite films incorporating high mass loadings of aluminum nanoparticle fuels and metal oxide oxidizers (thermite) within a polyvinylidene fluoride (PVDF) polymer matrix were constructed via repeatable direct write additive manufacturing (3-D Printing). High speed videography, Temperature-Jump/Time of Flight Mass Spectrometry (T-Jump/TOFMS), and 2D spatiotemporal temperature mapping were used to analyze the role of composition and particle loading with respect to ignition behavior and combustion performance. This study reveals that, while the ignition temperatures of films are relatively unvaried in pressurized environments, ignition temperatures in vacuum are strongly dependent on the inclusion of thermite material and the specific type of thermite utilized. Increasing thermite mass loading results in a reduction in film flame speed and mechanical integrity but increases flame temperature. Coupled time of flight mass spectrometry reinforces and elaborates on previous findings regarding the Al/PVDF reaction mechanism as it pertains to the coupled behavior of incorporating increasing amounts of metal oxides. TOFMS highlights carbon dioxide generation from the metal oxide interaction with PVDF, leading to unintended stoichiometric considerations and distinct changes in steady burn behavior which contribute adverse factors towards flame propagation.

†The results presented in this chapter have been previously published and are reprinted with permission from: Miles C. Rehwoldt, Haiyang Wang, Dylan J. Kline, Tao Wu, Noah Eckman, Peng Wang, Niti R. Agrawal, Michael R. Zachariah, *Ignition and combustion analysis of direct write fabricated aluminum/metal oxide/PVDF films*, Combustion and Flame, 2020, 211, 260-269. Copyright 2020 Elsevier.

4.1 Introduction

The fabrication of solid propellants employing metallic nanoparticles as an energy dense fuel has become a promising frontier in the search for novel materials with the potential for enhanced energy release rates. In recent years, the draw to research metal nanoscale energetics stems from their theoretically greater chemical energy density compared to traditional CHNO chemistry.¹³⁰ Despite reaction enthalpy considerations, reaction kinetics of traditional micron scale solid energetics are relatively slow, limited by the diffusion length scales between fuel and oxidizer. Contemporary formulations utilizing nanoscale fuels and oxidizers seek to increase specific surface area and reduce characteristic diffusion length scales for enhanced reactivity to approach that of molecular monopropellants such as 2,4,6-trinitrotoluene (TNT). Studies utilizing metal particles for energetic purposes commonly use aluminum nanoparticles as the fuel for metallized energetic composites due to its light weight, superior combustion enthalpy, and cost effectiveness compared to alternative nanoscale metal fuels such as titanium and tantalum. Formulations for solid propellants typically involve high mass loadings of reactive material incorporated into a polymer binder such as polyvinylidene fluoride (PVDF), nitrocellulose (NC), and hydroxyl-terminated polybutadiene (HTPB).^{37,63,163,164} Recently, fluorine containing polymer binders, such as PVDF and THV (copolymer of tetrafluoroethylene, hexafluoropropylene and vinylidene fluoride), have come to the forefront of experimentation and application due to their ability to act as a reactive binder in the formation of Al-F bonds.^{67,165,166} The fluoropolymer PVDF is primarily utilized for its mechanical strength, thermal stability, and solubility in a suitable solvent for expanded

materials processing.⁶⁷ From previous studies, it was shown that early onset fluoropolymer decomposition occurs through a gas phase exothermic pre-ignition reaction with the aluminum oxide shell, exposing the aluminum core to further fluorination.^{33,67,167}

Thermite systems (metal/metal oxide) have also been the focus of several studies as a means for high energy release for a variety of applications for which reactivity and flame speeds are enhanced when utilizing nanomaterials.^{37,95,165,168} The metal oxides (MO) considered in this study are copper(II) oxide, bismuth(III) oxide, and iron(III) oxide. While Fe_2O_3 is the most common oxidizer for traditional thermite systems, CuO is a well-studied gas phase oxidizer with favorable heat of formation, and Bi_2O_3 is a known condensed phase oxidizer with high oxygen ion mobility.^{13,34,53} This study assesses the ability to tune the energy release of stoichiometric aluminum-fluoropolymer propellant systems by incorporating nano-scale thermites at various mass loadings. Analysis of both intended and unintended consequences with respect to the fabrication process, chemistry, composite morphology, and apparent mechanical properties were documented.

In the past decade, additive manufacturing (AM) has been an increasingly active field of research in several disciplines with applications and research within the energetics community becoming more viable and sought out.¹⁰¹ The draw to additive manufacturing manifests from the desire for flexibility, potential scale up, and the ability to reproduce unique and highly customizable architectures down to the nanoscale⁹⁷ in the most cost effective and efficient manner.¹⁰¹ Although additive manufacturing of aluminum containing polymers has been recently explored by other

studies,^{103,108,163,164,169,170} a solvent-based layer-by-layer additive manufacturing technique was employed to fabricate thermite integrated energetic materials from a precursor solution. This method utilizes a suitable solvent to dissolve the polymer binder and allow for thorough mixing with suspended particles. This additive manufacturing technique was applied for polymer printing, explicitly described in the study conducted by Manjot et al., to allow for wide precursor variations with respect to viscosity, employed solvent, and solid loading.¹⁰⁵ The controlled translation and extrusion dynamics inherent to 3D printing allows for increased degrees of freedom for energetic materials to be printed quickly and precisely into a variety of patterns, shapes, and (micro)structures which may be characterized by Scanning Electron Microscopy (SEM).

The combination of high-speed videography, thermometry, and time of flight mass spectrometry diagnostics were utilized to probe and analyze important ignition characteristics and potential throttling behavior of energetic propellants integrated with readily available and well-studied nanoscale metal oxides. The results of this study may be used for future studies which focus on tunable architectures provided by this method of AM to probe the structure-function relation of film combustion performance complimentary to the behavior of reactive film constituents.

4.2 Methods/Experimental

4.2.1 Materials

Aluminum nanoparticles (nAl) (~80 nm) used in this study were purchased from Novacentrix. It was determined from thermogravimetric analysis (TGA) that the

passivated aluminum nanoparticles are 81% active by mass. Nanoparticle metal oxide oxidizers in the form of CuO (<50 nm), Fe₂O₃ (<50 nm), and Bi₂O₃ (90–210 nm) were purchased from Sigma Aldrich (Millipore Sigma). Poly(vinylidene fluoride) powder (PVDF) (MW = 534,000) was also purchased from Sigma Aldrich (Millipore Sigma) and N, N-dimethylformamide (DMF 99.8%) solvent was purchased from BDH chemicals. All chemicals were used as received. TEM images of all utilized nanoparticles are shown in Figure 4.1.

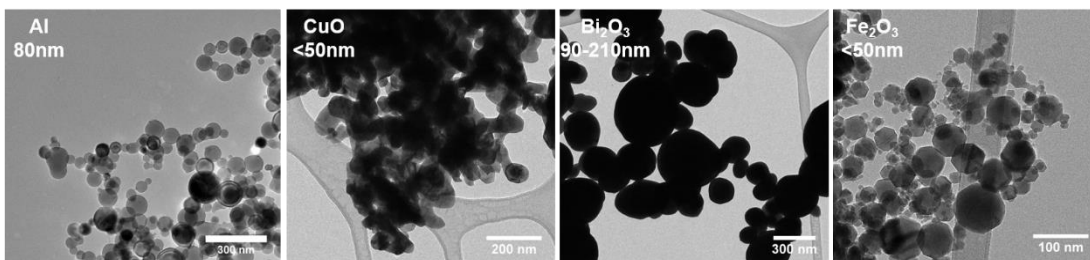
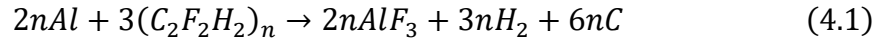
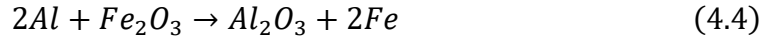
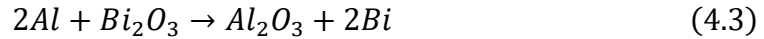


Figure 4.1: TEM of as received aluminum and metal oxide nanoparticles

4.2.2 Film fabrication

Energetic composites were fabricated using a System 30M pressure driven 3D printer purchased from Hyrel 3D (Additional Details in Appendix B). The low viscosity (~ 0.1 Pa·s) energetic precursor was utilized as a 3D printable ink in a direct write approach. Each precursor ink considered was formulated by dissolving a constant 100 mg/ml PVDF in DMF and adding the appropriate stoichiometric mass content of metal fuel and oxidizer Eqs. (4.1–4.4). The concentration of PVDF in DMF and level of particles suspended was chosen based off previous studies in the Zachariah group using electrospray for fabrication of similar films.^{63,166}

Binder (*n chain lengths*) Fluorination of Aluminum:**Oxidation of Aluminum:**

Stoichiometric mixtures of aluminum oxidized by metal oxide components incorporated within the films were considered by treating the parallel Al/PVDF reaction and thermite reaction as being mutually exclusive Eqs. (4.1–4.4). The individual mixtures and particle loadings are listed in Table 4.1 where the specific loadings correlate to 1/4 wt. content (no added thermite), 1/2 wt. content (low thermite loading), and 2/3 wt. content (high thermite loading) of total nanoparticle material in the films. These weight percentages were chosen to better observe the effects that the metal oxides may introduce as well as to test the previously documented mass loading limits of PVDF bound nanopowders.⁶³

Table 4.1: Energetic precursor formulations

Al Fuel (wt. %)	PVDF (wt. %)	Oxidizer: (wt. %)	Total Particle Loading (wt. %)
25	75	----	25
20.8	50	Bi ₂ O ₃ : 29.2	50
23.9	50	CuO: 26.1	50
26.5	50	Fe ₂ O ₃ : 23.5	50
18.1	33.3	Bi ₂ O ₃ : 48.6	66.7
23.2	33.3	CuO: 43.5	66.7
27.5	33.3	Fe ₂ O ₃ : 39.2	66.7

Precursor suspensions are sonicated up to 2 h for each component added, depending on particle loading, then left to stir for 24 h using a magnetic stir plate/bar.

Before printing, precursor inks are sonicated for 1 h then loaded into a 30cc disposable syringe equipped with a 21-gauge blunt Luer Lock needle and mounted to the extrusion pump of the 3D printer. Before printing, the ink is primed, and the glass printing bed heated to as high as 85 °C. Since the ink is in liquid form, the programmed printing routine is optimized for solvent evaporation before subsequent layer deposition. The drying process can be controlled by the temperature of the printing bed, the speed and extrusion rate of the print, and/or the volatility of the chosen solvent. Dry times for these prints were on the order of 10–15 s per pass. In order to study the 1D combustion performance of materials, single line strands were printed with a width roughly equivalent to the outer diameter of the extrusion needle (0.8 mm). Individual layer thickness may range between 5–20 μm /layer and depends strongly on the ink viscosity, print speed, and specific flow parameters (0.5–5 ml/hr). Multiple 3 cm long strands, like those in Figure 4.2c, were harvested from a larger 25 cm perimeter rectangular structure printed and carefully peeled from the glass printing bed.

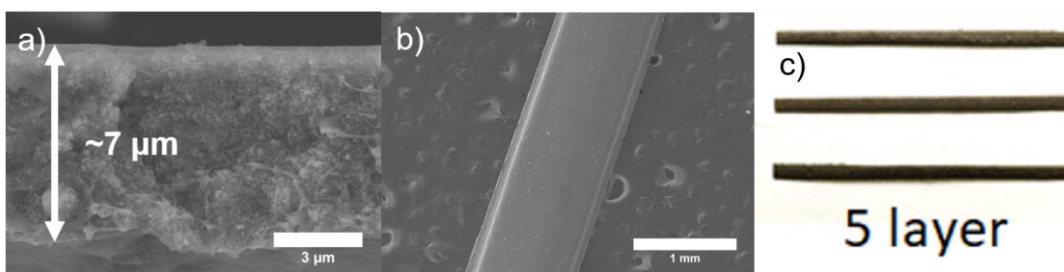


Figure 4.2: SEM images of a) Al/PVDF single layer film cross-section, and b)-c) 5-layer film morphology and combustion sample prep

Film porosity estimations were made using Eqs. (4.5) and (4.6) given their composition mass fractions (χ_i) as well as their theoretical and measured densities (ρ_{th} & ρ_m) for which these estimates are displayed in Table 4.2.⁶³

$$P = 1 - \frac{\rho_m}{\rho_{th}} \quad (4.5)$$

$$\rho_{th} = \sum_i \chi_i \rho_i \quad (4.6)$$

Table 4.2: Film mechanical and morphological properties.

Film Type (wt. %)	Porosity (%)	Density (g/cm ³)	Tensile Strength (MPa)	Young's Modulus (GPa)
Al (25%)-PVDF (75%)	11±5	1.8±0.2	44±2	1.18±0.10
Al (20.8%)-Bi ₂ O ₃ (29.2%)-PVDF (50%)	18±6	3.3±0.2	29±2	0.66±0.12
Al (23.9%)-CuO (26.1%)-PVDF (50%)	17±6	2.6±0.2	24±2	0.83±0.15
Al (26.5%)-Fe ₂ O ₃ (23.5%)-PVDF (50%)	20±6	2.3±0.2	18±6	0.47±0.07
Al (18.1%)-Bi ₂ O ₃ (48.6%)-PVDF (33.3%)	28±5	3.9±0.2	22±4	0.64±0.05
Al (23.2%)-CuO (43.5%)-PVDF (33.3%)	33±5	2.7±0.2	13±2	0.68±0.09
Al (27.5%)-Fe ₂ O ₃ (39.2%)-PVDF (33.3%)	-----	-----	4.4±1.6	0.14±0.02

4.2.3 Characterization

Films in this study were characterized based on their physical properties and reaction properties. Physical properties considered included thickness, reproducibility, morphology, mechanical integrity, and composition. Reaction properties considered included self-propagating combustion performance in an anaerobic environment, ignition in pressured and vacuum conditions, and the content of their condensed phase combustion products.

Cross-sections and top surfaces of each film are analyzed using Scanning Electronic Microscopy (SEM, Hitachi, SU-70 FEG-SEM) and compared to one another. Properties of precursor inks were characterized using an AR2000 rheometer mounted with a 40 mm 2" steel cone and the tensile strength of single layer films measured using a Shimazu Autograph AGS-X tensile tester.

For each film formulation, combustion was conducted in argon (~1 atm) and repeated in triplicate. A small cylindrical chamber with a gas valve inlet and outlet was

purged with argon for 5– 10 min and a mounting rod used to hold the films in place (Figure S4.1).

Film geometry was strictly maintained with approximately the same thickness, $(70 \pm 3) \mu\text{m}$, width, 0.8–1 mm, and length, 3 cm. Each film strand is sandwiched between two braided nichrome wires and anchored at the opposite end with double-sided tape. Films are ignited within the argon chamber using the nichrome wire and the combustion performance assessed using a Phantom v12.0 high-speed digital camera operating at 3000 (zoomed out view) and 10,000 (zoomed in view) frames per second (FPS) with an exposure of 200 and 20 μs , respectively. Self-propagating characteristic flame speeds are measured using videos processed in ImageJ manual tracking to obtain time resolved positions using data points with a known pixel to distance ratio at every 25–50 frames (Figure S4.2c). Two out of place gaps in the example data in Figure S4.2c represent the precisely spaced metal gratings in the foreground which block light from the flame at certain positions.

Temperature dependent reaction chemistry and possible mechanisms were diagnosed by conducting T-Jump/Time of Flight Mass Spectrometry (T-Jump/TOFMS) and implementing the diagnostic technique of Color Camera Pyrometry (CCP) described in the Zachariah group's previous work.¹¹⁶ This method of thermometry was developed by members of the Zachariah Research Group, Rohit J. Jacob and Dylan J. Kline. The method uses the black body radiation of hot particles as a metric for characterizing temperatures during combustion. The use of the spectral response of the RGB pixels of a high-speed color camera in tandem with the black body spectral distribution allows for the use of a temperature matching algorithm. The

algorithm calculates the intensity of the “red”, “blue”, and “green” light, as seen by the color camera Bayer filter, and produces three ratios based on these intensities. These three ratios are matched to empirical reference data for which the combination of the three ratios, within the smallest error range, corresponds to a specific temperature value. As a result, one may obtain thermometry of a selected area with a high time resolution. More on this method of pyrometry is described in their paper.¹¹⁶ CCP offers a post-processing method by which the grey body emissions of the film flame-front, as captured by the Bayer filter of the color camera, are processed to return 2-D temperature maps of the flame front as a function of time.¹¹⁶ T-Jump/TOFMS offers a method by which transient gas phase species can be detected prior to and after the potential ignition event on the timescale of a combustion event. The technique of T-Jump/TOFMS is outlined explicitly in Chapter 2 of this dissertation and within previously published papers from the Zachariah group. In short, a sufficiently thin layer of material ($<3 \mu\text{m}$) is printed directly onto a thin platinum wire ($76 \mu\text{m}$), illustrated in Figure 4.3, and rapidly heated ($\sim 3 \times 10^5 \text{ K/s}$) in a vacuum chamber (10^{-6} Torr) to temperatures as high as 1400 K .^{67,120}

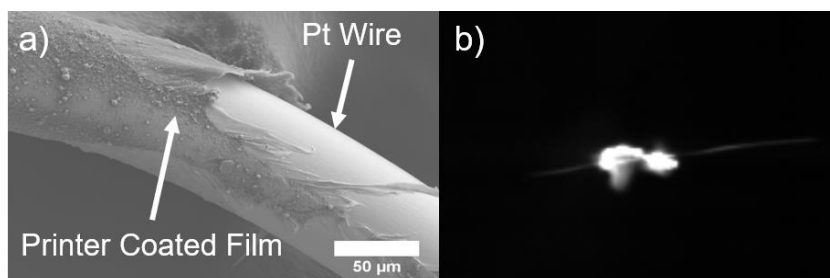


Figure 4.3: a) Al/MO/PVDF T-jump wire coating b) ignited via rapid joule heating (T-Jump)

Rapid heating is temporally coupled to species detecting mass spectrometry ($100 \mu\text{s/spectrum}$) and ignition visualizing high speed videography ($10^5 \text{ FPS}-10 \mu\text{s}$)

exposure).¹³⁷ Solid phase species of combustion products are collected for X-ray diffraction (XRD, Bruker C2 Discover, CuK α sealed X-ray tube) and SEM/EDS analysis to confirm possible reaction mechanisms for self-propagation.

4.3 Results and Discussion

4.3.1 Fabrication of Al/MO/PVDF films

Al/PVDF films are highly reproducible in both thickness and uniformity with respect to morphology through the direct write approach. SEM/EDS images in Figure 4.4a show that film cross-sections have a high degree of homogeneity between aluminum and PVDF. SEM cross-section analysis of 5-layer films containing thermite materials incorporating 50 wt.% particle loading are shown in Figure 4.4b– d. Despite the difference of metal oxide type and relative particle size range, each formulation printed with 5 layers resulted in films with predictable XRD patterns, nearly identical thickness, roughly 70 μm ($\sim 14 \mu\text{m}/\text{layer}$), and consistent uniformity. The same cannot be said, however, for 67 wt.% particle loading films for which their morphology will be discussed in a later section of this paper.

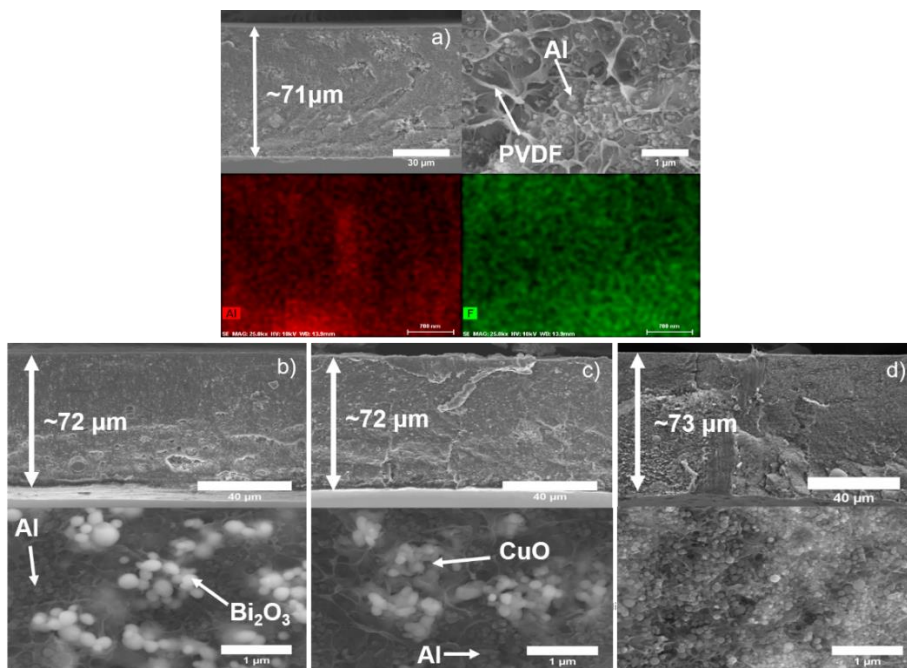


Figure 4.4: SEM cross-section of 5-layer ($\approx 14 \mu\text{m}/\text{layer}$) 3D printed a) Al/PVDF, b) Al/Bi₂O₃/PVDF, c) Al/CuO/PVDF, and d) Al/Fe₂O₃/PVDF Films

The second row of each column of Figure 4.4b–d reveals the contrast between the aluminum and metal oxide nanoparticles from SEM electron backscattering of heavier elements. Comparisons of the Bi₂O₃ and CuO particle sizes in relation to aluminum particles in Figure 4.4 show that although CuO nanoparticles are quoted to be smaller than 50 nm by Sigma Aldrich, they appear to have roughly the same distinct aggregate size as Bi₂O₃ particles (90–210 nm). Transmission Electron Microscopy (TEM) images of as received metal oxide particles in Figure 4.1 shows that CuO nanoparticles have smaller primary structures than Bi₂O₃, but are irregularly shaped with a higher degree of aggregation behavior compared to Fe₂O₃ nanoparticles. This leads to the conclusion that CuO particles lack of particle dispersion, either physically or chemically, leads to hindered dispersion of CuO particles in Al/PVDF films. Fe₂O₃ nanoparticles shown in Figure 4.4, unlike CuO and Bi₂O₃ particles, appear to be

indistinguishable from aluminum in both color contrast and particle size. From Figure 4.1 and Figure S4.3, Fe₂O₃ particles at 50 wt.% particle loading appear to have superior dispersion behavior of much smaller particles with no obvious regions of severe agglomeration.

Higher mass loadings of thermite material (67 wt.%) were added to the stoichiometric Al/PVDF mixture to study whether film performance can be enhanced with an increase in thermite density. Generally, adding more nano-scale particles has adverse effects during the printing process.¹⁷¹ The effects that each particle type has on printability and resulting film morphology becomes more apparent at higher mass loading.¹⁶⁴

The effects of printing film precursors with increasing amounts of nanomaterials include the following:

- Increased ink viscosity leading to increased likelihood that the printer nozzle will be clogged if the nozzle is too thin and/or the flowrate is below a certain threshold.¹⁶⁴
- Shear rate-controlled viscosity measurements of select precursor inks extruded at pipe flow shear rates on the order of 10^{-1} – 10^2 s⁻¹ show viscosities between 0.1–10 Pa·s while printing (Figure 4.5).
- Ink with the highest nanoparticle loading and smallest primary particle size displays viscosity values four orders of magnitude higher than the viscosity of the low particle loading ink, but with clear shear thinning behavior (Figure 4.5).

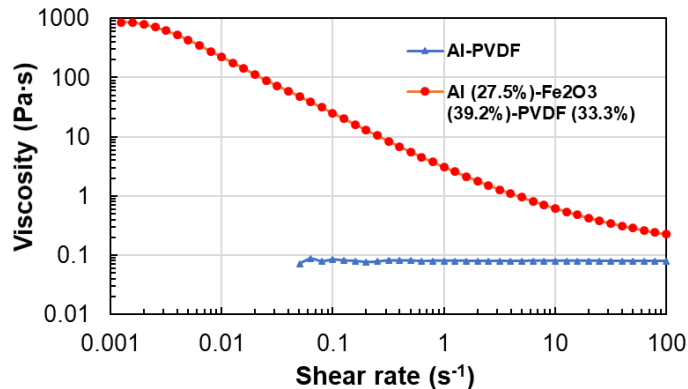


Figure 4.5: Shear rate-controlled viscosity measurements as a function of shear rate for the most viscous (red) and least viscous (blue) DMF based precursor inks

Adding nano-materials to precursor formulations results in the following observations to the characteristics of the product films:

- Other than the increased film density of the metal oxide species, composites with higher mass loading convey no significant difference in constituent homogeneity compared to the lower mass loading (Figure S4.3).
- Reduction in mechanical integrity and increase in film porosity formed due to rapid solvent evaporation, leading to extremely brittle films with irregular thickness profiles (Figure 4.6 and Figure 4.7) (Table 4.2).
- Small particle size, number of particles, and particle dispersiveness allows for enhanced intimacy with the polymer binder, causing a degradation in polymer elasticity and its ability to relax after vaporized solvent has displaced material (Figure 4.6 and Figure 4.7).
- Considering the density of the metal oxide type ($\text{Bi}_2\text{O}_3 > \text{CuO} > \text{Fe}_2\text{O}_3$) and nominal particle size ($\text{Bi}_2\text{O}_3 > \text{CuO} \geq \text{Fe}_2\text{O}_3$) (Figure 4.1), this order also reflects the gradual reduction in mechanical integrity ($\text{Bi}_2\text{O}_3 > \text{CuO} > \text{Fe}_2\text{O}_3$) (Figure 4.6 and Figure 4.7).

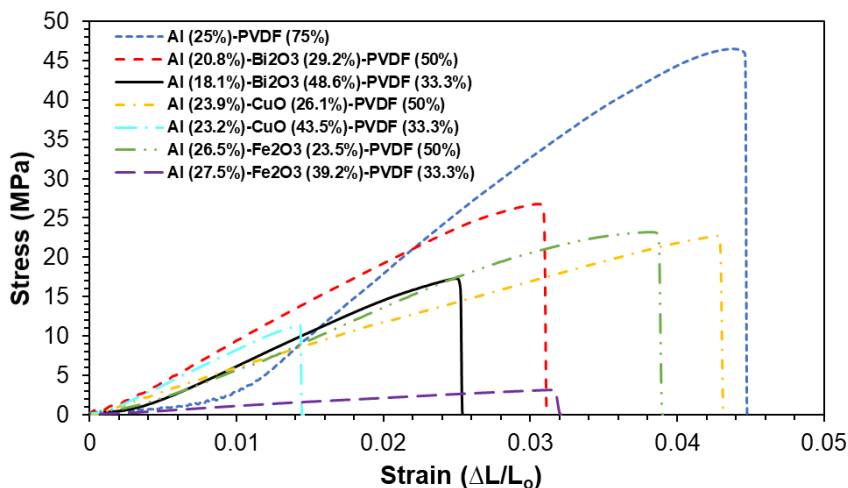


Figure 4.6: Stress-Strain curves of a single layer of the various film composites

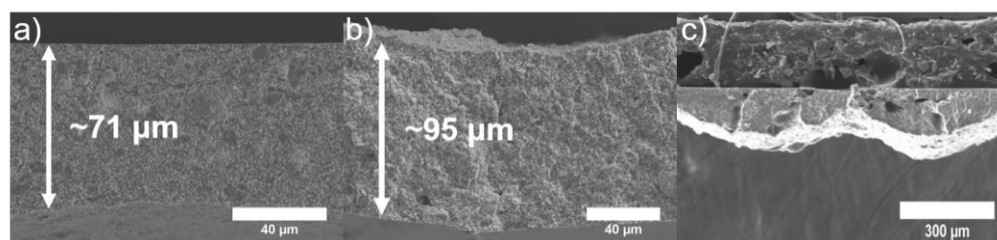


Figure 4.7: SEM images of the cross-section of a) Al/Bi₂O₃/PVDF, b) Al/CuO/PVDF, and c) Al/Fe₂O₃/PVDF at 67 wt. % particle loading

4.3.2 Film combustion

3D printed films often have similar physical appearances, but their combustion performance and behavior are quite different. A zoom in of propagation snapshots captured at 10,000 FPS are displayed in Figure 4.8a and the flame speed results of all compositions studied shown in Figure 4.8b-c. Due to its severe morphological inconsistencies shown in Figure 4.7 and Figure S4.4, the highest film loading of Fe₂O₃ was not considered for these measurements.

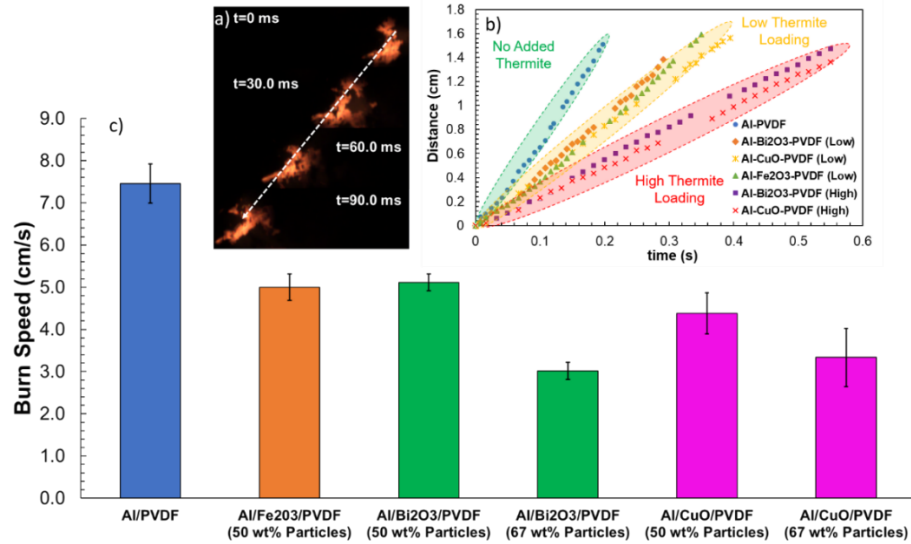


Figure 4.8: a) Snap shots of steady flame propagation of Al/CuO/PVDF with 50 wt. % particle loading accompanied by b) representative linear distance over time plots of each composition. Averaged flame speed results are consolidated in a c) comparative bar graph.

All combustion events are steady burning with a curved flame front. As Figure 4.9 illustrates, the characteristic combustion behavior of each composition can vary in terms of how product material is shed as thermite mass loading changes.

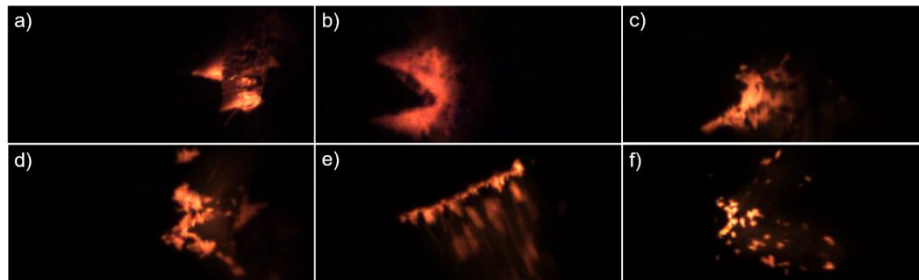


Figure 4.9: Characteristic film combustion (right to left) behavior of a) Al/PVDF, b) Al/Bi₂O₃/PVDF 50 wt. % particle loading, c) Al/CuO/PVDF 50 wt. % particle loading, d) Al/Fe₂O₃/PVDF 50 wt. % particle loading, e) Al/Bi₂O₃/PVDF 67 wt. % particle loading, and f) Al/CuO/PVDF 67 wt. % particle loading

The Al/PVDF composite appears to retain its burned material for a much longer time, curling on top of itself at times shown in Figure 4.9a. As thermite content

increases, material just behind the flame front is torn away and ejected at greater speeds (1–10 m/s), outlining a much clearer and thinner flame front (Figure 4.9e-f). Another interesting feature at the high loading of thermite content was the repeated observance of the flame to burn in a manner which favored one side of the film with a slanted flame front shown in Figure 4.9e. Although this behavior persisted for reasons unknown to us, flame fronts were still steady burning with flame morphology maintained and simply translating in time linearly. Further analysis of this behavior by Time of Flight Mass Spectrometry and Colored Camera Pyrometry will show that these observations are likely due to the sudden generation of nascent gaseous species originating in some capacity from the added metal oxides,¹¹⁵ carrying away still burning material which would otherwise contribute to the forward propagation of energy. This behavior would thus be intensified as more thermite content is incorporated and films become increasingly porous.

Figure 4.8c illustrates the hierarchy of combustion performance which is independent of the metal oxide species utilized. Homogenously incorporating thermite material within Al/PVDF films does not lead to enhanced burn speeds. As Figure 4.10 shows, XRD and EDS characterization of films burned in argon finds no evidence for any remaining reactant species with respect to aluminum and the corresponding metal oxide. These finds were the same for both thermite loadings.

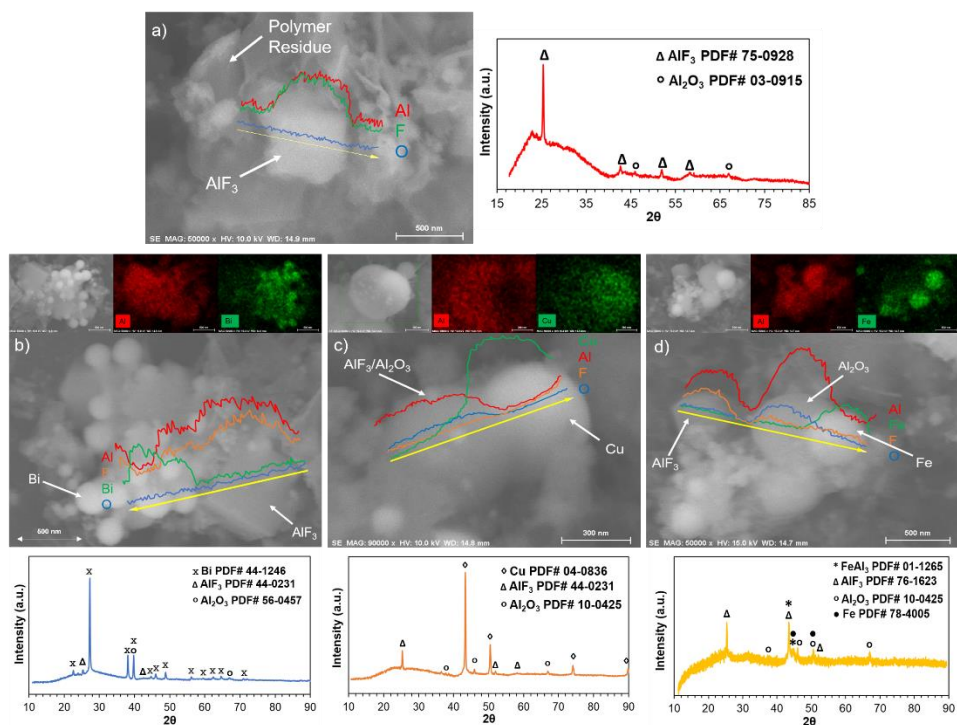


Figure 4.10: Combustion products analysis (SEM, EDS, XRD) of a) Al/PVDF, b) Al/Bi₂O₃/PVDF, c) Al/CuO/PVDF, and d) Al/Fe₂O₃/PVDF films ignited in an argon atmosphere

Evidence from EDS line scan characterization in Figure 4.10 shows that aluminum interacts with both the metal oxide and PVDF. The cubic AlF₃ and coalesced Al₂O₃-reduced metal product structures exist within the immediate vicinity of one another.^{63,169} Along with potential changes to composite dependent thermal diffusivity, it is likely that the kinetics of the Al/PVDF reaction are faster than the Al/MO reaction due to PVDF proximity and the relatively low temperature of the Al-PVDF pre-ignition reaction.⁶⁷ As a result, aluminum directly adjacent to PVDF would be consumed readily, increasing the characteristic length scale for which oxygen from the metal oxide would need to traverse to react with the remaining aluminum. The Al/PVDF reaction would thus be the main reaction driving flame propagation with the Al/MO reaction occurring just behind the flame front. The proposed burning mechanism based

on observations already conveyed in this paper, and those discussed later, is illustrated in Figure 4.11.

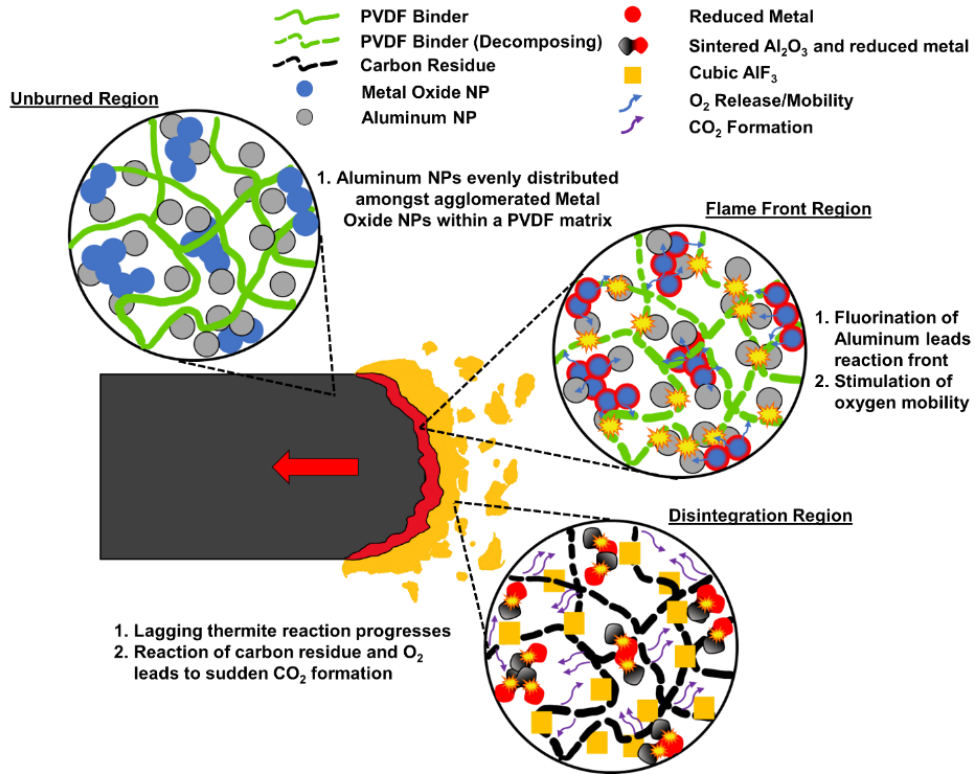


Figure 4.11: Illustration of the proposed mechanism for the observed burning behavior of Al/MO/PVDF films

Color Camera Pyrometry (CCP) post-processing of the highspeed videos was applied to gain more insight into the flame temperature and energy release of each corresponding film composition. Through CCP one can obtain the spatiotemporal temperature maps as well as the mean and median temperatures of the combustion event from each different film type. This data is displayed in Figure 4.12.

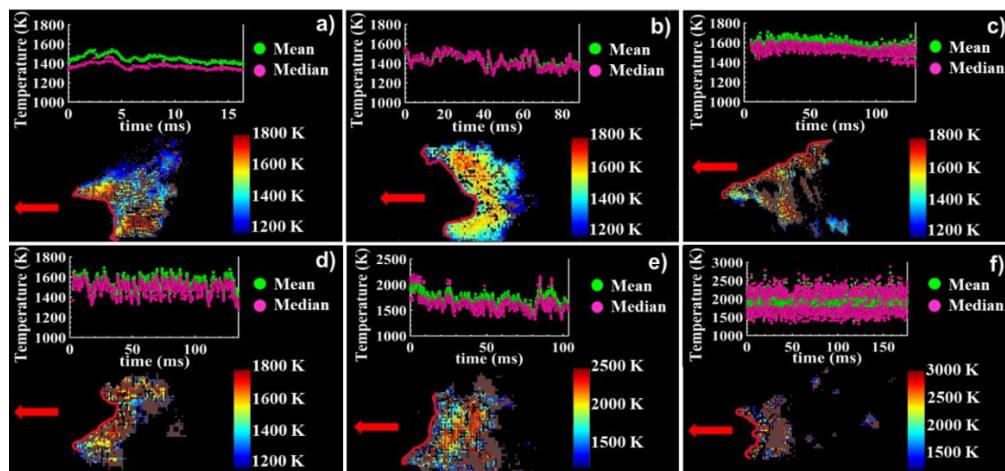


Figure 4.12: Snap shots of spatiotemporal temperature measurements made by color camera pyrometry on a) Al/PVDF, b) Al/Bi₂O₃/PVDF (50 wt.% particles), c) Al/Bi₂O₃/PVDF (67 wt.% particles), d) Al/Fe₂O₃/PVDF (50 wt.% particles), e) Al/CuO/PVDF (50 wt.% particles), and f) Al/CuO/PVDF (67 wt.% particles) films burning from right to left.

Temperature mapping and plots over time show that incorporating thermite material reduces flame speed, but it also increases the temperature of the flame front and the overall combustion event. While Al/PVDF films and those incorporating low particle loadings of Bi₂O₃ and Fe₂O₃ burn at temperatures between 1400 and 1600 K, those containing CuO burn hottest with temperatures reaching near 2500 K at the higher mass loading.¹⁶⁸ This diagnostic technique for simultaneous acquisition of flame speed and flame temperatures allows one to get a rough idea of the relative energy release rates of each energetic composite. The ratios of the energy release rate, Q , can be calculated using the measured mass density, ρ , of each film, their respective flame speeds, v_f , and their mean flame temperatures, T_f . Assuming there is a negligible difference between the cross-sectional area of each film type, the resulting ratio is defined by Eq. (4.7). The specific heat of each system, c_p , is calculated by considering respective mass fractions and the temperature averaged thermochemical values of each

component found in literature and the NIST Webbook.^{172,173} The specific heat of PVDF has been listed by vendors, such as Holscot and Solvay Specialty Polymers, to be roughly 1.4 (J/(g•K)). The calculated heat release ratio of metal oxide integrated films compared to stoichiometric Al/PVDF are displayed in Table 4.3.

$$\frac{Q_1}{Q_2} = \frac{\rho_1 v_{f_1} \overline{c_{p_1}} (T_{f_1} - T_o)}{\rho_2 v_{f_2} \overline{c_{p_2}} (T_{f_2} - T_o)} \quad (4.7)$$

Table 4.3: Film energy release comparison when compared to Al/PVDF.

Sample (wt. %)	T _F (K)	$\overline{c_p}$ (J/(g•K))	Energy Release Ratio
Al(25)/PVDF(75)	1370±30	1.33	1.00
Al(26.5)/Fe ₂ O ₃ (23.5)/PVDF(50)	1500±100	1.21	0.87±0.16
Al(23.9)/CuO(26.1)/PVDF(50)	1750±150	1.15	0.99±0.21
Al(23.2)/CuO(43.5)/PVDF(33.3)	2200±200	1.03	0.91±0.26
Al(20.8)/Bi ₂ O ₃ (29.2)/PVDF(50)	1470±50	1.01	1.04±0.16
Al(18.1)/Bi ₂ O ₃ (48.6)/PVDF(33.3)	1550±75	0.80	0.61±0.10

These results show that there is an overall trend of a reduction to the energy release rates with the inclusion of metal oxides. The largest ratio of energy release rate occurs for the low loading of the Al/Bi₂O₃/PVDF at a 4% increase. However, it is difficult to solidify this as such given the degree of propagated error stemming from temperature, density, and flame speed measurements. For Al/MO/PVDF films to consistently achieve higher energy release ratios, simply adding more thermite is not enough. One must be able to control the level of film porosity in order to predictively increase film density while achieving a similar flame speed and temperature. Thus, adding stoichiometric amounts of Al/MO to Al/PVDF for mass loadings up to 67 wt.% in this manner does not change the energy release rates of the energetic composite in any significant capacity.

It should also be noted that one may also discern the degree of gas generation which manifests itself in Figure 4.12 as the inability of the CCP to precisely assign a temperature value to the brown pixels. CCP is meant for temperature measurements of hot solid grey bodies, with brown pixels representing locations where large amounts of hot gas result in high temperature uncertainties, excluding them from the average temperature calculations.¹¹⁶ The degree of gas generation qualitatively increases with increasing metal oxide content as well as the ability of the metal oxide to release oxygen and/or produce transient gas product species. This behavior is highlighted primarily in Figure 4.12f where the film with the highest content of CuO displays a unique burning behavior resulting in a 1000 K wide mean temperature distribution as well as two distinct modes of median temperature values. The two median temperature modes are a quantitative manifestation of the previously described behavior illustrated in Figure 4.11. Vigorous gas generation results in material from the flame front being shed so quickly that it continues to burn independently of the main, hotter burning reaction front. As such, calculation results in Table 4.3 for the high loading of Al/CuO/PVDF only consider the upper band of median temperature values since they correlate to the temperature of the main flame front.

4.3.3 T-Jump/TOFMS analysis of Al/MO/PVDF films

Ignition properties and transient gas phase speciation of Al/MO/PVDF films were characterized using T-Jump/TOFMS at rapid heating rates in 1 atm argon and vacuum ($\sim 10^{-6}$ Torr). It must be noted that while T-Jump ignition analysis maybe performed in various gas environments, TOFMS may only be performed in vacuum (Chapter 2). The ignition temperature of both the thermite powder and the thermite

within the polymer were measured in each atmosphere and plotted against one another to probe the role of the thermite within the composites with respect to film ignition. Film and thermite powder ignition behavior in argon and vacuum are depicted in Figure 4.13 and Figure S4.5. Quantitative results are shown in Figure 4.14.

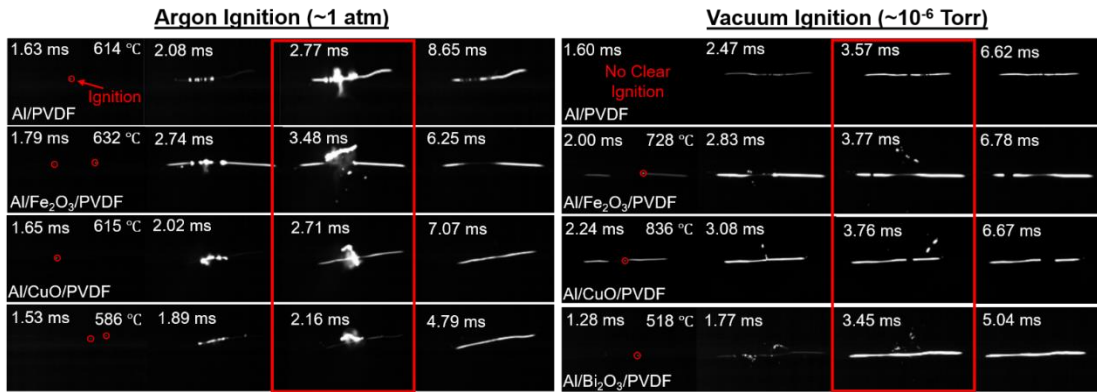


Figure 4.13: Ignition of the various Al/MO/PVDF composites in argon and vacuum environments

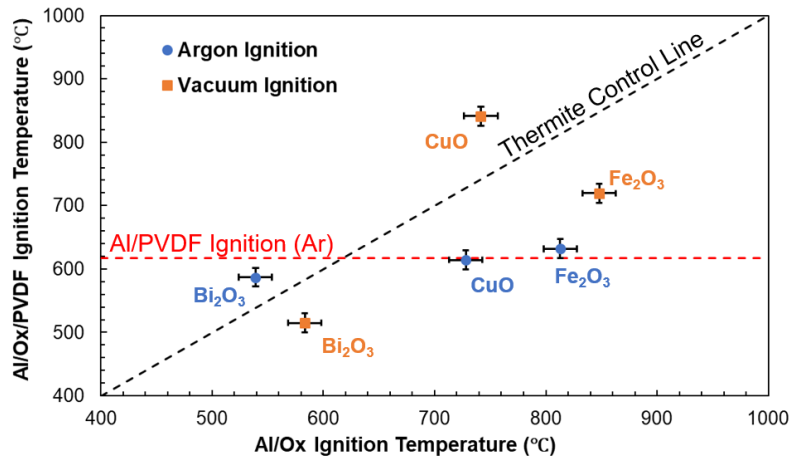


Figure 4.14: Ignition temperature of metal oxide specified powdered thermite relative to the ignition temperature of thermite integrated into Al/PVDF composites in argon and vacuum.

The ignition results in argon show that the inclusion of the metal oxide in Al/PVDF has a negligible effect on the ignition temperature when compared to Al/PVDF ignition which occurs at ~620 °C. However, in vacuum, the inclusion of

metal oxide particles has a clear impact on film ignition behavior where the ignition temperature is generally higher and closely correlated to the ignition of the powder thermite (Figure 4.14). Additionally, it does not appear that Al/PVDF ignites at all in vacuum (Figure 4.13).

As previously mentioned, the interaction of HF gas with the oxide layer of aluminum nanoparticles has shown to be a key facilitator in the fluorination of aluminum.⁶⁷ In a vacuum environment, the diffusivity of nascent gas species is at least 8 orders of magnitude greater than at atmospheric conditions. Nascent gas is effectively in the ballistic regime, making a swift exit away from the reaction zone around the wire before being able to effectively interact with aluminum. Temporal HF speciation data, provided by TOFMS in Figure 4.15, shows that HF gas is released as early as 460 °C, before ignition for all composites. It is interesting to note that repeated measurements of the release of HF within the Al/F₂O₃/PVDF system show a delayed release of HF in comparison to the other metal oxides. However, it is unclear, from the data presented here, why this happens.

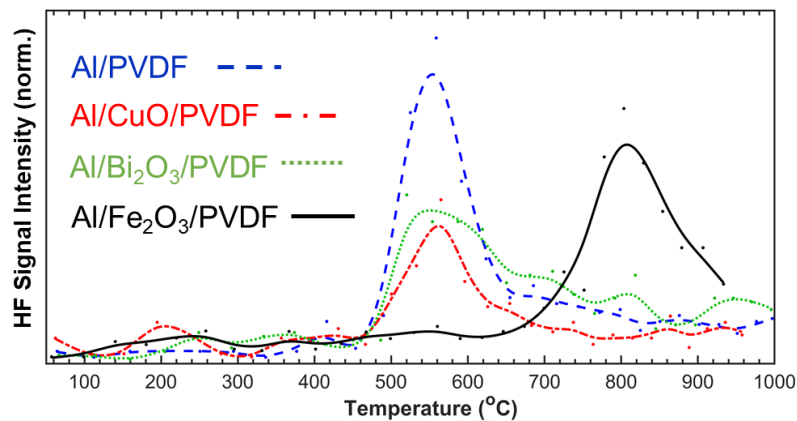


Figure 4.15: Normalized HF signal intensity of the various Al/MO/PVDF composites subject to T-Jump/TOFMS

The lack of ignition in vacuum reinforces that the Al/PVDF reaction is mediated by a gas phase interaction. The pre-ignition reaction is thus enhanced as the diffusivity of HF gas decreases in pressurized environments, resulting in more violent, binder constrained ignition events such as those in Figure 4.13. However, the films that do ignite in vacuum do so with the aid of the Al/MO reaction. It is in this way that ignition in vacuum is thermite controlled.

Figure 4.16 illustrates the full 10 ms averaged mass spectrum from T-Jump/TOFMS analysis of all energetic compositions for which many other gas phase species, both transient and omnipresent, are detected.

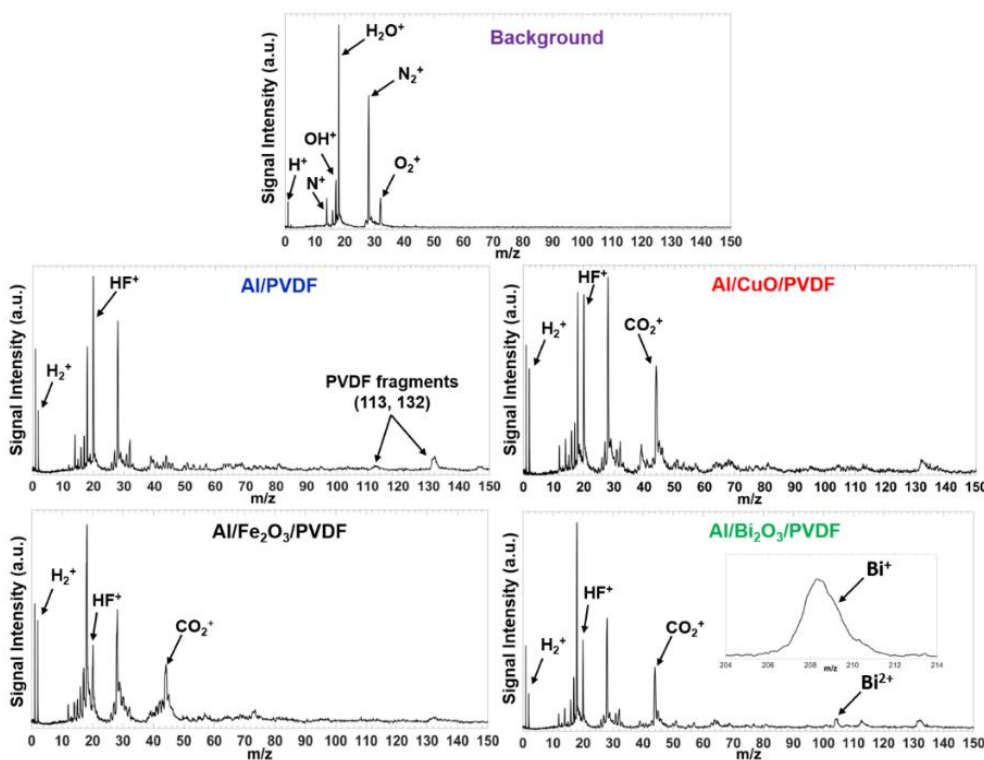


Figure 4.16: T-Jump/TOFMS Mass spectra of Al/MO/PVDF composites averaged over 10 ms

In addition to background air components, rapid heating of Al/PVDF reveals the decomposition species of PVDF in the form of HF gas ($m/z = 20$), molecular

hydrogen ($m/z = 2$), and other high mass gas species described in a previous paper.⁶⁷ The mass spectra of the metal oxide containing films also show the clear emergence of carbon dioxide ($m/z = 44$) and even vaporized bismuth ($m/z = 209$) in the case of Bi_2O_3 . Upon decomposition, PVDF decomposes to form carbon species which could provide a fuel source other than aluminum which can react with oxygen nascent from the metal oxide [8,9,18].^{67,108,167} The possible interaction between the metal oxide and PVDF was further considered in which MO/PVDF composites were subject to T-Jump/TOFMS with the results displayed in Figure 4.17.

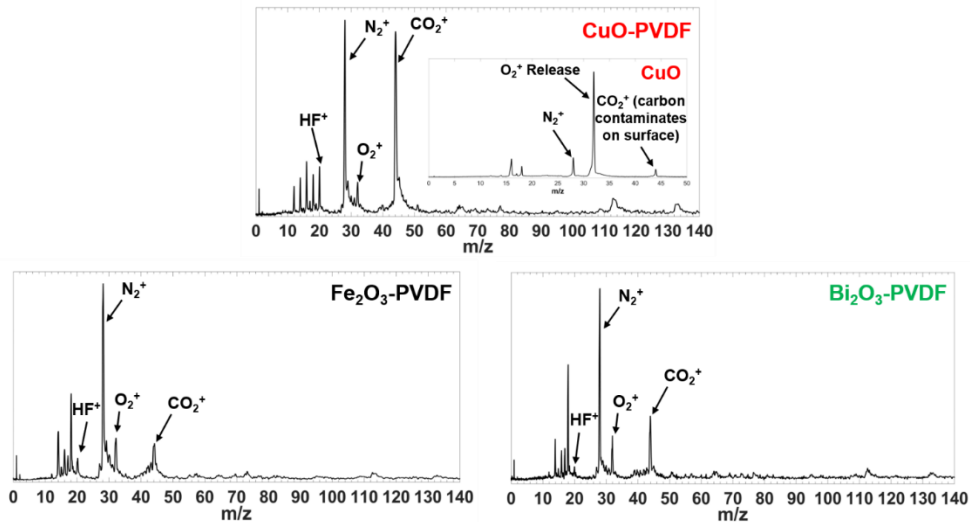


Figure 4.17: T-Jump/TOFMS Mass spectra of MO/PVDF composites averaged over 10 ms

The mass spectra from TOFMS once again displays the emergence of carbon dioxide, indicating the consumption of oxygen by the newly available carbon-based fuel. By comparison, T-Jump/TOFMS of bare CuO results in a sudden release of oxygen which dwarfs the signal intensity of all other species present (Figure 4.17). Instead of a large oxygen release signal, CuO/PVDF displays the largest CO_2 signal out of all the other compositions studied. Combined with SEM evidence of Al_2O_3

formation, this suggests that the metal oxide is reacting with both the aluminum fuel and carbon species nascent from PVDF decomposition. The availability of these nascent carbon species in pressurized environments is also suggested by the increased flame speed and vigor by which Al/PVDF films burn in air (Figure S4.2).⁶³ Films formulated in this study are thus inherently fuel rich and contributes to combustion performance deterioration as more metal oxide content reacts with carbon species instead of the provided aluminum.

Rectifying the stoichiometric imbalance internally without the assistance of oxygen from air while maintaining and improving mechanical integrity will prove to be a challenging endeavor. Further in-depth studies with respect to the interaction of the MO/PVDF content will need to be undertaken to better understand how they may affect the overall combustion performance with a metal fuel. The solution for wider variations in flame speed and energy release tunability maybe accomplished through architectural structure-function methods and/or modifying the printing process to include a wider variety of relevant film friendly constituents.

4.4 Conclusions

This study investigated the formulation and combustion performance of ink extrusion 3D printed energetic films incorporating high mass loadings of aluminum and relevant metal oxide nanoparticles within a PVDF binder. It was found that each of the resulting two component films were homogenously mixed with a high degree of geometric reproducibility between films with differing particle type and loading. However, as more thermite content is included, the mechanical integrity of the films is reduced and dependent on the physical characteristics of the added metal oxide nano-

powder. The ignition temperature in an argon atmosphere was shown to be controlled by the Al/PVDF reaction whereas the ignition temperature in vacuum is controlled by the Al/MO reaction. These results reinforce the necessity for a HF mediated gas phase reaction mechanism of Al/PVDF. Both ignition in vacuum and intrinsic energy release rates appear to be dependent on the type of metal oxide utilized. However, there does not appear to be much variation among the metal oxides with respect to self-propagating flame speeds in argon at atmospheric pressure.

Overall, increased thermite mass content in solvent based fabrication leads to increased porosity, decreased flame speeds, increased flame temperature, and diminished energy release rates. Integrated metal oxides appear to not only react with aluminum but also carbon species formed from PVDF decomposition, generating CO₂ and deviating from the predetermined mutually exclusive stoichiometric balance in the system. Film disintegration as well as differences in Al/PVDF and Al/MO kinetics appear to be adverse factors for film combustion performance. Energetically active additives of differing forms, other than metal oxides, may be supplemented by niche non-energetic constituents for future formulations which seek to enhance burning rates in a predetermined manner. Knowledge of the thermal diffusivity would be of great importance for future studies of the kinetics of such systems. Tuning content which facilitates kinetics and the mobility of chemically generated heat while systematically varying film architecture for the promotion of efficient thermal transport is necessary to the promotion of both flame velocity and energy release rates.

Chapter 5: High Temperature Interactions of Metal Oxides and a PVDF Binder

Summary:

Interactions between energetic material relevant nanoscale metal oxides (SiO_2 , TiO_2 , MgO , Al_2O_3 , CuO , Bi_2O_3) and polyvinylidene fluoride (PVDF) were investigated by Temperature-Jump/Time-of-Flight Mass Spectrometry (T-Jump/TOFMS) and thermogravimetric-differential scanning calorimetry (TGA-DSC). Scanning Electron Microscopy (SEM) and Transmission Electron Microscopy (TEM) were used to characterize the morphology of the compositions while X-ray diffraction (XRD) was utilized to analyze the condensed phase crystalline species at temperatures of interest. The exergonicity and exothermicity of HF gas with hydroxyl terminated metal oxide surfaces make HF the likely fluorine-bearing moiety and primary mode of the fluorinating reactions where terminal OH^- configurations are replaced by F^- in the formation of stronger metal-fluorine bond. However, not all compositions produce corresponding stable metal fluoride. The results show that while some of the investigated metal oxide-PVDF compositions enhance PVDF decomposition and release HF in larger quantities than PVDF, others release HF in smaller quantities than PVDF and even retard PVDF decomposition. The former compositions demonstrate exothermic, multi-step mass loss modes prior to neat PVDF mass loss and the relative intensity of HF gas increases as the temperature of the release point decreases, implying a correlation between HF release and the progression of exothermic behavior. An

interplay dynamic where surface interactions both lowers the onset of HF release and engages exothermically with HF gas subsequently is proposed.

5.1 Introduction

Binders in energetic formulations play a central role in the ability to fabricate practical compositions for a variety of propellant applications. Polymer binders are commonly employed to hold the fuel and oxidizer in close proximity so as not to impede reactivity and maintain mechanical integrity to withstand mechanical stresses. The fluoropolymer polyvinylidene fluoride (PVDF; 59 wt.% F) is an interesting material in its capability to serve as both a binder and potential oxidizer. Furthermore, PVDF has a low melting point ($\approx 150^{\circ}\text{C}$) and is highly soluble in compatible polar organic solvents, such as dimethylformamide (DMF), which make it attractive for use in contemporary additive manufacturing methods in rapid prototyping of material architectures.^{67,98,174,175}

Heterogenous reactive materials (RM) are compositions which are typically comprised of a metallic fuel and a metal oxide oxidizer. In this study I focus on composites of nanoscale metal oxides and PVDF to report on their chemical interactions. While past studies have highlighted the ability of some metal oxides to effect the mechanical wear,¹⁷⁶ crystal structure, and electroactive behavior of PVDF (α -phase vs. β -phase),^{100,177,178} I assess this relationship with respect to how PVDF may act as an acidic oxidizer in the presence of a variety of potential metal fuels^{11,68,179,180} for the exothermic production of volatile metal fluorides (*e.g.* SiF_4 , AlF_3 , TiF_4 , MgF_2 etc.).⁴³ PVDF based energetic systems typically contain nanoscale aluminum as a metal

fuel where prior studies have shown there to be a potentially unique pre-ignition reaction (PIR) at the interface of the fluoropolymer and hydroxyl terminated native aluminum oxide shell (3-4 nm thick). The native shell facilitates early onset release of the PVDF pyrolysis product of HF gas at elevated temperatures ($>300^{\circ}\text{C}$)¹⁸¹ as it etches the alumina shell and further exposes the aluminum core to fluorination.^{67,88,167,182,183} The temperature, rate at which HF gas is released, and exothermicity with the oxide shell have all been proposed to be rate limiting steps in the overall reaction rate of PVDF fluorinated metal nanoparticles.^{167,182-184}

Due to the prevalence of aluminum in energetic formulations, the aluminum oxide interaction with PVDF has been the primary system of study. The goal of this work is to broaden the scope of study and investigate general trends in high temperature, rapid heating pyrolysis of PVDF with other nanoscale metal oxides which make up the native oxide shell of less studied metal fuels (*e.g.* SiO_2 , TiO_2 , MgO , etc.). Relevant metal oxides commonly utilized as relatively strong oxidizers in nanoscale thermite (metal/metal oxide) formulations (*e.g.* CuO , Bi_2O_3) are also studied. The interaction with PVDF and metal oxide oxidizers is generally not considered, yet have been included as a competing nanoscale oxidizer in the form of intermixed nanoparticles or a high energy density replacement of the native oxide shell of the metal fuel.^{6,86,174,185}

The transient technique of Temperature-Jump/Time-of-Flight (T-Jump/TOFMS) is used as the primary diagnostic technique for monitoring the evolution of gas phase species during and after a rapid heating event. T-Jump/TOFMS synchronizes rapid heating ($\approx 10^5$ K/s) and gas phase chemical speciation (10 kHz) to

enable the characterization of metal oxide/PVDF chemistry under the rapid heating conditions expected in the combustion of analogous energetic systems.^{115,120,186} T-Jump/TOFMS is supplemented by traditional slow heating (10 °C/min) thermal analysis methods of thermogravimetric-differential scanning calorimetry (TGA-DSC) conducted in an anaerobic environment to account for the lack of thermal analysis capabilities of the T-Jump/TOFMS beyond simple temperature measurements. Scanning Electron Microscopy (SEM) and Transmission Electron Microscopy (TEM) are utilized to characterize both material length scales and morphology of the composition. Additionally, X-ray diffraction (XRD) is used as a method for chemical characterization of condensed phase crystalline species at temperatures of interest with respect to TGA-DSC measurements.

5.2 Experimental Methods

5.2.1 Materials

Nanoscale metal oxides of CuO (<50 nm), Al₂O₃ (<50 nm), and TiO₂ (≈21 nm) were purchased from Sigma Aldrich (Millipore Sigma) while Bi₂O₃ (≈80 nm), MgO (≈50 nm), and SiO₂ (60-70 nm) were purchased from U.S. Research Nanomaterials, Inc. Polyvinylidene fluoride (PVDF, 59 wt.% F, MW=534000 g/mol) powder was purchased from Sigma Aldrich (Millipore Sigma) and N, N-dimethylformamide (DMF 99.8%) solvent was purchased from BDH chemicals. All chemicals were used as received.

5.2.2 Thin Film Sample Preparation

Samples studied were thin film compositions of nanoscale metal oxide particles within a PVDF binder. Combining and mixing of each of the binary systems was done through a wet process by which a thoroughly mixed polymer/particulate precursor solution is either drop cast onto a thin platinum wire for T-Jump/TOFMS or dispensed onto a heated substrate to allow for solvent evaporation and material solidification for free standing structures.¹⁸⁵

Each precursor solution was formulated by first dissolving 100 mg/ml of PVDF in DMF and stirred via a magnetic stir bar for a minimum of 4 hours. Each respective sub-micron powder is added to the polymer solution with no stoichiometric considerations in mind but enough material to both enhance any potential intra-composition interactions and allow for ease of precursor dispensing. A mass loading of 50 weight percentage (wt.%) of sub-micron powder with respect to the polymer content was added to the polymer solution. The suspension was vortex mixed for 10 seconds, ultra-sonicated for 30 minutes to an hour, and physically stirred via magnetic stir bar for 18-24 hours.

The precursor suspension was treated as an ink for direct-write, micro-extrusion additive manufacturing for the fabrication of batches of free-standing films of the composition where the sub-micron powder is homogeneously imbedded within the polymer binder.¹⁸⁵ A System 30M pressure-driven 3D printer (Hyrel 3D) extrudes the precursor ink from a 10cc disposable syringe with a blunt 18-gauge Luer Lock dispensing needle in a layer-by-layer fashion onto a glass printing bed heated to 70 °C. The drying process is controlled by the temperature of the printing bed, the speed and

extrusion rate of the print (0.5-5 ml/hr), and the effectiveness of the solvent exhaust venting. Each subsequent layer is deposited after the previous layer has sufficiently dried. Resulting film thicknesses range between 7-10 μ m per layer with most films having a thickness between 40-50 μ m. Batches of rectangular sheet are printed from which multiple samples may be harvested for use in different material analysis techniques (*i.e.* XRD, TGA-DSC, and SEM).

5.2.3 Nanoparticle and Composite Characterization

Particle sizes and film composition were characterized by Transmission Electron Microscopy (Tecnai12) operating at 120 kV, Scanning Electron Microscopy (NNS450) operating at 20 kV accelerating voltage, and X-ray Diffraction Crystallography (PANalytical Empyrean Series 2). Utilizing images from TEM and SEM, specifics of the particle sizes are analyzed. Quoted sizes are taken directly from the manufacturers and represent average particle size or range of sizes. Figure 5.1 depicts aggregates of each metal oxide nanoparticle type through TEM which show the differences in size, aggregation behavior (*e.g.* tightly packed CuO), and particle morphology. The observed sizes of the metal oxide particles are all less than 200 nm with many primary particles noticeably smaller (*e.g.* SiO₂) or larger (*e.g.* Bi₂O₃) than what they are quoted as being. It should also be noted that while most metal oxide particle types are spherical, some particle types contain different levels of rod like architectures (*i.e.* Al₂O₃ and MgO).

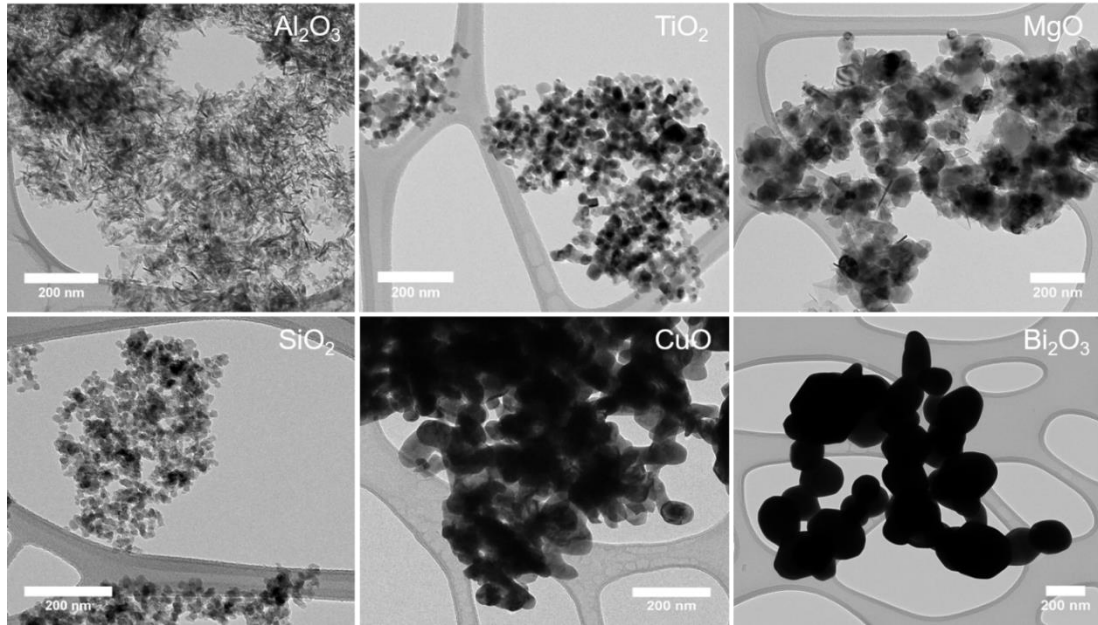


Figure 5.1: TEM depictions of aggregates of the metal oxide particles used in this study.

Noticeable differences in precursor suspension viscosity were observed due to differences in particle size and density when mixing with the PVDF dissolved DMF solution. The variance in extrusion viscosity resulted in an expected reduction in structural mechanical integrity as viscosity increased,¹⁸⁵ but ultimately inconsequential with respect to the methods of analysis conducted in this study. SEM cross-sections of the additively manufactured metal oxide/PVDF thin films are shown in Figure 5.2. One can make out the submicron architecture of cross-sections where larger individual particles or particle aggregates are distinguishable from the polymer matrix and with sizes that appear to be roughly one-to-one with the measured TEM length scales; suggesting that TEM particle sampling is likely representative of each respective particle size distribution.

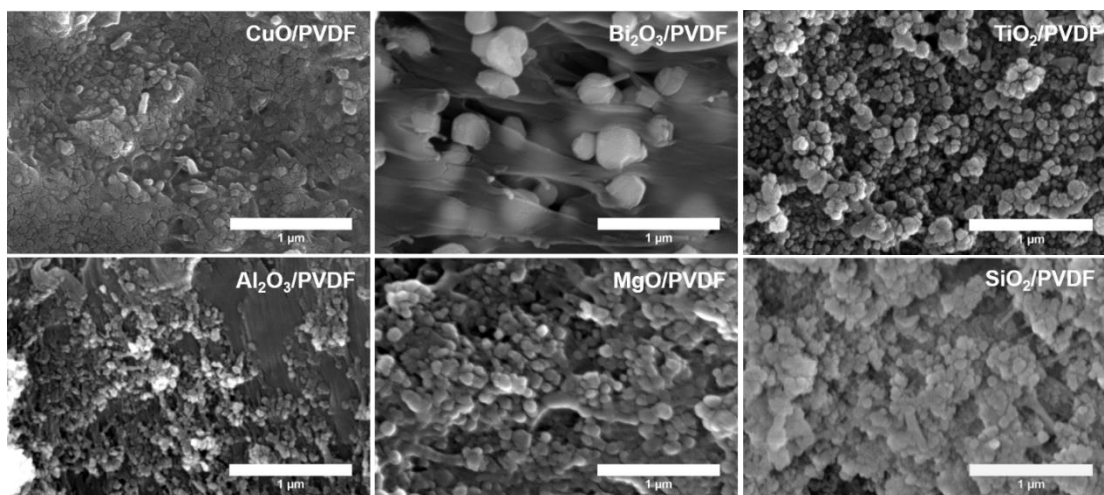


Figure 5.2: SEM cross-sections of all metal oxide/PVDF thin film compositions illustrating metal oxides encapsulated within the PVDF matrix.

5.2.4 Heating Experiments

5.2.4.1 Thermogravimetric Analysis-Differential Scanning Calorimetry (TGA-DSC)

Temperature resolved thermochemical analysis was conducted using a Netzsch STA 449 F3 Jupiter TGA-DSC operating in an argon environment with a flow rate of 70 ml/min. After conducting a correction run with an empty alumina pan, samples of each composition are loaded into the same open alumina pan and slowly heated from room temperature to 1000°C at 10 °C/s. Initial acquisition of TGA-DSC profiles are utilized to pin point temperatures of interest for iterative analysis of each material. TGA-DSC for each material was conducted in triplicate to ensure repeatability. Materials are arrested at the temperatures of interest and collected for XRD analysis.

5.2.4.2 T-Jump/Linear Time of Flight Mass Spectrometry

Rapid heating of metal oxide/polymer composites at ultra-high heating rates was conducted via temperature jump time of flight mass spectrometry (T-Jump/TOFMS), a technique described in greater detail by previous works.¹²⁰ The

apparatus features a coupling of a linear time of flight mass spectrometer with a T-Jump probe equipped with electrical feed throughs and directly loaded into the vacuum environment of an ionization chamber (70 eV electron-gun) held at $\sim 10^{-6}$ Torr. The technique of T-Jump utilizes rapid resistive heating to simulate combustion time scale heating rates ($>10^5$ K/s) where the probe is prepared by soldering 6-12 mm of 76 μm diameter platinum wire (OMEGA Engineering Inc.) between the copper leads of the electrical feedthroughs. A single input trigger synchronizes resistive flash heating by a 3 ms pulse (4-14 V), gas phase ionization for time resolved speciation, and data collection (mass spectra intensity, time, voltage, current) by a LeCroy 600 MHz oscilloscope at a rate of 10 kHz over a 10 ms collection period. Additionally, gas release of reaction products and intermediate species within the TOFMS chamber during chemical interactions of solid compositions is more apparent than would be detected in atmospheric conditions as the vacuum environment is devoid of molecular collisions necessary for full chemical conversion.

Electrical current readings are measured by a Teledyne LeCroy CP030A 30A 50 MHz current probe and combined with the oscilloscope measured voltage to experimentally determine resistance. Thermometry of the wire is obtained through the calibrated relationship between the temperature of the Pt wire and its resistance from the Callendar-Van Dusen equation. Several studies using this method have demonstrated the Pt wire reaching temperatures as high as ~ 1400 K at heating rates as rapid as $\sim 10^6$ K/s.^{115,120} The temperature of wires with coated material is most accurate with a sufficiently small amount of thermal mass (<10 μm thick, 5-20 μg) such that the material is approximately the same temperature as the wire.¹²⁰

In this experiment, samples are prepared by systematically drop casting a small coating of precursor solution onto platinum wires which are then placed in a vacuum oven at 130 °C for 5 hours to remove the remaining DMF solvent. Platinum wires with coated material of this type cannot be pre-flashed and thus require a surrogate wire with roughly the same dimensions to be flashed to get to the same approximate parameters before the experimental run. Measurements were repeated at least 5 times with raw data ported to MATLAB and processed through custom scripts to obtain calibrated mass spectrums as a function of time and wire temperature.¹²⁰

5.3 Results and Discussion

5.3.1 Slow Heating Thermochemical Analysis

Thermochemical analysis of metal oxide/PVDF thin films were carried out by slow heating (10 °C/min) thermogravimetric-differential scanning calorimetry in an anaerobic argon environment to supplement for the lack of gravimetric/calorimetric diagnostics of T-Jump/TOFMS. Analysis is conducted in a comparative manner to the thermal behavior of a neat PVDF thin film. The results are displayed in Figure 5.3.

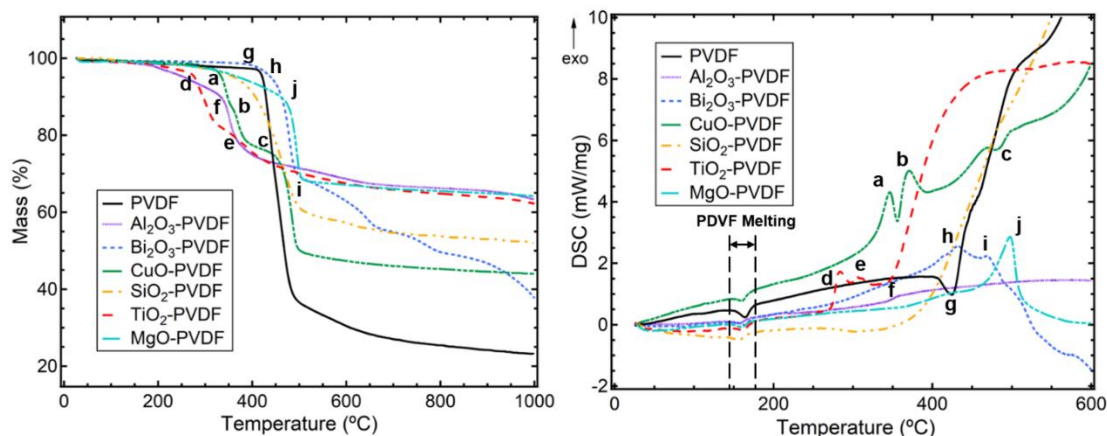


Figure 5.3: TGA-DSC of select metal oxide/PVDF thin films under an argon environment, heated at 10 °C/min.

PVDF, represented by the solid black curve, shows the previously documented melting endotherm at 150 °C followed by a sharp endothermic/exothermic decomposition process at 422 °C (Figure 5.3-g) which transitions to a more gradual decomposition mode. Volatile pyrolysis products largely consist of HF gas and fluorocarbon chain fragments from polymer chain cleavage accompanied by hydrogen transfer.^{181,187,188} Prior TGA studies conducted in air have observed 100% mass loss after PVDF decomposition. In our case, however, the remaining residue does not interact with ambient argon, resulting in no further significant mass loss beyond ≈ 700 °C at roughly 20% mass remaining.⁶⁷

Neat PVDF establishes the initial base thermochemical behavior of all compositions studied where DSC measurements show PVDF melting occurring for all compositions within the range of 145-155 °C. The thermochemical behavior of each of the composites beyond 200 °C displays a unique TGA-DSC profile as major mass loss events are multi-stepped and straddle the primary decomposition of neat PVDF. Much of the more gradual mass loss behavior directly following 200 °C is attributed to dehydration of the high energy, high specific surface area of the metal oxide nanoparticles and/or residual solvent evaporation. Material compositions of Al₂O₃/PVDF (Figure 5.3-f), CuO/PVDF (Figure 5.3-a/b), and TiO₂/PVDF (Figure 5.3-d/e) clearly demonstrate exothermic, multi-step mass loss modes occurring as much as ≈ 150 °C prior to neat PVDF mass loss. While remaining exothermic and multi-stepped, MgO/PVDF (Figure 5.3-j) and Bi₂O₃/PVDF (Figure 5.3-h/i) retard the primary mass loss mode attributed to the interaction of the metal oxide and PVDF during PVDF

decomposition. SiO₂/PVDF appears to have little to no effect on the decomposition behavior of PVDF.

XRD was used to characterize the condensed phase products surrounding featured temperature points of exothermic and endothermic behavior identified by TGA-DSC. The results of this analysis are consolidated in Figure 5.4.

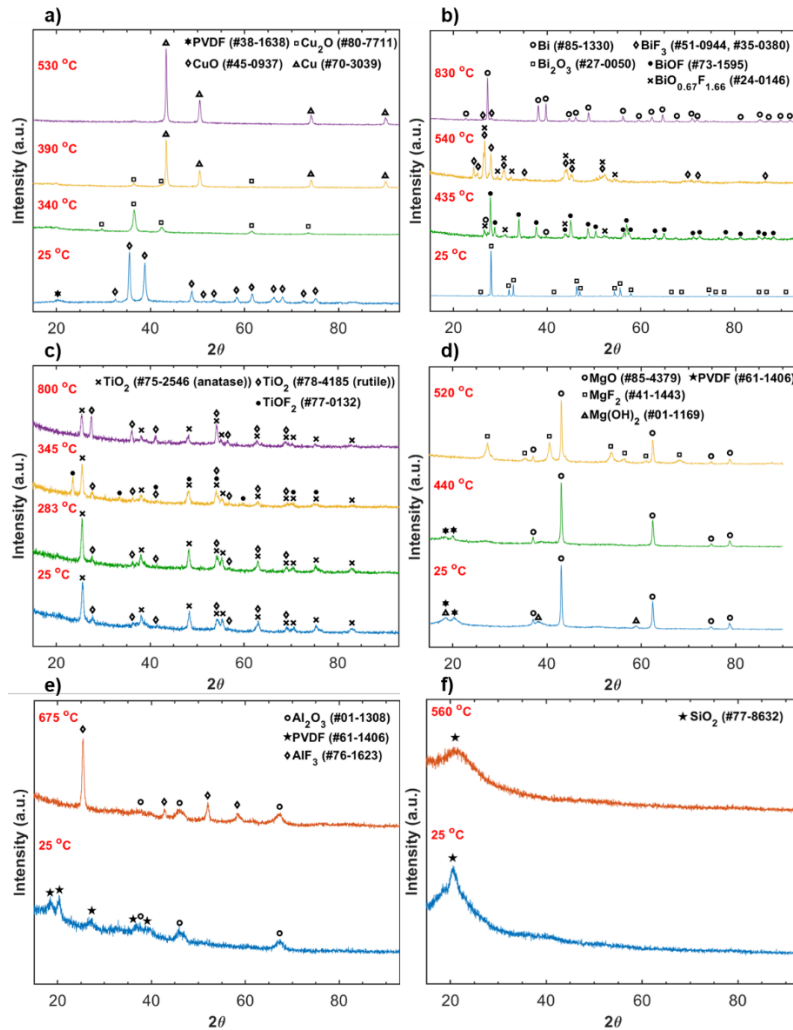


Figure 5.4: Temperature dependent XRD analysis of condensed phase TGA-DSC heated products of metal oxide/PVDF thin films: a) CuO/PVDF, b) Bi₂O₃/PVDF, c) TiO₂/PVDF, d) MgO/PVDF, e) Al₂O₃/PVDF, f) SiO₂/PVDF

This analysis method has been previously conducted by Li et al. for CuO/PVDF where I have reproduced the observations that the exotherms of Figure 5.3-a/b at 332 °C and 364 °C correspond to transitions of CuO to Cu₂O and Cu₂O to Cu, respectively, as the released oxygen reacts with PVDF (Figure 5.4a). Each of these transitions coincide with the release of CO₂ with PVDF treated more as a fuel than an oxidizer in which CuO ultimately fully reduces to Cu simultaneous to the decomposition of the remaining PVDF at 469 °C (Figure 5.3-c).¹⁸⁸ Aside from SiO₂/PVDF whose stable fluorine species, SiF₄ (SiF₃⁺ when ionized), is gaseous at room temperature, the CuO/PVDF composition is the only composite which does not form any fluorine containing compounds. Further XRD analysis of the temperature dependent condensed phase progression shows that the 5 compositions of note (excluding SiO₂/PVDF) can be separated into 3 groups: 1) Relatively simple, full transitions to the most stable, condensed phase fluorine compound (Al₂O₃/PVDF, MgO/PVDF), 2) Complex, metastable fluorination/oxyfluoride progression (TiO₂/PVDF, Bi₂O₃/PVDF), 3) No fluorination with enhanced reduction of the metal oxide compared to the neat metal oxide (CuO/PVDF). These three observed groups do not correlate with the temperature for which TGA-DSC observed interactions with PVDF will take place as the relatively early onset interaction mass loss compositions (Al₂O₃/PVDF, TiO₂/PVDF, CuO/PVDF) are spread out throughout each of these proposed groups.

To better understand the observed fluorination behavior and onset point of the interaction of PVDF, mechanisms of aluminum fluorination by PVDF previously investigated by Padhye et al. and Tunega et al. using Density Functional Theory (DFT) are considered. This model assumes that the alumina shell of aluminum particles

consists of several surface hydroxyl sites for both crystalline and amorphous surfaces. The interaction mechanism considers only the relatively elementary, yet most energetically favorable, exchange reaction where a fluorine-bearing moiety mediates the replacement of terminal OH⁻ configurations by F⁻ in the formation of stronger Al-F bonds.^{43,167,183} It is further assumed, here, that the metal oxides in this study also consist of similar hydroxyl sites to that of alumina. XRD analysis of MgO/PVDF in Figure 5.4d reinforces this point with observation of crystalline Mg(OH)₂ on either its surface or interior.

One may surmise the exergonicity of the progression of metal oxide fluorination, or lack of fluorination, behavior of HF fluorination of a general metal oxide based on simple Ellingham diagrams of standard Gibb's energies of formation for metal fluoride compounds relative to HF.^{66,189} At room temperature, the Gibb's energies of formation of CuF₂, HF, BiF₃, MgF₂, AlF₃, and TiF₄ are approximately -490, -550, -560, -1070, -950, and -780 kJ/mol of fluorine gas respectively.^{66,190} All values approach zero linearly as temperature increases, except for HF whose Gibb's energy of formation decreases at a shallow rate to -565 kJ/mol at 1100 K (827 °C)^{66,190}. As temperature increases, the Gibb's energy of formation of CuF₂ increasingly deviates from that HF gas, indicating the low probability of stable CuF₂ ever forming relative to HF gas. In much of the same manner, MgF₂ and AlF₃ formation are extremely exergonic compared to HF at each respective temperature point of condensed phase analysis (Figure 5.4d-e) and are largely stable or likely to form after HF liberation from the polymer chain.

This same analysis approach is difficult to apply for the formation of BiF₃ and TiF₄ as their Gibbs's energies are comparable to that of HF and their fluorination process appears slower and much more complex with the formation of metastable oxyfluorides. Bi₂O₃ fully reduces and produces CO₂ (Figure 5.5) much like CuO, albeit at a much slower rate, while TiO₂ has some of the earliest exotherms in DSC analysis but appears to be minimally effected in the condensed phase (no TiF₄ or TiF₃ observed) and eventually reverts to the more stable rutile structure after initially forming its oxyfluoride (Figure 5.4b-c). It should be noted that a major assumption of this analysis is that terminating hydroxyl sites are the primary mode of the fluorinating pre-ignition reaction as exothermic reaction enthalpies are maximized at these locations¹⁸³. Hydroxyl site considerations by Padhye et al. may add to this complexity as different types of hydroxyls sites require different energy amounts to break and depend heavily on crystal structure and oxygen vacancy.¹⁶⁷ Hydroxyl sites which form multiple bonds within vacated sites of TiO₂, Bi₂O₃, or any other similar metal oxide would make undergoing any substantial pre-ignition fluorination process increasingly unlikely.

5.3.2 Rapid Heating Time-of-Flight Mass Spectrometry

Coupled T-Jump/TOFMS of thinly coated metal oxide/PVDF sample on 76 μm Pt wire was used as a rapid heating and data acquisition tool to analyze, under combustion heating rates (10⁵-10⁶ K/s), pyrolysis products and intermediates. Both the intensity of HF and the potential effect that the inclusion of differing metal oxides has on the overall profile of each mass spectrum are of primary focus where time resolution of speciation is greatly enhanced over quadrupole mass spectrometer based analysis.¹⁸⁸

The resulting full mass spectrums averaged over a collection time of 10 ms from a 3 ms pulse heating at $\approx 3 \times 10^5$ K/s are displayed in Figure 5.5.

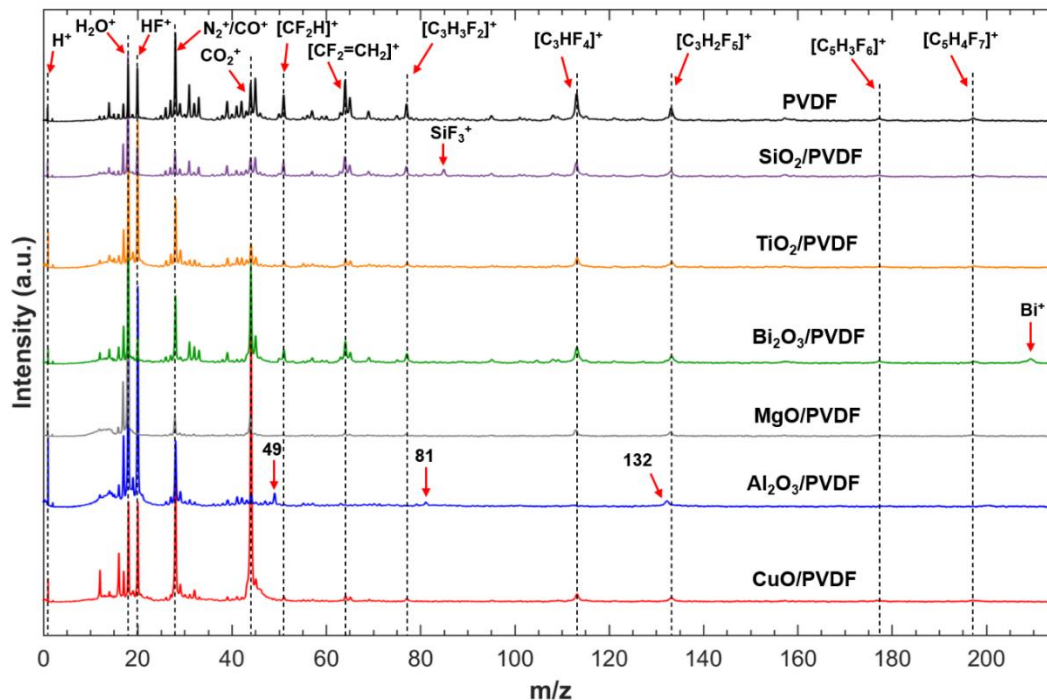


Figure 5.5: Averaged mass spectrum over a 10 ms collection period of rapidly heated Pt wires which are thinly coated with the selected metal oxide/PVDF compositions. The most notable mass species are label.

The PVDF control spectrum displays nearly identical mass spectrum patterns as observations conducted by previous PVDF pyrolysis experiments. As the main volatile, HF, appears in relatively large quantities, and main carbon chains are cleaved, several doubled bonded fragmentations are formed at an accelerated rate.^{181,187} More specifically, HF ($m/z=20$), allylic ions ($m/z=77, 95, 113$), alkyl ions ($m/z=51, 65, 133$), the VDF monomer ($C_2F_2H_2$, $m/z=64$), and their respective electron impaction fragmentations are observed in the measured mass spectrum.¹⁸⁷ Support for this pyrolysis mechanism initiated by HF release is demonstrated by time dependent

speciation of pyrolysis species in Figure 5.6 where HF gas is released $\approx 200 \mu\text{s}$ prior to the detection of higher mass species.

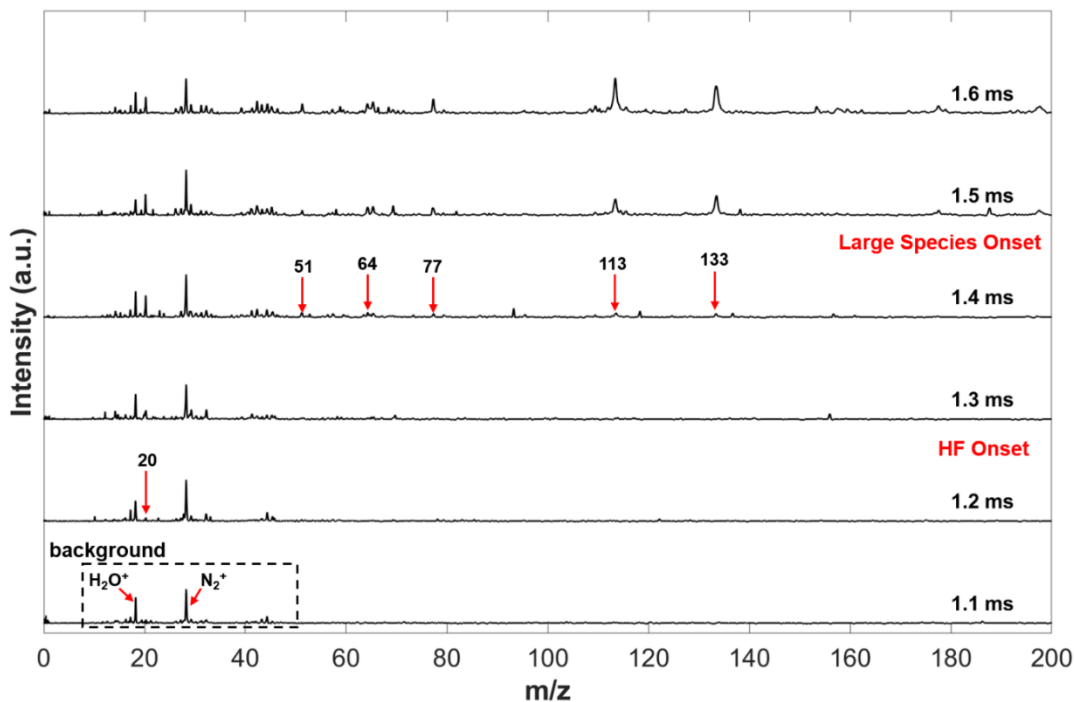


Figure 5.6: Time-dependent full mass spectra of rapidly heated PVDF ($\approx 3 \times 10^5 \text{ K/s}$) over 3 ms depicting onset HF release $200 \mu\text{s}$ prior to the detection of the large pyrolysis species.

Most metal oxide/PVDF compositions in this study reflect the same general pyrolysis behavior as neat PVDF with the notable exception of $\text{Al}_2\text{O}_3/\text{PVDF}$ whose unique mass spectrum does not contain any of the same higher mass species, but instead releases species of $m/z=132, 81, 49$. The degradation of PVDF generally separates itself from other hydrogenated fluoropolymers in theoretical models by the characteristic cyclization of depolymerized vinylidene fluoride to form trifluorobenzene ($\text{C}_6\text{F}_3\text{H}_3$; $m/z=132$).¹⁸⁷ However, models of trifluorobenzene formation reflect a low probability of formation during pyrolysis given the assumptions of the degradation model and thus

is not observed in corresponding experimental spectra.¹⁸⁷ The formation of trifluorobenzene in the case of Al₂O₃/PVDF suggests an alternative pyrolysis or interaction mechanism of PVDF with Al₂O₃ which may either be unique with respect to previously described degradation models, or better fulfills the assumptions of such degradation models.¹⁸⁷ Given the lack of any other large mass species normally indicative of fluoropolymer degradation, the former appears more likely.

Prior studies have suggested that the availability and rate of HF release is likely a driving factor in the fluorination mechanism responsible for the reaction rate of propellant systems where PVDF is the primary oxidizing agent.^{67,167} Quantitative analysis of the release behavior of HF volatiles was conducted by measuring the maximum intensity of HF (*m/z*=20) of each composition upon release relative to that of neat PVDF as a function of release temperature. These results are displayed in Figure 5.7.

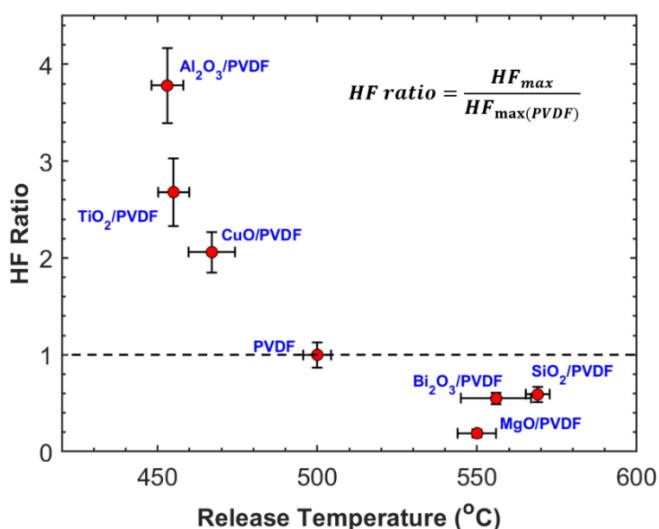


Figure 5.7: T-Jump/TOFMS measured relative HF release maximum (HF ratio) of metal oxide/PVDF compositions as a function of release temperature.

A clear correlation is illuminated from this analysis where the relative intensity of released HF gas increases dramatically as the temperature of the release point decreases with Al₂O₃/PVDF separating itself above all others. The compositions which release HF in larger quantities than PVDF versus those that release less HF than PVDF reflect the same grouping of compositions via TGA-DSC analysis in Figure 5.3. This similarity seems to suggest the correlation between HF release and the progression of exothermic behavior. Despite this finding, a primary question now arises from this analysis: Does the larger HF intensity at lower temperature occur due to a more exothermic interaction which locally increases temperature for further HF release, or does there exist some more fundamental surface interaction between the metal oxide surfaces and PVDF prior to HF release which allows HF gas to more easily be released?

The study conducted by Padhye et al. points out that a more crystalline shell of alumina acts as an upper limit in the reduction of the onset for the pre-ignition reaction as crystalline shells have higher concentrations of hydroxyl termination and therefore a greater concentration of surface reactions with the highest potential exothermicity.^{167,183} Since I cannot readily compare the degree of crystallinity between differing materials, this point maybe moot or incomplete. Our observations are more likely associated with an interplay dynamic where surface interactions both lowers the onset temperature of HF release and engages exothermically with HF gas after the fact as illustrated in Figure 5.8. The distinction between the two is most evident between the behaviors of MgO/PVDF compared to Al₂O₃/PVDF as observed by Figure 5.3 and Figure 5.7. MgO/PVDF releases very little HF following the onset temperature even

though both materials react readily and exothermically with PVDF to form some of the most stable metal fluorides. The formation of crystalline $\text{Mg}(\text{OH})_2$ may be to blame as an initial hinderance, but these results reinforce the notion that surface energy influences must be addressed for future modeling purposes.

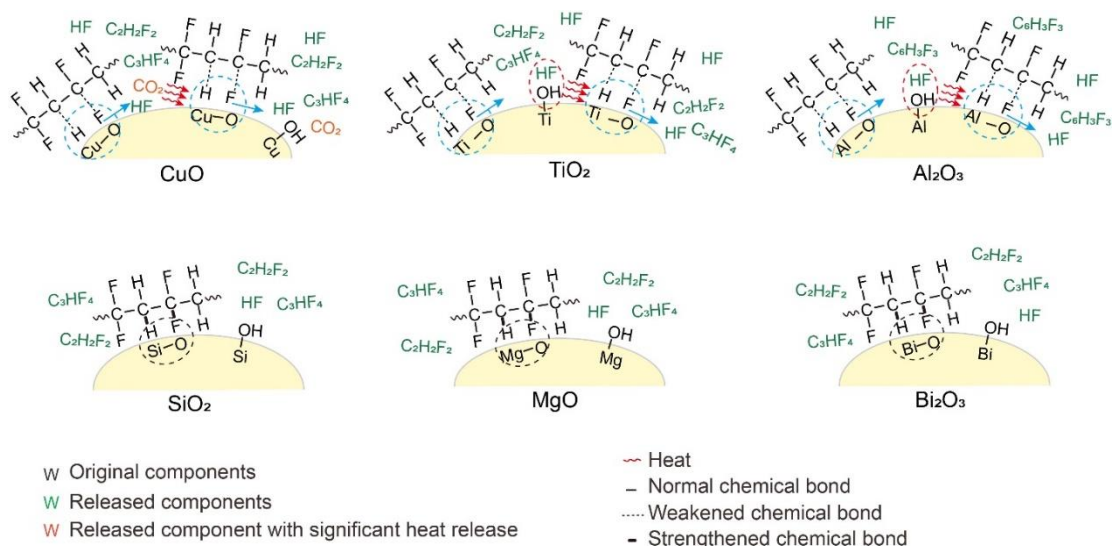


Figure 5.8: Initialization of the proposed interactions between the studied metal oxides and PVDF where those on the top layer release far more HF gas and react with decomposing PVDF at early temperatures compared to neat PVDF decomposition.

Despite having shown no evidence for any form of fluorination at all, CuO/PVDF releases twice as much HF as neat PVDF at a lower temperature. The primary exotherms in Figure 5.3-a/b are attributed to the formation of CO_2 ($m/z=44$) which is detected by mass spectrometry $\approx 200 \mu\text{s}$ prior to HF release (Figure S5.1).¹⁸⁸ Although T-jump/TOFMS of neat CuO nanoparticles, alone, releases CO_2 from the decomposition of naturally occurring copper carbonate (azurite or malachite),^{185,191} the intensity of CO_2 detection by mass spectrometry in Figure 5.5 is far too strong to be explained by the decomposition of copper carbonate. The lack of oxygen intensity points to a reaction that directly takes place between nascent oxygen gas from

CuO/Cu₂O and PVDF prior to HF release. The exothermicity may then further drive HF release (Figure 5.8). The importance of this observation is not that HF was released in larger quantities than neat PVDF, but that the exothermic event needed to drive that release need not be a fluorination event (Figure 5.8). CuO is driven to decompose to Cu₂O in a mass independent manner nearly 500 °C earlier than what has been documented based on our TGA-DSC results in Figure 5.3 and Figure S5.2. This highlights a mutually beneficial degradation behavior in the case of CuO/PVDF at slow heating rates (Figure S5.2). Additionally, this behavior more broadly suggests a two-step process where surface proximity interactions for early onset HF release and a relatively exothermic HF/metal oxide surface interaction are necessary to enhance fluorination progression.

5.4 Conclusion

This study investigates the role of nanoscale metal oxides (Al₂O₃, SiO₂, TiO₂, MgO, CuO, Bi₂O₃) in the pyrolysis of PVDF and subsequent interactions. The main volatile product from the pyrolysis of PVDF is HF gas which engages in previously proposed reactions with OH⁻ sites on metal oxide surfaces, replacing OH⁻ by F⁻ in the formation of stronger metal-fluorine bonds. However, corresponding stable metal fluoride may not be produced after the reaction. Aside from SiO₂/PVDF whose stable fluorine species, SiF₄, is gaseous at room temperature, analysis of the temperature dependent condensed phase progression shows that these compositions can mainly be divided into 3 groups: full transition to most stable fluorine compound (Al₂O₃/PVDF, MgO/PVDF), metastable fluorination/oxyfluoride progression (TiO₂/PVDF, Bi₂O₃/PVDF), and no fluorination with enhanced reduction of metal oxide

(CuO/PVDF). It is found that while Al₂O₃, TiO₂ and CuO enhance decomposition behavior and the HF release from PVDF, SiO₂, MgO and Bi₂O₃ suppress HF release and retard the onset of PVDF decomposition. The relative intensity of HF gas increases dramatically as the onset temperature of HF release decreases.

Compositions that release HF in larger quantities than PVDF demonstrate exothermic, multi-step mass loss modes prior to neat PVDF mass loss, suggesting a correlation between HF release and the progression of exothermic behavior. I propose that interactions between HF promoting metal oxides both lower the activation energy of HF release and engage exothermically with HF gas to promote further local HF release. However, the release of HF gas may be facilitated by alternative exothermic behavior prior to PVDF decomposition, as shown by significant CO₂ formation preceding HF release in the case of CuO/PVDF.

Al₂O₃/PVDF separates itself from other compositions based on its unique T-jump mass spectrum which produces the largest release of HF gas and generates trifluorobenzene instead of any of other the higher mass species observed in both neat PVDF and other compositions. Models of trifluorobenzene formation reflect a low probability of formation during pyrolysis, implying an alternative pyrolysis or interaction mechanism of PVDF with Al₂O₃. This suggests a potential difference in reaction mechanism which requires more sophisticated models to illustrate the interaction of Al₂O₃ and PVDF and how this interaction fundamentally differs.

Chapter 6: Numerically Evaluating Energetic Composite Flame Propagation with Thermally Conductive, High Aspect Ratio Fillers[‡]

Summary:

Thermally conductive, high aspect ratio additives offer a unique way to modulate heat transfer for flame propagation of energetic materials by creating “highways” along which released energy can transfer to unreacted regions. Flame propagation performance in dense energetic composites filled with randomly orientated additives of varied filler volume percentage (vol.%), aspect ratio (AR), and thermal conductivity was modeled using a 2D implicit finite element method. It was found that small additions (<20 vol.%) of high aspect ratio additives (AR>25) enhanced the total area burned by as much as ≈25% and the energy released by as much as ≈10%. While lower aspect ratio additives (AR<25) resulted in negligible enhancements due to the lack of thermally conductive pathways, large amounts of additives (>20 vol.%) oftentimes led to quenched flame propagation by excessive leeching of energy from the reactive front. Variations in additive thermal properties demonstrated a positive energy release enhancement with increasing thermal conductivity of additives ranging from 2 to 5 orders of magnitude greater than the energetic material. This study serves as a proof-of-concept to enhance energy release by increasing heat transfer with additives that can be readily incorporated into the energetic composites.

[‡] The results presented in this chapter have been previously published and are reprinted with permission from: Miles C. Rehwoldt, Dylan J. Kline, Michael R. Zachariah, *Numerically evaluating energetic composite flame propagation with thermally conductive, high aspect ratio fillers*, Chemical Engineering Science, 2020, 229, 116087. Copyright 2020 Elsevier.

6.1 Introduction

Advanced energetic and propellant systems are increasingly being viewed as good candidates for additive manufacturing. This is particularly so when considering the use of nanomaterials which make traditional casting difficult. These systems rely on high volume loadings of a sub-micron metal fuel and an oxidizer either in the form of a polymer binder or sub-micron source of condensed oxygen (*e.g.* metal oxides, ammonium perchlorate). For full utility, these materials must not only have high energy density, but must release its chemically stored energy in a rapid, stable manner and must be mechanically durable. One significant aspect of the operational characteristics of self-sustained combustion in these materials is heat feedback to maintain flame front propagation, which implies that thermal transport properties play an important role. These materials fall into a much broader class of polymer composites.

Characterizing the tunability of thermal and mechanical properties of multi-phase¹⁹² polymer systems has been difficult to explore both experimentally^{193–196} and theoretically^{197–199} despite its importance in a variety of applications which include energy storage for electronics,^{195,200} electrical shielding,^{193,201} and heat exchange technologies.^{193,195,202} Commonly used epoxies, acrylates, and fluoropolymers are poor conductors of heat and are generally treated as thermal insulators.²⁰³ Thermally conductive fillers like carbides,¹⁹⁵ metals,^{193,204} and carbon structures^{194,202,205,206} with various morphologies (*i.e.* fibers, spheres, flakes) are oftentimes utilized to modulate the composite's effective thermal conductivity. General candidate materials span a wide range of thermal conductivities as can be seen in Figure 6.1. Improvements to thermal conductivity in composites has been primarily observed with the addition of

thermally conductive fillers such as silver particles,¹⁹³ graphite,²⁰⁶ carbon fibers,²⁰⁵ and carbon nanotubes^{196,202} (CNTs).

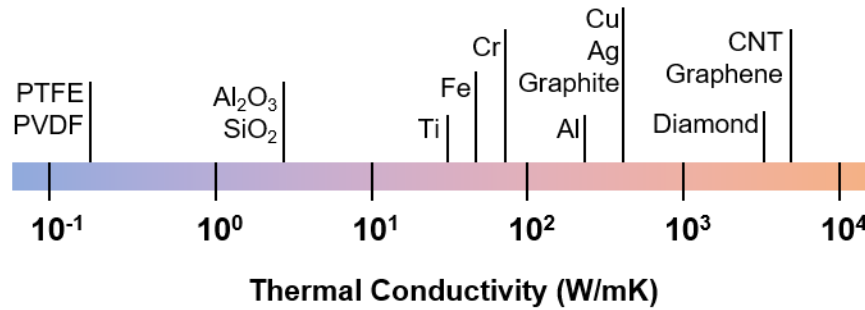


Figure 6.1: Spectrum of thermal conductivities typically used in polymer composites with tunable thermal properties

Despite the widespread experimental and theoretical work studying the effects of thermally conductive materials on the effective thermal conductivity of two-phase polymer systems, little modeling work has investigated the extent to which the inclusion of such materials effects flame propagation performance in self-propagating high temperature synthesis (SHS)^{78,207,208} and propellant systems.^{192,196,204,209} Systems of primary interest are those which imbed condensed phase energetic constituents in the form of micron to nanoscale metal fuels, oxidizers, and/or other applicational additives of various morphologies within a polymer matrix binder.^{20,63,77,96,111,118,122,185,210,211}

In this paper, I explore the inclusion of materials with high thermal conductivity as a means to augment the energy release rate in a dense composite.²¹² In the absence of convective heat transfer, flame propagation behavior is dependent on how fast energy can be generated (chemistry) and how fast that released energy can be transferred to unreacted areas (thermal diffusivity). Thus, for a composite material with

constituents having roughly the same order of magnitude of the specific thermal mass ($\sim 10^6 \text{ Jm}^{-3}\text{K}^{-1}$), ρc_p , the local flame behavior is explicitly a function of the local thermal conductivity.¹ The role of filler material parameters (*e.g.* volume percentage, material type, and geometric morphology) on composite properties have been explored with experimental studies which reference effective composite thermal conductivity theories, such as the Lewis-Nielson, Maxwell, and Percolation models.^{193,194,197-199} Experiments and Lewis-Nielson models have shown that the use of rods or fibers results in superior effective composite thermal conductivity over sphere-like morphologies at similar volume fractions since high aspect ratio additives tend to easily form a connective network along directions of interest.^{196,199,202,205}

Here, a 2D implicit finite difference numerical model of the heat equation is used to analyze flame propagation behavior of energetic systems with low thermal conductivity (*e.g.* Al/PVDF) which incorporate thermally conductive fillers of varied volume percentages (vol.%), aspect ratios (AR), and thermal conductivity. More specifically, I focus on a cross sectional area parallel to flame propagation in which rods of random azimuthal orientation lay in the plane. Results illuminate how thermal properties and materials distribution within the energetic composite correlates to flame front morphology, permeability of heat, rate of material consumption, and changes to overall energy release.

6.2 Modeling Structure

6.2.1 Thermal Transportation and Chemistry

Self-sustaining combustion of a dense reactive material involves heat transfer initiating rapid chemistry, which in turn drives more heat transfer.¹ The energy that is liberated during an exothermic reaction is converted to heat and observed as regions of temperature accumulation. Thermal gradients drive conductive energy transport from regions of high temperature to regions of low temperature through conductive pathways. For global flame propagation of a heterogenous reactive material to be self-sustaining, the combination of energy generated by chemistry and inward heat diffusion in local regions must equal or exceed outward heat diffusion in order to sustain the global reaction front.¹ Rapid heat transfer from adjacent reacted materials ensures a rapid accumulation of energy to stimulate further chemical reactions. Often, the primary limitation to the observed propagation rate is that chemistry is so fast that the process is limited by the transport of heat to the unreacted region.

Under these conditions, the governing dynamics is described by the 2D Heat Equation (Equation 6.1) in which only Fourier conductive heat transfer flux, $\dot{q}_{cond} = -k\vec{\nabla}T$, between discrete material regimes is considered with the assumption that the thermal conductivity is constant along conduction boundaries. Additionally, external volumetric heat input, P , and internal chemical energy generation, Q , need to be considered. I will discuss how the chemical generation term will be handled in a later section.

$$\rho c_p \frac{dT}{dt} |_{x,y} = \frac{\partial}{\partial x} \left(k \frac{\partial T}{\partial x} \right) |_x + \frac{\partial}{\partial y} \left(k \frac{\partial T}{\partial y} \right) |_y + (P + Q) |_{x,y} \quad (6.1)$$

It is assumed that material density is sufficiently large for mass diffusivity to be negligible compared to thermal diffusivity ($Le \ll 1$) so that mass diffusivity and convective behavior may be ignored.^{213,214} The effective local thermal conductivity at the boundaries of discrete material regimes is determined by estimating thermal resistance (Equation 6.2).^{192,198,213,215}

$$k_{eff} = \frac{2k_1k_2}{k_1+k_2}, \quad k_{p,q+\frac{1}{2}}^n = \frac{2k_{p,q+1}^n k_{p,q}^n}{k_{p,q+1}^n + k_{p,q}^n} \quad (6.2)$$

The specifics of discretization and numerical methods and solutions to the 2D Heat Equation are described in the supporting material.

The initial volumetric power input, P , (*e.g.* hot wire, laser, electrical) heats the material to the pre-defined ignition temperature, T_{ig} , and initiates volumetric chemical energy generation, Q . Since our intent is to focus on the role of heat transfer media, I simplify the chemistry as the product of the global specific reaction enthalpy of the energetic material, Δh_{rxn} , with the global conversion rate of the of the reactant material, $\frac{\partial \eta}{\partial t}$, which is proportional to the local concentration of reactant species.^{79,216–}

218

Several assumptions of chemistry are made to simplify the model while maintaining the integrity of analyzed trends:

- Chemical reaction time scale is much shorter than that of diffusion ($t_{rxn} \ll t_{diff}$).^{217,219–221}

- Chemical kinetics is linearized with the assumption of a sufficiently large activation energy for the onset of chemical energy output at T_{ig} (Heaviside Function).^{78,79,213,217}
- The adiabatic flame temperature, T_{ad} , serves as a surrogate for both the reaction enthalpy and the termination point of chemical energy generation (Heaviside Function).

Transient chemical energy generation is thus represented in Equation 6.3 in an implicit binary manner as a function of experimentally and theoretically determined temperature values (T_{ig}, T_{ad}) without the need for chemical conversion tracking.

$$Q = \Delta h_{rxn} \frac{\partial \eta}{\partial t} \cong \rho c_p \frac{T_{ad} - T_{ig}}{t_{rxn}} H(T - T_{ig}) H(T_{ad} - T) H(t_{rxn} - t_{ig}) \quad (6.3)$$

6.2.2 Physical Layout

The physical platform of this model emulates that of the studies done by Varma,²¹³ Grinchuk,²²² and Tang²²³ in terms of geometry and discrete composition layout (Figure S6.1). In accordance with a finite difference method, a constant volume²²³ 2D mesh grid in a constant pressure environment is established with each grid point representing a temperature node at the center of a square area which has a characteristic width, δ .^{224,225} The grid represents an $L_y \times L_x$ frame with $\frac{L}{\delta}$ nodes along a single primary axis (grid resolution). Given the symmetry of the grid, one may choose to use the dimensionless length, $\chi_c = \frac{x}{\delta}$, where $\delta < L$.

The material properties of each node area represent a reactive material sample which is below or equal to its theoretical maximum density. This material properties

may be varied to reflect the effects of composition morphology within the characteristic length. Each node area represents a composite of perfectly mixed implicit solid constituents which are no larger than the characteristic length. Applicable systems of this model must be constrained by the following assumptions:

- The scales of primary particle heterogeneity within the energetic composite is smaller than the characteristic length (Figure 6.2c).
- The thickness of the flame front is larger than the particle size and/or particle interspacing so that local flame propagation is treated as approximately quasi-homogenous.^{212,213,217,223,226,227}

With these assumptions, specific geometric distribution of constituents within each square cell, δ^2 , can be ignored and one can simply use bulk quantities. One may effectively vary the magnification of a system to different length scales while maintaining the relative resolution of the grid (at the potential cost of solution accuracy). Each temperature node consists of an effective bulk thermal conductivity, k , specific heat, c_p , and local density, ρ . A two-phase mixture¹⁹² is implemented by designating each node to be either energetic material or inert filler. This allows for a single effective thermal diffusivity value, α , to represent a single node of filler material, α_f , or energetic material, α_r . The filler material is a non-reactive material meant to simulate the physical existence of a material pore, longer range ($>\delta$) heterogeneity, a conductive additive, or any other relatively non-reacting niche filler. A mapping of discrete thermal diffusivities/conductivities of each grid point is generated as a visual for material distribution, as shown in Figure 6.2.

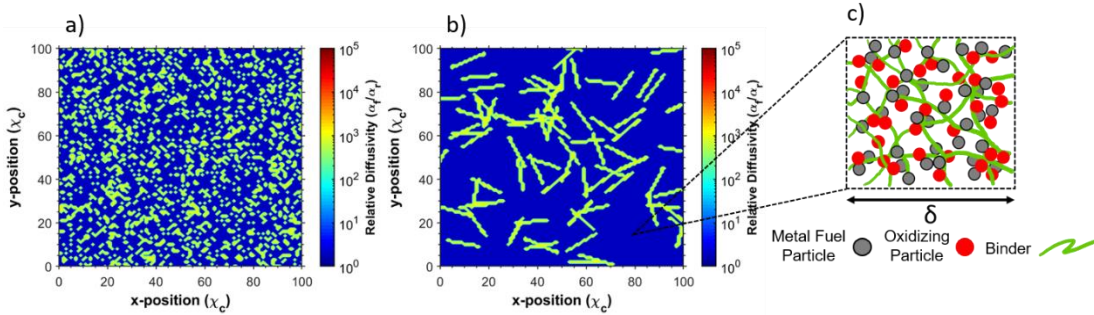


Figure 6.2: Relative thermal diffusivity ($\frac{\alpha_f}{\alpha_r}$) mapping with respect to volume fraction for a) simple homogeneously mixed, uniform distribution, and b) distribution of rod of variable aspect ratios as well as an example of c) the heterogeneity scaling of solid energetic constituents relative to δ .

The placement of filler material is randomized by house-built routines which aim to match the desired volume fraction of evenly distributed filler for a given calculation. Figure 6.2b represents fillers with a non-spherical morphology in the form of rods whose centers of mass are uniformly distributed. The aspect ratio of the additive (AR) is monodisperse and varied between calculations. However, the minimum geometries of the rods are constrained by the model to be no smaller than the characteristic length. As the aspect ratio of the sample approaches unity (AR=1), the distribution resembles the simple homogeneously mixed case shown in Figure 6.2a. As discussed above, a primary assumption is that the length scale of the energetic composite's components is much smaller than the resolution of the grid, therefore the energetic material appears to be perfectly mixed (Figure 6.2c).

6.2.3 Model Analysis and Parameters

The objective of this model is not to calculate specific numbers, but rather to flush out general trends for flame propagation behavior as a function of thermal properties, volume fraction of constituents, and the aspect ratio of incorporated rods. Although this model does not consider a specific system, many of the parameters for

experimental conditions and thermophysical properties reflect those that would be seen in typical studies on fluoropolymer-bound energetic composites.

Modeling of flame behavior is assessed with room temperature initial conditions ($T_a = 300$ K) using $\frac{L}{\delta} = 100$ (e.g. $\delta = 2 \mu\text{m}$, $L = 200 \mu\text{m}$). Boundary conditions are set to allow for convective heat flux, $\dot{q}_{conv} = h(T - T_a)$, between the material and environment. The nonlinearity of radiative heat transfer disqualifies its contribution in this model which utilizes linear algebraic methods.

Thermal properties of interest for conductive heat transfer flame modeling consist of the thermal mass (ρc_p), thermal conductivity (k), ignition temperature of the energetic material regimes (T_{ig}), adiabatic flame temperature of energetic material chemistry (T_{ad}), and characteristic time of reaction (τ_{rxn}). Given that the thermal mass for constituents of potential interest (e.g. Al, Ti, Cu, C, PVDF, Viton) have the same order of magnitude, the thermal mass of each material type throughout this analysis remains invariant at a value of $10^6 \text{ Jm}^{-3}\text{K}^{-1}$. The quantitative value of thermal conductivity of the energetic material has a lower bound based on the binder. Neat polymer binders such as Viton and PVDF have thermal conductivities of $\approx 0.2 \text{ Wm}^{-1}\text{K}^{-1}$ which increase with the addition of thermally conductive fuels.^{180,202,228,229} For simplicity, the energetic material possesses a thermal conductivity, k_o , of $0.4 \text{ Wm}^{-1}\text{K}^{-1}$ (double PVDF)²²⁸ with the inert rods having varied thermal conductivities higher than the energetic material. The chosen ignition temperature and adiabatic flame temperature are based on Al/CuO thermite composites which have a measured ignition temperature of ≈ 900 K, and a theoretical adiabatic flame temperature of ≈ 2800 K.^{124,185} The rough order of magnitude of the time of reaction is based on quasi-homogenous

flame propagation¹²⁵ and laminar flame theory²¹² with experimental observations of Al/CuO propellants which satisfy the assumption of fast chemistry.^{124,125}

6.3 Results

6.3.1 Role of Rod Aspect Ratio in Combustion Performance

Flame propagation modeling was carried out over a 500 μ s period. Energetic composites are incorporated with randomly oriented rods at varied volume percentages (vol.%=0%, 5%, 10%, 20%, 30%, 40%) and aspect ratios (AR=1, 5, 15, 25, 35, 45, 55). Modeling of each parameter set was repeated 5 times. Temperature mappings in Figure S6.3 illustrate overall flame morphology with hot spots designating zones undergoing transient exothermic chemistry. Analysis of flame propagation focuses on how the integration of thermally conductive rods ($k = k_o \times 10^4$) may assist proliferation of energy throughout the composites and enhance the amount of energy released within the combustion time interval. The energy release of the system may be expressed by Equation 6.4 which can be simplified to a dimensionless energy in Equation 6.5. The dimensionless energy release is defined as the relative change in the energy release of the composite compared to the case without rods.

$$\frac{\Delta E}{\Delta t} \approx \rho c_p \Delta T \frac{\Delta V}{\Delta t} = \rho c_p \delta (T_{ad} - T_{ig}) \frac{A_E}{\tau_{total}} \quad (6.4)$$

$$\frac{\left(\frac{\Delta E}{\Delta t}\right)_1 - \left(\frac{\Delta E}{\Delta t}\right)_o}{\left(\frac{\Delta E}{\Delta t}\right)_o} = \frac{\rho c_p \delta (T_{ad} - T_{ig}) \frac{A_E}{\tau_{total}}}{\rho c_p \delta (T_{ad} - T_{ig}) \frac{A_o}{\tau_{total}}} - 1 = \frac{A_E}{A_o} - 1 \quad (6.5)$$

The energy release of the composite is directly related to the cross-sectional burned area, A_E , of energetic material assuming that the propagation behavior is

relatively invariant along the thickness of the composite. The rods are incorporated to enhance pre-heating of material ahead of the main flame front. As such, analysis of flame propagation is assessed based on the degree of pre-heating, total area burned, and energetic material burned after the primary ignition transient. The pre-heated zone and total area burned are defined as the accumulation of temperature nodes which exceed 500 K and the ignition temperature (900 K), respectively. Given that the rods are non-energetic, the area of burned energetic material is simply a subset of the total area burned. An illustration, shown in Figure 6.3a, outlines each area type of interest with the distribution of rods superimposed.

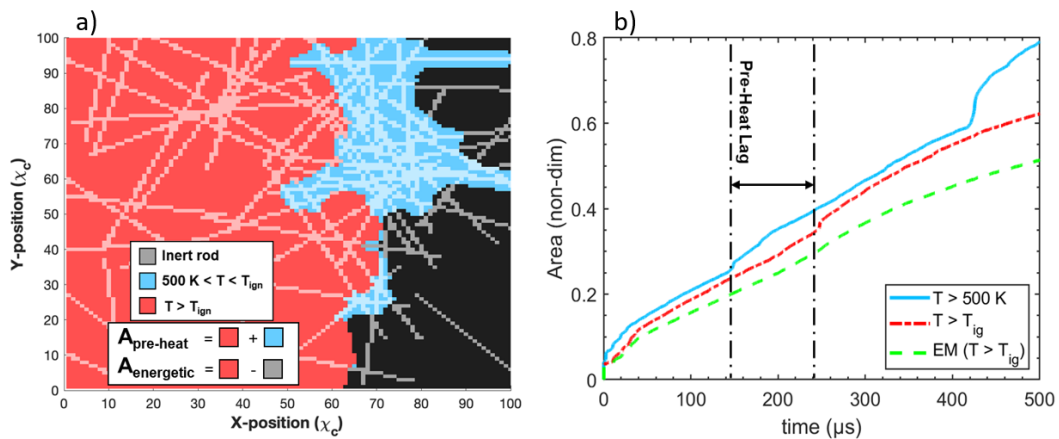


Figure 6.3: a) Flame front snapshot and b) time resolved behavior of the accumulated area of the pre-heated zone, total burned material, and burned energetic material for the case of AR=55, Vol.%=20, $t=480 \mu\text{s}$ (left to right propagation).

As suggested, the pre-heated area is always larger than the accumulated total area burned and the burned energetic material area. One can see from the snapshot of the pre-heated zone in Figure 6.3a that the heat preferentially flows along the direction of the rods, ahead of the outlined total area ($T > T_{ign}$). The time-resolved graph in Figure 6.3b depicts sudden jumps in the pre-heated area which corresponds to sudden increases in material conductivity due to local packing of the rods. These sudden

changes are mirrored by the total area burned after a lag time corresponding to the time necessary for heat to diffuse outward from the rods to initiate chemistry.

6.3.1.1 Flame Propagation and Energy Release Rates

Dimensionless comparisons of combustion performance between systems of various aspect ratios and volume percentages of rods are made in Figure 6.4 by plotting the percentage change in the total area burned, $\frac{A_{total}}{A_0} - 1$, and energy released relative to a composite with no rods added. Additionally, the ratio of accumulated pre-heated area relative to the total area burned is calculated to quantify how the role of pre-heating correlates to propagation behavior.

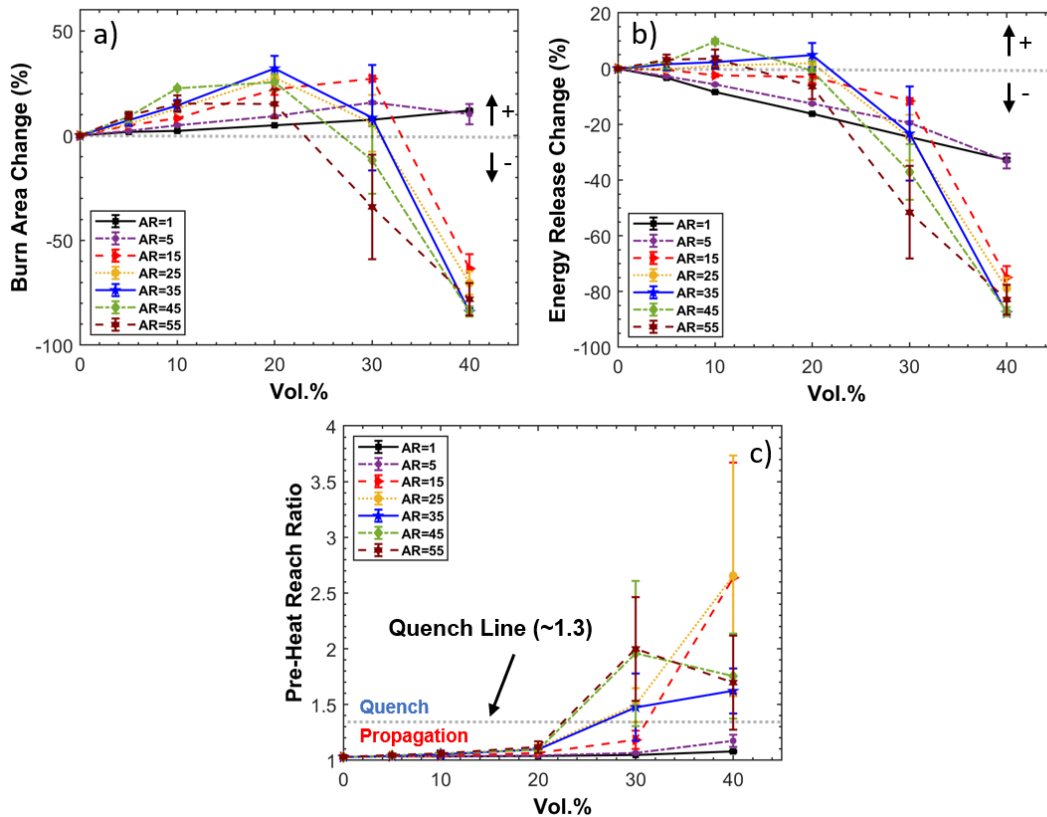


Figure 6.4: Effect of aspect ratio and vol.% of rods with a fixed thermal conductivity on a) the change in total area burned, b) energy released over the allotted burn time, and c) the extent of pre-heating during flame propagation.

The total area burned acts as surrogate for the flame propagation rate (Figure 6.4a) where it can be seen that the total area burned is enhanced by up to 25% for most rod aspect ratios up to ≈ 30 vol.%. Interestingly, the region of maximum enhancement between 10 and 30 vol.% appears to correlate to the range of volume percentages for which previous studies using carbon-based fillers (*e.g.* graphite, carbon nanotubes, carbon fibers) have experimentally observed the much-debated thermal percolation behavior.^{194,196,204,206} However, further increases to the vol.% of added rods results in a steep regression in total burned area as a result of reduced vol.% of energetic material. Increasing the aspect ratio of rods appears to enhance the total area burned and results in the onset of regressive behavior at lower vol.% due to further isolation of energetic material regions.

The energy release of the system in Figure 6.4b mirrors that of Figure 6.4a in terms of the general behavior with respect to vol.%. However, the energy released has a maximum enhancement of $\approx 10\%$ and a clear shift in the vol.% region which constitutes a positive enhancement. The 20 vol.% threshold marks the point in most of the ARs studied where replacing energetic material with thermally conductivity materials is no longer beneficial for energy release. The addition of thermally conductivity materials is also not guaranteed to be beneficial with the lower half of ARs tested ($AR < 25$) resulting in either negligible enhancements or reductions in energy release for vol.%=5, 10.

It appears that positive energy enhancement occurs for larger ARs and a range of low volume percentages (≈ 5 -10 vol.%). There also seems to be a threshold where

increases in AR no longer increase energy release rates. In Figure 6.4a-b, the trend of increasing aspect ratio with increased energy release and total area burned regresses once the aspect ratio is increased to AR=55. When evaluating even larger aspect ratio fillers, it becomes clear that the specific orientation of the rods becomes more important at lower vol.% since the likelihood of the rods pointing in a direction conducive for flame propagation diminishes. This behavior manifests itself in both the diminished enhancement to the total area burned and energy release as well as the standard error. As a result, there must exist a unique domain of volume percentages and aspect ratios for which the energy release rate and propagation rate are maximized for different energetic systems with randomly oriented rods of a specific thermal conductivity.

Combustion experiments studying directly biased thermally conductive pathways in energetic materials are limited in scope, but have shown to significantly enhance the effective thermal conductivity in two-phase systems.^{205,209} Modeling flame propagation using directionally manipulated rods is reserved for future works.

6.3.1.2 Pre-Heating of the Flame Front

The largest magnitude in the standard error for quantified values occurs at 30 vol.% in Figure 6.4a-b. This large error indicates a “do or die” region where there is nearly equal probability for flame propagation to either proceed or to quench. This behavior is linked to the competition between pre-heating which assists propagation and pre-heating which leeches the heat needed to sustain self-propagation. The precise behavior of pre-heating is likely dependent on specific thermochemical properties, but

the values of the ratio of the pre-heated area ($T > 500 K$) to the total area burned ($T > T_{ig}$) can offer insight.

The representative pre-heat ratio for a single propagation run is determined by calculating the ratio at each time step and averaging the values over the last two-thirds of the total time steps. This is done to neglect the transient behavior of the initial heating process and effects due to propagation which nears the boundary of the material (Figure S6.4). Figure 6.4c shows the reach of pre-heating increases as the vol.% increases for vol.% up to 30%. Additionally, both the values of the pre-heat ratio and the corresponding standard error at 30 vol.% clearly increases at higher aspect ratios. Increases in standard error and the pre-heat ratio express competing trends in which increases in aspect ratios may lead to propagation rate enhancements, but also may lead to increased likelihood of quenching. This trend breaks down at 40 vol.% since it is nearly assured that higher aspect ratios will quench before establishing a self-propagating flame front.

One may roughly define a “quench line” as a threshold pre-heat value for which the probability of propagation quenching meets or exceeds the probability of sustained flame propagation. The exact position of this line is not precise but can be estimated based on the sensitivity of the standard error with respect to the collective aspect ratios as the pre-heat ratio value increases. This pre-heat ratio value of the quench line was found to be ≈ 1.3 and corresponds to an accumulated pre-heat area which is roughly 30% larger than the accumulated total area burned.

6.3.2 Role of Rod Thermal Conductivity in Flame Propagation

Inert rods are integrated into the energetic material to take advantage of their thermally conductive properties. I analyzed the role of the thermal conductivity of rods with a constant aspect ratio (AR=45) on the total area burned and energy released over the total combustion time. Each volume percentage (vol.%=5, 10, 20) uses the same material mapping with varied rod thermal conductivity to focus on how the thermal conductivity, specifically, effects the total area burned and energy released. Figure 6.5 shows how the combustion behavior changes at different volume percentages as the thermal conductivity of the rods is varied by 5 orders of magnitude relative to the energetic material ($\frac{k}{k_o} = 1, 10, 10^2, 10^3, 10^4, 10^5$). An example of the flame behavior with varied rod thermal conductivity at 20 vol.% is rendered in the thermal mappings displayed in Figure 6.6.

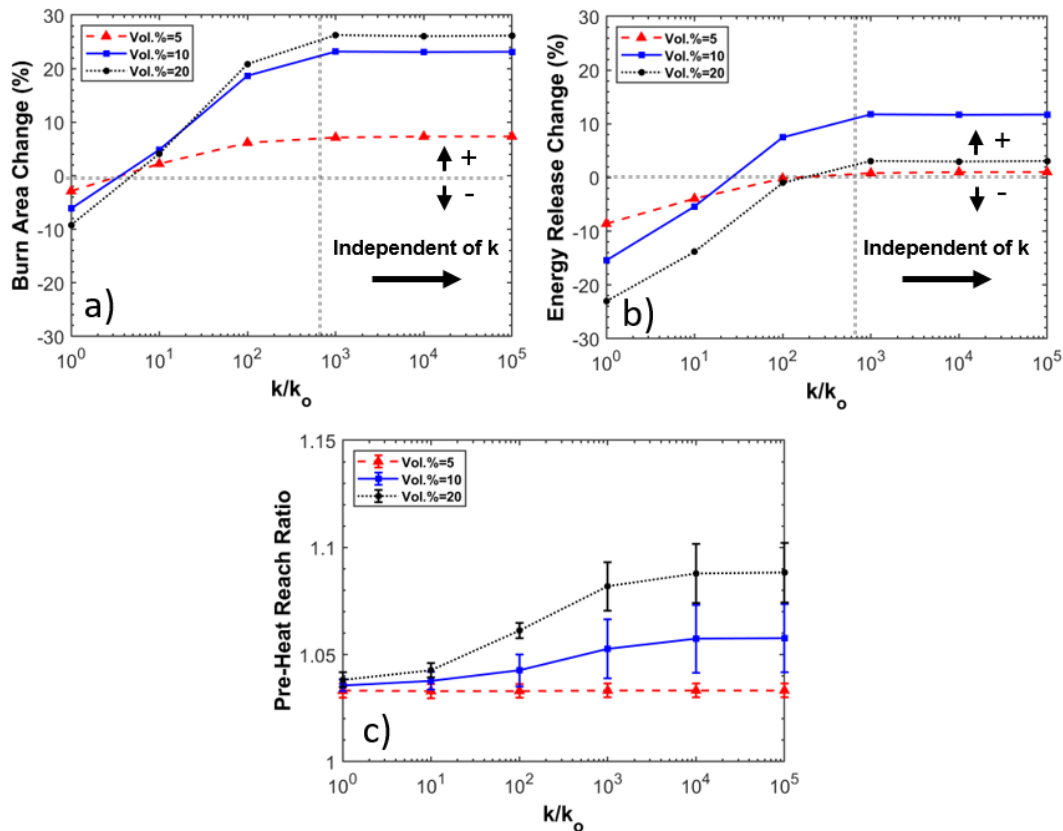


Figure 6.5: Effect of thermal conductivity and vol.% of rods with an aspect ratio (AR=45) on a) the change in total area burned, b) energy released over the allotted burn time, and c) the extent of pre-heating during flame propagation.

I once again observe that, while the total area burned is maximized for 20 vol.% rods, the energy release is maximized for 10 vol.% of rods. The extent of pre-heating is greatest at higher volume percentage and higher thermal conductivity. The standard error of the pre-heat ratio is calculated with respect to its fluctuations as a function of time (Figure S6.4) and is shown to increase with higher rod thermal conductivity. Although none of the parameters chosen resulted in quenching of the flame front, it can be inferred that higher thermal conductivity would result in an increased probability of quenching at higher vol. %. What is most interesting, however, is that all calculated values in Figure 6.5 reach a point where their behavior becomes effectively

independent of the thermal conductivity of the filler. With our chosen parameters, this thermal conductivity threshold occurs around $\frac{k}{k_o} = 10^3$. The thermal mapping of the flame front in Figure 6.6 illustrates how little total area burned is gained between 10^2 and 10^5 . Considering these findings, the search for sophisticated materials with exceeding large thermal conductivities may appear moot for this application.

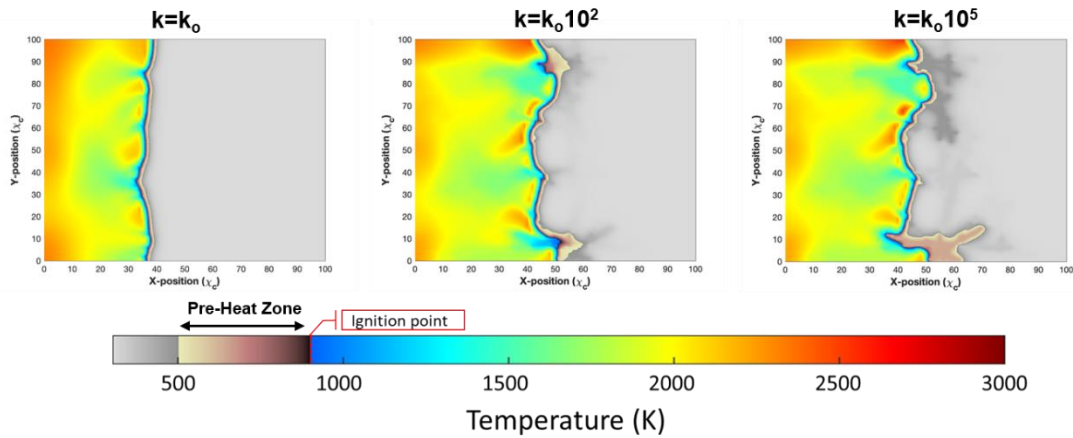


Figure 6.6: Thermal mapping of energetic material propagation integrating rods with varied thermal conductivities within an invariant AR=45 rod mapping of 20 vol.% at $t=325 \mu\text{s}$ (Propagation from left to right).

The thermal conductivity independent regime may manifest as due to the effective thermal conductivity at boundaries between nodes with different materials. As mentioned in section 6.2, the effective thermal conductivity is calculated based on the equivalent thermal resistance to heat flow across a boundary of discrete material domains (Equation 6.2).¹⁹⁸ While the effective thermal conductivity across the boundary for adjacent similar materials is equal to the bulk thermal conductivity, the effective thermal conductivity across boundaries of dissimilar materials can potentially be several orders of magnitude smaller. When the additive thermal conductivity is much larger than the thermal conductivity of the energetic material ($k \gg k_o$), it

becomes clear that there is an asymptotic behavior of the amount of heat which is able to flow across the boundary as rod thermal conductivity increases. The limiting step of flame propagation becomes reliant on the thermal conductivity of the energetic material itself.

6.4 Conclusion

In this study, a 2D finite element model is employed to evaluate the role of thermally conductive, high aspect ratio additives on propagation behavior in condensed phase energetic composites. Increases in the total area burned and energy released was observed when the connectivity of thermally conductive rods throughout the composites is optimized at minimal volume percentages ($AR > 25$, $vol.\% < 20$). In cases where the aspect ratio was too low ($AR < 25$) or additive $vol.\%$ was too high ($> 20 vol.\%$), the additive either offered no enhancement due to heat transfer limitations or quenched flame propagation through excessive heat transfer to non-energetic regions. Enhancements were reduced at aspect ratios which were too high, inferring the increased importance for rod orientation. Independently varied rod thermal conductivity for the same additive distribution led to increased enhancements in total area burned and energy release up to some critical thermal conductivity where enhancements to flame propagation performance no longer depended on the thermal conductivity of the additive. Such behavior appears to originate from limitations in heat transfer introduced by boundary resistances between material types. This study serves as a proof-of-concept for a method to enhance energy release by increasing heat transfer with additives in a manner that could be readily incorporated into the energetic composite manufacturing process.

Chapter 7: Spatially focused microwave ignition of metallized energetic materials[§]

Summary:

This study investigates the ability to locally ignite metallized propellants via microwave absorption. Metallized energetic composite films incorporating high mass loadings of aluminum and titanium nanoparticle fuels within a polyvinylidene fluoride (PVDF) polymer matrix were constructed by direct-write additive manufacturing (3D printing). Simulations of power absorption for both Ti and Al nanoparticles reveal that the passivating shell composition likely plays a significant role in the observed ignition phenomenon. Various architectures of interest were constructed for predictable microwave ignition and propellant propagation. It was found that, although aluminum nanoparticles and composites do not ignite via exposure to microwaves, titanium nanoparticles can be used as efficient reactive microwave susceptors enabling a localized ignition source. This approach enables various architectures of previously studied high energy Al/PVDF systems to be fabricated and outfitted with a microwave-sensitive titanium composite in strategic locations as a means of remote ignition for aluminum systems.

7.1 Introduction

Nanoenergetic materials are a class of exothermic heterogeneous solid mixtures with common applications in propellants, ignitors, and pyrotechnics. Nanoenergetics

[§] The results presented in this chapter have been previously published and are reprinted with permission from: Dylan J. Kline, Miles C. Rehwoldt, Charles J. Turner, Prithwish Biswas, George W. Mulholland, Shannon M. McDonnell, Michael R. Zachariah. *Spatially focused microwave ignition of metallized energetic materials*. Journal of Applied Physics, **2020**, 127 (5), 055901. Copyright AIP Publishing.

seek to enhance reactivity by incorporating nanoscale metallic particles for reduced diffusion length scale between fuel and oxidizer of high combustion enthalpy redox reactions. Although aluminum nanoparticles are the most commonly used nanometal in energetic research studies due to their high reaction enthalpy per gram and low cost, other energetic nanoscale metals such as tantalum²³⁰ and titanium¹²⁰ have also been researched in past studies for their niche physical and chemical properties aside from their theoretical reaction enthalpy. Energetic formulations for propellant applications commonly integrate nanopowder within a polymer binder, which itself may also act as either a fuel, as in the case of traditionally used hydroxylterminated polybutadiene (HTPB),²³¹ or an oxidizer, as in the case of fluorinated polymer binders such as polyvinylidene fluoride (PVDF)⁶³ or Viton.¹⁸⁰ Recent research utilizing metallic formulations of this type have favored a variety of additive manufacturing techniques such as layer-by-layer deposition¹⁰⁸ and stereolithography¹¹¹ over traditional casting methods for the prospect of fast prototyping of highly customizable architectures with tunable parameters¹⁰¹.

Coupled with efforts for enhanced customization of 3D printed propellants, research has been devoted to probing the ability to throttle both combustion and ignition behavior of propellants remotely by irradiating energetic materials with microwave energy (MW energy).^{232,233} Microwave radiation is defined by the frequency range of 300 MHz–300 GHz and is utilized under low power (≈ 1 mW) for communications and relatively higher power (≈ 1 kW) for dielectric heating of foods.

While the use of microwaves for heating has seen some success in applications for powder ceramic sintering,^{234,235} synthesis of materials,^{236–238} and demonstrating the

initiation of crystalline high explosive monopropellant materials, such as 1,3,5-Trinitro-1,3,5-triazinane (RDX),²³⁹ microwave heating of metals and metal composites has had limited utility. The relatively high electrical conductivity of metals results in optically dense materials with skin depths of a few micrometers at conventional microwave oven frequencies (2.45 GHz). This means that most of the electromagnetic (EM) radiation is reflected at the material surface.^{240,241} Modeling and experimental studies of metal powders demonstrated that a remedy for this problem is to use metallic powders that couple strongly with the magnetic field, as well as having particle diameters that are of the same order of magnitude as the skin depth for that material.^{242–244} Particles that are too large will only heat at the surface, while particles much smaller than the skin depth will absorb only a fraction of the transmitted radiation in the form of heat generated by induced eddy currents as a result of the oscillating magnetic field.^{242–244} As such, many experimental studies focusing on the heating of metal particles often utilize micrometer size powders that may also contain magnetic materials such as iron, cobalt, or nickel.^{236,244–246}

Although sintering of powders of magnetic metals as a result of microwave heating has been realized, these magnetic materials have poor energetic performance and often take several minutes (10–30 min) to sinter.^{235,236} Additionally, the enhancement of microwave absorption of size optimized aluminum particles (~3–4 μm) showed that the temperature to which the aluminum powder reaches from microwave irradiation is not enough to ignite the sample.²⁴² A follow-on study by Crane et al. looking at microwave heating of aluminum–iron oxide thermites demonstrated that the addition of microwave susceptors at ~10 weight percent (wt. %),

in the form of carbon-based materials, will enhance heating by microwave irradiation.^{247–249} However, this same study concluded that, while there was an enhancement of maximum temperature reached, the maximum reach of heating still fell short of the ignition threshold while also hindering reactivity and flame propagation speeds of samples ignited by other means. Meir and Jerby have been successful at igniting micrometer sized aluminum–iron(II,III) oxide (magnetite) thermites within several seconds using a low power (~100 W), localized solid-state microwave-drill for enhanced microwave coupling and confined heating.²⁴⁶ This approach has shown to be successful for this specific system; however, it is unclear whether this method will work for nanoscale systems with oxidizers that may not be magnetically sensitive.

This study investigates the ability to rapidly initiate energetically relevant metallized nanoscale compositions via efficient microwave coupling, while maintaining a high overall energy density, reactivity, and combustion performance. Preliminary microwave heating tests of prospective fuels in air showed that both micropowder and nanopowder aluminum did not demonstrate thermal ignition as a result of microwave heating. However, nanopowder titanium did demonstrate thermal ignition despite the aforementioned difficulties of using nanoscale nonmagnetic metals in microwave heating.^{243,244} As a result of this initial finding, this study analyzes this behavior more in depth and employs the use of additive manufacturing techniques in order to design composition architectures that retrofit previously studied propellants with microwave-sensitive nanoscale titanium compositions to realize spatially localized microwave-ignitable propellants. This work also sets the stage for the

fabrication of tailorable composite propellants that can be precisely and remotely ignited or staged by excitation of microwave-sensitive regions.

7.2 Methods/Experimental

7.2.1 Mie Theory Calculations

Calculations of the absorbed microwave intensity by an ensemble of metal nanoparticles were modeled using the Mie theory, which considered both bare metal spherical nanoparticles and metal nanoparticles with an oxide shell. It has been assumed that the microwave needle antenna uniformly irradiates a circular area of 25 μm diameter on the sample surface with electromagnetic power deliverance of 15 W at a frequency of 2.45 GHz (discussed in Sec. 7.2.5.). The absorption cross section, σ_A , for the bare metal particles and the coated metal particles is computed using BHMIE and BHCOAT subroutines, respectively.²⁵⁰ Due to the lack of studies regarding core-shell nanoparticle microwave absorption, a more detailed study of the mechanism of microwave absorption of core-shell systems has been performed in tandem with this article by Biswas et al., which has been generalized for a wider variety of materials.²⁵¹ The findings of this work, with respect to microwave heating of core-shell nanoparticles, are applied to the materials in question and discussed in Sec. 7.3.1.

7.2.2 Materials

Candidate materials studied in this project were determined based on three criteria: (1) high energy density nanoparticles, (2) the ability to act as an effective fuel for combustion, and (3) commercial availability with respect to cost. To meet the demands for high energy density, metallic nanoparticles were of primary interest due

to their significant transient energy release during oxidation in comparison to other potential fuels (such as carbon). Aluminum and titanium were metal fuels of primary consideration for reasons that are discussed in Sec. 7.3.1.

Aluminum nanoparticle powder (nAl) (~80 nm diameter and ~80% active by mass) used in this study was purchased from Novacentrix, and titanium nanoparticle powder (nTi) (30–50 nm diameter and ~70% active by mass) was purchased from U.S. Research Materials, Inc. Titanium and aluminum nanometals are depicted in Figure 7.1 and are identical to those used in Chapters 3 & 4, respectively. Nanometals were used as received with the active content (unoxidized metal content) of the nanoparticle core-shell structure determined using thermogravimetric analysis (TGA) from previous studies.^{67,120}

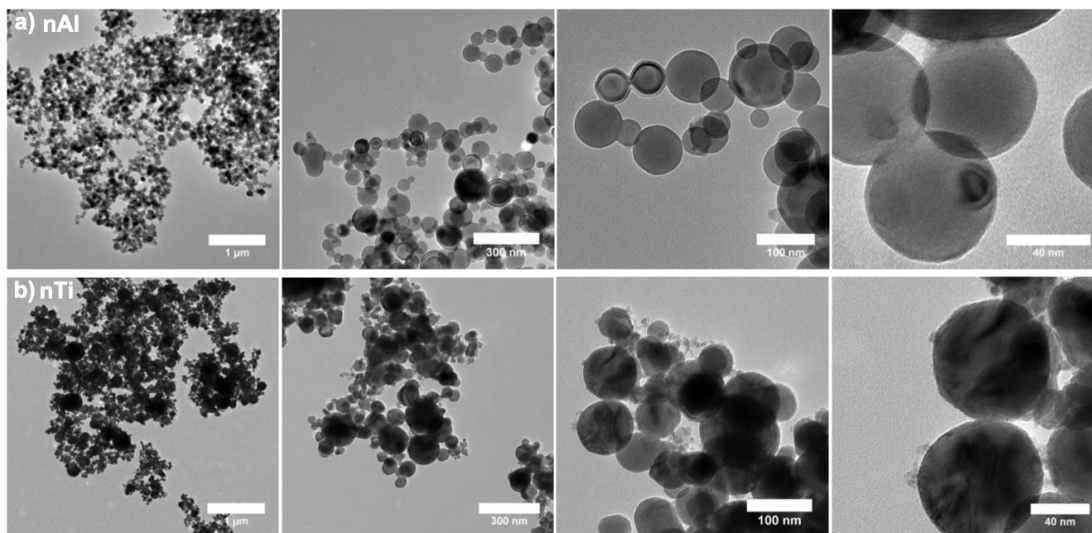


Figure 7.1: Transmission electron microscopy images of the as-received (a) nano-Aluminum (Novacentrix) and (b) nano-Titanium (US Research Materials). Images taken with a FEI Tecnai12

Two different nominal sizes of micrometer aluminum powder, 3–4.5 μm (Figure 7.2a) and 10–14 μm (Figure 7.2b) in diameter, were purchased from Alfa Aesar

and tested as received for preliminarily microwave absorption experiments. Poly(vinylidene fluoride) powder (PVDF, molecular weight = 534 000 g/mol) was purchased from Sigma Aldrich (Millipore Sigma), and N, N-dimethylformamide (DMF 99.8%) solvent was purchased from BDH chemicals. All chemicals were used as received.

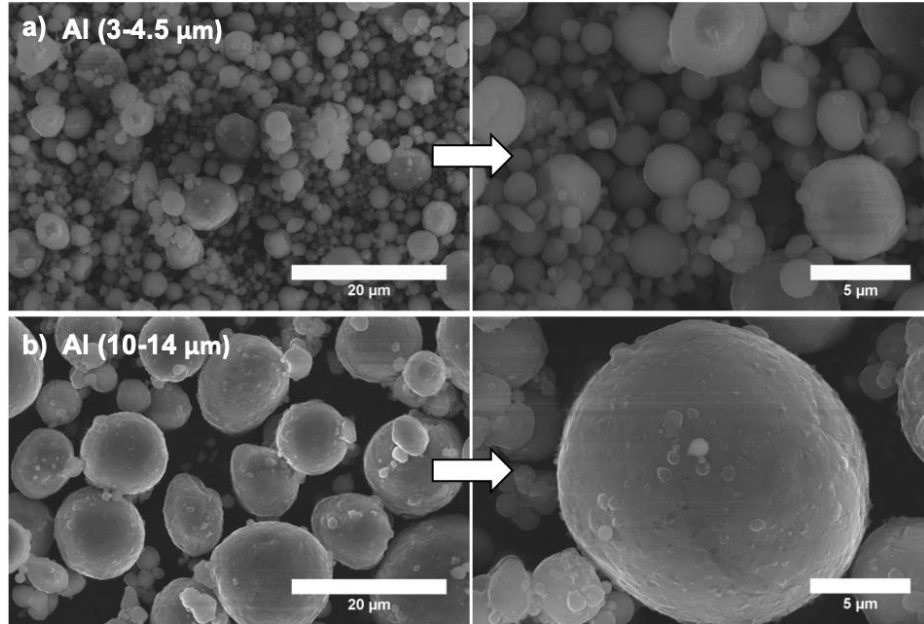


Figure 7.2: Scanning electron microscopy images of the cross-section for as-received (a) 3-4.5μm diameter Al micron particles (Alfa Aesar) and (b) 10-14μm diameter Al micron particles (Alfa Aesar). Images taken with a FEI NNS450

7.2.3 Film fabrication

Energetic composites were fabricated in the same manner as those in Chapter 4 using a System 30M pressure-driven 3D printer purchased from Hyrel 3D. An energetic precursor is utilized as a 3D printable ink in a direct-write, layer-by-layer additive manufacturing approach to create customized multi-composite architectures with distinct ignition and propagation zones along the structure of the propellant. Each

precursor 3D printable ink considered was formulated by dissolving a constant 70 mg/ml PVDF in DMF and adding various mass loadings of metal content in a similar way to past studies of such materials.^{72,180}

Individual mixtures and particle loadings are listed in Table 7.1 where the specific loadings of fuel and oxidizer are formulated with various equivalence ratios, Φ , for one or more of the following reasons: stoichiometric conditions⁶⁷ for maximized energy output, ease of printability, enhanced propagation speed, and the optimization for microwave ignition sensitivity.

Table 7.1: Energetic precursor formulations.

Fuel Type (wt.%)	PVDF (wt.%)	Equivalence Ratio (Φ)
Al: 25	75	1
Al: 65	35	5.3
Ti: 35	65	1
Ti: 50	50	1.9
Ti: 65	35	3.5

Precursor suspensions are sonicated for 1 h for each component added and then stirred for 24 h using a magnetic stir plate/bar. The additive manufacturing technique is solvent-based and relies on the evaporation of DMF, which was aided by maintaining the print bed at 70 °C. The drying process is controlled by the temperature of the printing bed, the speed and extrusion rate of the print, and solvent exhaust venting. Dry times were on the order of 15–30 s after deposition with the resulting four-layer film thickness generally being 30–40 μm (7–10 $\mu\text{m}/\text{layer}$). Figure 7.3 depicts magnified cross section images of homogeneously mixed Al/PVDF and Ti/PVDF samples printed with four layers at $\sim 8 \mu\text{m}/\text{layer}$.

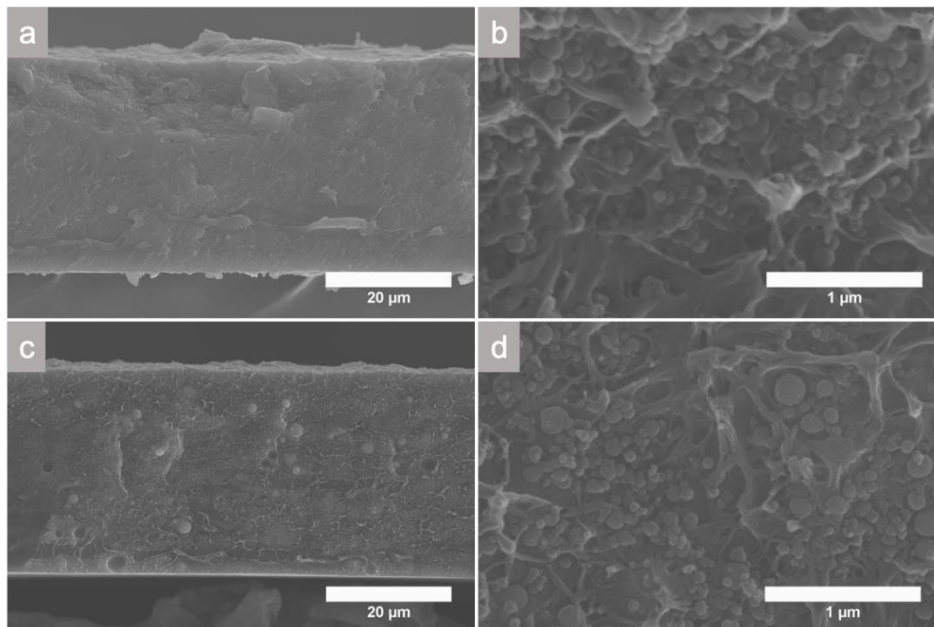


Figure 7.3: Scanning electron microscopy images of the cross-section for (a-b) Al/PVDF and (c-d) Ti/PVDF films. Each printed sample is 4 layers thick. Images taken with FEI NNS450.

A minimum of four layers of printed material are required to effectively remove the samples from the printing surface. Films for flame speed and ignition tests are printed in rectangular sheets from which multiple free-standing thin strands (1 mm \times 2 cm) may be harvested. More complex architectures are printed using multiple printing codes (Appendix B) designated for specific formulations, which work in tandem to complete the final multicomponent architecture. Multicomponent architecture prints have layers of different formulations printed directly on top of a previous layer in a partial-layering scheme.

7.2.4 Burn rate characterization

Combustion performance of printed energetics was evaluated using 1 mm-wide energetic strands that were cut from larger printed sheets and burned in a controlled atmosphere. As previously discussed in Chapter 4 and shown in Figure S4.1, the strands are loaded into a glass cylinder closed off with rubber stoppers that have gas inlets and electrodes. The strands are mounted between two braided nichrome wires and anchored at the opposite end with double-sided tape. Strands are ignited by resistively heating the nichrome wire and the combustion event was recorded using a high-speed camera (Phantom Miro M110) recording at 10 000 frames/s. The burn rate is calculated by tracking the pixel coordinates of the flame front as a function of time and considering the pixel/distance ratio determined from the precisely spaced metal plates in the foreground of the video.

Burn rate experiments for all samples were performed in both air and argon environments to reduce the dependence of oxygen on the observed ignition and propagation characteristics. Anaerobic combustion tests used argon (Airgas 99%) to purge the glass tube for ~5 min followed by the simultaneous closure of the inlet/outlet prior to the ignition event.

7.2.5 Focused microwave ignition

To precisely localize the ignition of the microwave-sensitive energetic composites, a needle-based, coaxial microwave emitter was designed and suspended over the printed films.²⁴⁶ A critical characteristic of this design is the ability to concentrate microwave energy into an area much smaller than the chosen wavelength.

In this configuration, a solid-state power amplifier (AMCOM AM206545SF-3H) with a peak gain of 32 dB drives a 2.45 GHz, 10 dBm continuous wave tone from a microwave signal generator (DS Instruments SG12000). This brings the peak power output of the device to approximately 42 dBm, or 15 W (see Figure 7.4). A coaxial-solder pin adapter was soldered to a nickel-plated straight pin (Singer 0.025 in. diameter). The printed film sample sits on a glass slide, and the slide is positioned over a grounded surface. A simulation of the electric fields through Ansys HFSS illustrates that the field intensity (~ 100 kV/m) is most concentrated between the pin and ground plane with the sample in its path. This field is an order of magnitude lower than the dielectric breakdown point of air at 1 atm (~ 3000 kV/m) and does not result in electrostatic discharge (ESD) events.

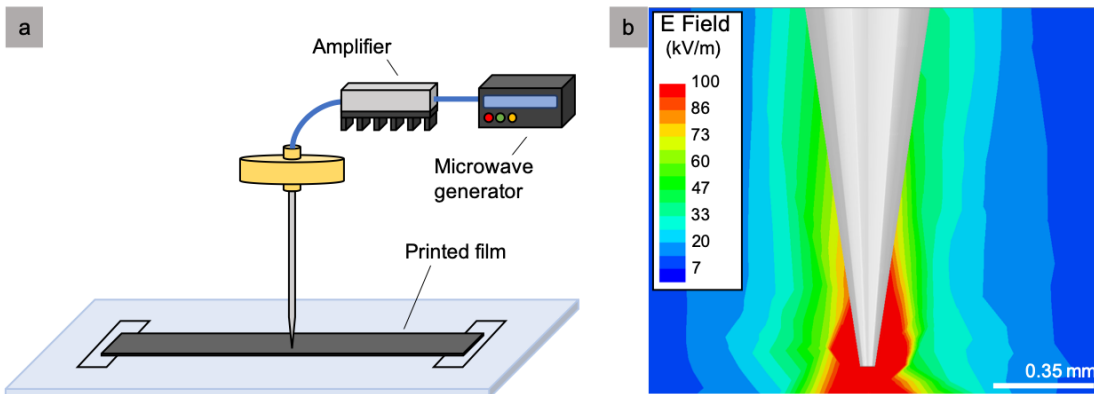


Figure 7.4: (a) Needle-based microwave ignition experiment at 2.45 GHz. Peak power of the entire system is ≈ 15 W. (b) Simulations of the electric field at the tip of the needle for a frequency of 2.45 GHz (using Ansys HFSS and an auto-generated mesh).

Since the working distance from the emitter to the sample is much smaller than the operating wavelength, sample exposure is in the “near-field” of the electromagnetic (EM) field, implying there will be some coupling between the sample and the antenna. Concentrating microwave radiation in the far-field down to a point would require a

large antenna design and sample size but would result in the same phenomenon and observations presented here.

Combustion events of the needle-based microwave ignition experiments were observed using a high-speed camera (Phantom Miro M110), which was triggered simultaneously with the power input to the microwave amplifier. Samples tested in argon with the microwave needle assembly were placed inside a glass tube with gas inlets. A small sample of the material was placed inside the tube, the tube was purged with argon, and the needle was then placed through an opening in the tube to access the interior for sample heating. Videos recorded used the same high-speed camera as was used in the other experiments described.

7.3 Results and Discussion

7.3.1 Microwave absorption of metals and material selection

Efficiency of microwave heating is closely related to material properties such as the electrical conductivity (σ), permittivity (ϵ), and permeability (μ) when interacting with electromagnetic radiation of a certain frequency (ω). As such, the total averaged power dissipated (P_d) within a material is linked to these properties in their ability to couple with the electric field (E) and magnetic field (H) of the incident electromagnetic radiation. A steady-state electromagnetic energy balance between the energy flux delivered by the microwave to the surface of the material, described by the Poynting vector, and the time averaged energy dissipated per unit volume yield equation 7.1.

^{241,250} The permittivity, $\epsilon = \epsilon_o(\epsilon'_r - j\epsilon''_r)$, and permeability, $\mu = \mu_o(\mu'_r - j\mu''_r)$, are generally complex with the real parts representing a measure of energy storage from

the EM wave within the material and the imaginary part representing the energy dissipated within the material,²⁴⁰

$$P_d = \frac{1}{2}\sigma|E|^2 + \frac{1}{2}\omega\varepsilon_o\varepsilon_r''|E|^2 + \frac{1}{2}\omega\mu_o\mu_r''|H|^2 \quad (7.1)$$

Each term on the right side of equation 7.1 represents, from left to right, the conduction, dielectric, and magnetic heat losses, respectively, where the solution to the electric and magnetic field throughout the volume of the material may be solved by using the Maxwell equations for materials.^{241,250} The general form of this solution is a traveling plane wave with an exponential attenuation factor to represent the loss of energy of the incident radiation. The characteristic attenuation factor is related to what is colloquially known as the skin depth of a material and represents the length scale to which incident electromagnetic radiation may penetrate a material to efficiently heat.^{241,243,250} The skin depth is dependent on the frequency of the incident electromagnetic radiation and the electrical conductivity of the material. Metals generally have a skin depth on the order of a few micrometers where the optimal size of particles for absorption of microwave energy is of the same order of magnitude as the skin depth.^{243,244} Based on this information, and the previous findings mentioned in Sec. 7.1, working with nanometals should be intrinsically difficult given that nanoparticles have diameters that are two orders of magnitude smaller than the skin depth.

Having set the candidate criteria (as discussed in Sec. 7.2), this study began by studying the most-widely used metal fuel—aluminum. Aluminum-based energetics are well-studied in the literature and incorporation into a polymer [particularly poly(vinylidene fluoride), PVDF] has proven successful in making solid propellants

that can be readily manufactured.^{63,180} Unfortunately, the initial investigations into microwave heating of Al proved unsuccessful, which led to considerations of using a reactive metal as an initiator for aluminum-based composites. As this paper will demonstrate, titanium nanoparticles and titanium-based composites proved to be highly successful at igniting via microwave exposure. The reasons for its effectiveness are discussed below.

A comparison of microwave power absorption by ensembles of aluminum and titanium nanoparticles in an inert medium was conducted using the Mie theory.^{250,251} The intensity fraction absorbed is given by equation 7.2 where I_{abs} is the absorbed intensity, I_0 is the incident intensity, σ_A is the absorption cross section, N is the number density of particles, and d is the path length (as characterized by the layer).²⁵² Equation 7.2 is derived from the Beer–Lambert law, which is a valid assumption since the scattered radiation is small given that the particle size is much smaller than the wavelength of light and the scattered radiation from other particles would not interact.

$$\frac{I_{abs}}{I_0} = 1 - e^{-\sigma_A N d} \quad (7.2)$$

The effective relative complex permittivity for Ti and Al were estimated using the Drude model approximation for metals at relatively low frequencies ($\tilde{\epsilon}_r \approx \tilde{\epsilon}_r' - j \frac{\sigma}{\omega \epsilon_0}$).^{241,250,253} For an operating frequency of 2.45 GHz, the approximate effective relative permittivity is dominated by the analogous effective imaginary loss term, $\tilde{\epsilon}_r''$, which in general would directly result in both the Joule heating and dielectric loss terms in equation 7.1.^{244,253} However, the approximation of highly conductive particles results in the Joule heating term being the dominant term. Finally, since both metals

are nonmagnetic, the magnetic permeability for all materials is assumed to be 1. Calculated values for all aforementioned constants can be seen in Table 7.2.^{240,244,254,255}

Table 7.2: Complex dielectric constant and complex magnetic constants used in calculations to estimate the intensity fraction absorbed and the maximum temperature.

<i>Material</i>	$\widetilde{\epsilon}_r'$	$\widetilde{\epsilon}_r''$	μ'	μ''	<i>Source</i>
<i>Al</i>	0	2.5×10^8	1	0	²⁴⁴ , Azo Materials
<i>Al₂O₃ (amorphous)</i>	9.8	1×10^6	1	0	²⁴⁰
<i>Ti</i>	0	1.3×10^7	1	0	²⁴⁴ , Azo Materials
<i>TiO₂ (amorphous)</i>	33	10.4	1	0	²⁵⁵
<i>TiN</i>	15	4.2	1	0	²⁵⁴

Figure 7.5a shows the resulting Mie theory fractional microwave extinction as a function of layer thickness of a composite comprised of 80 nm metal particles. Most interesting is that, even though as-received core-shell nTi is an effective microwave absorber relative to core-shell Al in the experiment (discussed in Sec. 7.3.2.), the Mie calculation indicates otherwise for bare particles.

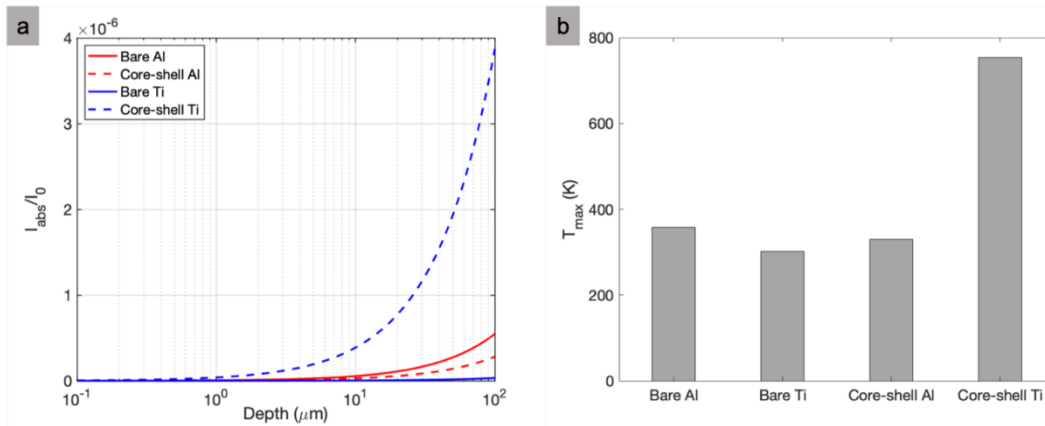


Figure 7.5: (a) Calculated fraction of microwave (2.45 GHz) intensity absorbed for bare and core-shell Al and Ti nanoparticles in a 25 μm diameter cylinder as a function of depth and (b) the estimated maximum temperature after being exposed to a microwave input of 15 W for 0.5 s. Physical properties used in calculation are provided in Table 7.2.

When one considers nanoparticles, a nontrivial fraction of the mass is concentrated in the passivating shell. The shell composition of core-shell nanoparticles may be characterized by a combination of x-ray photoelectron spectroscopy (XPS) and

x-ray diffraction (XRD). Aluminum naturally forms a 2–10 nm amorphous passivating oxide (Al_2O_3) shell that can dramatically impact combustion performance and material properties at small particle sizes.^{61,256} Titanium nanoparticles readily acquire a shell of similar thickness, but instead demonstrate, from XPS, mixed molar compositions of TiN (~20% by number) and TiO_2 (~80% by number) when exposed to air.¹²⁰ Considering this difference in the shell composition, previous studies regarding the microwave sensitivity of metals by other groups may have failed to consider the impact that the passivating shell may have on the interaction of the electromagnetic field with the internal pure metal content.²⁴³

Figure 7.5a shows the calculated absorbed microwave (2.45 GHz) intensity for the passivated Al and Ti nanoparticles where the inclusion of the shell significantly impacts the estimated absorbed intensity. Although bare Al nanoparticles are expected to absorb more power than similarly sized Ti particles, the inclusion of nTi passivating shell increases the intensity absorbed by an order of magnitude over the Al equivalent. This suggests that the shell must play a significant role in the heating of metal particles. The transparency of Al_2O_3 does not enhance the absorbed fraction of the metal nanoparticles,²⁴⁰ while the material properties of TiN and TiO_2 increase the power fraction absorbed of the otherwise inferior microwave absorbing bare Ti particles.²⁵¹

The material properties alone do not explain why aluminum nanoparticles are so drastically inefficient at coupling with microwaves compared to Ti nanoparticles since both particle types are exposed to the same method of heating. Models considering bare metal particles suggest that heating is dominated by induced eddy currents from the magnetic field.^{243,244} However, even micrometer sized aluminum

particles cannot be efficiently heated. As particles are reduced to the nanoscale, the magnetic contribution drastically diminishes, further ruling out any significant heating from microwave absorption. Concurrent work by the Zachariah research group expanding the system to a core–shell system has shown, from the Mie theory approach, that the behavior of the previous models is recaptured. Additionally, this model shows that the core–shell structure at these length scales, in combination with the material properties of the core–shell, can significantly enhance the dissipation of power through the electric field of the microwave to several orders of magnitude higher than the magnetic field contribution when at its peak.²⁵¹

The maximum achievable temperature of the coated and bare metal particles was estimated using the calculated power fraction absorbed, the thermophysical properties of the contents (heat capacities retrieved from the NIST WebBook and averaged over the core–shell system on a mass basis), and assuming a power input of 15 W for 0.5 s over a circular area with a ~ 25 μm diameter. The particles are assumed to be perfectly insulated with volumetric heating throughout the entire particle, therefore these results would represent the upper bound of the temperature reach over the 0.5 s heating interval. When accounting for the passivating shell on the Ti and Al particles, the added power absorption contribution by the Ti shell increases the estimated temperature to ≈ 750 K-above the documented ignition temperature of Ti in air (~ 670 K).¹²⁰ The increased power transmission provides more efficient heating of the higher energy density Ti core, leading to thermal ignition.

7.3.2 Microwave sensitivity of metal powders

Potential nanopowder fuels for solid propellant precursor materials were tested in air for sensitivity to microwaves by first observing whether the bare powder would absorb enough microwave energy to be heated to sufficiently high temperatures for ignition. Consistent with the previous literature, aluminum particles were unable to be sufficiently heated with microwaves, independent of the particle size.²⁴² Aluminum particle sizes ranging from 80 nm–14 μm were unable to ignite with microwave energy, reaffirming the poor coupling to the sample and potential hindrance by the oxide shell of Al_2O_3 .²⁵⁷ In contrast to the results for the aluminum particles, titanium nanoparticles subject to the microwave needle assembly demonstrated heating phenomena within several milliseconds of the microwave amplifier being powered (see Figure 7.6a).

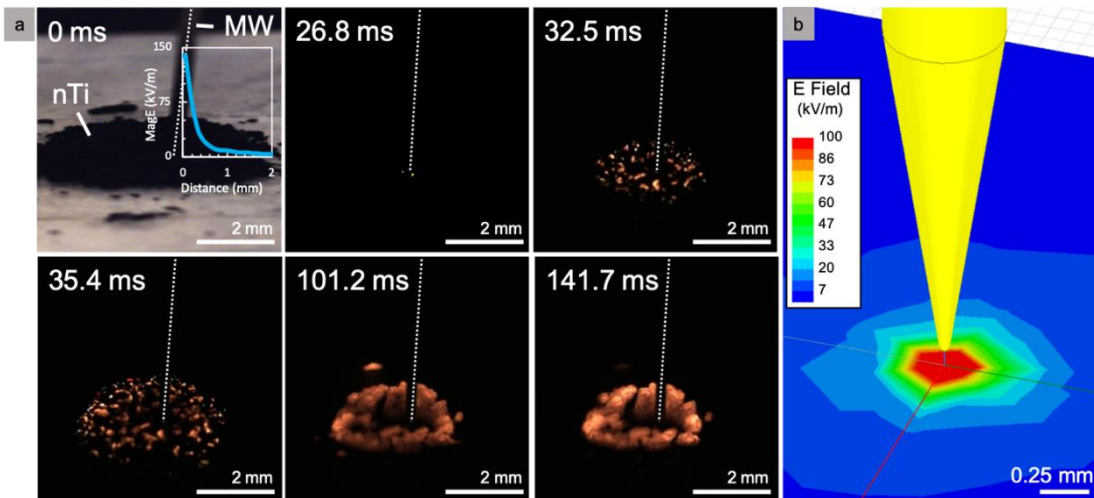


Figure 7.6: (a) Ignition of nano-Ti powder in air (50nm diameter) using microwave needle apparatus imaged using a high-speed camera. $t=0$ defined as starting time for power supplied to the applicator. Dashed white line indicates position of needle. (b) Simulation of the experiments in (a) showing the near field electric field on the ground plane performed using Ansys HFSS and an auto-generated mesh.

The heating event appears to originate from a single location that is approximately near the location of the maximum electromagnetic field. The heat is quickly transferred to the surrounding particles from this hotspot as the Ti begins reacting with the O₂ in air until the sample is uniformly heated. One important consideration in these experiments would be the impact of electrostatic discharge (ESD) (arcing) within the spacing between the particles that could transfer enough energy to start the reaction.²³⁷ However, no visible anisotropic discharge events were identifiable for any of the samples tested during the ignition process.

Microwave heating of Ti nanoparticles was also performed in an inert atmosphere in order to demonstrate heating without reactive heat generation. This was done using the microwave needle assembly which was placed into an argon environment using a glass tube with gas inlets and a small opening at the top for microwave needle access. Upon powering the microwave amplifier, the metal powders immediately surrounding the antenna began to heat to glowing temperatures within milliseconds. However, unlike the experiments performed in air, the particles would continually glow without the heat being transferred to nearby particles due to the lack of O₂ and N₂, preventing the exothermic formation of TiO₂ or TiN (see Figure S7.1). These results demonstrate that not only can Ti nanoparticles be heated to high temperatures using microwaves, but also the high temperatures achieved are not solely dependent on the Ti reaction with air. The heating of Ti nanoparticles in air merely enhances the heat generation for thermal propagation away from the localized microwave source through its strongly exothermic reaction with air. The sensitivity of the Ti particles to microwaves further alludes to the importance of shell composition

on particle heating. Experimentally, core-shell Ti nanoparticles can couple to microwaves more efficiently, thus heating faster and ultimately achieve thermal ignition as opposed to core-shell Al nanoparticles that are unable to be heated via this method.

As mentioned previously, the observed heating and ignition of the samples by microwaves is likely attributed to (1) the unique shell composition of the Ti nanoparticles and (2) the lower ignition temperature of Ti particles in air. Electrical conductivities of materials found in the nano-Ti shell (TiN, TiO₂), while having a wide range of reported values depending on the crystal structure and physical architecture, are consistently larger than those for the Al₂O₃ found on the exterior of the Al nanoparticles.^{240,244,254,255} Microwaves couple well with Ti nanoparticles as a result of unique material properties and its core-shell structure. The entire particle is heated via Joule heating originating from the dynamic nature of electromagnetic waves, resulting in frictional heat caused by induced eddy currents and shell enhanced induced polarization from the magnetic and electric components of the microwave, respectively.^{243,244,251}

7.3.3 Microwave sensitivity of metallized propellants

Although the potential to ignite Ti-based energetic materials remotely using microwaves has been demonstrated thus far, the applications of the mixtures tested are limited in scope. Pure metal powders react rather slowly despite their high energy density. One particularly interesting application of remote ignition would be solid propellant mixtures since they have received renewed interest with the rise of additive manufacturing.^{101,108,111,163,165} By incorporating metal particles into an energetic

polymer solution, solid propellants can be easily manufactured by additive manufacturing technologies with tailorable architectures to produce custom performances based on their physiochemical properties.

Solid energetic precursors of Ti/PVDF were prepared with varying weight percentages of Ti, as shown in Table 7.1, to investigate the role of Ti metal particles on ignition. It was expected that the addition of PVDF to the Ti particles would impact the ignition of the materials, especially considering that particles would be predominately encapsulated in the polymer throughout the film. It was observed that at an equivalence ratio (Φ) of 1, Ti (35 wt. %)/ PVDF (65 wt. %) will not be ignited by microwave radiation, but increasingly Ti fuel rich compositions will ignite more readily and consistently. Ti (50 wt. %)/PVDF (50 wt. %) was found to be a lower bound for microwave ignitability for which heating was inconsistent at times. Additionally, the level of Ti particle inclusion must also be balanced with printability where Ti (65 wt. %)/PVDF (35 wt. %) was found to be the upper bound for Ti loading. A summary of these results is presented in Table 7.3. An important note is that electrical percolation may be contributing to the microwave sensitivity of these composite propellants; however, all results and calculations presented thus far suggest that the as-received Ti nanoparticles would ignite irrespective of percolation.²⁵⁸ A detailed analysis on percolation thresholds is beyond the scope of this article but should be considered in future research.

Table 7.3: Free-standing burn velocities in air and argon environments and ability to be ignited with microwaves.

Sample	Metal wt.%	Environment	Burn Velocity	MW Ignition
Al / PVDF	25	Air	$\approx 14 \pm 1$ cm/s	N
		Argon	$\approx 7 \pm 1$ cm/s	N
	65	Air	$\approx 27 \pm 2$ cm/s	N
		Argon	$\approx 15 \pm 4$ cm/s	N
Ti / PVDF	35	Air	$\approx 1 \pm 0.5$ cm/s	N
		Argon	-----	N
	65	Air	$\approx 4 \pm 0.1$ cm/s	Y
		Argon	$\approx 1 \pm 0.1$ cm/s	Y

When tested with the needle-based microwave applicator, Ti/PVDF samples containing 65 wt. % Ti were readily ignited within 10 ms of power being delivered to the samples with the propellant films consistently propagating to completion in air (see Figure 7.7) and argon (discussed in Sec. 7.3.4.).

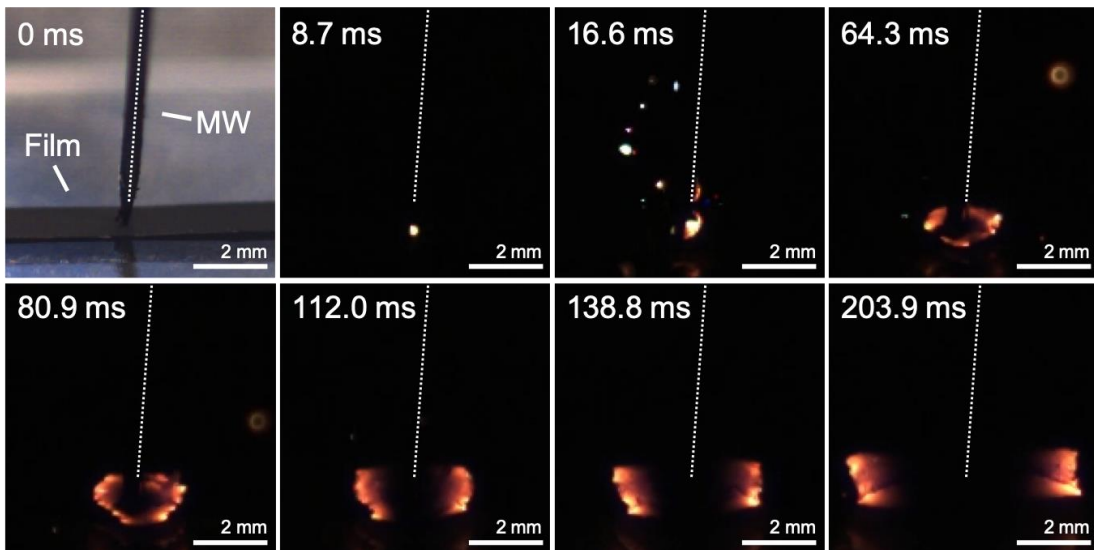


Figure 7.7: Ignition of Ti/PVDF (65 wt.% Ti) film in air using microwave needle apparatus imaged using a high-speed camera. $t=0$ defined as starting time for power supplied to the applicator. Dashed white line indicates position of needle.

Upon ignition of the sample, a bright ignition point becomes clear with particles being ejected from the surface shortly after. Within 65 ms, a uniquely shaped circular

reaction front with an approximate width of ~ 0.3 mm began propagating from the hotspot until it reached the edge of the film at which point the propagation became linear. The flame structure of the Ti/PVDF films during combustion strongly resembles those that are seen in Al/PVDF combustion events with a long, hot reaction tail, which generates a significant amount of soot; however, a detailed study is reserved for future research. While the structure of the flame will be explored in future work, the bidirectional and steady propagation of the Ti/PVDF film opens unique avenues by which to employ this material as a remote ignition source with high targetability.

7.3.4 Controlled-environment combustion characteristics of metallized propellants

Flame speed experiments of Al/PVDF and Ti/PVDF were performed in air and argon environments to evaluate the potential for implementation into a solid propellant. Al/PVDF has been previously investigated as an additively manufactured solid propellant; however, Ti/PVDF has yet to be fully studied.^{67,72,180} While air would likely be the environment for combustion of these materials, argon was also considered to study flame self-propagation performance within an environment devoid of both oxygen and nitrogen.

Results of the average burn velocity of four samples of Al/PVDF and Ti/PVDF at different mass loadings of metal fuel are presented in Table 7.3 where the burn velocity of Al/PVDF samples consistently outperforms the Ti/PVDF equivalents (Figure 7.8).

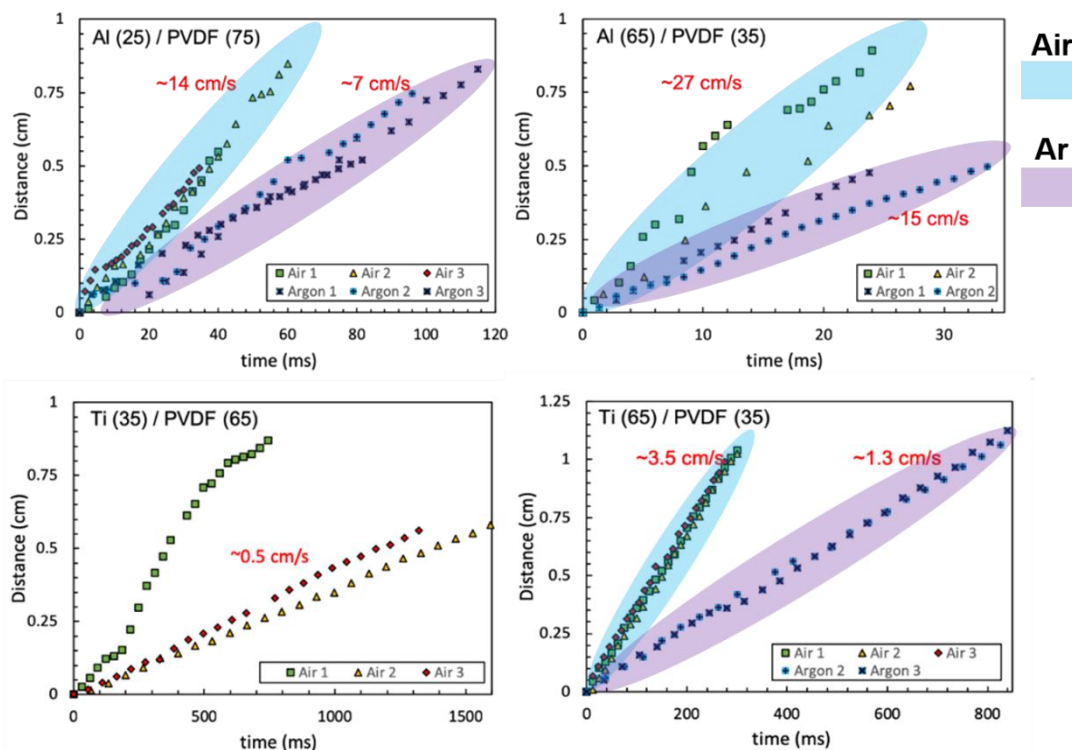


Figure 7.8: Distance vs. time data used to estimates for the propagation rate of Table 7.3 compositions in air and argon

While the inert argon environments do substantially impact the burn velocities of both sample types, Al/PVDF is still able to burn at faster rates with lower metal loadings than Ti/PVDF did in air. Furthermore, low-Ti-content energetic samples were unable to sustain combustion in the inert environment. It is believed that the kinetics of the Ti/PVDF reaction in an argon environment are not favorable since XRD analysis of post-combustion products predominately show TiF_3 and TiC as the primary products (see Figure S7.2), whereas one would expect the formation of TiF_4 . This indicates that either the reaction is not going to completion or the complete sublimation of any TiF_4 products. In contrast, when the Ti/PVDF samples are burned in air, the Ti also exothermically reacts with O_2 , which would assist in any shortcomings in the energy release due to incomplete reactions with PVDF.

From these results, one can see that while both Al/PVDF and Ti/PVDF samples can propagate in both air and argon environments, the Al/PVDF samples would be more desirable as a conventional solid propellant since it would be able to generate more thrust by releasing similar amounts of stored energy over shorter periods of time. However, the insensitivity of aluminum to ignition by microwave radiation limits the ability of the propellant to be utilized in remote-initiation situations. Considering the limitations between the propellant formulations, it would be desirable to have a microwave-sensitive propellant that does not have reduced performance. A potential architecture is explored in Sec. 7.3.5.

7.3.5 Architecting of a microwave-initiated solid propellant

The results presented thus far in this work suggest that, while Ti/PVDF may not be an optimal solid propellant choice with a slow propagation velocity, it can be readily ignited in both aerobic and inert environments using targeted microwave radiation and will steadily propagate in these environments at high mass loadings of Ti. Although Al/PVDF does not have the same microwave sensitivity, its relatively superior combustion performance as a propellant and relatively low manufacturing cost still would likely steer most rocketeers toward using Al/PVDF (or some other aluminum-based metallized composite) as a primary propellant mixture.^{37,103,112,180,210} As such, this work also investigated the potential incorporation of Ti/PVDF in an igniter application for Al/PVDF propellants that are additively manufactured.

An Al/PVDF precursor ($\Phi = 1$) was prepared and printed four-layers high (~ 30 μm) using a direct-write additive manufacturing method. A Ti (65 wt. %)/PVDF (35

wt. %) layer was then printed in a smaller segment on top of the Al/PVDF sample. A depiction of the sample can be seen in Figure 7.9 with scanning electron microscopy/energy-dispersive x-ray spectroscopy (SEM/EDS) images demonstrating a clear separation between the Al/PVDF and Ti/PVDF layers that were printed.

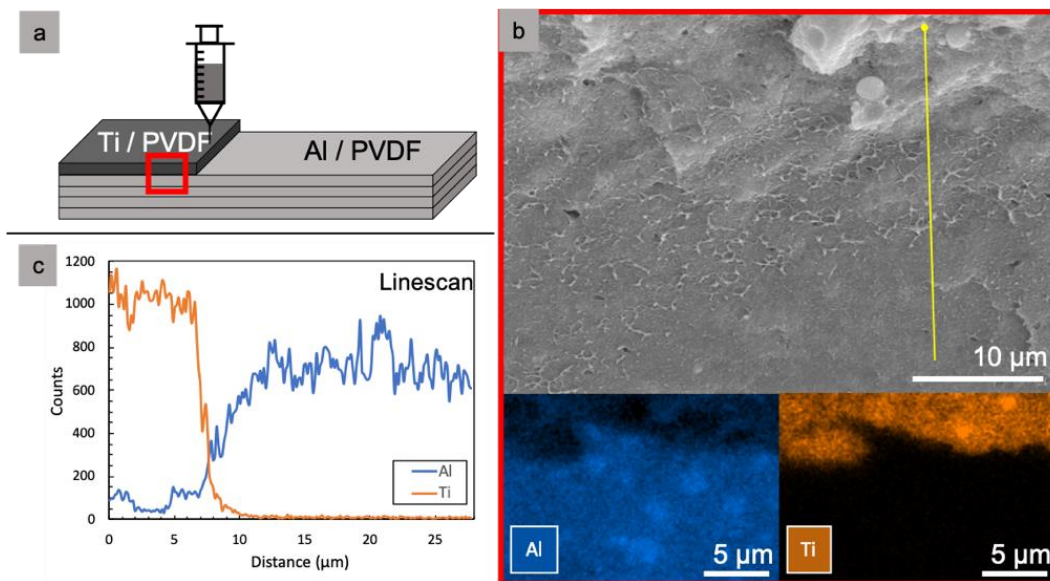


Figure 7.9: (a) Depiction of the architecture for a layered Al/PVDF, Ti/PVDF propellant that can be initiated with microwaves where layers 1-4 are Al/PVDF ($\Phi=1$) and layer 5 is Ti/PVDF (65 wt.% Ti) ($\approx 35 \mu\text{m}$ thick). (b) SEM/EDS image of layered film cross-section as outlined in a. (c) EDS line scan results for line drawn in b.

A line scan of the sample originating from the Ti/PVDF sample shows that the single Ti/PVDF layer is $\sim 7 \mu\text{m}$ thick and that the Al/PVDF section is $\sim 4\times$ thicker than the Ti/PVDF domain with a total thickness of roughly $35 \mu\text{m}$.

Combustion experiments were performed using the needle-based apparatus in aerobic and inert environments, which yielded positive results for Ti/PVDF to act as a microwave-sensitive ignition source for Al/PVDF. Figure 7.10 shows that the microwave sensitized Ti/PVDF layer printed on top of the larger Al/PVDF strand can be ignited $\sim 30 \text{ ms}$ after power is supplied to the microwave needle.

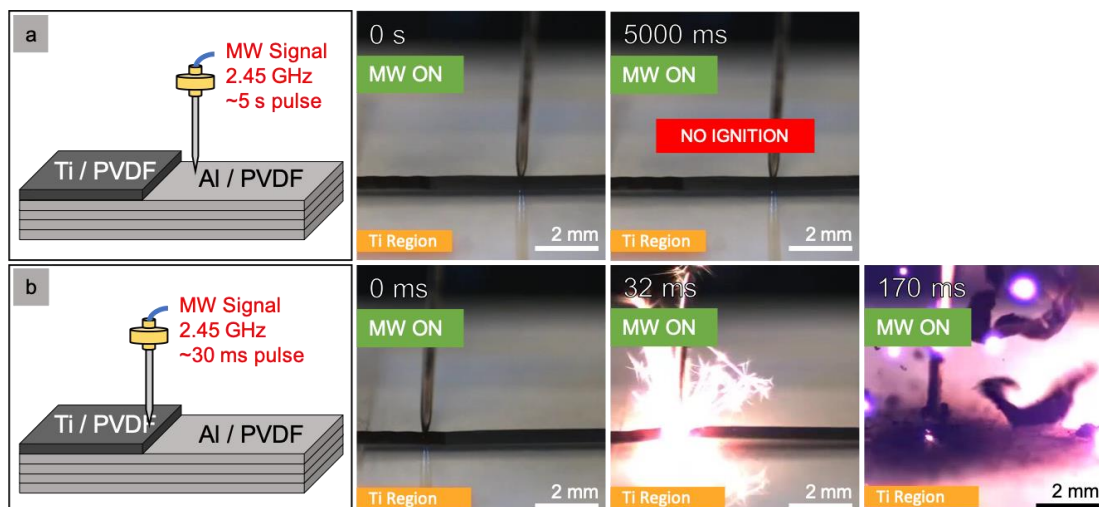


Figure 7.10: Microwave needle ignition of a layered Al/PVDF, Ti/PVDF propellant where layers 1-4 are Al/PVDF ($\Phi=1$) and layer 5 is Ti/PVDF (65 wt.% Ti). (a) Al/PVDF region does not ignite when exposed to microwave radiation and (b) Ti/PVDF layered region ignites and propagates into Al/PVDF region.

Within 20 ms after the Ti/PVDF ignition, the exothermic reaction then transfers enough heat to the underlying Al/ PVDF layers to rapidly (<1 ms) reach its ignition temperature of ~ 620 °C, leading to sustained propagation.⁷² Figure 7.10 also demonstrates how the ignition location can be selectively placed over and captures the reaction propagation transition from the Ti/PVDF into the Al/PVDF.

By making a specific segment of solid propellant remotely initiated using selectively placed microwave-sensitive materials, this work sets up the development of remotely staged, additively manufactured solid propellants. Currently, solid rocket motors do not have an “off” switch like their liquid rocket engine counterparts. Incorporating a small, inert “quenching” region with low thermal conductivity into a solid rocket motor assembly, followed by another microwave-sensitive ignition source, could provide “checkpoints” between different stages of the rocket and even a moderate throttle control (multiple segments simultaneously) using only a directional microwave

radiation source and an antenna. The design of the solid propellant could be readily implemented using more sophisticated additive manufacturing techniques and would significantly improve the versatility of solid rocket motors for civilian and military applications.

7.4 Conclusions

This work investigated the localized ignition of metal powders and metallized 3D printed propellants via microwaves. Materials were subjected to microwaves via a needle applicator, which was able to ignite titanium nanopowders and energetic composites containing high mass loadings of Ti (~65 wt. %). Aluminum powders and Al/PVDF propellants were unable to be heated with the needle applicator after 30 s of exposure. Titanium's observed interaction with microwave radiation is unexpected from the point of view of models which focus on bare metallic nanoparticle–microwave coupling with no consideration of the native oxide layer composition. These observations reveal the necessity of rigorous models that consider the properties and role of the oxide layer of energetic metallic nanoparticles in microwave heating. Despite the superior microwave absorption of nanoscale titanium, the superior burn velocity and reduced cost of Al/PVDF make it a more attractive propellant for traditional propulsion applications. The Ti/PVDF composite proved to be a suitable microwave-based igniter for solid propellants in both aerobic and inert environments. This work sets the stage for studies that focus on the shell composition for enhanced microwave coupling of heterogeneous energetic systems as well as for highly tailorable combustion of solid rocket propellants that can be remotely ignited and staged with directed microwave radiation.

Chapter 8: Summary and Future Works

8.1 Conclusion Summary

The breath of my Ph. D. works ranged from computational modeling, additive manufacturing of energetic material composites, and mass spectrometry to TEM/SEM analysis, microwave response analysis of energetic nanomaterials, catalysis research, and analysis of air sensitive materials. The primary studies undertaken in this dissertation have used the rapid heating/diagnostic tools utilized by my predecessors to both reinforce findings from prior studies and build upon them for uncovering novel conclusions of energetic materials formulations and performance.

The work of chapter 4 had a simple objective which bore more complicated yet revealing results. Does adding the most widely used nanoscale aluminum thermites to additively manufactured aluminum/PVDF propellants effect ignition behavior or improve combustion performance? Not only does increased thermite mass content decrease flame speed and diminish energy release rates, the choice of thermite type does not seem to matter significantly in this regard. Higher thermite mass content uncontrollably leads to more porous films from DIW additive manufacturing and reduced mechanical integrity. However, choice of thermite was found to be significant for predicting the ignition behavior of the thermite integrated compositions under rapid heating conditions. The ignition temperature in vacuum environments are controlled by the ignition temperature of the thermite composition, whereas the ignition temperatures in pressurized, inert argon environments were controlled by the ignition temperature of Al/PVDF. These results, combined with the sudden release of HF gas

in all cases before ignition and the lack of Al/PVDF ignition in vacuum, reinforce the necessity for a HF mediated gas phase reaction mechanism of Al/PVDF.

In chapter 4's study of Al/MO/PVDF compositions, integrated metal oxides appear to not only react with aluminum but also carbon species formed from PVDF decomposition, generating CO₂ and deviating from the predetermined mutually exclusive stoichiometric balance in the system. Further investigations in Chapter 5 showed that metal oxide oxidizers and passivating oxide shells have non-negligible interactions with the PVDF binder upon heating. Thermochemical analysis shows complex HF gas mediated fluorination mechanisms with surface bound hydroxyl groups which need not result in a stable metal fluoride. While Al₂O₃, TiO₂, and CuO enhance decomposition behavior and HF release, SiO₂, MgO, and Bi₂O₃ suppress HF release and retard the onset of PVDF decomposition. The relative intensity of HF gas increases dramatically as the onset temperature of HF release decreases. Interactions between HF promoting metal oxides appear to both lower the onset of HF release and engage exothermically with HF gas to promote further local HF release. Furthermore, the exothermic facilitation of HF gas release does not necessitate initial HF surface interactions as demonstrated by significant CO₂ formation preceding HF release in the case of CuO/PVDF which does not form any metal fluoride products yet promotes HF release.

Interestingly, Al₂O₃/PVDF separates itself from other compositions based on its unique T-jump mass spectrum which produces the largest release of HF gas and generates trifluorobenzene instead of any of other the higher mass species observed in both neat PVDF and other compositions. This behavior suggests a potential difference

in reaction mechanism which requires more sophisticated models to illustrate how the unique interaction between Al_2O_3 and PVDF fundamentally differs.

Chapter 3 and 7 moved beyond aluminized systems with the study of nano-energetic systems utilizing titanium fuel. The addition of nano scale Ti offered niche capabilities and further highlighted the importance of characterizing the oxide shell of the metal fuel. The study of the reaction mechanism of Ti/ KClO_4 in chapter 3 revealed the lack of pre-ignition sintering of Ti aggregates at rapid heating conditions and resistance to water oxidation. Although energetically less favorable than nano aluminum, Ti both maintains its nano structure prior to gas phase oxidation and contains reactive crystalline TiN within the amorphous TiO_2 oxide shell. Each of these properties may contribute to its relatively lower ignition temperature in air and potential for enhanced reactivity in thermite mixtures.

In in the same manner for which TiO_2 led to the early onset of PVDF decomposition observed in chapter 5, the importance of the oxide shell of titanium in chapter 3 persisted as a point of catalysis for the early onset of single step KClO_4 decomposition and rapid oxygen release under rapid heating conditions. Electromagnetic models considering the core-shell structure in Chapter 7 even demonstrate that while bare titanium and aluminum respond negligibly to microwave radiation, core-shell titanium particles could be heated to ignition via incident microwaves once the specific composition and core-shell structure were accounted. Furthermore, nanoscale titanium bound PVDF energetic compositions above 50wt.% could consistently be microwave ignited in both aerobic and inert environments. Combining Ti/PVDF and Al/PVDF films through DIW additive manufacturing makes

it then possible to utilize and strategically position Ti/PVDF material to act as a microwave-based ignition point to supplement for the lack of microwave sensitivity of the superior Al/PVDF propellant.

The results from chapter 6 offer an alternative method of tuning burn rates and energy release rates by modeling how the combustion performance of a dense mixture of nano-energetic material varies as a function of added vol.%, aspect ratio, and thermal conductivity of a relatively inert additive (*e.g.* carbon fibers, copper rods). 2D combustion simulations showed that the synergic relationship between randomly oriented thermally conductive rods and a nanoscale energetic composition lead to increases in the total area burned and energy released when the connectivity of thermally conductive rods throughout the composites is optimized at minimal volume percentages ($AR > 25$, $vol.\% < 20$). Aspect ratios which were too low ($AR < 25$) offered no significant enhancements due to limited heat transfer reach and additive vol.% which were too high (> 20 vol.%) quenched flame propagation through excessive heat transfer to non-energetic regions. Thermally conductive rods with a thermal conductivity three orders of magnitude larger than the composite energetic material demonstrated a 25% gain in burn rate and 10% gain in energy release rate when optimized for vol.% and aspect ratio. These results are far more significant than that of Chapter 4. Furthermore, this study demonstrated that even increases in the thermal conductivity of the rods has its limits with respect to enhancements to flame front propagation. Independently varied rod thermal conductivity for the same additive distribution initially leads to increased enhancements in total area burned and energy release. However, the percent enhancement plateaus and effectively becomes

independent of thermal conductivity after reaching some critical thermal conductivity. Any further enhancements would require directional biasing of high aspect ratio rods but would also eliminate the isotropic behavior of flame propagation behavior.

As what happens with any Ph.D. research analyzing potentially novel analytical or material preparation techniques, each project came with its challenges, some more than others. Given the number of topics I attempted to cover during my tenure, my experience was unfortunately littered with several projects that, for one reason or another, stalled or the results were less than ideal for practical purposes. The remaining subsections of this chapter gives insight to the mistakes, struggle areas, and progress achieved with respect to some of my more prominent unfinished projects with the goal for future projects to improve upon experimental designs and publish on genuinely novel works.

8.2 In situ TEM Heating of Select Perovskite Particles

8.2.1 Introduction

Perovskites materials are a class of chemical compounds which are representative of the same crystal structure ($A^{2+}B^{4+}O^{2-}_3$) for which many cations may be embedded or doped within the structure.^{259,260} This allows for chemically customizable perovskite materials which have been utilized primarily for applications in solar cell technology, electrolysis cells, catalysis for hydrocarbons, membranes for oxygen separation, and LEDs.^{58,261–264} Past research employed the perovskite structure as a base feature with respect to their application in systems which partake in both fast and slow redox reactions.^{58,265} More specifically, lanthanum based micro-scale and

nanoscale perovskite materials, synthesized via aerosol spray pyrolysis, are used as the primary oxidizer in chemical looping studies and studies which seek to tune the transient combustion and ignition behavior of nanoscale thermite systems based on the bond energy, electronegativity, and oxygen vacancy of the constituents in the perovskite structure.^{58,265} In both applications, the lanthanum based doped perovskites, such as LaCrO₃, LaCoO₃, and LaFeO₃, express distinct variations with respect to oxygen storage capacity in chemical looping experiments and a spectrum of oxygen release/ignition temperatures (800-1200°C) with respect to thermite systems subject to ultra-fast heating rates ($\sim 10^6$ °C/s).^{58,265} Given the novel utilization of these materials, more contemporary characterization techniques are necessary to understand their underlying behaviors.

The FEI Titan STEM (Scanning Transmission Electron Microscopy) equipped with Electron Energy Loss Spectroscopy (EELS) diagnostic capabilities at Oak Ridge National Lab allows for unprecedented observations into the behavior of synthesized doped perovskite materials. This instrument, coupled with the versatile Protochips Atmospheric In-Situ Heating Gas Reaction Cell, offers the ability to observe real time morphological characteristics of these perovskites in applicable environments with relevant heating parameters to better understand previously documented results.^{58,265} Specifically, these unique capabilities are focused on analyzing the mobility of oxygen within the perovskite structure and demonstrate, visually, how the behavior of transient oxygen mobility within each perovskite type may connect to macroscopic observations.²⁶⁶

8.2.2 Experimental Instrumentation, Materials and Approach

This work was conducted as a collaboration between the Zachariah Research Group and with Dr. Raymond Unocic of Oak Ridge National Lab whose previous studies focused on the oxidation behavior of NiAl particles using the Atmospheric cell.²⁶⁷ The study relies on the coupling of the FEI Titan S aberration-corrected TEM-STEM and the Protochips Atmospheric Micro-electromechanical System (MEMS) for which the experimental setup is shown in Figure 8.1. Specifics of each instrument can be found on the Oak Ridge National Lab and Protochips webpages but are briefly described here.

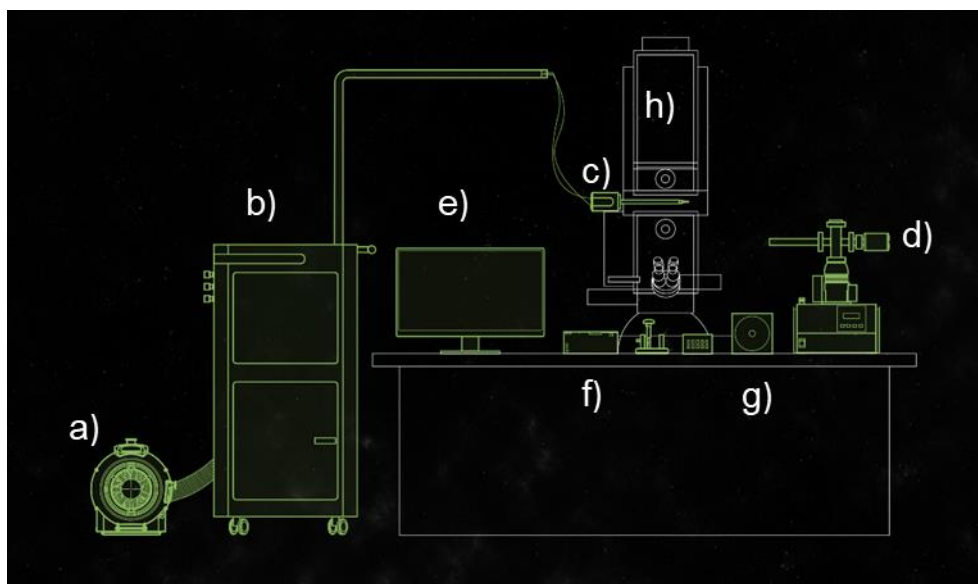


Figure 8.1: Protochips Atmospheric System for TEM: a) Scroll pump, b) Gas manifold, c) Holder, d) Leak check station, e) Software, f) Power Supply, g) E-Chip calibration file, and h) FEI Titan TEM-STEM.

The FEI Titan TEM-STEM is a probe-corrected microscope which features a Gatan Quantum EELS and Gatan Imaging Filter (GIF), with dual-EELS and fast spectrum imaging capabilities, an ‘extreme Schottky’ high-brightness field emission gun (X-FEG), and variable operating voltages (60, 120, and 300 kV). The Instrument

is equipped with high-angle annular dark field (HAADF), annular dark field (ADF), and bright field (BF) STEM detectors for sub-Å imaging. Recent upgrades to the instrument include the addition of a large active area (60mm²) EDAX silicon drift detector (SDD) for high-collection-efficiency energy dispersive X-ray spectroscopy (EDS), enabling the simultaneous acquisition of EDS and EELS spectrum images. The sample chamber pressure operates at 10⁻⁷ Torr with the option for elevated pressures when using the Protochips Atmospheric Cell. For my experiments, data acquisition was conducted using 300 kV beam voltage, 2.63 nA beam current, and a dwell time of 1.6 μs/pixel over a 512x512 frame. Optimization of EELS mapping resolution is not just matter of time in terms of the number of scans over a certain pixel resolution. One must also consider the time scale at which particle drift within the TEM becomes significant. Therefore, dwell times and areas of analysis must be chosen such that the resolution of the mapping is enhanced enough for a proper analysis while limiting the degree of object drift.

The Protochips Atmospheric system creates an in-situ reaction chamber inside the TEM microscope, enabling atomic resolution imaging of dynamic nanoscale processes under realistic conditions. Featuring self-aligning parts, automated workflows, and EDS capabilities, the atmospheric cell allows for novel studies of experiments which previously could only be conducted under vacuum. A single o-ring gasket forms a hermetic seal that safely confines gasses between two E-chip membranes, allowing for imaging of samples at pressures as low as 1.0 Torr and as high as 760 Torr. Highlighted by its automatic gas handling (Figure 8.1b) and redundant safety features, the gas manifold controls atmospheric conditions in the

holder and can mix any gas (up to 3 at a time) without calibration with integrated flow and pressure sensors for precise delivery. Despite these enhanced capabilities, the heater of the atmospheric cell only has a maximum temperature ramp rate of 5 °C/s, 5 orders of magnitude smaller than the heating rate of the T-Jump ignition experiments.^{58,115,120} Experiments requiring faster heating may be conducted using the standard Protochips heating chips which can heat a sample as high as 1000 °C/ms in vacuum.^{120,230}

Case study experiments were conducted at the Center for Nanophase Material Sciences (CNMS) at Oak Ridge National Lab over an 8-day period split by two separate visits. Perovskite materials used for preliminary experimentation were those which were immediately available and demonstrated variable behavior in previous ignition and chemical looping experiments. Therefore, as previously mentioned, the lanthanum-based perovskites of LaCrO_3 , LaCoO_3 , and $\text{La}_{0.6}\text{Sr}_{0.4}\text{CoO}_3$ and were chosen as candidates for this case study to compare how differences in the B-site species and doping of the A-site species within the perovskite structure effects the observations made in this study. XRD characterization was conducted to confirm the crystal structure of each perovskite type and TEM conducted at University of California, Riverside to select the batches which contained mostly solid particles (Figure 8.2).

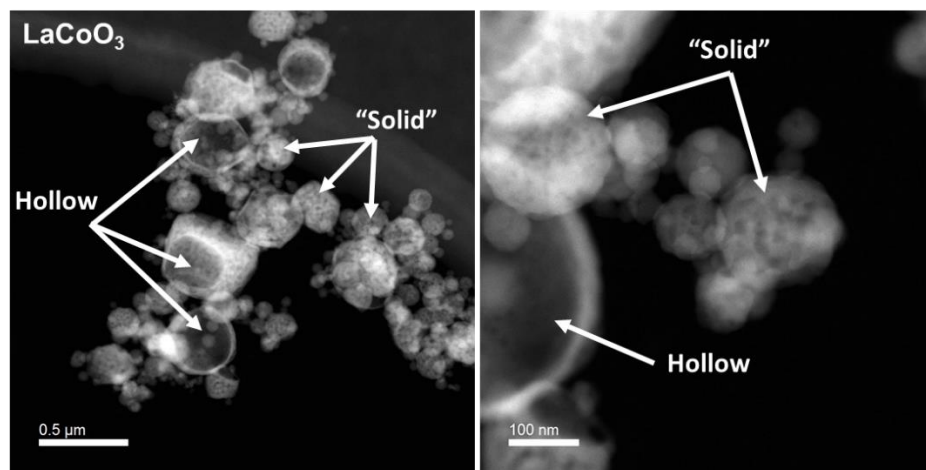


Figure 8.2: TEM images taken at UCR of LaCoO₃ particles which highlight the morphological mixture of particles.

Many of the perovskite batches synthesized have a mixture of hollow and solid particles as a result of the synthesis process for which the solid particles are selectively focused on during the experiments at Oak Ridge National Lab. Although the solid particles are thought to be “solid”, TEM imaging throughout this section reveal that these particles are more like an extremely compact aggregation of small primary units which make the “solid” spherical particle appear internally porous with clear grain boundaries and contrast between areas of lower and higher density. These particle batches are used as a direct comparison to previous experimentation, but it is unclear what consequences, if any, this will have during in-situ heating TEM experiments.⁵⁸

Sample preparation was conducted at the CNMS by first suspending <1 mg of each perovskite type in hexane and sonicating for 15-20 minutes to reduce aggregation for effective particle dispersion. Particle suspensions of each type are deposited on to their own Si₃N₄ Protochips E-chip using a micropipette with the assistance of an optical microscope. If necessary, the suspension should be diluted to reduce the resulting density of particles deposited. The E-chip is connected to the Atmospheric cell and gas

manifold connectors with pre-check tests run to ensure gas vessel integrity and electrical connection between the leads of the E-chip and TEM probe. The TEM probe is inserted into the FEI Titan TEM-STEM and the Atmospheric cell purged with nitrogen gas, evacuated, and refilled with the gas of interest. Gasses of interest included nitrogen for a relatively inert environment, oxygen for an oxidizing environment, and a $\text{H}_2(4\%)/\text{Ar}(96\%)$ gas mixture for a reducing environment. Each sample in the Atmospheric cell is subject to a heating protocol which is programmed into the Protochips software prior to data acquisition. In general, the heating protocol heats a chosen particle aggregate to 700 °C at a rate of 1-5 °C/s, held for 5-10 minutes, then increased in temperature at the same rate to temperatures up to 1000 °C in increments of 50 °C with 5-10 minute temperature holds in between. During the heating process, videos of the heating process are recorded in order to capture real time morphological changes. Active focusing and object centering is thus necessary in order to not lose track of the sample for which the temperature holds are essential for image focusing to acquire usable data. EELS elemental mapping is performed prior to and after each heating protocol to determine potential species mobility as well as morphological changes and valence state changes. I would later find that an additional plasma cleaning process of the Atmospheric cell would be necessary to remove surface contaminants on the exterior of the closed cell. Additionally, samples are pre-heated during the nitrogen purging step to 300 °C to burn off interior surface contaminants of the closed cell which become evident during EELS scans as shown in Figure 8.3. The 300 °C mark would serve as the main starting and ending point in all heating protocols

were EELS mappings would be taken after significant drift of the particles in the TEM subsided.

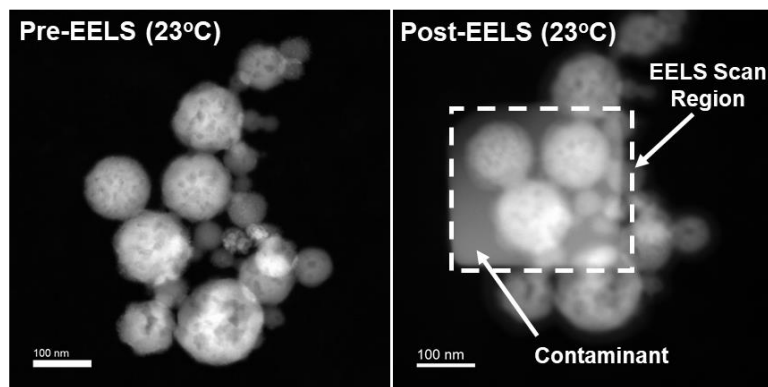


Figure 8.3: Initial TEM images of perovskite nanoparticles and first attempt at EELS scans highlighting the need for pre-heating of material to 300 °C.

8.2.3 Results and Discussion

Prior to using the Atmospheric Cell, LaCoO_3 samples were deposited onto the Si_3N_4 E-Chips for preliminary testing of the high ($\sim 10^6$ °C/s) and low (≈ 5 °C/s) heating rates in vacuum. Heating at $\sim 10^6$ °C/s resulted in buckling and fracturing of the Si_3N_4 substrate with no ability to record the event. Additionally, heating to 1000+ °C for both heat rates resulted in a failure of the Si_3N_4 substrate where the particle aggregate appears to rapidly disintegrate while puncturing a hole through the substrate. An example of this is shown in Figure 8.4 where both the EELS mapping for cobalt and HAADF images are depicted.

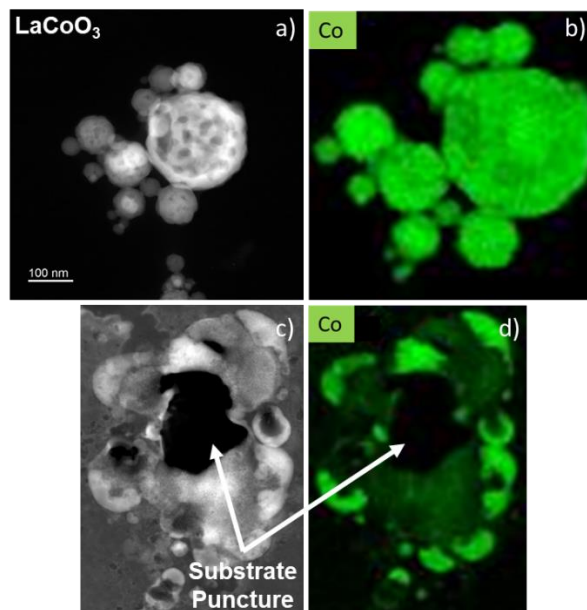


Figure 8.4: LaCoO₃ nanoparticle aggregate imaging a) prior to and c) after heating with b)-d) EELS mapping illustrating the splattering of cobalt atoms around the substrate puncture.

The heating protocols would be implemented based on these initial findings such that, after preheating to 300 °C at 5 °C/s, the temperature would rise to 700 °C at 5 °C/s and be raised in temperature by 1 °C/s in 50 °C increments to no higher than 1000 °C for all cases. Heating of the LaCoO₃ sample in vacuum past 1000 °C had resulted in a product for which the true morphology of the particle, up to the point of disintegration, had not been properly documented. Instead of preparing a new LaCoO₃ sample, a test sample of La_{0.6}Sr_{0.4}FeO₃ sample was loaded as it was already prepared to be loaded. As in the LaCoO₃ case, a small aggregate of mostly solid nanoparticle spheres are first imaged and EELS mapping performed. Upon reaching ≈850 °C and heating to 1000 °C, significant morphological changes in the aggregate structure were observed as shown in Figure 8.5.

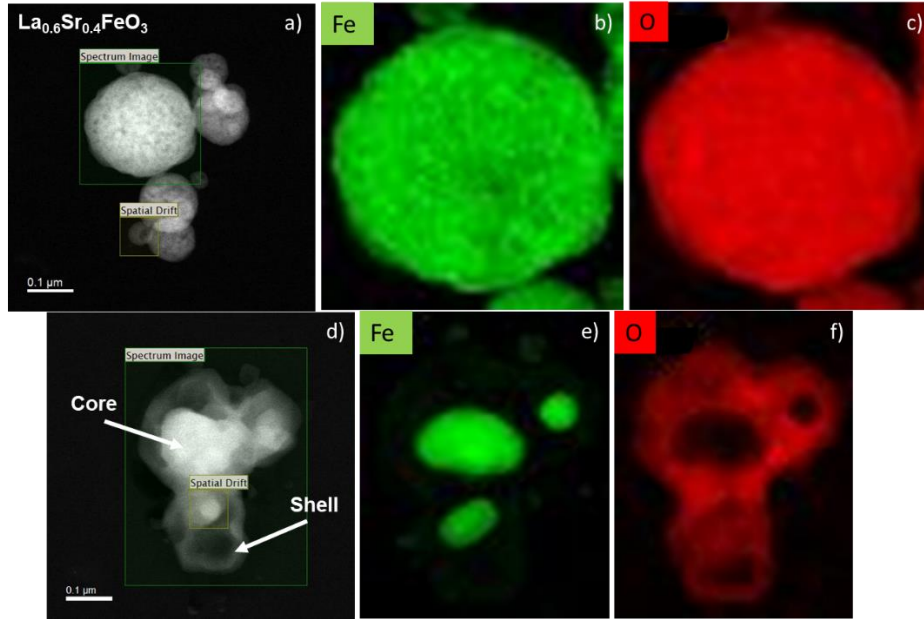


Figure 8.5: a)-c) TEM image and EELS mapping of $\text{La}_{0.6}\text{Sr}_{0.4}\text{FeO}_3$ prior to heating with a d)-f) core-shell type structure forming upon reaching 1000 °C.

The entire aggregate appears to sinter together while simultaneously forming a core-shell structure with the migration of higher density iron atoms towards the center and lower oxygen atoms towards the edges. Lanthanum was difficult to map in this sample for reasons unknown to me. The same general experiment was conducted in the Atmospheric cell with the heating of primary samples of LaCoO_3 , LaCrO_3 , and $\text{La}_{0.6}\text{Sr}_{0.4}\text{CoO}_3$ in 760 Torr nitrogen gas. A graphical representation of the programmed heating protocols and instances of EELS measurements are shown in Figure 8.6.

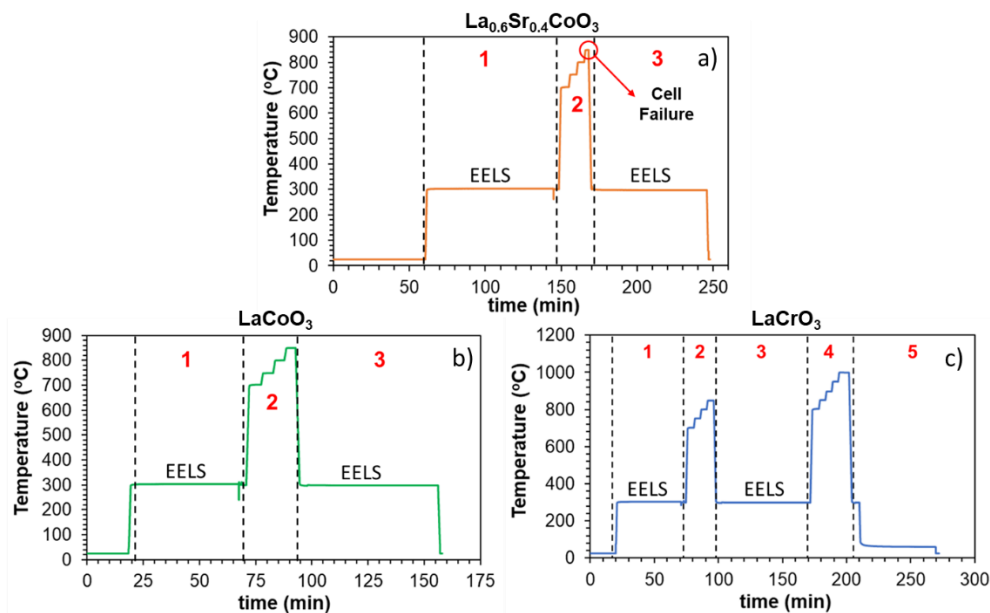


Figure 8.6: Heating protocols for $\text{La}_{0.6}\text{Sr}_{0.4}\text{CoO}_3$, LaCoO_3 , and LaCrO_3 samples.

The $\text{La}_{0.6}\text{Sr}_{0.4}\text{CoO}_3$ sample was the first sample to be heated in the nitrogen atmosphere. As Figure 8.6a shows, the sample is preheated to 300 °C, ramped to 700 °C, and then heated to 850 °C in increments of 50 °C. Heating to 700 °C resulted in immediate sintering and significant morphological changes which intensified with higher temperature. 850 °C was not meant to be its final temperature in which heating to 850 °C in 760 Torr nitrogen gas resulted in instrument failure of the Atmospheric cell as pointed out by Figure 8.6a. Although the Atmospheric cell had failed, heating of the E-chip was maintained, and the post-heating sample was able to be recovered. HAADF images and EELS mapping for this sample are displayed in Figure 8.7.

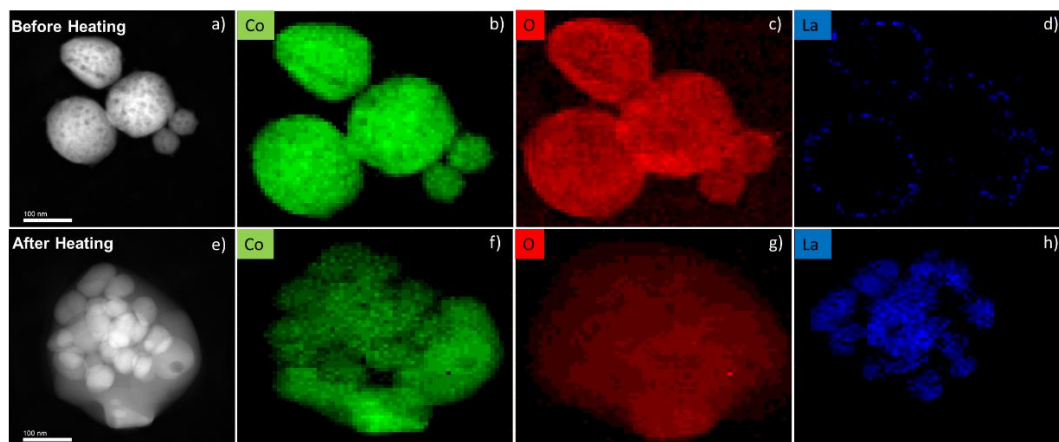


Figure 8.7: TEM imaging and EELS elemental mapping of $\text{La}_{0.6}\text{Sr}_{0.4}\text{CoO}_3$ a)-d) before and e)-h) after the proscribed heat protocol under 760 Torr nitrogen gas.

Much like Figure 8.5, the morphology has drastically changed as result of sintering, having nearly formed a coalesced sphere. The lanthanum signal mapping once again is not well defined in the before heating mapping as it appears that it only resides on the surface. However, in contrast to Figure 8.5 the lanthanum atoms appear to be the species which migrates towards the center, making up the cluster of higher density spherical features within the interior. Cobalt and oxygen do not appear to have separated from each other much at all with the oxygen signal having decreased in apparent signal intensity compared to its corresponding before heating EELS mapping. Strontium was not considered for EELS mapping due to its location in the energy spectrum relative to the other species. Including strontium would result in reduced energy measurement resolution.

Due to the prior failure of the Atmospheric cell, the LaCoO_3 sample was heated in nitrogen up to 850 °C and then cooled back down to 300 °C, as Figure 8.6b shows. Once again, sintering onset occurs at roughly 700 °C and is enhanced at higher

temperatures. Corresponding HAADF images and EELS elemental mapping are shown in Figure 8.8.

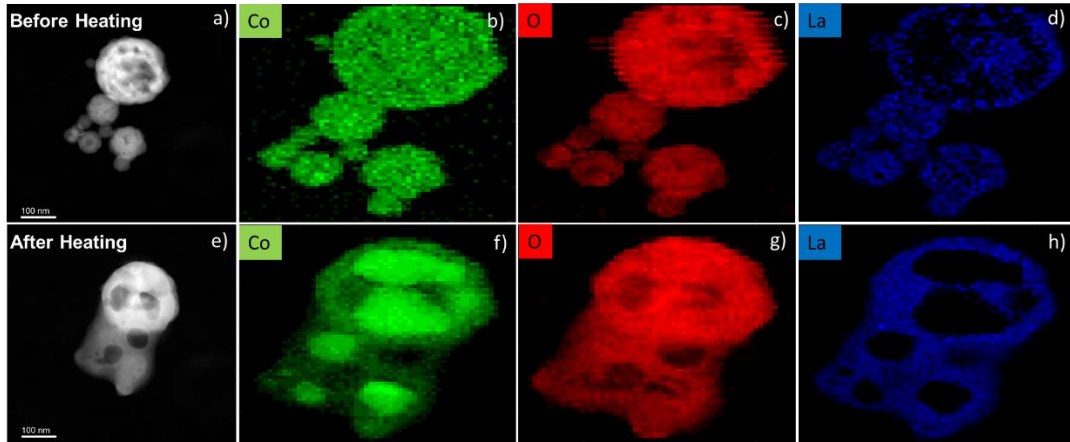


Figure 8.8: TEM imaging and EELS elemental mapping of LaCoO_3 a)-d) before and e)-h) after the proscribed heat protocol under 760 Torr nitrogen gas.

The baseline EELS mapping for lanthanum produced a more compelling mapping which roughly depicts its presence throughout the aggregate. Although the LaCoO_3 aggregate sinters, it does not appear to sinter to the same degree as $\text{La}_{0.6}\text{Sr}_{0.4}\text{CoO}_3$ with respect to its progress towards spherical coalescence at equivalent temperatures. The cobalt atoms migrate towards the interior and separates from the lanthanum atoms more so than the oxygen atoms in which both appear to occupy mostly the exterior of the sintered aggregate.

LaCrO_3 would initially be subject to the same heat treatment as LaCoO_3 , but as Figure 8.6c and the resulting HAADF images show in Figure 8.9, LaCrO_3 appears to be strongly resistant to sintering with essentially no changes to morphology. Risking Atmospheric cell failure, the temperature was raised to 1000 °C where it was observed that the aggregate continued to maintain its nanostructure.

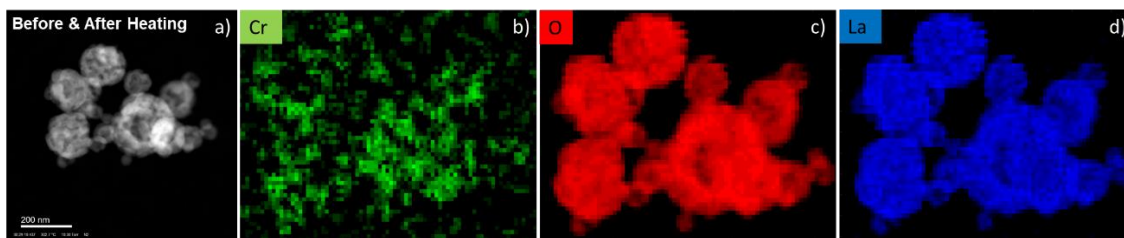


Figure 8.9: TEM imaging and EELS elemental mapping of LaCrO_3 before and after the proscribed heat protocol under 760 Torr nitrogen gas.

The chromium EELS mapping is less than ideal but remains constant before and after heating and one can infer that it is roughly uniform throughout. The oxygen and lanthanum EELS mappings remain invariant through the heating process, illustrating the immobility of the atoms within the lattice. What is most interesting about this behavior was that the Atmospheric cell did not fail despite doing so in several prior attempts with other samples not documented here. One may surmise that the failure mode of the Atmospheric cell was due to the release of oxygen from the perovskite as it rose in temperature, compromising the seal of the membrane which was already operating at its pressure specification limits of 760 Torr. The failure mode effectively acts as an indirect indicator of how easily oxygen is released from the perovskites and is potentially correlated to the degree of aggregate sintering. This could explain why the intensity of oxygen detection in the post heated sample of $\text{La}_{0.6}\text{Sr}_{0.4}\text{CoO}_3$ is so low compared to LaCoO_3 and LaCrO_3 whose Atmospheric cell did not fail at equivalent temperatures. This notion is supported by the previous study by the Zachariah Group which showed weaker bond average bond energy of $\text{La}_{0.6}\text{Sr}_{0.4}\text{CoO}_3$ compared to LaCoO_3 which correlated to an oxygen release temperature and aluminum thermite ignition temperature of LaCoO_3 which is 100 °C higher.⁵⁸ This additionally supports the notion that strontium doping of the LaCoO_3 crystal lattice

results in early onset particle sintering and ease of oxygen gas liberation from the crystal lattice. According to Wang et. al., LaCrO_3 does not release gaseous oxygen nor does the aluminum thermite ignite within T-Jump temperature range.⁵⁸ It can be reasonably assumed that the bond energy and corresponding aluminum thermite ignition temperature would be even higher than LaCoO_3 considering the results observed here and that the family of similar chromium perovskites in the study by Wang et.al. have some of the highest bond energies and aluminum thermite ignition temperatures measured in the study.⁵⁸

As of the writing of this document, the last experiment conducted in this study was whether one could use EELS valence state mapping to track the progress of metallic oxidation and reduction in a chemical looping type scheme.²⁶⁵²⁶⁶ LaCoO_3 was the sample of focus where a heating protocol consisting of four separate regions as shown in Figure 8.10.

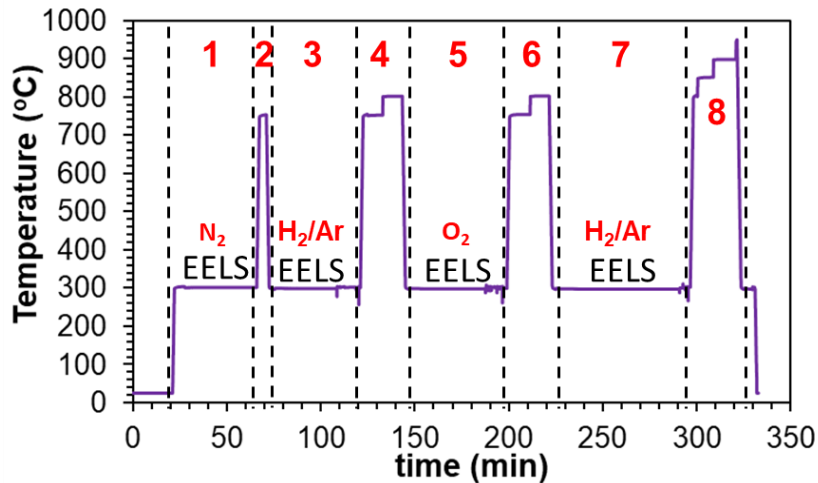


Figure 8.10: Heating protocol for simulating chemical looping experiments with cycling of H_2/Ar and O_2 environments

Temperatures of interest and hold times for simulating chemical looping are those based on the work done by Liu et.al.²⁶⁵ In order to eliminate any contaminations

and establish a relatively consistent morphology during cycling, heating to 750 °C is first carried out in nitrogen gas and held for 5 minutes. After cooling and establishing a baseline EELS mapping, the atmospheric cell is purged and filled with 760 Torr of reducing H₂/Ar. The sample is heated to 750 °C at 5 °C/s, held for 10 mins, increased to 800 °C, held for another 10 mins, cooled back down to 300 °C, and another EELS mapping taken. This same process was repeated after purging and filling with oxygen gas. In theory, this one cycle should be representative of additional cycling. However, heating under H₂/Ar was conducted again at higher temperatures to assess if higher temperatures would enhance the reduction process. The initial temperature started at 850 °C in which the Atmospheric cell failed at 950 °C. No significant morphological changes occurred during steps 3-7 in Figure 8.10 so it is difficult to make any conclusions from this simulated cycling which could be correlated to macroscopic measurements made by Liu et.al.²⁶⁵

EELS elemental mapping alone does not give any additional insight given that it only tracks the atom locations, not the valence state of the atom in question. The dual EELS capabilities of the FEI Titan TEM-STEM allow one to microscopically characterize the spatial distribution of the valence states of the atoms from the EELS data acquisition.²⁶⁶ Unfortunately, this is where the study has stalled due to scheduling conflicts, the need for higher resolved and better acquired EELS mappings, and a need for a third-party collaborator with expertise in EELS valence state data analysis.

8.2.4 Conclusions

Although not entirely conclusive, the observations made in this study act as a starting point for rigorous future studies with a more focused objective. This study centrally analyzes how perovskite nanoparticles such as LaCoO_3 , LaCrO_3 , and $\text{La}_{0.6}\text{Sr}_{0.4}\text{CoO}_3$ behave under in situ TEM heating in 1 atm of nitrogen gas. Except for LaCrO_3 , it was observed that heating to temperatures above 700 °C resulted in sintering of the nanoparticle aggregate with interior migration and separation of either the B-site or doped A-site metal atoms within the perovskite structure. A hierarchy of the degree of sintering can be ascertained from TEM images at comparable temperatures with Atmospheric cell failure acting as an indirect indicator of oxygen release. The higher degree in particle aggregate sintering the lower the temperature at which the Atmospheric cell fails ($\text{La}_{0.6}\text{Sr}_{0.4}\text{CoO}_3 < \text{LaCoO}_3 < \text{LaCrO}_3$). Additionally, the sintering behavior can be correlated to the average lattice bond energy and oxygen release temperatures determined from previous studies where the lower bond energy ($\text{La}_{0.6}\text{Sr}_{0.4}\text{CoO}_3 < \text{LaCoO}_3 < \text{LaCrO}_3$) and temperature of oxygen release ($\text{La}_{0.6}\text{Sr}_{0.4}\text{CoO}_3 < \text{LaCoO}_3 < \text{LaCrO}_3$) corresponds to a higher degree of sintering ($\text{La}_{0.6}\text{Sr}_{0.4}\text{CoO}_3 > \text{LaCoO}_3 > \text{LaCrO}_3$). Future studies which continue this work with respect to simulating chemical looping experiments in reducing and oxidizing atmospheres is strongly encouraged. The novelty of this experimental approach in spatially characterizing the apparent mobility of atomic species and dynamics of metallic valence states within the particle structure during the cycling process would contribute greatly to understanding their microscopic mechanics. However, it is advised to select solid perovskite nanoparticles with as little interior structure features

as possible and choose perovskite systems which maintain nanostructure. Quantitatively, this would correspond to perovskites with relatively high average bond energy, such as the doped perovskite family of $\text{La}_{1-\delta}\text{Sr}_\delta\text{CrO}_3$, to limit the potential for Atmospheric cell failures and isolate the role of morphological dynamics due to aggregate sintering.

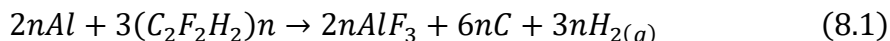
8.3 MBMS Characterization of Energetic Films

8.3.1 Introduction

The fabrication of energetic nanocomposites employing metallic nanoparticles has become a promising frontier in the search for new materials with a high-energy density. Enhanced reactivity derived from increased specific area, higher mass diffusivity, and decreased diffusion lengths between fuel and oxidizer make these materials highly desirable as a fuel source in solid propellant systems.^{27,268} Typically, solid propellants utilize polymer-based binders which not only provide the composites their mechanical integrity but can also act as an oxidizing source, as in the case of fluoropolymer binders.^{7,95} The ability to probe reaction dynamics in such transient energetic systems is critical to the analysis of fast chemistry processes such as rapid thermal decomposition, ignition, and combustion of energetic materials. Previous work utilizing Linear Time-of-Flight Mass Spectrometry coupled with platinum wire rapid heating ($\sim 10^6$ K/s, T-Jump/TOFMS) characterized the reaction mechanism of Al/PVDF material at combustion time scales within the operational high vacuum environment ($\sim 10^{-6}$ Torr).⁶⁷ This work proposed a reaction mechanism which stated that the prerequisite for ignition and self-sustaining combustion of the material relies

on the decomposition of PVDF to hydrogen fluoride (HF) which reacts exothermically with core-shell aluminum nanoparticles to form aluminum fluoride (AlF₃) and hydrogen gas (H₂).⁶⁷

Fluorination of Aluminum:



With the rise of additive manufacturing as a means for rapid prototyping of energetic materials incorporating nanomaterials with novel architectures,⁹⁷ it is of great interest to explore structure-function relationships of energetic materials with respect to not only modes of combustion, but also how microscopic and macroscopic architectures may affect the resulting combustion product species when burned in differing environments.^{63,72,90,98} As mention previously in Chapter 2, although the T-Jump/TOFMS system has the capability to report time resolved speciation of gas phase products at sample rates as high as 10 kHz, it does not have the capability to probe real time flame products of relatively large samples (>30 μg) at elevated pressures.

A Molecular Beam Mass Spectrometer (MBMS) coupled with high speed videography was developed to probe the atmospheric reaction mechanism of thin film laminates comprised of readily available nano-aluminum and the fluoropolymer Poly(vinylidene fluoride) (Al/PVDF). The motivations and specifics of the MBMS mechanics are detailed in Chapter 2 but are reiterated briefly here. Unlike the TOFMS system, the ignition and combustion of the film within the MBMS system occurs outside of the of the ionization region, eliminating any chance of damage to the system's electronics by violent ignition events. This allows for the study of larger, more architecturally complex samples within a chemical environment which is rich in

gaseous collisions. As a result, various reaction products not seen in vacuum may be detected during the full duration of flame propagation (≈ 1 second), allowing the reaction to be studied under practical conditions. The MBMS possesses the essential feature of a sudden transition from a continuum environment to one which is collisionless, creating an ultra-cold ($\approx 1-3$ K) supersonic molecular beam which enables the preservation of the sample (Figure 2.8).^{140,142} Additionally, the MBMS system has enhanced mass spectrum resolution utilizing the systems Reflectron design which doubles the focal length of the flight tube.

This study serves as a preliminary study on how one may effectively operate the MBMS system in probing the transience of product species of Al/PVDF energetic systems with various constituents comprised of differing chemistries, length scales, and architectures. Additionally, this study assesses the potential utility of synchronizing MBMS speciation with Color Camera Pyrometry (CCP) for spatiotemporal temperature mapping as a function of species detection.¹¹⁶ Characterization of the combustion performance and product species of Al/PVDF films with additional niche additives is conducted by utilizing the Al/PVDF mass spectrum as a baseline reference. In general, additives need not contribute energetically to the system but are used to take advantage of other utilities they may possess. Mesoporous silica and iodine are used as case study materials for MBMS analysis as they have been the focus of many studies of energetic materials. Previous studies suggest that films with homogeneously dispersed mesoporous silica have enhanced energy transfer properties as a result of efficient convective flow transfer, leading to increased flame propagation speeds.²¹⁰ Heterogeneous energetic materials incorporating iodine containing chemicals have had

several studies conducted with respect to their potential tunability in biocidal applications.^{77,121,151,269,270} The release of iodine in energetic materials can in general be carried out using a secondary iodine containing oxidizer whose product is iodine gas, or the use of solid iodine which sublimates as a result of energy release from energetic components.^{121,271} In this case study, condensed phase iodine (I₂) powder is utilized as a means of comparison to mesoporous silica.^{151,269} Both materials are not expected to contribute significantly as an energetic constituent and will thus serve as benchmarks for tangential compositions with similar prospective applications.

8.3.2 *Materials and Experimental Approach*

Materials:

Nano-Aluminum (nAl) ($\approx 85\text{nm}$) was purchased from Novacentrix and determined to be 81% active via thermogravimetric analysis (TGA). Poly(vinylidene fluoride) powder (PVDF) (MW=534000), dimethylformamide (DMF) (99.8 wt. %) solvent, and neat Iodine (99.8 wt. %) were purchased from Sigma-Aldrich (Millipore Sigma). Mesoporous Silica (99 wt. %) ($\approx 1\ \mu\text{m}$) was synthesized through the process of spray drying.²⁷² High-speed video was taken using a Phantom Vision Research Miro M110 digital color camera digital running Phantom 692 software and operating at 3000 fps. A quartz tube ($\approx 1\ \text{m}$) was purchased from Quark Glass, melted at the end by a hydrogen flame, and sanded down in order to create a small orifice (100-200 μm diameter) at the end.

Film Synthesis:

The fabrication of Al/PVDF films was conducted using the proven technique of scalable electrospray^{63,273} assembly but may also be fabricated using layer-by-layer

additive manufacturing techniques.^{72,108} A precursor solution is first prepared by dissolving 70mg/ml PVDF in DMF, mixing in aluminum nanoparticles, sonicating the solution for 1 hr, adding the niche additive material, sonicating the solution for 1 hr, and finishing with 24 hrs of stirring on a magnetic stir plate. The amount of added aluminum powder is based on the stoichiometric ratio of aluminum and PVDF (25 wt.% Al/ 75 wt.% PVDF). Mass loadings of I₂ (20 wt. %) and SiO₂ (5 wt. %) are based on previous studies for which their inclusion was based upon.^{151,210}

The electrospray assembly technique involves the application of an electrical field to a nozzle containing the electrically conductive precursor solution. The applied field results in a deformation of the shape of the fluid at the nozzle tip caused by the crowding of charges at the air-liquid interface. This behavior introduces hydrodynamic instabilities which lead to Coulombic forces overcoming cohesive forces and atomizing the precursor solution into a fine, monodispersed spray.^{63,95,273} The spray is deposited and dried on a grounded rotating aluminum foil substrate resulting in the direct fabrication of nanoparticle polymer composite laminates which can be peeled from the aluminum foil.⁹⁵ The nature of this assembly process makes it possible for these structures to be synthesized at much higher precursor viscosities and therefore made highly tunable in size, shape, and reactant content.^{63,90,95,96,98,273}

Characterization:

Combustion of stoichiometric Al/PVDF films was conducted in ambient air and 1 atm N₂ environments with ignition of Al/PVDF in the vacuum of the T-Jump/TOFMS used as a reference. Combustion of each sample occurred at the end of the 10-mm diameter quartz tube near the sampling orifice while the atmosphere was maintained

by a constant inlet and outlet flow of gas (Figure 2.8). Electrospray synthesized films (5-8 mm × 2.5-3.5 mm × ≈0.10 mm) were sandwiched between two thin nichrome wires (0.10" diameter) anchored to the ends of two copper leads and ignited via Joule heating from an external power supply. During combustion, hot gaseous products rapidly expand through the ≈100 μm sampling orifice at the end of the quartz tube into an intermediate region of relatively low pressure (~10⁻⁴ Torr), and into the E-gun (70 eV) ionization chamber (~10⁻⁶ Torr) through an adjacent skimmer cone with an inner diameter of 450 μm (Figure 2.8). As mentioned in the introduction of this section, the sudden transition from a continuum environment (reaction event) to one which is collision-less (E-gun ionization region/flight tube) creates an ultra-cold supersonic molecular beam which preserves and directs the flow of product species until reaching the detector of the mass spectrometer.¹⁴³ Time-dependent mass spectra data is collected with a 600 MHz Teledyne LeCroy Oscilloscope and saved to MATLAB for further analysis and processing.

Typically, the level of materials used in MBMS sampling (1-50 mg) is large enough such that the ability to measure the ignition temperature of the energetic material or release temperature of certain chemical species is lost. Thus, the assumption of the platinum wire temperature being approximately that of the material, as is the case in T-Jump characterization, is no longer valid.^{115,120,230} However, one may use the method of Color Camera Pyrometry (CCP), as briefly described in Chapter 4, in order to measure the spatiotemporal temperature profile of the flame using the same high-speed Phantom Vision Research Miro M110 camera.¹¹⁶

In general, high speed videography is synchronized with speciation and initiated by using a function generator outputting a square waveform (1-3 kHz) to the pulsar power supply of the biasing voltage plates, the camera trigger input, the heating mechanism, and the trigger input of the oscilloscope. The camera was focused upon the last 3-4 inches of the quartz tube closest to the sampling orifice to capture the combustion event (Figure 8.11). A mirror is needed to capture the combustion event since line of sight videography is obstructed.

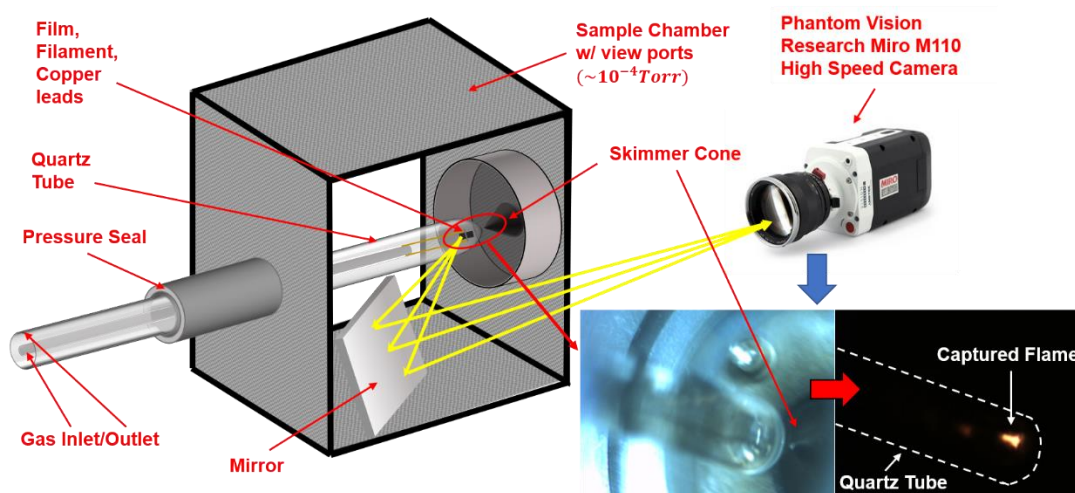


Figure 8.11: Quartz tube/camera setup within the vacuum environment of the sampling region of the MBMS

8.3.3 Results and Discussion

As a simple base line, Al/PVDF samples were heated to ignition in both the T-Jump/TOFMS and MBMS systems (Chapter 2). Figure 8.12 illustrates the resulting averaged mass spectra as measured by each instrument in their respective anaerobic environments (T-Jump/TOFMS in vacuum and MBMS combustion in 1 atm N_2). Although the mass spectra analysis of each instrument is time resolved, the mass spectrum averaged over the entire recorded time allows one to clearly observe which species truly appear above the noise.

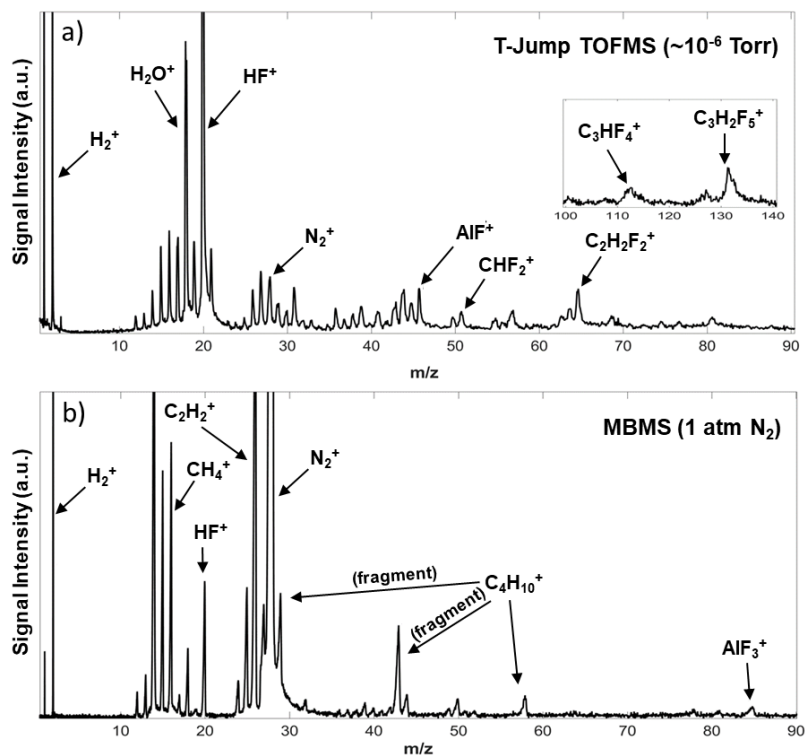


Figure 8.12: Al/PVDF combustion mass spectra in a) Vacuum ($\sim 10^{-6}$ Torr) for T-Jump/TOFMS ignition product sampling and b) 1 atm N_2 for MBMS combustion product sampling.

Along with background air (N_2^+ , O_2^+ , H_2O^+) and corresponding fragmentations (OH^+ , O^+ , H^+ , N^+), several intermediate and radical species with mass to charge ratio (m/z) values between 30 and 140 are detected in the vacuum environment. These species have roughly the same signal intensity and are formed just prior to and immediately following ignition. Many of these species are decomposition products of PVDF such as CHF_2^+ ($m/z=51$), $\text{C}_2\text{H}_2\text{F}_2^+$ ($m/z=64$), C_3HF_4^+ ($m/z=113$), and $\text{C}_3\text{H}_2\text{F}_5^+$ ($m/z = 133$) which have been characterized in independent pyrolysis studies.^{187,274} Conversely, the MBMS mass spectrum from Al/PVDF combustion (Figure 8.11b) illustrates a chemical landscape which is devoid of the same mass species depicted in the vacuum spectrum (Figure 8.12a). The MBMS spectrum is rich in relatively stable

products such as methane (CH_4 , $m/z=16$), the relatively high enthalpy species acetylene (C_2H_2 , $m/z=26$)²⁷⁵, butane (C_4H_{10} , $m/z=58$), and other lower mass hydrocarbons which can be identified by matching their fragmentation patterns to those patterns documented in the NIST Webbook. The relatively unstable intermediate species have virtually no opportunity to interact with other molecular species given their long mean free path in the vacuum environment. The elevated atmosphere in the sample region of the MBMS provides an environment conducive to intermediate and radical species collisions resulting in the prevalence of the observed stable products. Although detection of HF ($m/z=20$) and H_2 ($m/z=2$) was achieved in both systems, the final product species of anhydrous AlF_3 ($m/z=84$), was detected only in the MBMS. The formation of AlF_3 in the vacuum environment of the T-Jump/TOFMS is limited by the interaction of HF with aluminum. The global reaction between HF and Al becomes one which is fuel rich due to the swift exit of gaseous HF from the reaction region.⁷² As a result, only the intermediate species of aluminum monofluoride (AlF , $m/z=46$) is potentially detected, signifying the initiation of reaction.³² The conditions of the MBMS allow for continuous interactions of HF and Al, favorable to the formation of AlF_3 which, according the NIST Webbook, has a relatively high vapor pressure above ≈ 1500 K.^{67,72}

Sampling of combustion products through the $100\ \mu\text{m}$ sampling orifice proved to be more difficult than what is theoretically laid out in Chapter 2. Positioning of the sampling orifice must have the area of the opening be parallel with the opening of the skimmer cone at an optimal distance away. This process can be difficult and tedious but can be greatly aid by monitoring and maximizing the real-time signal intensity, and

by using a xyz-stage manipulator with flange connections. Additionally, the small sampling orifice of the quartz tube can easily clog with soot depending on the combustion environment and composition of the energetic films. This severely disrupts the molecular beam and leads to the extinction of combustion species being detected. Clogging of the orifice happened most often with larger sample quantities with relatively violent combustion events having burned in anerobic environments. As a result, several experimental runs were conducted with the best mass spectra from the combustion of Al/PVDF, Al/PVDF/I₂ (20 wt.%), and Al/PVDF/SiO₂ (5 wt.%) shown in Figure 8.13. Combustion with energetic composites which generate mostly gas products (nitrocellulose) or are burned in air help to alleviate the clogging problem.

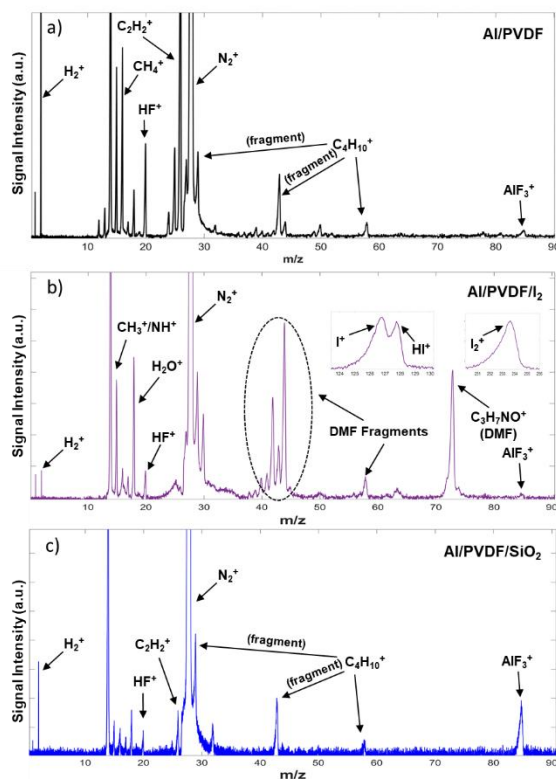


Figure 8.13: a) Al/PVDF combustion average mass spectra in N₂ with additives: b) 20 wt.% I₂ and c) 5 wt.% SiO₂

While the average mass spectrum of Al/PVDF/SiO₂ is nearly identical to the average mass spectrum of Al/PVDF with respect to the types of chemical species detected, the mass spectrum of Al/PVDF/I₂ combustion contains notable heavy species of molecular iodine (I₂⁺, m/z=254), atomic iodine (I⁺, m/z=127), and hydrogen iodide (HI⁺, m/z=128). Additionally, the inclusion of I₂ has evidently made it harder for the solvent to evaporate post fabrication when compared to the Al/PVDF and Al/PVDF/SiO₂ composites. A large amount of DMF (C₃H₇NO⁺, m/z=73) and its fragments (NIST Webbook) is detected and dominates the mass spectrum in this range of mass values. The excess, unevaporated DMF clings onto the I₂ crystals, making it harder for the DMF to evaporate from the composite.

The characteristic temperature of combustion for each system was initially qualitatively inferred by the intensity and transience of the production of sublimated AlF₃ being detected for each system. Higher combustion temperatures could enhance the volatility of AlF₃ sublimation, leading to higher concentrations of the chemical species being detected. Figure 8.13c shows that the AlF₃ intensity is highest in Al/PVDF/SiO₂ combustion and lowest in Al/PVDF/I₂ combustion. This suggests that Al/PVDF/SiO₂ may burn hottest and Al/PVDF/I₂ burn coolest. The combination of the relatively high mass loading of I₂ and excess DMF act as a heat sink leading to their evaporation/sublimation and ultimately a lower overall predicted flame temperature. The flame speed enhancement caused by the addition of mesoporous silica to the Al/PVDF film may also suggest an increase to the temperature during burning.²¹⁰ The previous study conducted by the Zachariah Group suggest mesoporous silica increases

the rate of HF production while simultaneously promoting flame propagation via convection due to its porous nature.²¹⁰ The analysis of time resolved speciation of HF and AlF₃, shown in Figure 8.14, appear to reinforce the findings from that study.

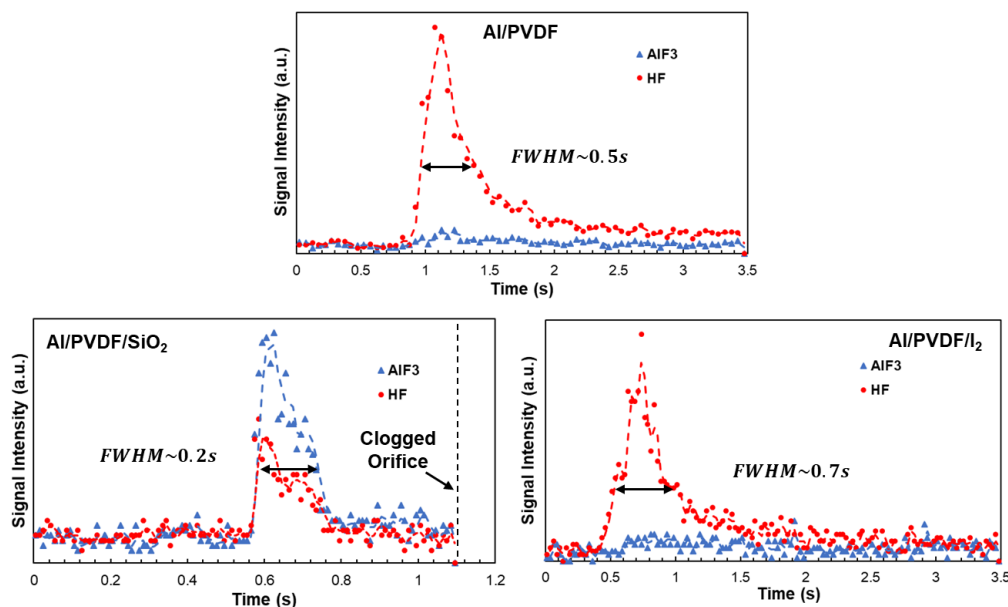


Figure 8.14: Species over time of HF and AlF₃ detected as products from the combustion of Al/PVDF, Al/PVDF/SiO₂, and Al/PVDF/I₂ in 1 atm N₂.

Al/PVDF, Al/PVDF/SiO₂, and Al/PVDF/I₂ laminates of equivalent geometries were burned in 1 atm N₂ where the absolute time of detection of a species is relative to the trigger signal received by the oscilloscope from the trigger box. However, the absolute time of emergence of species detection depends on how the nichrome wire delivers heat to the film during the ignition process (trigger box initiated). The only useful analysis is the relative time of detection between species within a single combustion event and how the behavior compares with systems of varying compositions. HF and AlF₃ signals from Al/PVDF/SiO₂ combustion are detected at the same time with a significantly stronger transient signal intensity of AlF₃ compared to the AlF₃ originating from Al/PVDF and Al/PVDF/I₂ combustion. Whether or not the

AlF₃ product was detectable, the widths of each HF peak in Figure 8.14 act as a rough indicator of how long the combustion event occurred, suggesting that the film with mesoporous silica consumes the oxidizing agent faster, resulting in increased flame speed and a potentially hotter flame temperature.

Quantitative temperature measurements of the combustion event are captured by synchronizing speciation and initiation with high-speed videography of the flame within the quartz tube (Figure 8.11). High-speed videos are processed using the CCP software to obtain temperature mappings within the flame as a function of time (Figure 8.15).

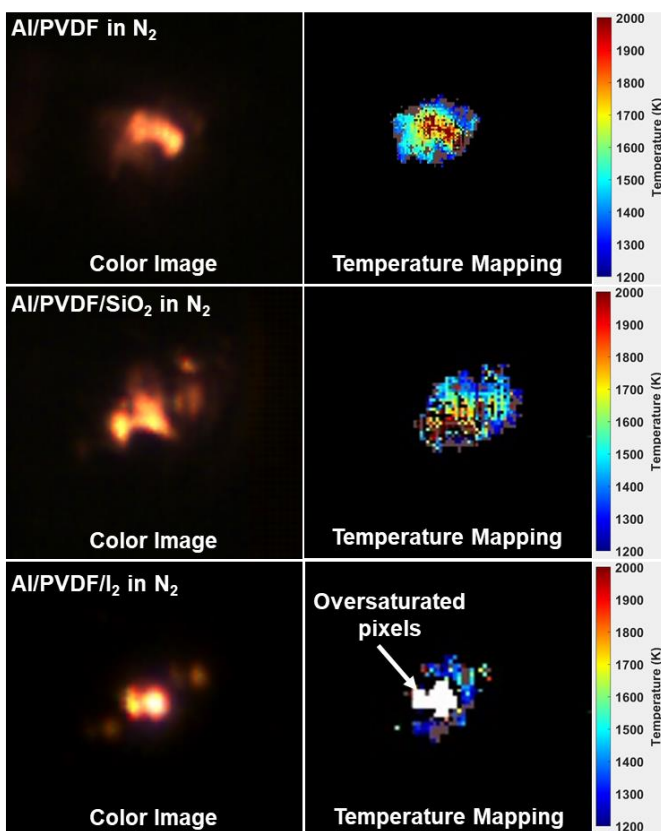


Figure 8.15: Spatial mapping of the temperature distribution of the flame from the combustion of Al/PVDF-based energetic films within the quartz tube of the MBMS.

As one may predict, the distribution of the flame temperatures in each case is one which is hottest in the center and coolest towards the outer perimeter. It should be noted that limitations of pixel resolution, inflexibility of camera perspective, and reflections within the quartz tube make obtaining a clear image which accurately represents the thermal landscape difficult for precise thermal analysis. Additionally, each material composite burns differently with respect to the intensity of emitted light. Adjustments to the camera light exposure (10-250 μ s) are necessary to avoid oversaturation which results in null temperature measurement at each respective pixel. Nevertheless, one may plot the mean temperature of each flame as a function of time for a more quantitative analysis for comparison (Figure 8.16).

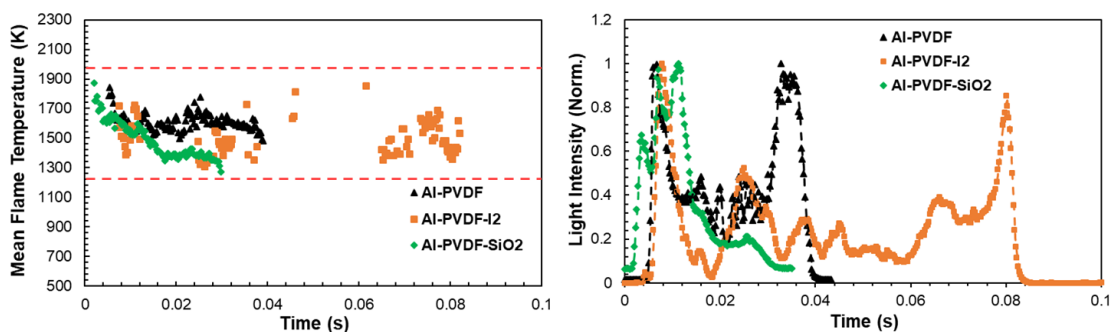


Figure 8.16: Mean spatial flame temperature and corresponding light intensity from Al/PVDF composite combustion.

The most interesting result from temperature plot in Figure 8.16 is that the combustion temperature of each material is roughly the same with the spatial mean temperatures in the range of 1300-1900 K for all combustion events in 1 atm N_2 at any given time. These results are in direct contradiction to the initial qualitative analysis which attempts to link the level of AlF_3 detection to the temperature of the reaction. However, the light intensity plot shows that the main combustion event of Al/PVDF/SiO₂ occurs roughly 1.5 times faster than the Al/PVDF combustion event

and nearly 3 times faster than the Al/PVDF/I₂ combustion event. What I am observing in this case is that the intensity of AlF₃ production in these systems appears to be linked to the burn rate, or reactivity, of the films and not the temperature of combustion. Faster burning of the material may indicate more efficient combustion with respect to reactivity and result in higher concentrations of product species which are sampled and contribute to a higher detection intensity. This result is in good agreement with the findings in Figure 8.14 and the mesoporous silica study by Wang et.al. which observed enhanced burn rate of materials as a result of material porosity and the ability of mesoporous silica to initiate PVDF decomposition at lower temperatures compared to the baseline Al/PVDF composite.²¹⁰

Thus far, this study has shown the ability to detect transient species of combustion products and perform thermometry on the combustion event. One of the main goals of this preliminary study is to assess whether synchronizing these experimental techniques can link the behavior of the flame with the evolution of the mass spectrum of detected product species. This experiment was conducted in air as to observe the evolution of how released organic species from the initial Al/PVDF reaction maybe consumed by the diffusion limited reaction with air, generating carbon dioxide. Speciation of acetylene and carbon dioxide over 2.5 seconds are shown in Figure 8.17a with a time scale comparison to the combustion event shown in Figure 8.17b.

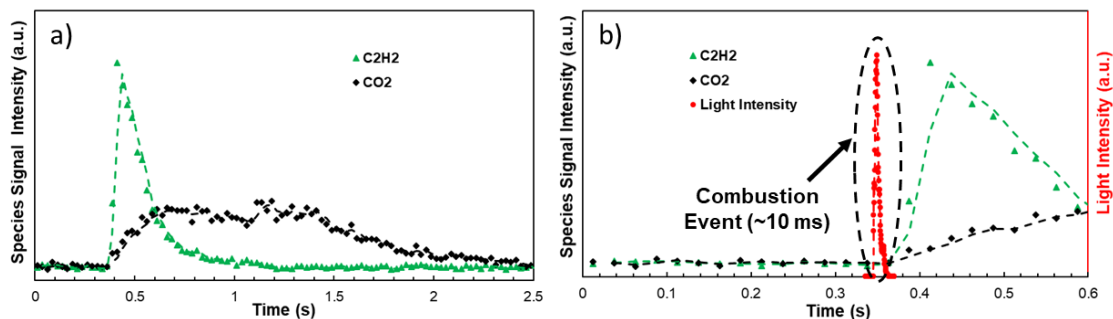


Figure 8.17:a) Evolution of acetylene and CO₂ product species of Al/PVDF combustion in air compared with the b) time scale of the combustion event.

Figure 8.17a illustrates the initial emergence of the acetylene intermediate followed by its immediate disappearance as O₂ in air reacts with acetylene to form CO₂. However, when plotted with respect to the absolute time after the trigger pulse, one can see that the entirety of the combustion event occurs before the detection of any combustion products above the background noise. Species evolution lags the combustion event by its ≈ 10 ms combustion time where the full combustion event is roughly two orders of magnitude shorter than then the length of time where products are detected. Within the combustion time frame, it is likely that gaseous reactant, intermediate, and product species thoroughly mix in the relatively stagnant flow region behind the choked flow of the sampling orifice. Additionally, all temperature measurements in prior observations in N₂ are conducted within this same 10 ms time frame (Figure 8.16). The revelation of these findings makes it highly unlikely to make any correlations in time between species appearance/disappearance with flame temperature and relative light intensity using this technique.

8.3.4 Conclusions

This work reports on a preliminary study conducted to assess how molecular beam time-of-flight mass spectrometry (MBMS) may be coupled with color camera pyrometry to effectively characterize transient combustion products of previously studied Al/PVDF-based energetic films when burned in 1 atm environments. Comparisons of mass spectra of Al/PVDF in vacuum and 1 atm N₂ demonstrate a fundamental difference in the mass spectra collected in each environment with relatively stable product species, such as butane and acetylene, forming under pressurized conditions. The detection of transient product species and acquisition of spatiotemporal temperature mappings of the combustion events individually reinforce the findings made by previous works and may be expanded to include composites of expanded architectures and constituents. While the mean flame temperatures of each composite studied are nearly the same, the enhanced reactivity of Al/PVDF/SiO₂ lead to increased efficiency in the generation of the main reaction product of AlF₃. The inclusion of condensed I₂ in Al/PVDF films at relatively large mass loadings lead to reduced reactivity and limited DMF solvent evaporation. These findings suggest the need for better drying practices after fabrication as well and the use of iodine containing oxidizers instead of condensed I₂ as a means for enhanced reactivity while also releasing I₂ for biocidal applications. Despite these findings, time resolved correlations between the synchronized speciation and combustion behavior appear to be unfounded. The species detection lags the combustion event for which the time scale of combustion is two orders of magnitude faster than the time scale of species detection. Correlations between synchronous temperature measures of the reaction region within the quartz

tube and the detection of reaction products should only be made if the time for a molecule to reach the detector is much smaller than the reaction time scale (*e.g.* catalysis experimentation). However, the use of MBMS for relatively slow reaction kinetics would defeat the purpose of using its enhanced mass resolution capabilities needed for transient chemical systems over the smaller, more refined quadrupole mass spectrometers used in several catalysis studies.

8.4 The Role of Isotope Labeling in Thermite Systems

The ability to identify and map the progression of chemical reaction pathways is a pervasive endeavor within the chemical sciences community in order to better understand underlying physics or use the knowledge to progress in tangential undertakings and applications. This task can be difficult even in relatively slow reacting systems, especially in cases where the reacting molecular species are made up the same set of elements (*i.e.* organic chemistry). Each of these atoms have naturally occurring stable isotopes where the nucleus of the same atom type can contain a different number of neutrons, changing its atomic mass and relative energetic stability. The premise of isotope labeling exploits the fact that the natural abundance of non-radioactive isotopes of common reactive elements such as, hydrogen (^1H , ^2H), carbon (^{12}C , ^{13}C), oxygen (^{16}O , ^{17}O , ^{18}O), and nitrogen (^{14}N , ^{15}N) are heavily skewed to one isotope species over the other. On average, one would experimentally find that more than 99% of molecules consisting of one or more of these atoms are made up of ^1H , ^{12}C , ^{16}O , and ^{14}N (NIST Webbook). Theoretically, this means that one may use the relatively small abundant isotopes as tracers for the progression of chemical interactions which can be used to map chemical pathways and mechanisms of reaction. Experimentally, this involves

artificially concentrating the abundance of an isotope within one of the react species as to differentiate itself from other reactant species with similar atomic composition.

Detecting these species is a matter of probing the intrinsic differences among isotopes which primarily amounts to the difference in mass. Some experimental techniques distinguish the molecular species with the isotope tracer through spectral analysis by measuring and noting how the addition of neutrons changes the energy spacing between quantum energy states of the molecules involved.^{276,277} Most often, though, mass spectrometry is used as the simplest method to explicitly measure the mass of molecules sampled from a reaction regime. The relative abundance of species may be measured in order to filter out the sequence of species which propagates the labeling isotope as a function of the reaction progression.²⁷⁸

Here, I focus on the ability to precisely probe oxygenation pathways originating from metal oxides in thermite reactions by means of chemically doping the metal oxides with O¹⁸ labeled isotopes and analyzing thermite reaction behavior with T-Jump/Time of Flight Mass Spectrometry (Chapter 2). Nano-aluminum oxidation theory is a hotly debated topic within the energetic materials community with several modeling and experimental efforts trying to probe its oxidation behavior in various systems under various conditions.^{12,34,46,53,128,279–281} By coupling isotope labeling to T-Jump/TOFMS for a thermite system, I propose that one may be able to better decipher aluminum particle oxidation at combustion time scales by distinguishing oxygen contain product species which form as a result of oxygen transport originating from the metal oxide as opposed to oxygen originating from the native oxide shell of aluminum nanoparticles or elsewhere.

8.4.1 T-Jump/TOFMS Analysis of Isotope Labeled Nanoscale CuO

Preliminary data was acquired in collaboration with Dr. Kim Huynh, formerly of Eichhorn Group at the University of Maryland, College Park. We focused on the nano-thermite system of Al/CuO given its prevalence in literature, various applications as an energetic material, and relative ease of synthesis with respect to CuO. Assessing the ability of CuO to be effectively labeled and analyzed was first undertaken with isotope labeled nanoscale (<10 nm) copper(II) oxide (Cu¹⁸O) which was synthesized under anerobic conditions using water enriched with ¹⁸O.

The nominal Cu¹⁸O powder is washed with water to remove the NaCl byproduct and dried in the vacuum transfer chamber of an argon glovebox. The powder is brought out of the glovebox prior to T-Jump/TOFMS analysis (Chapter 2), dispersed in hexane, and coated on the 76 μm Pt wire of the T-Jump probe. The sample is flash heated to ≈1400 K over a 3 ms interval and the mass spectra of the heating event collected over 10 ms with a resolution of 1 mass spectrum per 100 μs. The cumulative mass spectra over the 10 ms collection time for commercial CuO (US Research Nanomaterials) and synthesized Cu¹⁸O reveals the major rapid pyrolysis products shown in Figure 8.18.

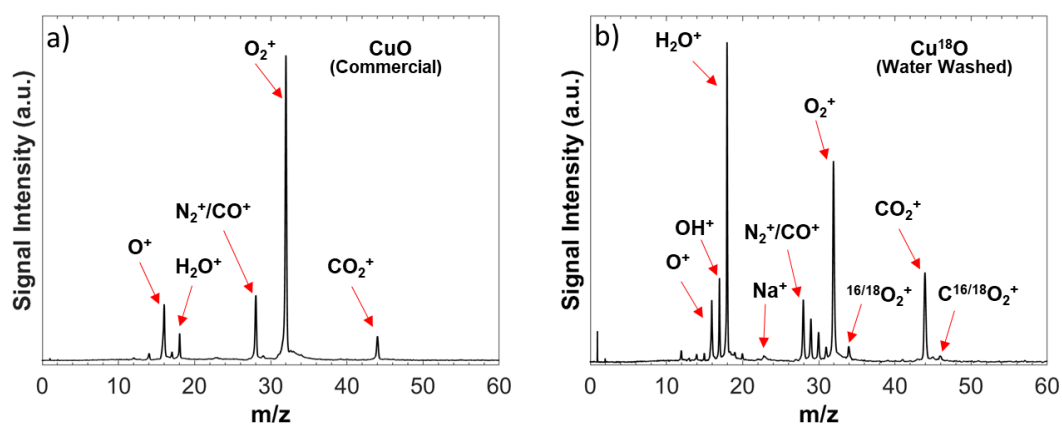


Figure 8.18: Average mass spectrum of a) commercial CuO and b) water washed Cu¹⁸O.

As Figure 8.18 shows, both the commercial CuO and nominal Cu¹⁸O powder release molecular oxygen with the dominant ¹⁶O isotope upon heating. Closer analysis of O₂, CO₂, and H₂O signals in the Cu¹⁸O spectrum shows the emergence of what appears to be O₂ and CO₂ species with mixed ¹⁶O and ¹⁸O isotopes (m/z=34, 46) as well as H₂O with an ¹⁸O isotope (m/z=20). The time resolved speciation of these signals in Figure 8.19 confirms the small release of the mixed isotope species emerging at the same time as the corresponding purely ¹⁶O isotope species.

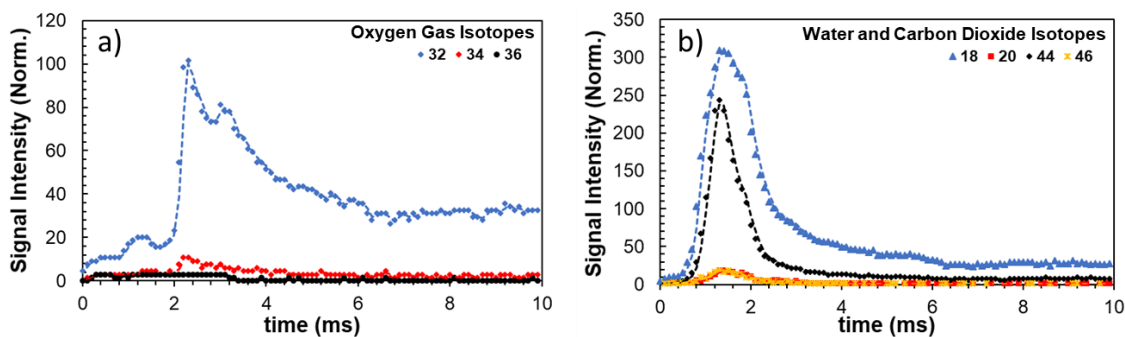


Figure 8.19: Time resolved mass spectrum analysis for Cu¹⁸O with respect to a) O₂ isotopes and b) water and carbon dioxide isotopes.

Examining the lack of purely ¹⁸O molecular oxygen and carbon dioxide was conducted with the assumption that the Cu¹⁸O powder could be undergoing isotopic exchange^{282,283} during either the washing process, exposure to air during wire coating process, or both. The major steps for reducing the potential for isotopic exchange included skipping the water washing process and utilizing the Air Sensitive Sample Holder (ASSH) attachment developed by former Zachariah Group member, Jeffery DeLisio.^{130,284} The ASSH attachment, shown in Figure 8.20, allows for the Pt wires of the T-Jump probe to be coated while inside the glovebox.

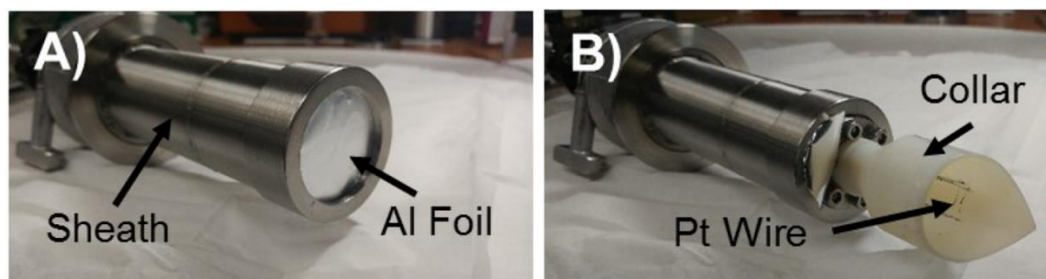


Figure 8.20: Air Sensitive Sample Holder (ASSH) with a) sheath and cap design with b) 3D printed collar for puncturing of the aluminum foil seal.¹³⁰

Cu¹⁸O nanopowder is dispersed in dry hexane, coated on the Pt wires, and are capped and sealed. A custom-made sheath and cap design creates a vacuum seal at the junction of the probe flange and an air tight seal at the end of the probe to ensure temporary isolation of the coated sample from the environment (Figure 8.20a). The T-Jump probe is removed from the glovebox and transferred to the roughing pump of the T-Jump/TOFMS instrument. The roughing port is purged with nitrogen gas for 5 minutes after which the aluminum foil seal is punctured using a 3D printed collar as the probe is extended within the roughing port (Figure 8.20b). Following the aluminum seal being breached, the inlet and outlet of the nitrogen gas purge are closed simultaneously, and the roughing port brought down to vacuum conditions ($\sim 10^{-2}$ Torr). T-Jump/TOFMS is conducted once the sample chamber is reduced to $\sim 10^{-6}$ Torr and detection of off gassing species from the 3D printed collar is minimized or negligible. The resulting cumulative Cu¹⁸O mass spectrum and time resolved speciation of molecular oxygen isotopes are shown in Figure 8.21.

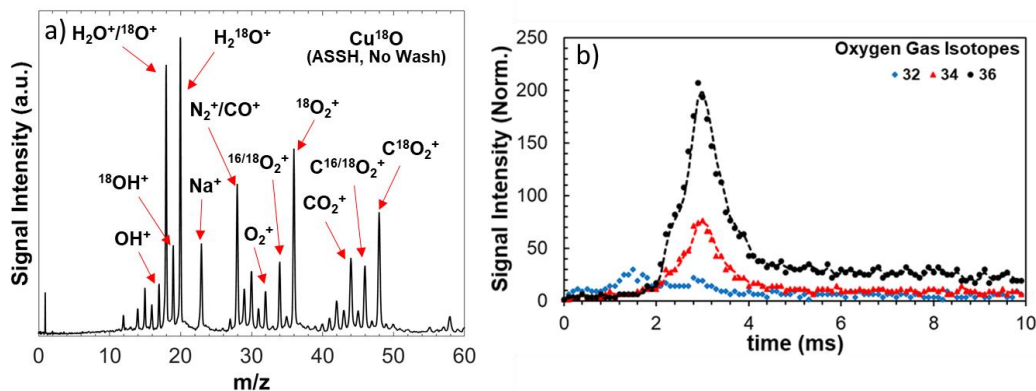


Figure 8.21: a) Cumulative mass spectrum and b) time resolved O_2 isotope speciation from T-Jump/TOFMS of $Cu^{18}O$ nanopowder prepared using air-free and water-free methods.

The nominally air-free, water-free preparation process of $Cu^{18}O$ synthesis and handling resulted in a mass spectrum for which released molecular oxygen is dominated by the ^{18}O isotope. While the time of oxygen release is identical, the relative signal intensities of O_2 isotopes in Figure 8.21b is in direct contrast to that in Figure 8.19a. $^{18}O^{18}O$ is now the dominate species of molecular oxygen released with virtually no $^{16}O^{16}O$ oxygen released. The $^{16}O^{16}O$ detected is due to the residual background air signal with no corresponding rise in signal intensity at the time of oxygen release compared to $^{16}O^{18}O$ and $^{18}O^{18}O$. Similar behavior is observed for the water ($m/z=20$) and carbon dioxide ($m/z=44, 46, 48$) isotope signals (Figure 8.22).

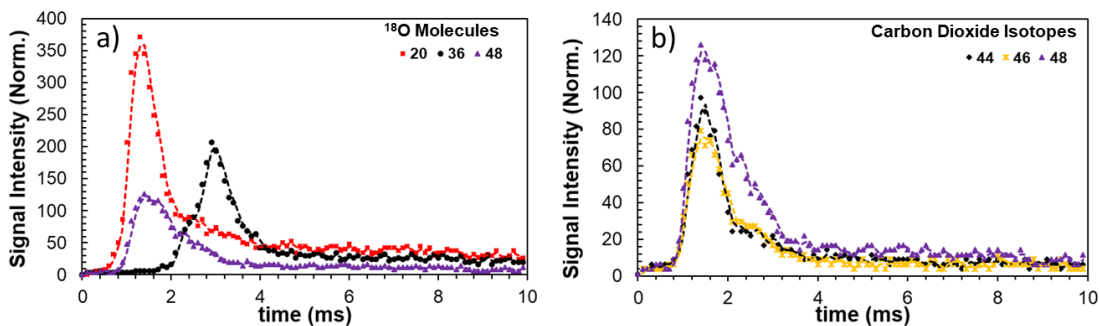


Figure 8.22: Time resolved speciation of a) major ^{18}O containing molecules (water, carbon dioxide, oxygen gas) and b) all carbon dioxide isotope species.

Figure 8.22 confirms the detection of heavy water, oxygen, and carbon dioxide with the time and sequence of their detection being identical to their ^{16}O counterparts in Figure 8.19. The strength of signal intensity of ^{18}O carbon dioxide and water may reinforce the original assumption of isotopic exchange. Water commonly adsorbs to the high specific surface area of nanoparticles during the preparation process with residual carbon species coating the surface when suspended in hexane. As a result, detection of water and carbon dioxide is common when nanoscale metal oxide particles are flash heated (Figure 8.18a).^{72,115} While carbon dioxide production may very well be as a result of some surface reaction with the coated carbon species and heated metal oxide, adsorbed ^{16}O water can only attain an ^{18}O through the process of isotopic exchange when adsorbed to the Cu^{18}O surface. The existence of ^{18}O water alone should not be unexpected as ^{18}O enriched water could have adsorbed to either the Cu^{18}O surface or unwashed NaCl byproduct during the synthesis process and not fully evaporated from the surface while under vacuum. However, the strong mass spectrum signals from both isotope species of water (Figure 8.21) make it completely plausible that isotopic exchange may occur at the particle surface during preparation. It is more likely, though, that the major instance of isotopic exchange occurs during the water washing step given the seemingly inevitable adsorption of both water isotopes during both preparation processes and the drastic difference in mass spectra in Figure 8.19 and Figure 8.21.

8.4.2 *Future Mechanistic Studies*

It is quite apparent from this initial study that Cu^{18}O was successfully synthesized and may serve as an oxidizer in thermite reactions. However, it is strikingly

clear that any further analysis of such materials must be prepared through methods which isolate the synthesized particles as much as possible from ambient air and water and undergo a washing step free of water. Here, the Cu^{18}O material prepared using air-free, water-free preparation methods skipped the washing step altogether as the strong Na^+ mass spectrum signal in Figure 8.21a demonstrates. In general, it is ideal to eliminate the NaCl byproduct through a washing process as to better formulate perspective thermite mixtures. The washing process would need to be further analyzed as to which solvent would be best to use for hindering potential isotopic exchange while effectively removing NaCl . Thermogravimetric Analysis (TGA) in tandem with TOFMS may be used as a tool to quantify the level of remaining NaCl after washing by measuring the mixture mass loss as a result of NaCl vaporization. Furthermore, the integration of the powder into a thermite mixture with a metal powder will extend the preparation time as the thermite mixture must have the isotope labeled metal oxide dispersed in dry hexane in a glovebox, brought out for sonication, brought back in the glovebox to introduce the metal nanoparticles, brought back out again for sonication, then finally brought back into the glovebox for Pt-wire coating before being loaded into the mass spectrometer.

While CuO is used as a case study material for initial studies of this diagnostic technique, it would be useful to synthesize other ^{18}O labeled, well studied metal oxides such as Fe_2O_3 and Bi_2O_3 which have differing thermochemistry and modes of oxygen transport compared to CuO .^{13,34} Additionally, control experiments focusing on mass spectrometry of thermite systems of various equivalence ratios using commercial nanoscale metal oxides should be conducted to identify oxygen containing gas phase

intermediate and/or product species which would serve as a point of focus for quantifying mechanisms of oxygen transport in the isotope labeled thermite mixtures. Further analysis of such systems is reserved for future studies and collaborative efforts.

Supplemental Information

Chapter 2 Supplemental Figures

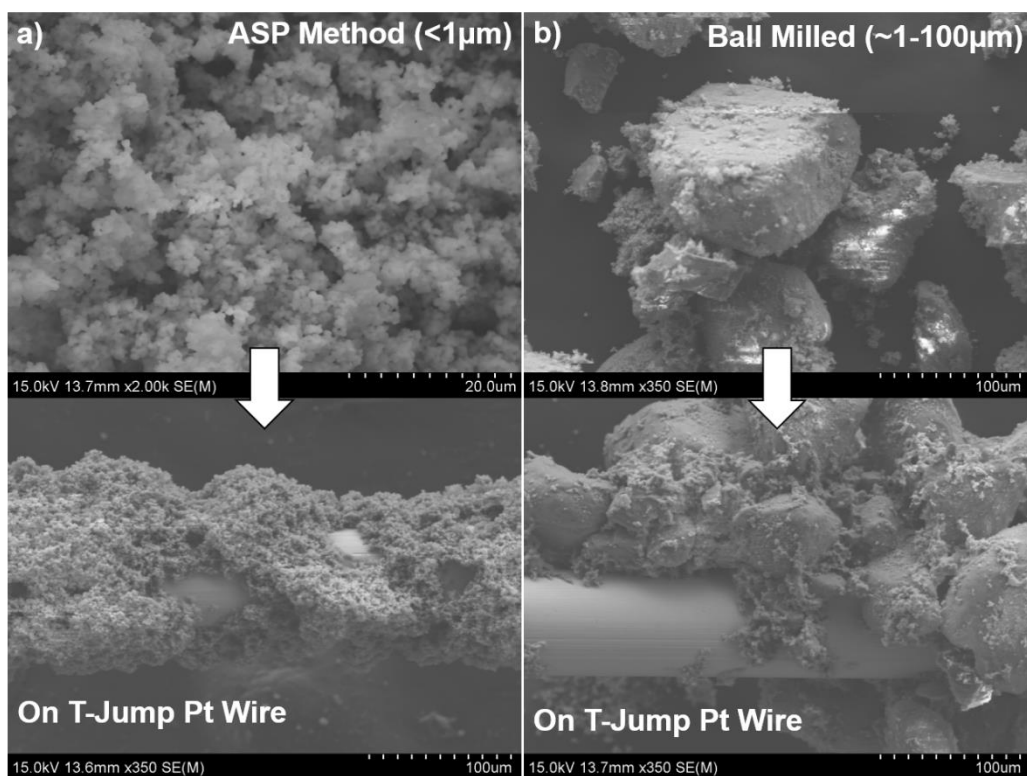


Figure S2.1: KClO_4 particles coated on T-Jump Pt wire with particles prepared by the a) aerosol spray pyrolysis method and by b) ball milling. Ball milling results in particles which are harder to coat on the $76\mu\text{m}$ Pt wire.

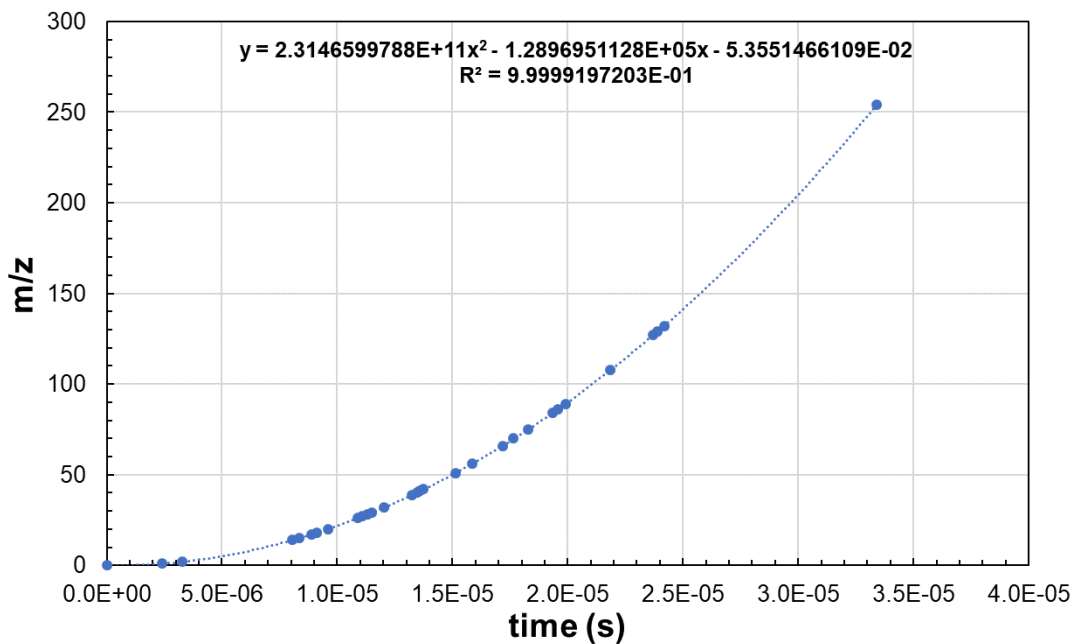


Figure S2.2: Example of the mass-time calibration for TOF collected in 2019.

Chapter 3 Supplemental Figures

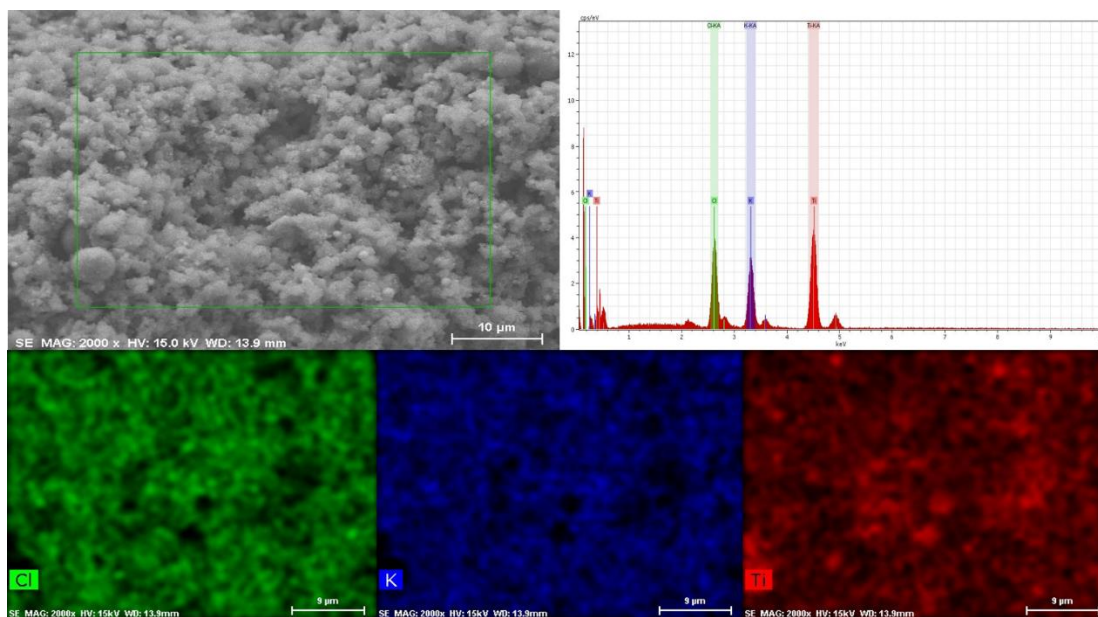


Figure S3.1: EDS of homogeneously mixed nTi/KClO₄ powder composite.



Figure S3.2: Protochips In Situ microscopy TEM heating probe.

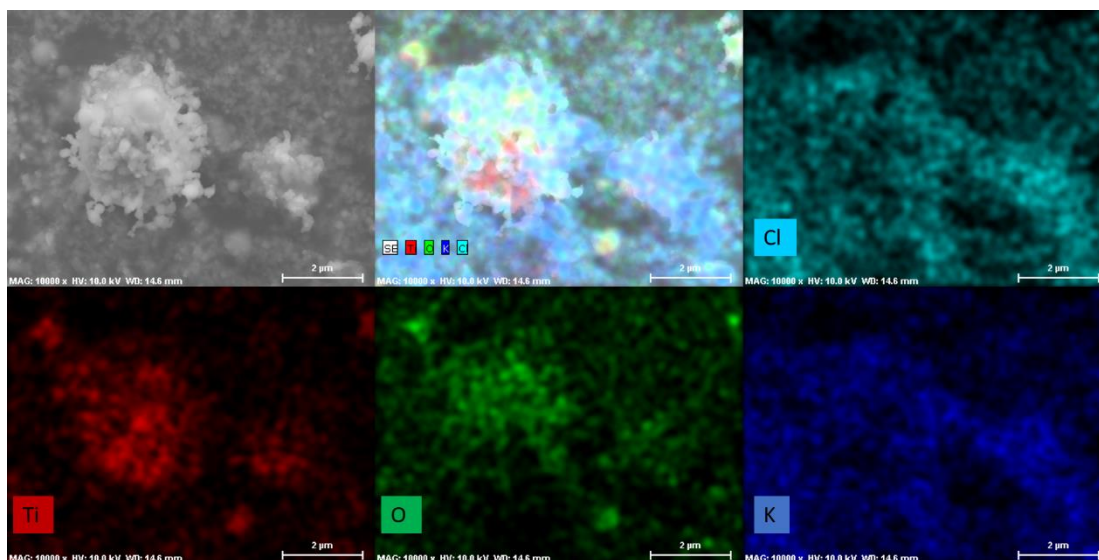


Figure S3.3: Post combustion products collected on carbon tape depicting titanium oxide formation with KCl first being vaporized by the heat of reaction then condensing on the surface of the titanium oxide.



Figure S3.4: Aluminum and Titanium nanoparticles immersed in water for 3 days (Titanium remains unreacted).

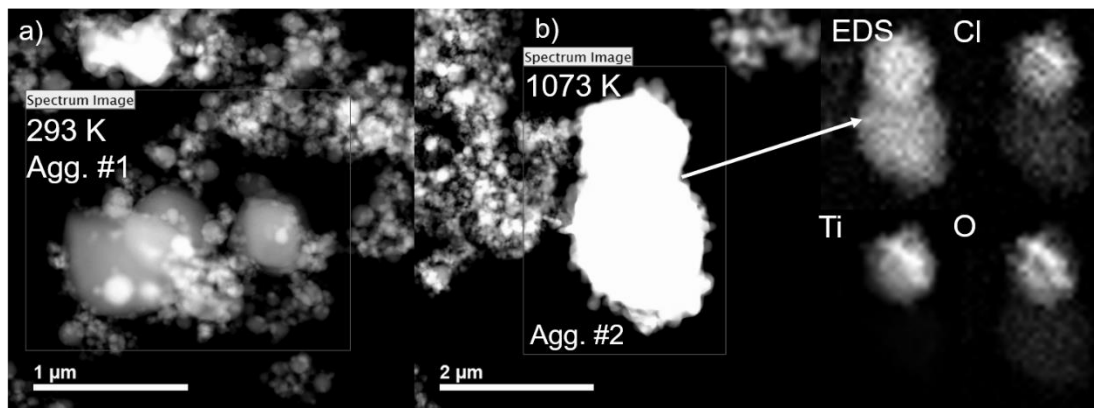


Figure S3.5: Comparison of a) room temperature TKP aggregate with a b) TKP aggregate which has been heat past the melting point of KCl and TEM elemental mapping performed.

Chapter 4 Supplemental Figures

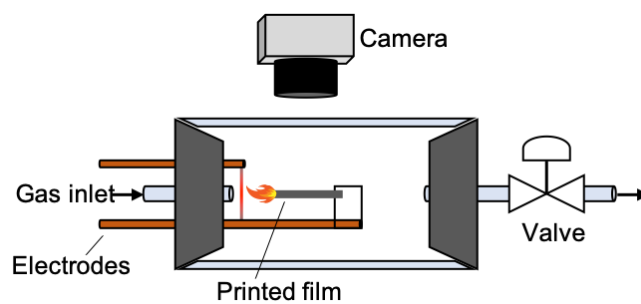


Figure S4.1: Quartz tube argon chamber for simultaneous film combustion and high-speed videography.

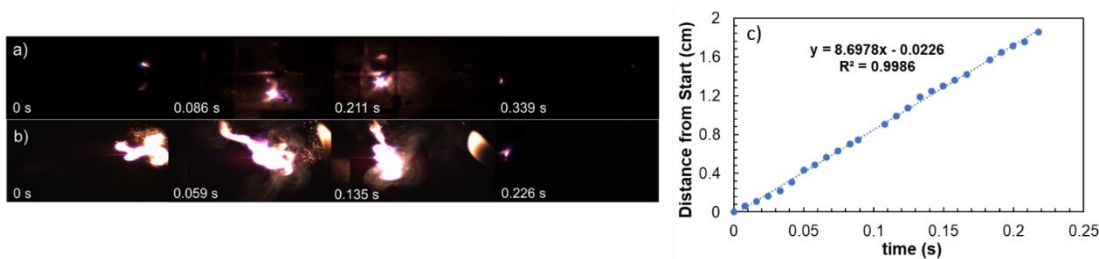


Figure S4.2: Combustion of Al/PVDF in a) argon and b) air captured at 3000 FPS and c) tracked using Image J to obtain flame speeds.

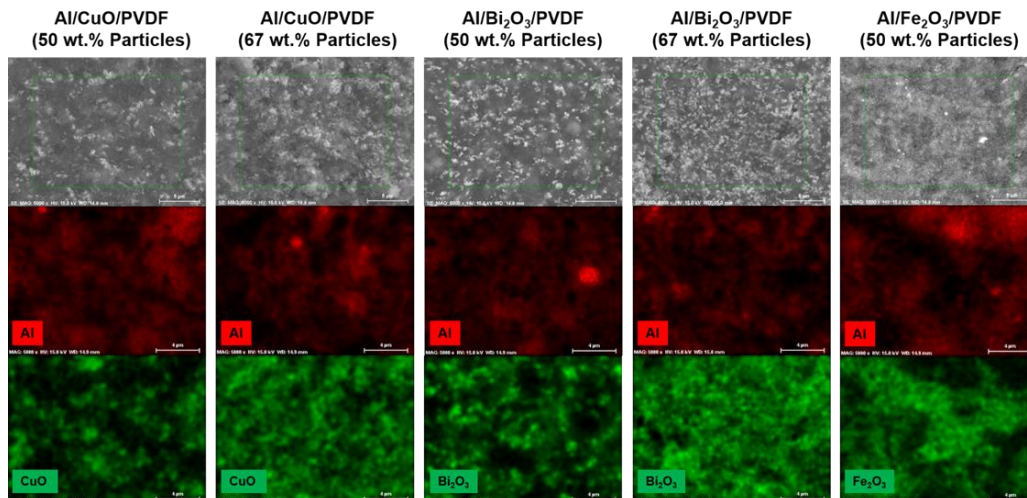


Figure S4.3: EDS homogeneity analysis of the cross-section of films with various metal oxides and particle loadings.

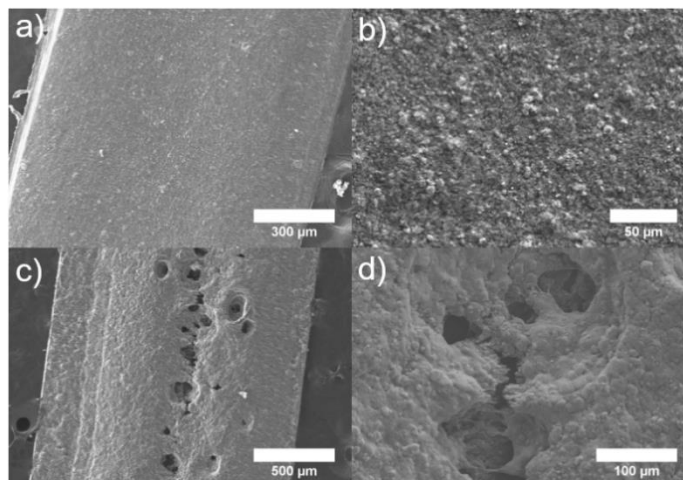


Figure S4.4: SEM images of the top surface of Al/Fe₂O₃/PVDF films at a)-b) 50 wt. % particle loading and c)-d) 67 wt. % particle loading.

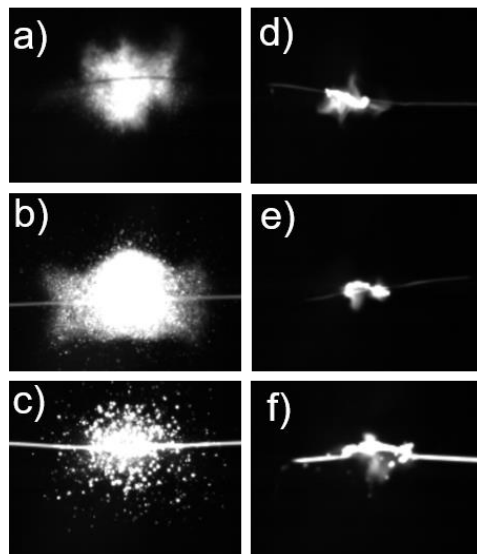


Figure S4.5: Comparison of a) Al/Bi₂O₃, b) Al/CuO, c) Al/Fe₂O₃ thermite ignition to d) Al/Bi₂O₃/PVDF, e) Al/CuO/PVDF, f) Al/Fe₂O₃/PVDF film ignition in argon.

Chapter 5 Supplemental Figures

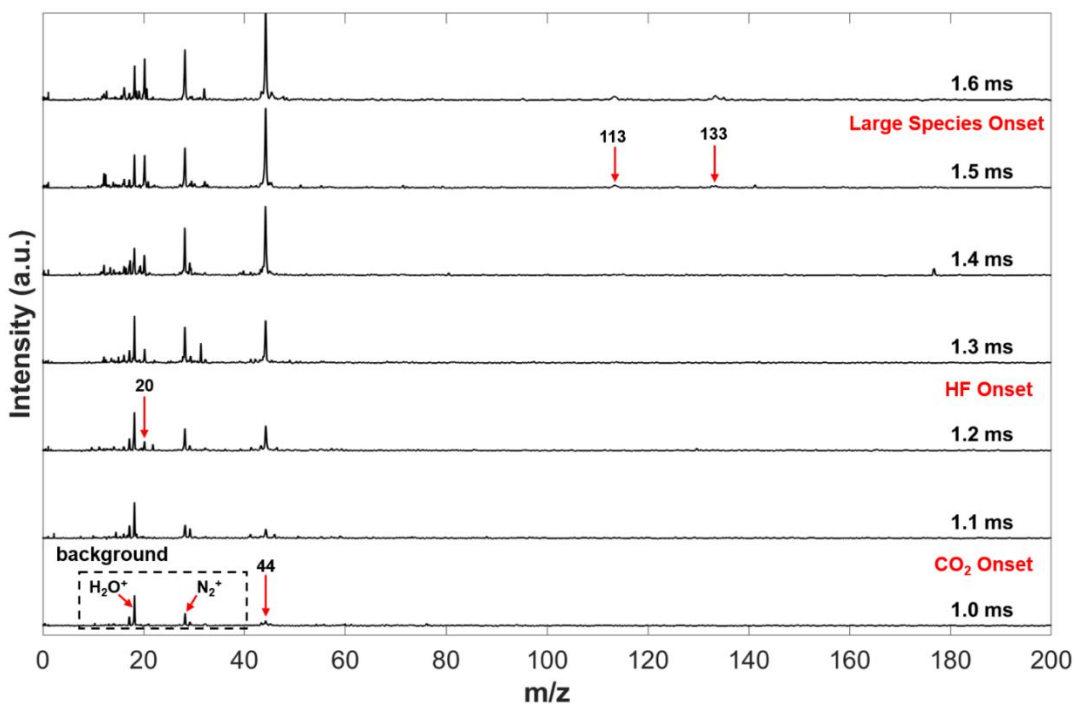


Figure S5.1: Time-dependent full mass spectra of rapidly heated CuO/PVDF ($\approx 3 \times 10^5$ K/s) over 3 ms depicting onset CO₂ prior to HF release and subsequent release of larger pyrolysis species.

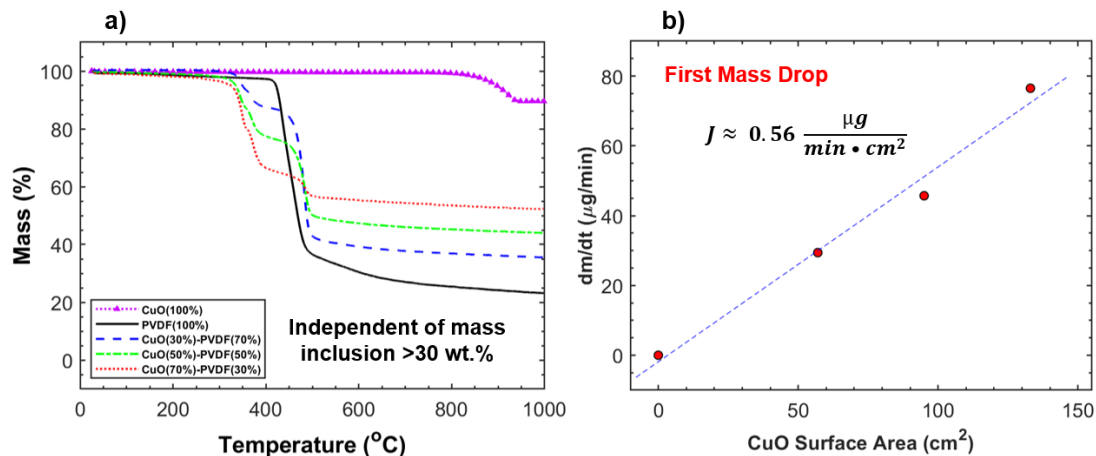


Figure S5.2: CuO/PVDF a) TGA profile and b) resulting rate of mass loss as function of CuO mass.

Chapter 6 Numerical Methods

The implicit finite difference approach for this model uses the Backward Time, Centered Space (BTCS) definitions (backward Euler scheme) for the first time derivative and second spatial derivative, respectively, with corresponding truncated errors, $O(\Delta t)$, $O(\Delta x)^2$, and $O(\Delta y)^2$.^{225,285,286} Numerical solutions to the governing equation using the implicit finite difference approach are unconditionally stable in which a system of equations is simultaneously solved for all temperatures in the next time step.^{213,224,287} Indices p , q , n represent the y -coordinate, x -coordinate, and time coordinate, respectively. Heat enters and leaves the node at each of the four boundaries outlining the grid area shown in Figure S6.1. Each temperature node is numbered based on the scheme of $T_{p,q}^n \equiv T_{(q-1)L_x+p}^n$ where the physical grid is $L_y \times L_x$.

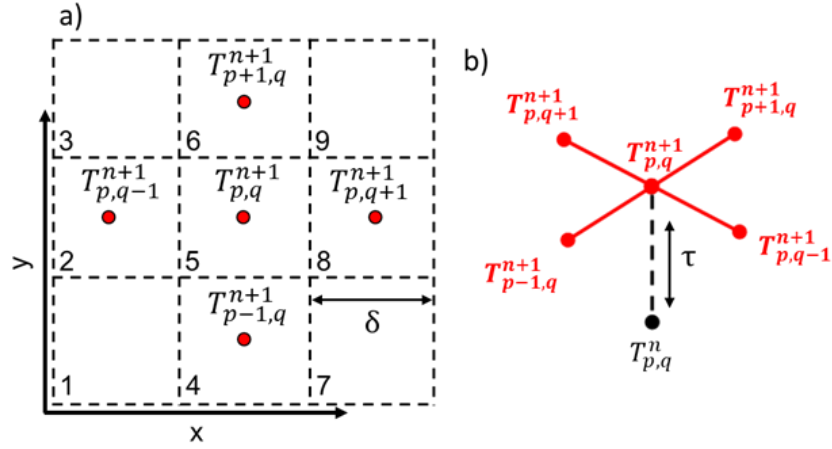


Figure S6.1: a) Grid of relevant temperature nodes for position index p,q at the $(n+1)^{\text{th}}$ time step with b) visualization of the implicit finite difference method using adjacent temperature nodes in the previous time step.

The energy balance shown in Equation S6.1 considers only the Fourier Law conduction flux, $\dot{q}_{cond} = -k\vec{\nabla}T$, crossing a conduction area, A_c , over iterations of characteristic time (time step), τ , between adjacent interior temperature nodes of density, ρ , and separated by a characteristic length, δ . Additionally, energy is generated within the node volume, V , as a result of initial power input and chemistry. Given the volume of a node to be the cube of the characteristic length and assuming that the thermal conductivity is constant along the boundary of conduction, Equation S6.1 can be written in the more familiar Heat Equation form of Equation S6.2.

$$m c_p \frac{dT}{dt} |_{x,y} = -k_{x-\frac{\delta}{2}} A_c \frac{\partial T}{\partial x} |_{x-\frac{\delta}{2}} + k_{x+\frac{\delta}{2}} A_c \frac{\partial T}{\partial x} |_{x+\frac{\delta}{2}} - k_{y-\frac{\delta}{2}} A_c \frac{\partial T}{\partial y} |_{y-\frac{\delta}{2}} + k_{y+\frac{\delta}{2}} A_c \frac{\partial T}{\partial y} |_{y+\frac{\delta}{2}} + (P + Q) |_{x,y} V \quad (S6.1)$$

$$\rho c_p \frac{dT}{dt} |_{x,y} = \frac{\partial}{\partial x} (k \frac{\partial T}{\partial x}) |_x + \frac{\partial}{\partial y} (k \frac{\partial T}{\partial y}) |_y + (P + Q) |_{x,y} \quad (S6.2)$$

Initial input power, P , can be applied at any location until either a certain amount of time has lapsed or until the desired pre-designated temperature is reached.

Chemical energy generation, Q , is the primary means of supplied energy leading to self-propagation of the flame front. A timer is started in each node once it exceeds T_{ig} so that chemistry ceases after the time allotted for chemistry (t_{rxn}) has elapsed (Heaviside Function). For this case study, a fixed time step of 40 ns is used for which 600 chemistry time steps ($\tau_{rxn} = 24 \mu\text{s}$) are allotted for each chemistry event. These values are rough orders of magnitude and not necessarily specific to any one system. Reaction times of energetic systems of this type typically range from 10-100 μs or more.^{5,57}

The thermal conductivity is spatially dependent in a discrete manner as illustrated by the 3D step-function in Figure 6.2a-b. One must consider, numerically, the change in thermal conductivity as a function of position as well as defining the thermal conductivity at node boundaries. For second order spatial accurate discretization, the change in heat conduction as a function of spatial coordinates in Equation S5.2 can be written as shown in Equation S5.3.

$$\frac{\partial}{\partial x} \left(k \frac{\partial T}{\partial x} \right) \Big|_x = k \frac{\partial^2 T}{\partial x^2} + \frac{\partial k}{\partial x} \frac{\partial T}{\partial x} \cong \frac{k^n_{p,q+\frac{1}{2}} + k^n_{p,q-\frac{1}{2}}}{2} \frac{T_{p,q+1}^{n+1} - 2T_{p,q}^{n+1} + T_{p,q-1}^{n+1}}{\Delta x^2} + \frac{k^n_{p,q+\frac{1}{2}} - k^n_{p,q-\frac{1}{2}}}{\Delta x} \frac{T_{p,q+1}^{n+1} - T_{p,q-1}^{n+1}}{2\Delta x} \quad (\text{S6.3})$$

The change in the conductive heat flux along the y-direction may be written in a similar fashion to Equation S6.3 where $\Delta x = \Delta y = \delta$ represent the characteristic length scale of the grid point with the number of grid points equal to $(\frac{L_x}{\delta})(\frac{L_y}{\delta})$ where L_x and L_y represent the total width and length of the grid. Defining an effective local thermal conductivity at the boundaries (half-integer points) of discrete material regimes is accomplished by using the idea of thermal resistance.^{192,198,213,215} The thermal

resistance is analogous to electrical resistance in which the thermal resistance between two nodes is equal to the sum of the thermal resistance from one node to the boundary and the boundary to the second node, $R_{th} = R_1 + R_2$, as **Error! Reference source not found.** illustrates.

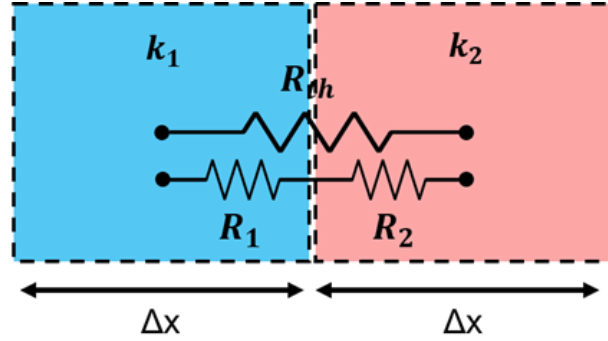


Figure S6.2: Thermal resistance approach for defining effective thermal conductivity at the boundary of discrete thermal conductivity distribution.

The effective thermal conductivity at each boundary can then be derived and defined by Equation S6.4.

$$k_{eff} = \frac{2k_1k_2}{k_1+k_2}, \quad k_{p,q+\frac{1}{2}}^n = \frac{2k_{p,q+1}^n k_{p,q}^n}{k_{p,q+1}^n + k_{p,q}^n} \quad (S6.4)$$

The left side of Equation S6.2 is discretized by taking the product of the backward time definition of the time derivative, the density, and specific heat of the node in question (Equation S6.5).²¹³ The characteristic time value, τ , is linked to the chosen characteristic length in order to maintain the level of accuracy in the model ($\frac{\tau}{\delta^2} = const.$).

$$\rho c_p \frac{dT}{dt} |_{x,y} \cong (\rho c_p)_{p,q}^n \frac{T_{p,q}^{n+1} - T_{p,q}^n}{\Delta t} \quad (S6.5)$$

The implicit method is implemented such that $T_{p-1,q}^{n+1}$, $T_{p+1,q}^{n+1}$, $T_{p,q-1}^{n+1}$, $T_{p,q+1}^{n+1}$, and $T_{p,q}^{n+1}$ are collected and solved simultaneously with a system of equations over the entirety of the temperature grid. The system of equations is represented in matrix form by the general equation $A\vec{x} = \vec{b}$ where \vec{x} is the column vector representing the T^{n+1} grid temperatures, \vec{b} is the column vector representing the sum of the T^n temperatures and temperature increases, β^n , as a result of volumetric energy inputs, and matrix A which maps \vec{x} to \vec{b} . The ordering of the temperature nodes within \vec{x} and \vec{b} is with respect to the numbering scheme shown in Figure S6.1 where the physical 2D grid is reshaped into a column vector of $L_x L_y$ elements. As a result, matrix A must reflect this reshaping where each row of the matrix elements is representative of each equation in the system when applied to the matrix algebra. The $L_x L_y \times L_x L_y$ square matrix is varied between time steps.

Significant changes in thermal conductivity, density, and/or heat capacity of a node as a result of phase or chemical changes (*e.g.* melting or final products) may be considered by establishing time/temperature dependent logic which is independent of the matrix math but reflected by the evolution of the matrix elements of A through each time step of the calculation. This may be visually represented by the dynamic behavior of the previously shown thermal diffusivity mapping over each time iteration (Figure 6.2).

An example solution setup for a 3x3 temperature grid (Figure S6.1) with constant temperature boundary conditions is shown below in Equation S6.6. Interior node rows are those for which the central temperature node in Equation S6.6 is an interior node. The matrix elements for each interior node row represents a unique set

of 5 non-zero elements ($\lambda, \gamma, \omega, \varphi, \varepsilon$) representing the interactions between the central temperature node and 4 adjacent temperature nodes. Due to the physical grid being 3x3 in this example, there exists only one interior node represented by one central interior node row and eight boundary nodes represented by eight boundary node rows. For a general $L_y \times L_x$ physical grid, matrix A begins with $L_y + 1$ boundary node rows, followed by $L_x - 2$ repetitions of $L_y - 2$ interior node rows and 2 boundary node rows, and ending with $L_y - 1$ boundary node rows. When considering alternative boundary conditions, such as convective boundaries, the boundary rows will in general have unique matrix elements which emulate that of the interior node rows but with less non-zero elements depending on the boundary type (*e.g.* corner(3) or edge(4)). One may solve for \vec{x} using Equation S6.7 and reshape the solution back to the physical grid representation.

$$A_{9 \times 9} \vec{x}_9 = \vec{b}_9 \rightarrow \begin{pmatrix} 1 & 0 & 0 & 0 & 0 & 0 & 0 & 0 & 0 \\ 0 & 1 & 0 & 0 & 0 & 0 & 0 & 0 & 0 \\ 0 & 0 & 1 & 0 & 0 & 0 & 0 & 0 & 0 \\ 0 & 0 & 0 & 1 & 0 & 0 & 0 & 0 & 0 \\ 0 & \lambda & 0 & \gamma & \omega & \varphi & 0 & \varepsilon & 0 \\ 0 & 0 & 0 & 0 & 0 & 1 & 0 & 0 & 0 \\ 0 & 0 & 0 & 0 & 0 & 0 & 1 & 0 & 0 \\ 0 & 0 & 0 & 0 & 0 & 0 & 0 & 1 & 0 \\ 0 & 0 & 0 & 0 & 0 & 0 & 0 & 0 & 1 \end{pmatrix} \begin{pmatrix} T_1^{n+1} \\ T_2^{n+1} \\ T_3^{n+1} \\ T_4^{n+1} \\ T_5^{n+1} \\ T_6^{n+1} \\ T_7^{n+1} \\ T_8^{n+1} \\ T_9^{n+1} \end{pmatrix} = \begin{pmatrix} T_1^n + \beta_1^n \\ T_2^n + \beta_2^n \\ T_3^n + \beta_3^n \\ T_4^n + \beta_4^n \\ T_5^n + \beta_5^n \\ T_6^n + \beta_6^n \\ T_7^n + \beta_7^n \\ T_8^n + \beta_8^n \\ T_9^n + \beta_9^n \end{pmatrix} \quad (\text{S6.6})$$

$$A\vec{x} = \vec{b} \rightarrow \vec{x} = A^{-1}\vec{b} \quad (\text{S6.7})$$

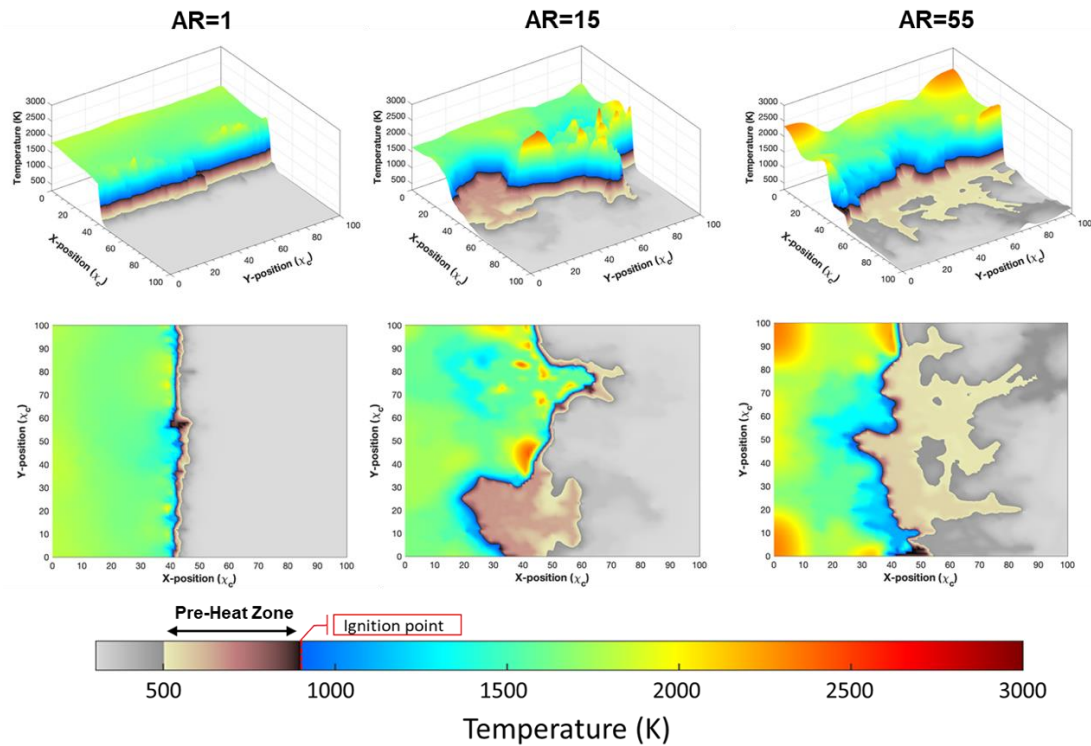


Figure S6.3: Thermal mapping of energetic material propagation incorporating rods of constant thermal conductivity ($k=k_0 10^4$) with varied aspect ratios at 30 vol.% at $t=325 \mu\text{s}$ (Propagation from left to right)

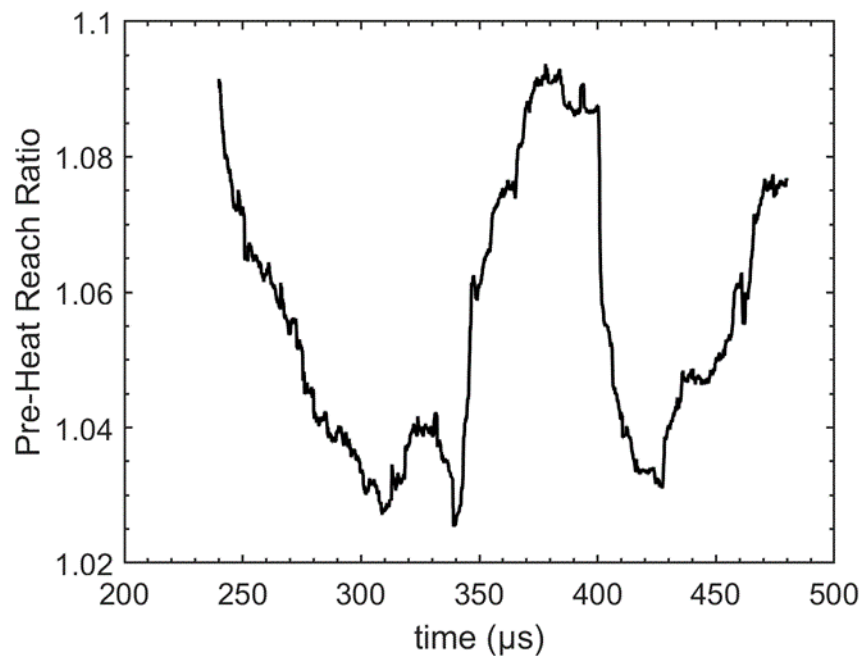


Figure S6.4: Truncated fluctuations of the extent of pre-heating as a function of time during flame propagation.

Table of Parameters

Physical Property (SI units)	Symbol
Thermal Diffusivity (m^2s^{-1})	α
Temperature (K)	T
Initial Input Power (Wm^{-3})	P
Chemical Energy Input (Wm^{-3})	Q
Characteristic time (s)	τ
Characteristic length (m)	δ
Aspect Ratio (Dimensionless)	AR
Thermal Conductivity ($\text{Wm}^{-1}\text{K}^{-1}$)	k
Input Energy Temperature Rise (K)	β
Heat Flux Area (m^2)	A_c
Area of Energetic material burned (m^2)	A_E
x-position index (Dimensionless)	p
y-position index (Dimensionless)	q
time index (Dimensionless)	n
Specific Heat ($\text{JKg}^{-1}\text{K}^{-1}$)	c_p
Mass (Kg)	m
Mass Density (Kgm^{-3})	ρ
Frame Length (m)	L
Length Variable (Dimensionless)	χ_c
Time Variable (Dimensionless)	t_c
Convection Heat Transfer Coefficient ($\text{Wm}^{-2}\text{K}^{-1}$)	h
Chemical Conversion value (Dimensionless)	η

Chapter 7 Supplemental Figures

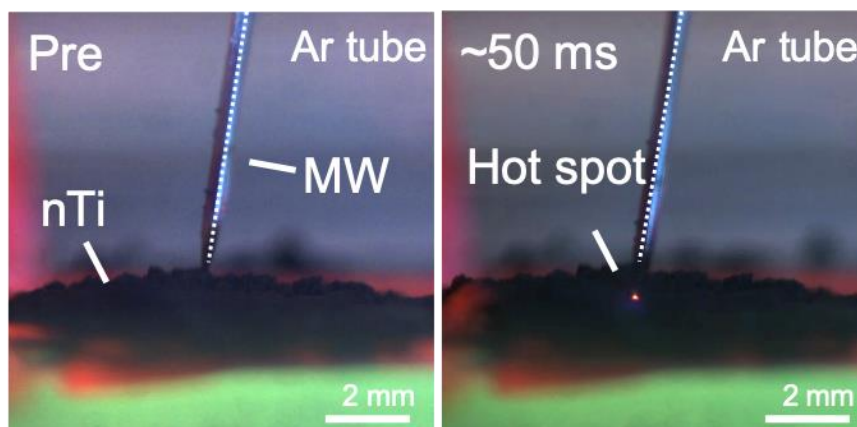


Figure S7.1: Images from microwave heating and ignition experiments for nano-titanium as performed in a glass tube with an inert Argon environment. Right image shows small heating point immediately around the microwave source.

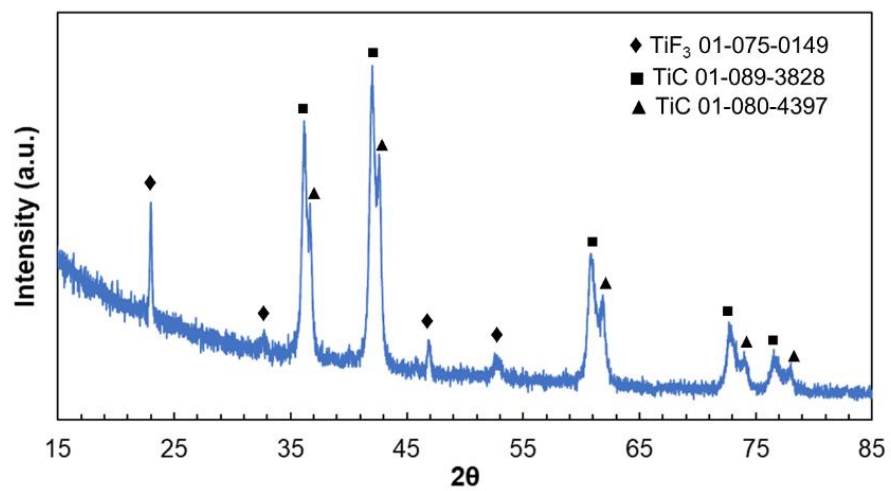


Figure S7.2: Ti-PVDF argon environment post combustion products.

Appendices

Appendix A: Specifications and Maintenance of the T-Jump/TOFMS System

This section serves to highlight specific aspects of the Zachariah group linear time-of-flight machine when coupled to the T-Jump method as described in Chapter 2.

The following is a list of things to consider:

- When soldering platinum wires, it is best to solder the sides of the leads as opposed to soldering where the platinum wire first contacts with the copper leads. The smallest bit of solder on the suspended portion of the wires will cause the platinum wire to break up heating, even if it is much lower than the temperature that it would normally break.
- The T-Jump/Linear Time-of-Flight instrument was completed in 1992 using Jordon TOF Products Inc. builds. The way in which the voltages on the voltage plates were arranged and the schematic of the instrument itself has changed several times with publications from the Zachariah group reflecting these changes [16,22,57,58].^{115,137,288,289} The specific changes are documented by Jordan TOF Products Inc. were the default settings listed on their webpage do not apply to the current instrument setup (2020). In 2010, a voltage liner was integrated within the system and the voltages applied such that the detection of energetic materials species was optimized. Due to these changes, some species which were detected in some papers may no longer be detected in current experiments.

- The TOF power supply, in general, allows there to be voltages which may steer ions in the xy-plane. In this specific orientation, these voltages are all the same such that there is no ability to “steer” and adjust the path of ions. The voltages put on these plates have been set so that they have the same voltage as the liner (-1500V). The electrical schematic of the machine (Figure 2.5) discussed here is with respect to the year 2019.
- The process for starting up the T-Jump/TOFMS goes as follows:
 - Make sure all flanges are properly tightened in a star pattern with a fresh copper O-ring, if necessary.
 - Make sure that the gate valve of the ionization chamber is properly closed and that each section (E-gun assembly, pressure gauges, leak valves, etc.) has been properly sealed.
 - Turn On the two mechanical backing pumps connected to the three turbo pumps (one for the two small turbo pumps, one for the larger turbo pump) until the thermocouple pressure gauge reads ≈ 10 Torr.
 - Turn On the three turbo pumps until up to full speed, according to the pre-set parameters. The pressure gauge should read 1-2 mTorr (lowest this gauge can read)
 - The instrument should now stay pumping down for 48 hours before experimental usage.
 - The ion gauge can now be turned on and should read a pressure of $\sim 10^{-7}$ Torr when the ionization chamber is sealed. If the ion gauge reads 10^{-7}

¹⁰, this means that the wire clip that is normally attached to metal lead is not attached or is poorly clipped.

- DO NOT turn on any electronic components of the TOFMS until the operating pressure range of 10^{-7} - 10^{-5} Torr has been reached. Failure to do so will result in arcing of high voltages resulting in damage to the electrical circuits and compromising of the electron ionization source.
- Powering down the T-Jump/TOFMS
 - Ensure that the ionization gate valve is closed and that all electronics and the e-gun are TURN OFF.
 - Turn OFF turbo pumps until all pumps are fully powered down (0 Hz) and the thermocouple pressure gauge reads ≈ 10 Torr.
 - Turn off mechanical backing pumps
 - DO NOT attempt to open the chamber until the chamber pressure has slowly risen to atmospheric pressure.
- The MCP detector must never be exposed to air for long periods of time. Any level of humidity in the air will corrupt the sensors of the detector if exposed for longer than an hour or two. The active detector region must NEVER be touched with bare hands. If the TOF tube needs to be removed for maintenance of electrical components, the flange holding the MCP detector array must be placed into a separate chamber to be pumped down on by a mechanical pump (Scroll Pump is ideal) until after the TOF tube has been fully assembled and ready to be placed back.

- When taking the TOF tube off, be careful of the fragile electrical components which extend into the interior of the instrument. To take off the TOF tube, the tube must be first lifted fully up, as to clear the exterior of the ionization chamber, then out. Having at least two people engage in this task is ideal.
- After the ionization chamber has been pumped down for 48 hours, the electronics maybe turned on. The pulsar power supply must be first to be turned on and set to 200V. Turn on the liner voltage and set to -1500V. Turn on the accelerating voltage on the external power supply to -1500V. Turn on TOF power supply and E-gun power supply. Set the detector voltage to 3000-3500V with the e-gun energy set to 70V (70eV) at a maximum filament current of 10mA.
- Given the violent nature of the energetic materials inside of the ionization chamber, electronics are subject to being compromised. If one is experiencing issues of masses showing up at times not corresponding to the calibration curve and/or not showing up at all when they previously were, the problem maybe with the pulsar power supply and remote pulsar box. For troubleshooting of this, consider the following:
 - After having set the pulsar supply voltage to 200V, ensure that the voltage is not now at 0V either with or without the trigger signal being input. If the voltage is now at 0V, the plates have shorted and caused some components to burn out. This can be as a result of the generations of many ions from sampling too much material or that the T-Jump probe was extended too far within the system and touched the voltage plates.

To fix this, first use the pulsar repair kit provided by Jordan TOF Products Inc. to replace the electronic components. Be careful to inspect all other electrical components to ensure that no other components have not burned out. If other components are burned out, these will need to be taken out and soldered back into place.

- If the problem persists with the pulsar voltage appearing to be at 200V, now check to see whether the 200V remains at 200V. Pay close attention to the voltage dial and slowly increase the accelerating voltage to - 1500V. If the voltage of the pulsar power supply increases as the accelerating voltage increases, there exists a high resistance short of the voltage plates. This results in the changing of the electric field experienced by the ions and thus the time/mass measured. The only way to fix this is to take off the TOF tube and then carefully remove and clean all the electrical plates and ceramics. Depending on the severity of the contamination, the ceramic pieces will need to be replaced from Jordan TOF Products Inc. Replacing some these ceramic pieces is non-trivial and will need to be removed with great care.

Appendix B: Solution-Based Additive Manufacturing with Hyrel 3D System

This section covers more of the specifics of the hardware and parameters used for additive manufacturing of energetic materials presented throughout this dissertation. Additionally, this appendix also describes some preliminary findings from attempts of printing energetic materials through a UV curing process. The specifics of print execution and points of note will be discussed along with frequently used print architectures.

B.1 Hardware and Instrument Parameters

The Printer and Dispensers:

The Zachariah Group utilizes two layer-by-layer additive manufacturing printers from Hyrel 3D (hyrel3D.com). The two printers in use are the Engine SR and System 30M where the latter has the same main printer hardware and software (Repetrel) as the former. The major difference between the two printers is that the System 30M integrates a plastic enclosure for better environmental control with respect to venting. Unlike many other printing systems, the Hyrel 3D printers utilize a modular printing head scheme where a fixed array of up to four individual printing/non-printing heads with differing capabilities (*e.g.* filament-based heads, reservoir-based heads, cooling fan, laser engraver, etc.) can be easily attached for different prototyping tasks within the same printing unit. Both printers in the Zachariah lab share the same set of modular heads where the main objective of the prints is to additively manufacture precursor solutions of solvent/particle/polymer through an evaporation-solidification

process.^{72,105,180} In order to accomplish this task, reservoir-based flow heads were individually purchased for use of disposable **BD syringes (only type of disposable syringes which fit the head molds)** with 1/4-1/2" blunt luer lock dispensing nozzles.

Current (Fall 2020) modular heads on the Hyrel 3D v3 software include:

- 1 SDS-10 extruder (10cc)
- 1 SDS-10 extruder (10cc) with 365 nm crosslinking LED array
- 1 SDS-30 extruder (30cc)
- 1 SDS-30 extruder (30cc) with 365 nm crosslinking LED array
- 1 MK1-250 Extruder (Standard hot flow Filament-Based Head)
- 1 Quiet Storm Cooling Fan
- 2 Pressure gauge stage leveling indicators

The Stage:

In general, the printers operate by using the modular heads to dispense a loaded precursor solution onto a heated glass substrate in a specific, predefined pattern. The printing bed is, by default, a flat aluminum bed for durability and effective stage heating up to ≈ 80 °C. Depending on the degree of venting, especially in the System 30M, the printing bed will never reach the pre-set temperature since the act of venting will actively cool the bed. The aluminum stage should be leveled properly prior to printing with the assistance of a pressure gauge stage leveling indicator (modular head). Stage maneuvering occurs through three independent belt systems for spatial movement in three dimensions (x-axis connected to the stage arm, y-axis connected to the modular head array arm, z-axis column connected to the printer spine). Video resources for

further specifics of stage leveling can be found on the Hyrel 3D (hyrel3D.com). In order to preserve the uniformity and cleanliness of the aluminum bed, several 1/8" thick glass panes were purchased. Resulting prints effectively adhere to the glass in which the thin glass panes can be easily heated to the desired temperature, effortlessly cleaned, easily removed from the main stage, or quickly replaceable if broken or damaged. Be sure to assess whether the glass pane is also level when placed on the aluminum bed to ensure a uniform printing area.

Printing a Desired Architecture (Gcode):

Printed patterns are processed by the printer software using Gcode. Gcode scripts can be input manually or by converting a CAD STL file in which a 3D rendering preview of the architecture is displayed within the software interface. Manual Gcode files can be written directly into a text file by hand for simple prints. However, this task can be extraordinarily time consuming if the print is sufficiently long or complex. For this reason, along with the unpredictability of mechanical properties of resulting prints, nearly all architectures I design for printing are generated in Matlab for the simple ability to nest looping features of multi-layered prints. Each Matlab script prints the body of the Gcode syntax to a text file and saved as a Gcode file within the printer software. The main print parameters I designate within the Gcode are the initialization conditions of the print, the coordinate sequence for the movement of the printing head, the print speed (mm/min), dispensing flow rate (mm/hr), and whether each movement is a dispensing step or not. Additionally, the software allows for in situ changes in the flow rate (flow multiplier), dispensing pulses per microliter, bed temperature, and

relative position of the stage to the printing head. This feature allows for optimization of printer settings for new precursor inks with differing flow properties and evaporation behavior of the solvent as the print proceeds. Typically, a section of Gcode is written with a “skirt” routine which is not part of the main print but done in order to assess the printing behavior prior to engaging in the main print.

Solvent-based Precursor Ink Dispensing Techniques and Strategies:

Ink formulation and optimal dispensing of the precursor can be excessively time consuming. As mentioned previously, the precursor solution includes a solvent, dissolvable polymer binder, nanoscale metal fuel, and an additional additive which may also be dissolvable. All these constituents will contribute to the change in viscosity of the precursor and directly affect the printability of the ink. Viscosity will increase as the polymer concentration increases, particle loading increases, particle density decreases, particle size decreases, and/or particle agglomeration decreases.⁷² The viscosity can be so great that the printed layer may be able to mechanically support the next layer without spreading or needing to dry fully.

At some point, the syringe head may clog as a result of the combination of high viscosity, poor mixing, agglomeration of particles, and recrystallization of some dissolvable constituents at the mouth of the dispensing head. The following are methods I have utilized to alleviate clogging issues and ensure stable printing behavior throughout the duration of the print:

- Decrease the gauge size of the luer lock dispensing nozzle to widen the extrusion area and reduce resistance to flow. Precursor inks are typically

printed with dispensing areas as small as 22-gauge and as large as 14-gauge. Most of my prints use an 18-gauge blunt luer lock needle (1/4-1/2") in order to avoid clogging while maintaining print resolution. Many inks have a "icing" constancy and tend to print smoother when switching to a tapered luer lock dispensing head with a similar gauge.

- Proper mixing of the precursor ink is essential for not only the resulting material but also in terms of preventing clogging of the dispenser. Solvent-based solutions should be sonicated in a glass vial for 30-45 minutes after the addition of each nanomaterial type in order to reduce nano-powder agglomeration. A magnetic stir bar should then be added, and the solution put on a magnetic stir plate for at least 24 hours of mixing. Repeat this process if needed, but always sonicate the sample for at least 30 minutes before loading into the syringe for printing. If the precursor ink is too viscous for magnetic stir plate mixing, the solution should be transfer to a planetary mixing cup (THINKY USA) and mixed for no more than 3 minutes at 2000 rpm. It should be noted that sonication works best in rigid vessels such as glass. The solution does not sonicate well in the plastic planetary mixer containers.
- Manually prime the ink flow immediately before starting the print by using the lever action tab connected to the PCB of the modular printing head and ensure that the ink steadily flows. It is advised to keep a small cup underneath the dispensing area when positioned in the "HOME" location to catch the ink when primed or finishing a print. Additionally, **it is imperative that the exposed PCB region where the heating leads of the stage connect to the stage arm**

be covered with tape or equivalent measure. Ink dripping into this region could cause damage to the circuit board powering the heated stage which may lead to a fire hazard from a potential short circuit. If this does occur, be aware of the printer status, turn off the printer power, and use isopropanol alcohol to clean the area as much as possible. The stage leads can be easily detached from the stage arm if necessary and, if damage is significant, contact Hyrel 3D for additional assistance.

- Adjusting the flow rate through the dispenser is a simple fix to the clogging by effectively having the dispenser apply a greater pressure to the syringe plunger. The flow rates are set with respect to the gauge size of the dispenser nozzle and can be adjusted within the manual parameters of the active modular head controls under the “Control” tab of the printing software. The flow rate can be directly changed in situ by adjusting the flow multiplier value in the same control region. It should be noted that changing the print speed (F#) in the Gcode of the print will also indirectly change the flow rate. Changing the speed of print will not lead to the same result being produced, making it essential to keep the print speed constant when making samples for a study. Caution is advised when trying to use adjustments to the flow rate as a means of alleviating clogging issues. While the flow rate helps to prevent a blockage in the first place, the enhanced flow being printed at a potentially faster spatial pace will undermine the quality and uniformity of the print. The solvent based prints need a residence time for which to dry before the next layer is to be printed. If the flow rate is too high, the precursor does not dry fast enough and

often leads to inhomogeneities in film morphology from a combination of inhomogeneous evaporation behavior and too much solvent penetrating into the previously printed layer. Printing too fast could lead to the case where the previously printed layer is nowhere near dry enough before the next dispensing pass. It is for these mentioned reasons that optimizing printed patterns for speed, dry time, and efficiency is essentially. As an example, for relatively low viscosity prints I typically print with an 18-gauge 1/2" dispensing head with a flow multiplier of 0.1 (Lowest), print speed of F400, bed temperature of ≈ 70 °C, and wide active printing area.

- A better alternative to adjusting the flow rate is to change how the modular printing head applies pressure to the syringe plunger. This parameter is the “pulses per microliter” and can alleviate clogging without changing the flow multiplier or print speed. For example, a change from 20 pulses per microliter to 60 pulses per microliter meant the difference between an ink clogging and flowing. All viscosities of interest to me operate at the 60 pulses per microliter setting. Inks with higher viscosity may be accommodated by a combination of further increasing this number and small changes to the flow multiplier.
- Calibrate the height of the luer lock dispensing end so that it is as close as possible to the glass stage without colliding into the next layer. This allows for better wetting of the deposition region and prevents the ink from wetting around the mouth of the dispensing area which may act as a nucleation point where material may dry, potentially leading to a clog. The Gcode is written so that the stage moves a certain distance (≈ 10 μm for relatively low viscosities,

≈100-400 μm for relatively high viscosities) away from the dispensing head as the height of the print increases. The distance change per layer is a rough guess of the needed separation height based off preliminary print observations and SEM images of average thickness per layer. The separation distance of the dispensing nozzle and the printed subject can be adjusted in situ if necessary.

- Adjust the temperature of the printing bed to optimize for solvent evaporation rate. Solvents with a higher volatility (*e.g.* Ethanol) should use a lower bed temperature to slow down the evaporation rate such that the solvent does not easily dry before being deposited and lead to a clog of the dispenser. In the case of lower volatility solvents (*e.g.* Water or DMF) at 70 °C, there is little risk of the solvent drying before being deposited on the printing bed. DMF is the most common solvent I use for dissolving of fluoropolymer binders of interest (Viton, PVDF) for which the bed temperature should be set to no lower than 60 °C. It should be noted that although the higher bed temperature enhances the evaporation rate for drying purposes, this may also cause irregularities with respect to film morphology due to the turbulence of evaporation of the precursor layer closest to the heat source. In addition to the dry time considerations, it is for this reason that printing a thin layer of precursor ink is important. The venting action of the System 30M helps to allow for a lower optimal bed temperature as result of additional drying of the solvent due to enhanced mass transfer of the evaporated solvent from above.

Ultra-Violet (UV) Resin Precursor Ink Dispensing Techniques and Strategies:

The availability of the modular printing heads equipped with an array of 365 nm crosslinking LEDs allows one to print precursor inks with the ability to be photocured using a technique called Ultraviolet Digital Light Processing.¹⁰¹ Instead of solvent evaporation leaving behind solid products, the entirety of the ink is solidified when exposed to UV light, catalyzing polymerization of the ink. Typical photocurable inks may include a UV curable monomer (30-50%) as a reactive diluent and crosslinker, a UV curable oligomer (50-80%) as the primary binder for mechanical integrity, a UV wavelength specific photo-initiator (1-5%) which converts light energy to the formation of free radicals for polymerization of the monomer and oligomer, and a desired additive.¹⁰¹ This process is illustrated simply in Figure B.1.

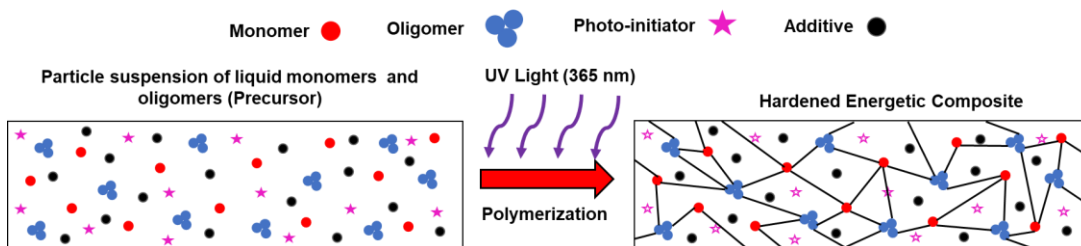


Figure B.1: Photo-polymerization process of UV curable materials

With this technique, I attempted to print metallized energetic materials within the UV curable system to expand upon work done by Dr. Steven Son's group who printed ammonium perchlorate (AP) and low loading aluminum based energetic materials with the assistance of UV curing technology.^{111,113} Due to the evaporative process of solvent-based printed materials, films were intrinsically porous and added a weakly controlled parameter to flame propagation behavior. By producing energetic materials through a fumeless UV curing process, one can manufacture dense materials with minimal porosity. The films could potentially contain high mass loadings of

energetic particulates with more than 70 wt.% while also broadening potential particle additives whose morphology may have been previously changed by dissolution and recrystallization.

My attempts to print UV curable films used a proprietary, multifunctional monomer sample (SR494) obtained from Sartomer and combined with the 365-405nm activated photo-initiator Phenylbis(2,4,6-trimethylbenzoyl)phosphine oxide (PTPO) purchased from Sigma Aldrich. Preliminary bench testing showed that adding just 1 wt.% of PTPO was enough to polymerize the monomer within seconds of illumination, solidifying the entire precursor ink to a hard acrylate with minimal shrinkage and no evaporation of potentially harmful chemicals. Extrusion prints using the System 30M Hyrel 3D printer required syringes be wrapped in aluminum foil and the use of metal luer lock dispensers to ensure that the ink would not polymerize inside of the syringe from reflections off the glass printing surface. Additionally, the intensity of the LED array may need to be adjusted to prevent the suspension from curing too quickly and solidifying to the end of the dispensing nozzle. The System 30M enclosure was wrapped in an anti-UV adhesive film and UV attenuating goggles made available for the operator to reduced eye exposure to UV radiation.

Early successes were made in printing structures with either just the monomer and photo-initiator or the monomer, photo-initiator, and up to 70 wt.% of white additives such as KClO_4 and AP. KClO_4 and AP sub-micron particles were spray dried and solid photo-initiator crushed with a mortar and pestle prior to mixing in order to reduce powder size for better distribution when mixed.¹²⁰ The suspension of liquid monomer, photo-initiator, and additive powder were placed in a glass vial and

sonicated for 30 minutes. Depending on the mass loading of solids, the solution may be too viscous for standard magnetic stir bar mixing. If too viscous, the suspension is transferred to a plastic a THINKY USA planetary mixing container for mixing at 2000 rpm for 2 minutes. It should be noted that sonication should not exceed 30 continuous minutes and the planetary mixing for no more than 3 minutes due to the possibility of unintentional polymerization of the suspension as result of vessels heating up from the mixing/sonication process. If not immediately using all the sample for printing, the remaining material should be stored in a cool environment with no exposure to light to prevent slow polymerization.

The addition of increasing amounts of nanometals such as aluminum, titanium, and tantalum elongated the polymerization process with the metals reflecting much of the incident UV light. Increasing photo-initiator mass loading did not counter this issue but was found to be improved somewhat by utilizing the heated printing stage in combination with use of the adjustable intensity UV LEDs to accelerate the polymerization process. Despite this improvement and given that mass loadings of 40 wt.% or more of metal nanoparticles are needed for propellant like combustion performance, the polymerization time is just too slow and does not effectively penetrate through the entire thickness of the deposited layer.¹¹³ Additionally, the monomer is non-energetic and has a liquid density of ≈ 1.1 gm/ml. This means that for a 3 ml precursor solution, it would require 3 grams of energetic material just to reach the 50 wt.% mark. Reaching the 70 wt.% loading using aluminum thermites proved nearly impossible due to exorbitant material demands and extreme difficulties in mixing several grams nanoscale energetic materials in a 3 ml solution. For these reasons, along

with the safety concerns of working with that amount of nanomaterial, the project, with respect to the metallized UV curable materials, ended. Only materials which allow for UV penetration throughout the entirety of the deposited layer and contain both energetic constituents and a polymer which contributes energetically, like PVDF or nitrocellulose, should be utilized for additive manufacturing of energetic materials using this method.^{63,67,113,118}

B.2 Frequently used Architecture and Gcode Scripts

As mentioned previously, the body of a Gcode script is generated in Matlab, saved as a text file, and saved as a Gcode file type. Each script uses the same initialization and ending routine, therefore only the main printing routine is generated each time in Matlab. The following is an example script of the initialization and ending syntax:

```
; Initialization  
G21 ; use millimeters  
G90 ; absolute coordinates  
G0 Z5 ; lift head to avoid collisions  
G28 X0 Y0 ; home X and Y  
G92 X0 Y0 ; reset origin: X and Y  
G0 X0 Y0 ; move to desired origin  
G92 X0 Y0 ; reset origin: X and Y  
M83 ; relative extruder coordinates  
M756 S0.2 ; set flow for the first layer please  
G21 ; set units to millimeters  
G90 ; use absolute coordinates  
M82 ; use absolute distances for extrusion  
G92 E0 ; reset extrusion distance  
M756 S1.0  
M790 ; execute any new layer actions  
  
:-----  
[MATLAB GENERATED BODY HERE]  
:-----  
  
; Ending  
G92 E0 ; reset extrusion distance  
M107 T10 ; turn off fans and lasers  
M104 S0 ; turn off temperature  
M140 S0 ; turn off the hot bed.  
G91 ;  
G1 Z5.0 ; Drop bed 5mm for extra clearance  
G90 ; absolute  
G28 X0 Y0 ; home X axis  
G92 X0 Y0 ; confirm we are at zero  
M84 ; disable motors  
M30 ; End of program
```

The following Matlab scripts and corresponding top-down view of frequently used patterns for consistent and uniform production of materials for characterization.

Dual Rectangular Films

As the name would suggest, a single printing head prints two adjacent rectangular films. The top-down view is shown in Figure B.2.

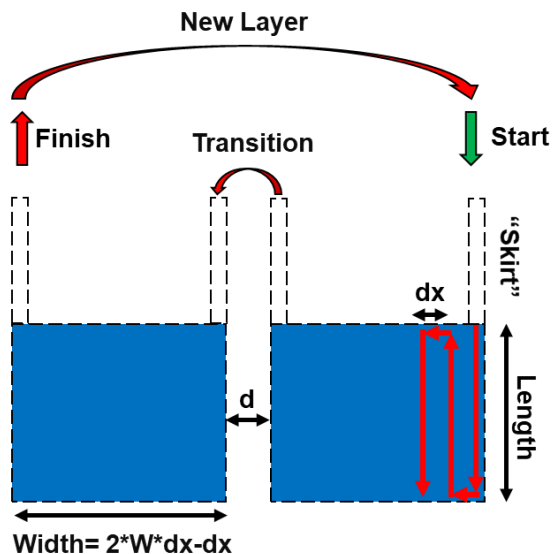


Figure B.2: Dual rectangular print design

This simple design of adjacent n -layer thick rectangular thin films was designed to quickly print a single uniform material laminate with a large, flat surface area for thermal diffusivity, electrical conductivity, and x-ray diffraction characterization. As mentioned in Chapter 7 of this dissertation, multiple thinner width stands can be cut and harvested from one of the printed sheets for combustion analysis of free-standing energetic materials. Additionally, even smaller pieces may be cut for TGA-DSC thermochemical analysis and SEM architectural and morphological characterization.

The printed path consists of an initial “skirt” region followed by adjacent passes of a specified length for which the edges of the dispensing ink must connect with one

another for a continuous rectangular sheet to be printed. The spacing between the mid points of adjacent passes can be adjusted by varying the width step size, dx , such that the spacing is optimized for minimal overlap of printed area. The width step size can also be made large enough for total separation of adjacent passes if a “snake” pattern would be desired. Since the step size is along the x-direction, the width of the rectangle is a function of the number of times the pass pattern repeats itself, W . After traversing the pre-determined number of pass repetitions, the print enters another “skirt” region from which the printing head makes a non-extrusion transition movement over a distance, d , to another “skirt” region which represents the start of the next rectangular print. The print proceeds the same as the first and ends the way the first rectangular print started. If more layers are desired, the printing head will make another non-extrusion movement back to the start of the first rectangle and repeats the entire printing routine. After completion of the print and removal of the rectangles from the glass substrate, the irregular features near the edges are removed with a straight blade. The corresponding Matlab script embodies this repetitive nature by nesting the periodic pass behavior of each individual rectangle within the periodic behavior of starting a new layer.

Script B1: Matlab script to generate the Gcode for printing adjacent rectangles

```
Adjacent Filled Rectangles (Dual Syringe Potential) F400 and 0.1>=FM
%Open .txt file
fileID = fopen('Practice.txt','w');

d=35; %spacing between syringe needles (measure exactly or underestimate)

dx=0.6; %width step size (Change for varied separation between passes)
dz=0.01; %height step size
x=120;%start x
y1=100;%start y
z=0.10; %start z
W=10; %distance integer in x-direction (width)
```

```

if 2*W*dx-dx >= d % width may not exceed 35mm

    fprintf(2,'Caution! Width too long\n')

    fclose(fileID);
    clear;
else

prompt='How many layers?\n';
L=input(prompt); %# of passes/layers

prompt_1='Desire Print Speed (e.g. 250 mm/min, 100 mm/min)\n';
F=input(prompt_1); %Print Speed

prompt_2='Film Length? (mm)\n';
Length=input(prompt_2);

y2=y1+Length;

fprintf(fileID,';Bi-Layers = %i\n',L);
fprintf(fileID,';Length = %fmm\n',y2-y1);
fprintf(fileID,';Width = %fmm\n',2*W*dx-dx);
fprintf(fileID,'\n');

%Skirt
fprintf(fileID,';Skirt\n');
fprintf(fileID,'G0 X%f Y30 Z%f E6 F%i\n',x,z,F);
fprintf(fileID,'G1 X%f Y%f Z%f E6 F%i\n',x,y1,z,F);

for i=1:L %Layer Height changing
    fprintf(fileID,'\n');
    fprintf(fileID,';Layer %i\n',i);

    for j=1:W %Individual Film passes (Film 1)

        fprintf(fileID,'G1 X%f Y%f Z%f E6 F%i\n',x,y1,z,F);
        fprintf(fileID,'G1 X%f Y%f Z%f E6 F%i\n',x,y2,z,F);
        fprintf(fileID,'G1 X%f Y%f Z%f E6 F%i\n',x+dx,y2,z,F);
        fprintf(fileID,'G1 X%f Y%f Z%f E6 F%i\n',x+dx,y1,z,F);

x=x+2*dx;
    end
    fprintf(fileID,'G1 X%f Y%f Z%f E6 F%i\n',x-dx,y1-30,z,F);

    x=(x-dx)+d-(2*W*dx-dx); %Jumping to next film
    z=z+2;

    fprintf(fileID,'\n');
    fprintf(fileID,'Next Film: Layer %i\n',i);
    fprintf(fileID,'G0 X%f Y%f Z%f E6 F%i\n',x,y1-30,z,F);
    z=z-2;
    fprintf(fileID,'G1 X%f Y%f Z%f E6 F%i\n',x,y1-30,z,F);

    for n=1:W %Individual Film Passes (Film 2)

        fprintf(fileID,'G1 X%f Y%f Z%f E6 F%i\n',x,y1,z,F);
        fprintf(fileID,'G1 X%f Y%f Z%f E6 F%i\n',x,y2,z,F);
        fprintf(fileID,'G1 X%f Y%f Z%f E6 F%i\n',x+dx,y2,z,F);
        fprintf(fileID,'G1 X%f Y%f Z%f E6 F%i\n',x+dx,y1,z,F);

x=x+2*dx;
    end
    fprintf(fileID,'G1 X%f Y%f Z%f E6 F%i\n',x-dx,y1-30,z,F);

    x=(x-dx)-d-(2*W*dx-dx); %jumping back to film 1
    z=z+2;
    fprintf(fileID,'G0 X%f Y%f Z%f E6 F%i\n',x,y1-30,z,F);
    z=z-2;
    z=z+dz;
    fprintf(fileID,'G1 X%f Y%f Z%f E6 F%i\n',x,y1-30,z,F);

end
fclose(fileID);
end

```

Dual Printing Head, Dual Rectangular Multi-Component Films

Script B1 may also be utilized to print a laminate film composed of layers with alternating materials. Conducting a print of this type requires two modular printing heads placed in fixed adjacent slots, and thus will overlap during the second rectangle of the first printing head and the first rectangle of the second printing head. For one head to execute the same printing parameters as the other, one of the heads must be set to act a “clone” with respect to the “master” head. The diagram of the print routine is shown in Figure B.3.

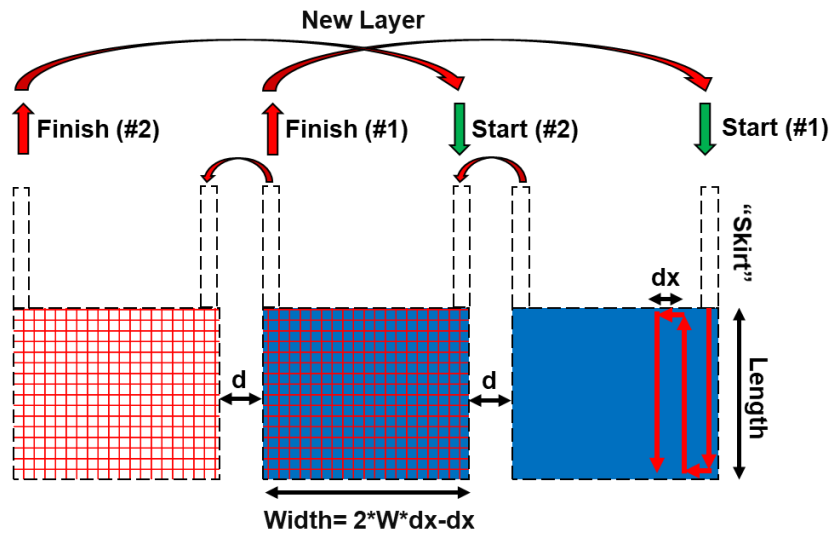


Figure B.3: Dual Printing Head, Dual rectangular print design

This method allows the center rectangle to be printed with multiple compositions with the first printing head depositing a layer of one composition on top of a dried layer of a differing composition deposited by the second printing head. The print also simultaneously prints outer rectangles of the separate material with half the thickness. For this print design, the transition distance, d , is set to the distance between printing heads and requires that the width of the rectangle not exceed this value so that

the first rectangle of the first printing head does not overlap with the first rectangle of the second printing head. One of the major difficulties with printing with two printing heads is that it can be difficult to calibrate the printing heads such that the dispensing nozzles are level throughout the print. Calibration first requires that the stage be as level as possible and then requires that the setscrews on the back of each printing head be loosened so that dispensing nozzle slides down to meet the glass substrate. Specifics and illustrations of this process can be found on the Hyrel 3D webpage. While this method of multi-composition layering is fully automated, one could obtain the same result using a single printing head by printing a set number of layers of one material, unload one syringe, load the other syringe, print another set of layers, and repeat. This would result in a multi-component version of Figure B2 with the obvious downside that the single syringe technique would require the print to be monitored throughout the entire print.

Print Routine for Precursor Deposition on Microscope Coverslips

A main feature of the Zachariah Group is the ability to capture highly resolved ($\approx 1 \mu\text{m}/\text{pixel}$) behavior of flame propagation of energetic materials with the use of high speed videography ($\sim 10^5$ FPS) coupled to a microscope lens.⁷⁷ The staging of experiments of this type often requires printed energetic material to uniformly adhere to thin microscope coverslips. The diagram shown in Figure B.4 illustrates the printing routine I used to make such prints and how the resulting samples may be reshaped for ideal experimental subjects.

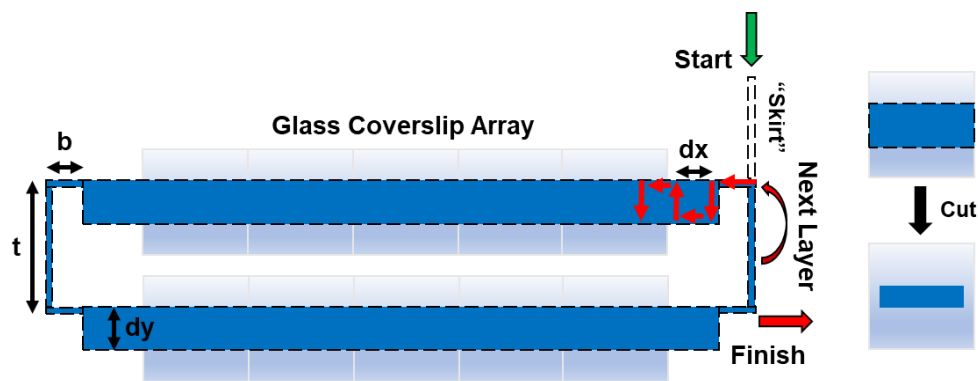


Figure B.4: Print design for printing on glass coverslips

The printing scheme is designed to optimize the number of coverslips printed on while allowing for sufficient drying time and relatively short total printing times. As with the other previously mentioned prints, the length in the x-direction is a function of the step size, dx , and the number of times the pass pattern repeats itself. A buffer length, b , was added to give the operator a region which to assess the whether the dispensing nozzle will clear the height of the glass coverslips. The width, dy , of the print is constrained to be roughly a third of the width of the glass coverslips where the separation of the coverslips is characterized by the separation length, t . This print routine uses a single printing head, but, as mentioned previously, layers of differing composition may be manufactured by exchanging the syringe after a set number of layers. The glass cover slips typically act as a heat sink during combustion of the energetic material and may quench the propagation as a result. Therefore, it is advised that films be at least $\approx 100 \mu\text{m}$ thick. After printing is completed, a razor is used to remove each coverslip from the array. Additionally, excess material along the print edges, in the form of irregularities in uniformity, are cut away (Figure B4). Prints with Viton A polymer is are ideal materials for printing on the glass coverslips as a result of its superior adhesion. The glass/material interface appears supremely flush and remains

firmly fixed to the coverslip even after further post-print shaping. In comparison, PVDF films may also be printed in this way but cannot be reshaped after printing due to its relatively poor ability to remain fixed to the coverslips after printing. This may be explained by the coupling of PVDF's higher Young's Modulus compared to Viton and the degree to which PVDF shrinks while drying.^{72,180} However, higher particle loadings (>50wt.%) integrated in PVDF based films have shown to have better adhesion due to the reduced role of PVDF in effectively binding the material (Material is more brittle).^{72,290} The Matlab script of the Gcode body is presented below.

Script B2: Matlab script to generate the Gcode for glass coverslip prints

```
%Generating a gcode for prints onto glass coverslips
syms x y z W F

%Open .txt file
fileID = fopen('Film for Glass Slides.txt','w');

dx=1.0; %width step size (Change for varied separation between passes)
dy=6; %width of each slot
dz=0.010; %height step size
x=20;%start x
y=80;%start y
z=0.1; %start z
W=50; %distance integer in x-direction (width)
b=8; %buffer to slides
t=50; %separation between slide arrays vertically

prompt='How many layers?\n';
L=input(prompt); %# of passes/layers

prompt_1='Desire Print Speed (e.g. 250 mm/min, 100 mm/min)\n';
F=input(prompt_1); %Print Speed

fprintf(fileID, 'Layers = %i\n', L);
fprintf(fileID, 'Width = %fmm\n', dy);
fprintf(fileID, 'Length = %fmm\n', 2*W*dx);

fprintf(fileID, '\n');
%Skirt
fprintf(fileID, 'Skirt\n');
fprintf(fileID, 'G0 X%f Y20 Z%f E6 F%i\n', x, z, F);
fprintf(fileID, 'G1 X%f Y%f Z%f E6 F%i\n', x, y, z, F);

for i=1:L %Layer Height changing
    fprintf(fileID, '\n');
    fprintf(fileID, 'Layer %i\n', i);
    fprintf(fileID, 'G1 X%f Y%f Z%f E6 F%i\n', x+b, y, z, F);

    for j=1:W %Individual Film passes (Slot 1)

        fprintf(fileID, 'G1 X%f Y%f Z%f E6 F%i\n', x+b+(2*j-1)*dx, y, z, F);
        fprintf(fileID, 'G1 X%f Y%f Z%f E6 F%i\n', x+b+(2*j-1)*dx, y+dy, z, F);
        fprintf(fileID, 'G1 X%f Y%f Z%f E6 F%i\n', x+b+2*j*dx, y+dy, z, F);
        fprintf(fileID, 'G1 X%f Y%f Z%f E6 F%i\n', x+b+2*j*dx, y, z, F);

    end
end
```

```

fprintf(fileID, '\n');
fprintf(fileID, ';Transition to Next Array\n');
fprintf(fileID, 'G1 X%4f Y%4f Z%4f E6 F%i\n', x+2*b+2*W*dx, y, z, F);
fprintf(fileID, 'G1 X%4f Y%4f Z%4f E6 F%i\n', x+2*b+2*W*dx, y+t, z, F);
fprintf(fileID, 'G1 X%4f Y%4f Z%4f E6 F%i\n', x+b+2*W*dx, y+t, z, F);

fprintf(fileID, '\n');
fprintf(fileID, ';Next Slot: Layer %i\n', i);

for n=1:W %Individual Film Passes (Slot 2)
    fprintf(fileID, 'G1 X%4f Y%4f Z%4f E6 F%i\n', x+b+2*(W-(n-1))*dx, y+t, z, F);
    fprintf(fileID, 'G1 X%4f Y%4f Z%4f E6 F%i\n', x+b+2*(W-(n-1))*dx, y+t+dy, z, F);
    fprintf(fileID, 'G1 X%4f Y%4f Z%4f E6 F%i\n', x+b+2*(W-(n-1))*dx-dx, y+t+dy, z, F);
    fprintf(fileID, 'G1 X%4f Y%4f Z%4f E6 F%i\n', x+b+2*(W-(n-1))*dx-dx, y+t, z, F);
end

fprintf(fileID, '\n');
fprintf(fileID, ';Back to Start\n');
fprintf(fileID, 'G1 X%4f Y%4f Z%4f E6 F%i\n', x, y+t, z, F);
fprintf(fileID, 'G1 X%4f Y%4f Z%4f E6 F%i\n', x, y, z, F);
z=z+dz;
end

fclose(fileID);

```

Print Routine for Deposition of Single Pass Energetic Strands

The above laminate structures are great architectures for printing materials which are geometrically uniform and printed continuously over a wide area. However, these types of laminate structures generally work better for relatively lower viscosity precursor inks. Higher viscosity inks as a result of high particle loading can be extremely brittle and will break apart if one attempts to cut away a sample of the material from the larger batch.^{112,118} Flame speed tests typically utilize a thin strand of printed material which can be dispensed by a single pass of the printing head to produce propellant burn sticks.¹¹² As a result, one can create a Gcode which produces an architecture made up of only a single pass with multiple layers. In order to accommodate potential printing on glass coverslips, the simplest architecture for this purpose is a square perimeter with the potential for multiple layers. A print routine diagram is shown in Figure B.5.

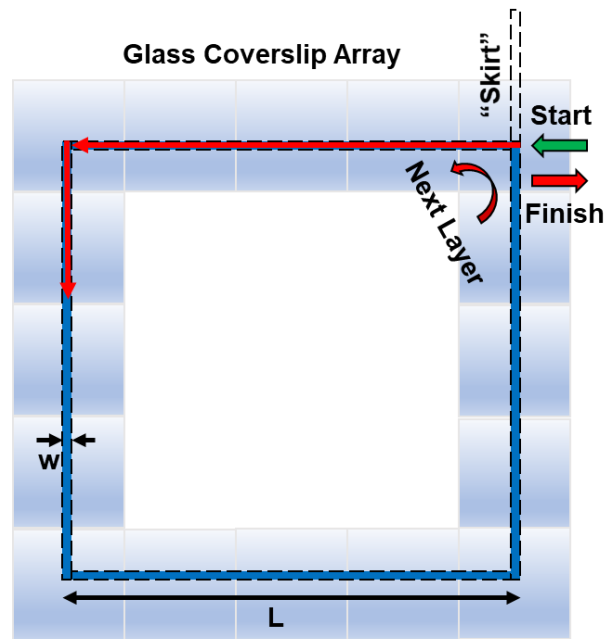


Figure B.5: Print design for printing of viscous, high particle loading inks on glass coverslips

The length of the square is pre-determined by the corresponding Matlab script (Script B3) and the width, w , is solely dependent on the gauge of the dispensing nozzle. Cross-sectional morphology of resulting stick thickness are generally non-uniform along its width such that the edges noticeably taper off from the center.^{112,118} This behavior is to be expected of liquid precursors as the ink disperses immediately after being deposited. The degree of tapering depends strongly on the ink mechanical properties before and during the drying process with differing binder combinations yielding different morphological results.¹¹² The Matlab script for generating the Gcode body is presented below.

Script B3: Matlab script to generate the Gcode for a square perimeter print

```
%Square Perimeter
syms x y z %Printer coordinate variables
%Single Syringe Multi-Pass Square Perimeter

%Open .txt file
fileID = fopen('Square Perimeter.txt','w');

prompt=('# Layers?\n');
Layers=input(prompt); %# of layers

dz=0.025; %height step size
L=80; %length (mm)

x=60;%start x
y=60; %start y
z=0.1; %start z

prompt_1='What F# (mm/min)? (e.g. 250,500)\n';
F=input(prompt_1);

%Skirt
fprintf(fileID, ';Skirt\n');
fprintf(fileID, 'G0 X20 Y20 Z%4f E6 F%4f\n', z, F);
fprintf(fileID, 'G1 X%4f Y20 Z%4f E6 F%4f\n', x, z, F);
fprintf(fileID, 'G1 X%4f Y%4f Z%4f E6 F%4f\n', x, y, z, F);

fprintf(fileID, '\n');
for i=1:Layers %Layer Height changing
fprintf(fileID, ';Layer %i\n', i); %Starts new layer #i

%Outer Perimeter
fprintf(fileID, 'G1 X%4f Y%4f Z%4f E6 F%4f\n', x, y, z, F);
fprintf(fileID, 'G1 X%4f Y%4f Z%4f E6 F%4f\n', x+L, y, z, F);
fprintf(fileID, 'G1 X%4f Y%4f Z%4f E6 F%4f\n', x+L, y+L, z, F);
fprintf(fileID, 'G1 X%4f Y%4f Z%4f E6 F%4f\n', x, y+L, z, F);
fprintf(fileID, 'G1 X%4f Y%4f Z%4f E6 F%4f\n', x, y, z, F);
fprintf(fileID, '\n');

z=z+dz;
fprintf(fileID, '\n');
end

fclose(fileID);
```

Appendix C: Matlab Scripts for T-Jump/TOFMS

Script #1 (C-0): Auto-temperature fix to account for contact resistance:

```
%Used for TOFMS
%Autofixes temperature start with an initial guess of the contact resistance.
%Plots an average first plot of the temperature/heat rate vs. time.
%Works for both sequence and real time scope data collecting modes.
%Works with both old and new temperature probes.
%Must be adapted to accommodate Iridium Wire (A bit Complicated)
%%Last Modified on 06/28/17 by H.Chen to optimize the calculation of R_c.

maxTime = 10;
T_start_upper_lim = 35;
T_start_lower_lim = 33;
tracked_species = 32;

%% Initial guess for contact resistance

%%current_mod=1; %conversion factor from current probe
t_Temp=t_T;T_temp=T;

prompt='Enter 1 for old probe or 2 for new probe\n    ';
temp=input(prompt);
if temp == 1
    current_mod=-200;
end
if temp == 2
    current_mod=-1;
end

%%prompt='Contact Resistance? 0 to keep same\n    ';
%%temp=input(prompt);
%%if temp~=0
%%    R_c=temp;
%%end

%% Recalculate T and remove bad points

if any(t_T==0) %checks for any in correct t in
    [row,~]=find(t_T==0);
    for i=1:length(row)
        t_T(row(i),1)=t_T(row(i)-1,1)+t_T(6)-t_T(5); %changes zeros to next in sequence
        T(row(i),1)=T(row(i)-1,1);
    end
end
if any(Volts==0) %checks for any in correct t in
    [row,~]=find(Volts==0);
    for i=1:length(row)
        Volts(row(i),1)=Volts(row(i)-1,1);
    end
end
if any(Current_raw==0) %checks for any in correct t in
    [row,~]=find(Current_raw==0);
    for i=1:length(row)
        Current_raw(row(i),1)=Current_raw(row(i)-1,1);
    end
end

R_o=0.033618*wire_l/(1+0.003908*20-0.0000005775*400); %Resistance at 0C for wire
Current=Current_raw*current_mod;
R=Volts./Current-R_c;

T=real((-0.003908+sqrt((0.003908)^2-4*(-5.775e-7)*(1-R./R_o)))/(2*-5.775e-7));

%% Calculate average T curve
pulse_width=1000*t_T(find(T>300,1,'last'));
% Makes into a column vector rather than a row vector,
% ONLY NEEDED for IN AIR RUNS
%t_T=t_T';Volts=Volts';Current_raw=Current_raw';T=T'; % Makes into a column vector rather than a
row vector
%% Smoothes T data
%figure
pulse_t=length(t_T);
if any(t_T(2:pulse_t)==0) %checks for any in correct t in
    [row,~]=find(t_T(2:pulse_t)==0);
```

```

    for i=1:length(row)
        t_T(row(i)+1,1)=t_T(row(i),1)+t_T(6)-t_T(5); %changes zeros to next in sequence
        T(row(i)+1,1)=T(row(i),1);
    end
end

if any(T==0) || any(imag(T)~=0) %checks for any values are imaginary or zero and fixes
    [row,~]=find(T==0 | imag(T)~=0);
    for i=1:length(row)
        T(row(i),1)=T(row(i)-1,2);
    end
end

y=smooth(T,100);
for i=1:ceil(pulse_width*10);xx(1,1+(i-1)*5:i*5)=(i-1)*10^-4:10e-6:(i-1+0.45)*10^-4;end % makes a
x data set that covers only time during measurement
if xx(end)>pulse_width/1000;xx=xx(1:find(xx<=pulse_width/1000,1,'last'));end
while ~all(diff(t_T(1:pulse_t)));pulse_t=pulse_t-50; end;
yy=spline(t_T(1:pulse_t),y(1:pulse_t),xx');
pulse_width=1000*xx(find(abs(diff(yy))<100 & diff(yy)~=0,1,'last')+1);
T_start=yy(find(diff(yy(1:round(length(yy)/10))<-5,1,'last')+1);

if T_start < T_start_upper_lim
    R_End = R_c;
    R_Begin = 0.001;
else
    R_End = 1;
    R_Begin = R_c;
end

while T_start > T_start_upper_lim || T_start < T_start_lower_lim
    %% Recalculate T by changing R_c

    if T_start < T_start_lower_lim
        R_End = R_c;
    end

    if T_start > T_start_upper_lim
        R_Begin = R_c;
    end

    if (R_End-R_Begin)<0.0001
        error('Could not find R_c in the pre-set range');
    end

    R_c = (R_Begin+R_End)/2;

    R_o=0.033618*wire_l/(1+0.003908*20-0.0000005775*400); %Resistance at 0C for wire
    Current=Current_raw*current_mod;
    R=Volts./Current-R_c;

    T=real((-0.003908+sqrt((0.003908)^2-4*(-5.775e-7)*(1-R./R_o)))/(2*-5.775e-7));

    %% Calculate average T curve
    pulse_width=1000*t_T(find(T>300,1,'last'));
    % Makes into a colum vecto rather than a row vector,
    % ONLY NEEDED for IN AIR RUNS
    %t_T=t_T';Volts=Volts';Current_raw=Current_raw';T=T'; % Makes into a colum vecto rather
than a row vector
    %% Smoothes T data
    %figure
    pulse_t=length(t_T);

    y=smooth(T,100);
    for i=1:ceil(pulse_width*10);xx(1,1+(i-1)*5:i*5)=(i-1)*10^-4:10e-6:(i-1+0.45)*10^-4;end %
makes a x data set that covers only time during measurement
    if xx(end)>pulse_width/1000;xx=xx(1:find(xx<=pulse_width/1000,1,'last'));end
    while ~all(diff(t_T(1:pulse_t)));pulse_t=pulse_t-50; end;
    yy=spline(t_T(1:pulse_t),y(1:pulse_t),xx');
    pulse_width=1000*xx(find(abs(diff(yy))<100 & diff(yy)~=0,1,'last')+1);
    T_start=yy(find(diff(yy(1:round(length(yy)/10))<-5,1,'last')+1);

end

t_T_start=xx(find(diff(yy(1:round(length(yy)/10))<-5,1,'last')+1)*1000;
t_fit=ceil(10*t_T_start)/10:1:pulse_width;
T_fit=smooth(spline(xx*1000,yy,t_fit));

```

```

T_fin=yy(find(abs(diff(yy))<100 & diff(yy)~=0,1,'last')+1);
t_T_fin=xx(find(abs(diff(yy))<100 & diff(yy)~=0,1,'last')+1)*1000;

figure()
plot(t_fit,T_fit)

xlabel('time (ms)','FontSize',18,'FontWeight','bold','FontName','Arial');
ylabel('Temperature (deg. C)','FontSize',18,'FontWeight','bold','FontName','Arial');
set(gca,'FontSize',14,'FontName','Arial');

%axis([0 3 0 1000])

figure()
plot(t_T,T)
xlabel('time (s)','FontSize',18,'FontWeight','bold','FontName','Arial');
ylabel('Raw temperature (deg. C)','FontSize',18,'FontWeight','bold','FontName','Arial');
set(gca,'FontSize',14,'FontName','Arial');

```

Script #2 (C-1) Ignition Temperature and Heating Rate Output Script

```

%Script which gives the ignition temperature as well as the temperature
%rate at the found ignition time
%Change FPS when necessary

pulse_width=1000*t_T(find(T>300,1,'last'));
% Makes into a colum vecto rather than a row vector,
% ONLY NEEDED for IN AIR RUNS
%t_T=t_T';Volts=Volts';Current_raw=Current_raw';T=T'; % Makes into a colum vecto
rather than a row vector
%% Smoothes T data
figure
pulse_t=length(t_T);
if any(t_T(2:pulse_t)==0) %checks for any in correct t in
    [row,~]=find(t_T(2:pulse_t)==0);
    for i=1:length(row)
        t_T(row(i)+1,1)=t_T(row(i),1)+t_T(6)-t_T(5); %changes zeros to next in
sequence
        T(row(i)+1,1)=T(row(i),1);
    end
end

if any(T==0) || any(imag(T)~=0) %checks for any values are imaginary or zero and fixes
    [row,~]=find(T==0 | imag(T)~=0);
    for i=1:length(row)
        T(row(i),1)=T(row(i)-1,2);
    end
end

y=smooth(T,100);
for i=1:ceil(pulse_width*10);xx(1,1+(i-1)*5:i*5)=(i-1)*10^-4:10e-6:(i-1+0.45)*10^-
4;end % makes a x data set that covers only time during measurement
if xx(end)>pulse_width/1000;xx=xx(1:find(xx<=pulse_width/1000,1,'last'));end
while ~all(diff(t_T(1:pulse_t)));pulse_t=pulse_t-50; end;
yy=spline(t_T(1:pulse_t),y(1:pulse_t),xx');
pulse_width=1000*xx(find(abs(diff(yy))<100 & diff(yy)~=0,1,'last')+1);
T_start=yy(find(diff(yy(1:round(length(yy)/10)))<-5,1,'last')+1);
t_T_start=xx(find(diff(yy(1:round(length(yy)/10)))<-5,1,'last')+1)*1000;
t_fit=ceil(10*t_T_start)/10:.1:pulse_width;
T_fit=smooth(spline(xx*1000,yy,t_fit));
[AA]=plot(t_T*1000,T,xx*1000,yy,t_fit,T_fit);
set(AA(2),'LineWidth',6)
axis([0 4 0 1500])

text(t_T_start+.1,T_start,[num2str(t_T_start) ', ' num2str(round(T_start))])

T_fin=yy(find(abs(diff(yy))<100 & diff(yy)~=0,1,'last')+1);
t_T_fin=xx(find(abs(diff(yy))<100 & diff(yy)~=0,1,'last')+1)*1000;
text(t_T_fin+.1,T_fin,[num2str(t_T_fin) ', ' num2str(round(T_fin))])

```

```

hold on
plot([t_T_start, t_T_fin],[T_start, T_fin], 'LineStyle','none', 'LineWidth',1.5, 'Marker','o', 'MarkerSize',10, 'Color',[1 0 0])
hold off

text(.1,1400,['Pulse Length = ', num2str(t_T_fin-t_T_start) ' ms'])

%% plots T and spectra VS time
figure
B=plot(t_fit,T_fit);
%Plot style of T fit
set(B(1), 'LineStyle','-','LineWidth',2.5, 'Marker','none', 'MarkerSize',10, 'Color',[0 0 0])

axis([0 10 0 1500])

%% Find T ignition

t_ign=input('what is the time of ignition (ms) -type 0 to ignore this section\n ');

ign_loc=find(t_fit<t_ign,1,'last');
T_ign=T_fit(ign_loc)+(T_fit(ign_loc+1)-T_fit(ign_loc))/(t_fit(ign_loc+1)-t_fit(ign_loc))*(t_ign-t_fit(ign_loc))

hold on
plot([t_ign t_ign],[ -5 3000], 'LineStyle','--', 'Color',[.9 0 0])
hold off
text(t_ign-.75,T_ign+150,'T_ign');
text(t_ign-.75,T_ign+75,[num2str(T_ign,'%4g') 'C']);
text(t_ign-.375,T_ign+35,'\rightarrow', 'fontSize',25, 'color','r', 'rotation',-5);

%% Find T_rate ignition
dt=1*10^(-2); %time btwn frames at 100000 fps (ms)
t_1=t_ign-dt;
t_2=t_ign+dt;

ign_loc1=find(t_fit<t_1,1,'last');
T_1=T_fit(ign_loc1)+(T_fit(ign_loc1+1)-T_fit(ign_loc1))/(t_fit(ign_loc1+1)-t_fit(ign_loc1))*(t_1-t_fit(ign_loc1));

ign_loc2=find(t_fit<t_2,1,'last');
T_2=T_fit(ign_loc2)+(T_fit(ign_loc2+1)-T_fit(ign_loc2))/(t_fit(ign_loc2+1)-t_fit(ign_loc2))*(t_2-t_fit(ign_loc2));

dT=T_2-T_1;
T_rate_ign=(dT/(2*dt))*1000 % (K/s) or (Celsius/s)

```

Script #3 (C-2) T-Jump/TOFMS Matlab Script for Spectrum and Temperature Profile

```

%Temporary Setup with variable calibration
%% Initial Variables

conv=2.31221*10^11; %Conversion Factor may need tweeking from session to session (save labbooks)
ts=0.315439*10^-6; %ToF offset (calibrated 7/18/14)

max_mass=300;

R_c1=.15; %contact resistance wire 1
R_c2=.15; %contact resistance wire 2 (calibrated 7/18/14)
current_mod=-1; %conversion factor from current probe

species=[28]; %Species of interest- set to zero to ignore

```

```

%% Initialize Scope

% Create a TCPIP object.
interfaceObj = instrfind('Type', 'tcpip', 'RemoteHost', '127.0.0.1', 'RemotePort',
1861, 'Tag', '');

% Create the TCPIP object if it does not exist
% otherwise use the object that was found.
if isempty(interfaceObj)
    interfaceObj = tcpip('127.0.0.1', 1861);
else
    fclose(interfaceObj);
    interfaceObj = interfaceObj(1);
end

% Create a device object.
deviceObj = icdevice('lecroy_basic_driver.mdd', interfaceObj);
set(interfaceObj, 'InputBufferSize', 2000000);

% Connect device object to hardware.
connect(deviceObj);

%Create goup objects
groupObj_util=get(deviceObj,'Util');
groupObj_util=groupObj_util(1);
groupObj_wave = get(deviceObj, 'Waveform');
groupObj_wave = groupObj_wave(1);

%sets up scope functions
invoke(groupObj_util,'sendcommand','VBS app.Math.F2.View = True');
invoke(groupObj_util,'sendcommand','VBS app.Math.F2.MathMode = OneOperator');
invoke(groupObj_util,'sendcommand','VBS app.Math.F2.Source1 = C1');
invoke(groupObj_util,'sendcommand','VBS app.Math.F1.View = True');
invoke(groupObj_util,'sendcommand','VBS app.Math.F1.Zoom.NumSelectedSegments=1');
invoke(groupObj_util,'sendcommand','VBS app.Math.F3.View = True');
invoke(groupObj_util,'sendcommand','VBS app.Math.F3.Zoom.NumSelectedSegments=1');
invoke(groupObj_util,'sendcommand','VBS app.Math.F4.View = True');
invoke(groupObj_util,'sendcommand','VBS app.Math.F4.Zoom.NumSelectedSegments=1');

%% Get start time from Channel 1

num_seg=get(deviceObj.Sequence(1), 'Segment'); %number of segments

%Select segment 1
invoke(groupObj_util,'sendcommand','VBS app.Math.F2.Zoom.SelectedSegment=2');
invoke(groupObj_util,'sendcommand','VBS app.Math.F2.Zoom.NumSelectedSegments=1');

% Read Data
[Y1,X1,~,~,~] = invoke(groupObj_wave, 'readwaveform', 'traceB');

start_time = 0; %end of pulse, start of ToF calc
index = 2;

while start_time == 0
    if (Y1(index)<1) && (Y1(index-1)>1) % finds point where pulse ends
        start_time = X1(index);
    end
    index=index+1;
end

max_ToF=(max_mass./conv).^5; % How much data to collect, base on a max mass
[~,max_index]=find(X1>max_ToF+start_time,1, 'first');

%% Loop to collect each spectra

spectra=zeros(max_index-index+1,num_seg);
Volts=zeros(length(X1)*num_seg-num_seg,1);
t_T=zeros(length(X1)*num_seg-num_seg,1); %time for Temperature

```

```

Current_raw=zeros(length(X1)*num_seg-num_seg,1);
pulse_width=0; %heating pulse width

for i=1:1:num_seg

    %Select segment on Scope for F1 (channel 2)
    %seg_select = ['VBS app.Math.F1.Zoom.SelectedSegment=' int2str(i)];
    invoke(groupObj_util, 'sendcommand', ['VBS app.Math.F1.Zoom.SelectedSegment='
int2str(i)]);

    [Y,~,~,~] = invoke(groupObj_wave, 'readwaveform', 'traceA'); %reads Spectra Data
spectra(:,i)=Y(index:max_index);

    %read C3,C4 data and move segments until end of heating pulse
    if pulse_width==0
        invoke(groupObj_util, 'sendcommand', ['VBS app.Math.F3.Zoom.SelectedSegment='
int2str(i)]);
        invoke(groupObj_util, 'sendcommand', ['VBS app.Math.F4.Zoom.SelectedSegment='
int2str(i)]);

        %reads C3 data
        [Y,X,~,~,~] = invoke(groupObj_wave, 'readwaveform', 'traceC');
        t_T(2-i+(i-1)*length(Y):(i)*length(Y)-i,1)=X(1:length(X)-1)+10^-4*(i-1);
    %reads the time, plus 100us for each segment
        Volts(2-i+(i-1)*length(Y):(i)*length(Y)-i,1)=Y(1:length(Y)-1);

        if i>5 %if voltage is below 1 finds time of end of pulse
            for j=1:20
                if Y(length(Y)-1-j)~=Y(length(Y)-1-j-1)
                    break
                end
            end
            if j==20
                pulse_width=i;
            end
        end

        %reads C4 data
        [Y,~,~,~,~] = invoke(groupObj_wave, 'readwaveform', 'traceD');
        Current_raw(2-i+(i-1)*length(Y):(i)*length(Y)-i,1)=Y(1:length(Y)-1);

    end

end

%% Convert X-axis to m/z

ToF=X1(index:max_index)-start_time;%-ts; % Time of Flight (same for all segments)
mass=zeros(length(ToF),num_seg); % m/z
t=zeros(length(ToF),num_seg);

%Calculates m/z (5/29/2019)
a1=2.3146599788*10^(11);
b1=-1.2896951128*10^(5);
c1=-5.3551466109*10^(-2);

for j=1:num_seg
    %mass(:,j)=conv.*(ToF).^2;
    mass(:,j)=a1.*(ToF).^2+b1*(ToF).^1+c1;
    t(:,j)=(j-1)/10;
end

%% Temperature Calculation
t_T=t_T(1:(length(Y)-1)*pulse_width);
Volts=Volts(1:(length(Y)-1)*pulse_width);
Current_raw=Current_raw(1:(length(Y)-1)*pulse_width);

```

```

prompt='Wire 1(red) or 2(black)?   Type anything else to skip T calc \n   ';
wire=input(prompt);
if wire==1
    R_c=R_c1;
elseif wire==2
    R_c=R_c2;
end

if ~isempty(wire) && (wire==1 || wire==2)
    prompt='Wire Length (mm)? \n   ';
    wire_l = input(prompt);

    R_o=0.033618*wire_l/(1+0.003908*20-0.0000005775*400);   %Resistance at 0C for wire
    Current=Current_raw*current_mod;
    R=Volts./Current-R_c;

    T=(-.003908+sqrt((0.003908)^2-4*(-5.775e-7)*(1-R./R_o)))/(2*-5.775e-7);

end

clear R Current Xl Yl X Y j i max_index
%% Plot things
%3D plot
figure
plot3(mass,t,spectra,'Color',[0 0 0])
box off;
view(-20, 65);
axis([0 50 0 5 0 .1])

%plot T
if wire==1 || wire==2
    figure
    plot(t_T,T)
    axis([0 6e-3 -50 1300])
end

%species with time
if species(1)~=0
    peak_int=peak_with_t(species,0.5,mass,t,spectra);   %calls function to find peaks
    figure
    plot(peak_int(:,1),[peak_int(:,2:length(peak_int(1,:)))])
end
%% Save data

prompt='Run # for saving?   (Type 0 or hit enter to skip save)   \n   ';
save_num=input(prompt);

%Check to see if file already exists
while ~isempty(save_num) && exist(['Run_',int2str(save_num),'.mat'],'file')==2
    prompt='File already exists.  Overwrite (y/n) \n   ';
    str=input(prompt,'s');
    if str=='n'
        prompt='Run # for saving?   (Type 0 or hit enter to skip save)   \n   ';
        save_num=input(prompt);
    elseif str=='y'
        break
    end
end

if save_num~=0 && ~isempty(save_num)

save(['Run_',int2str(save_num),'.mat'],'mass','t','spectra','t_T','T','R_c','wire_l','
Current_raw','Volts','conv','ts')
end

% Delete objects.
delete([deviceObj interfaceObj]);
clear wire prompr str groupObj_util groupObj_wave

```

Appendix D: Arduino Script Example for T-Jump Nano

```
1 void setup() {
2   pinMode(5, OUTPUT); // input to push button for single shot
3   pinMode(4, INPUT); // output to push button for single shot
4   pinMode(3, OUTPUT); // signal sent to single shot segment of circuit
5   pinMode(11, OUTPUT); // signal sent to repeating pulses
6   pinMode(10, OUTPUT); // input to switch for repeating pulses
7   pinMode(9, INPUT); // output to switch for repeating pulses
8   Serial.begin(250000); //
9 }
10
11 void loop() {
12
13   static int heat_trig = 0; // pre (0), during (1), or post (2) trigger
14   static int osc = 0; // determines whether or not to send trigger to oscilloscope
15
16   unsigned long heat_time = 5000; // total time for heating in microseconds
17   static unsigned long heat_start; // stored value for heating start time
18   unsigned long heat_end; // stored value for heating finish time
19   float pulse; // value calculated to determine pulse length
20   static unsigned long current; // stored value for current time in loop
21
22   digitalWrite(5, HIGH); // sets input of trigger for heating to high
23   digitalWrite(10, HIGH); // sets input of oscilloscope to high
24
25   // if the heating trigger has been pushed and the trigger was reset
26   if (heat_trig == 0 && digitalRead(4) == HIGH) {
27     osc = 1; // turn on oscilloscope triggering signal
28     heat_trig = 1; // indicate internally that the heating trigger was pushed
29     heat_start = micros(); // record the time right before heating in microseconds
30     digitalWrite(3, HIGH); // start heating
31   }
32
33   // if the trigger has been pushed before and the oscilloscope switch is open
34   if (osc == 1 && digitalRead(9) == HIGH) {
35     digitalWrite(11, HIGH); // send pulse to oscilloscope
36     delayMicroseconds(20); // delay execution for 20us
37     digitalWrite(11, LOW); // stop pulse to oscilloscope
38   }
39
40   // if the trigger was pushed, continually record the time
41   if (heat_trig == 1) {
42     current = micros();
43   }
44
45   // if the time the wire has been heating is equal to or greater than the desired time
46   if ((current - heat_start) >= heat_time && heat_trig == 1) {
47     digitalWrite(3, LOW); // stop heating
48     heat_end = current; // record time at which the wire stopped heating
49     pulse = (heat_end - heat_start) / 1000; // calculate pulse width length based on start and end times
50     heat_trig = 2; // indicate internally that the heating pulse was triggered and was finished
51
52     // Serial.print("Start Time: ");
53     // Serial.print(heat_start/1000,3);
54     // Serial.println("ms");
55
56     // Serial.print("End Time: ");
57     // Serial.print(heat_end/1000,3);
58     // Serial.println("ms");
59
60     Serial.print("Heating Time: "); // display heating time in serial
61     Serial.print(pulse, 3);
62     Serial.println(" ms");
63     Serial.println();
64   }
65
66   // if the oscilloscope triggering switch was turned off
67   if (digitalRead(9) == LOW) {
68     osc = 0; // reset oscilloscope triggering
69   }
70
71   // if the heating trigger was pulsed and concluded but the button was not pushed again
72   if (digitalRead(4) == LOW && heat_trig == 2) {
73     heat_trig = 0; // reset heating trigger state
74   }
75 }
76 }
```

Script D-0: Arduino IDE code used to simultaneously trigger a continuous collection signal and a single shot heating signal.

Appendix E: 2D Flame Front Model MATLAB Script

```
%% Flame Propagation 2D Implicit Model
% Miles C. Rehwoldt - mcrehwoldt@gmail.com
% Dylan J. Kline - dkline@umd.edu
% University of Maryland College Park
% University of California Riverside, Zachariah Group

% Last updated 03/7/2021

% Overall:
% This code is intended to model the reaction front of energetic composites
% composed of nanoparticles and microparticles on a scale which can
% illustrate the large scale flame front corrugations as a result of small scale
% particle reactions which are intrinsically heterogeneous (High Loading Thermites).

% Includes convective boundary conditions
% Dynamic thermal conductivity at each interior node which is distributed
% randomly with different geometries. The idea of thermal resistance is
% used to quantify the effective thermal diffusivity at mesh area boundaries.

% Implicit model with dynamic adjustment to heat transfer, unconditionally
% stable.

% Setup and Modeling Characteristics:
% Will be modelled in space with transient values at meshpoints at geometric
coordinates
% (nanoparticle aggregate points) representing the propagation of the front.
% This model will assume a constant temperature in an area of  $\Delta^2$  for
% each meshpoint with logic to increase temperature as a function of space, time,
discrete
% temperature gradients, implicit chemistry (Adiabatic Flame temperature), and
temperature check points (heaviside/dirac delta emulation logic).

clear

savepath = uigetdir('Select folder to save data in');

%% Film setup
Y=input('What material distribution? Manually Added (0), Variable(1), Simple(2),
Percolating Rods(3) ? : ');
gr=input('Grid Resolution (um)?: ');
gridsize = 200; % um

%Establishing the mesh grid (200um x 200um)
y=0:(gridsize/gr); %establishes positional coordinates based on the chosen grid size
x=0:(gridsize/gr);
dim = [size(x,2) size(y,2)]; % putting this here in case someone wants to

%% Film setup-Manual Architecture
if Y==0

%Bi-Layers
d=10;
M=zeros(length(x),length(y));

M(1:101,1:5)=1;
M(1:101,6:10)=0;
M(1:101,11:15)=1;
M(1:101,16:20)=0;
M(1:101,21:25)=1;
M(1:101,26:30)=0;
M(1:101,31:35)=1;
M(1:101,36:40)=0;
M(1:101,41:45)=1;
M(1:101,46:50)=0;
M(1:101,51:55)=1;
M(1:101,56:60)=0;
M(1:101,61:65)=1;
```

```

M(1:101,66:70)=0;
M(1:101,71:75)=1;
M(1:101,76:80)=0;
M(1:101,81:85)=1;
M(1:101,86:90)=0;
M(1:101,91:95)=1;
M(1:101,96:101)=0;

D_p=logical(M==1); %logical mapping of "pore" values
D_m=logical(M==0); %logical mapping of energetic material (Inverse Mapping of "pore"
value)

filestring = sprintf('%i bi-layers_2',round(d)); % automated file naming

image(D_p)

end

%% Film setup - Variable sizes
if Y==1
void_p = 0.40; % Void percentage in fracton form
pore_dilate_mean = 2; % Average of the gaussian distribution function for
determining dilation
pore_max = 4; % Maximum desired pore size, must be an odd number
pore_dilate_sigma = 0.5; % Sigma for the gaussian function of pore dilation
strel_shape ={'diamond'}; % Dilation shape, diamond was nice, square might also work

box_size = 2e-6; % size of grid boxes (m), 2um
mat_size = 101; % number of elements in grid

% Making the Film
edges = 0; % Number of times something ended up on the edge
j = 1; % Counter variable
filled_p = 0; % Current filled percentage in decimal form
pore_image = false(mat_size); % Final image showing the pores

f = waitbar(filled_p,'Voiding :');

% Looping to label the pores
while filled_p <= void_p

    pore_dilate(j) = abs(round(normrnd(pore_dilate_mean,pore_dilate_sigma))); %
    randomly choose the dilation size using gaussian distribution %
    if pore_dilate(j) > pore_max %
    Checking to see that the pore isnt larger than a maximum size
        pore_dilate(j) = pore_max; % Fixing
    end
    it if it is larger than the pore size
        end
        strel_rand = randi([1 size(strel_shape,2)]); % Shape
    to choose for dilation (if there is more than one option)
        bg = false(pore_max*2+1); % bg is
    a temporary holding variable
        bg(pore_max+1,pore_max+1) = 1; % Label
    the center point as true
        bg = imdilate(bg,strel(char(strel_shape(strel_rand)),pore_dilate(j))); %
    Dilating the pore
        bg = imrotate(bg,randi(180)); %
    randomly rotating the pore

        randpt = randi(mat_size, 2, 1); % Random
    point in the overall image for the placement of the pore

    % checking the bounding box point for the pore to be placed
    top = round(randpt(1)-size(bg,1)/2);
    bottom = round(randpt(1)+size(bg,1)/2);
    left = round(randpt(2)-size(bg,1)/2);
    right = round(randpt(2)+size(bg,1)/2);

    % If the pore is on the edge, enter this loop to place it correctly on
    % the edge as if it had been cropped.

```

```

    if top<=1 || bottom>=mat_size || left<=1 || right>=mat_size

        % cropping amount for the bounding box
        cropamt = abs([(top<=1)*(top-1), (bottom>=mat_size)*(bottom-mat_size),
        (left<=1)*(left-1), (right>=mat_size)*(right-mat_size)]);

        bgog = bg; % bgog is
the original pore before cropping
        bg = bg(cropamt(1)+1:end-cropamt(2), cropamt(3)+1:end-cropamt(4)); % cropped
bg

        % New bounding box points for the pore
        top = top+cropamt(1);
        bottom = bottom-cropamt(2);
        left = left+cropamt(3);
        right = right-cropamt(4);

        % Correcting the size of the box if something weird happened
        temp = pore_image(top:bottom-1, left+1:right);
        if size(temp,1)~=size(bg,1)
            bg = vertcat(bg,false(1, size(bg,2)));
        end
        if size(temp,2)~=size(bg,2)
            bg = horzcat(bg,false(size(bg,1),1));
        end

        % Placing the cropped pore in the image
        pore_image(top:bottom-1, left+1:right) = pore_image(top:bottom-1,
left+1:right) + bg;

        edges = edges+1; % increase the amount of pores that ended up on the edge

    else
        % If it didnt hit the edge, then just place the pore as is
        pore_image(top:bottom-1, left:right-1) = pore_image(top:bottom-1, left:right-
1) + bg;
    end

    ptlist(j,:) = randpt; % record the center point of
the random point
    j=j+1; % increase the counter
    filled_p = sum(sum(sum(pore_image)))/mat_size^2; % update the filled percentage
    waitbar(filled_p/void_p) % update the waitbar with the
filled percentage

end

close(f)

%For Shaped Pores
% D_p=pore_image;
% D_m=~pore_image;

%For shaped particle clusters
D_m=pore_image;
D_p=~pore_image;

% figure
% histogram(pore_dilate,'BinWidth',1)

filestring = sprintf('variable5_sigma%i_voidp%i',pore_dilate_sigma,round(void_p*100));
% automated file naming

end

%% Film setup - Simple distribution
if Y==2

void_p=0.5; %porosity
%-----

```

```

%establishes the discrete diffusivity mapping, the positions are time
%independent
M=rand(length(x),length(y));
D_p=logical(M<void_p); %logical mapping of "pore" values
D_m=logical(M>void_p); %logical mapping of energetic material (Inverse Mapping of
"pore" value)

filestring = sprintf('simple_voidp%i',round(void_p*100)); % automated file naming

end

%% Film setup - Percolating rods
if Y==3

% add_mass_p = input('Additive mass percentage: ')/100; % desired additive mass
percent in decimal form
% add_density = 8960; % additive density (kg/m3),
8960 for Cu, 2100 for CNF
add_vol_p = input('Additive volume percentage: ')/100; % desired additive mass percent
in decimal form
AR = input('Aspect ratio of additive: '); % aspect ratio of particles,
must be a whole number
run_num = input('Run #: ');

% Option to use mass percentages if needed in future
% metal_mass = 0.50; % mass percent of metal fuel
% metal_density = 2700; % density of metal (kg/m3): al = 2700, ti = 4506, c =
2266
% binder_mass = 1-metal_mass; % mass percent of binder
% binder_density = 1750; % density of binder to be added (kg/m3), used PVDF
% bulk_density = metal_mass*metal_density + binder_mass*binder_density; % estimated
density of whole propellant

mat_size = fix((gridsize/gr)+1); % number of grid points

% Vtot = (1-add_mass_p)/bulk_density + add_mass_p/add_density; % estimating a "total
volume"
% void_p = add_mass_p/add_density/Vtot; % determining volume percent
additive
void_p = add_vol_p;

% Making the Film
edges = 0;
i = 0;
filled_p = 0;

blackim = false(mat_size);

if AR ==1

    blackim = zeros(mat_size); % initialize a blank matrix
    k = round(void_p*mat_size^2); % number of boxes to be filled in grid
    blackim(randperm(int64(mat_size^2),k)) = 1; % random placement of number of
particles in box
    blackim=logical(blackim); % converts to logical

else

    f = waitbar(filled_p, 'Percolating :');

    while filled_p < void_p

        bg = false(AR);
        temp = true([AR 1]);

        bg(round(AR/2), :) = temp;
        ang = 170+20*rand;
        bg = imrotate(bg,ang);

        randpt = randi(mat_size, 2, 1);

```

```

top = round(randpt(1)-size(bg,1)/2);
bottom = round(randpt(1)+size(bg,1)/2);
left = round(randpt(2)-size(bg,1)/2);
right = round(randpt(2)+size(bg,1)/2);

if top<=1 || bottom>=mat_size || left<=1 || right>=mat_size

    %endpts = [randpt(1)-size(bg,1)/2+1, (randpt(1)+size(bg,1)/2), (randpt(2)-
size(bg,1)/2+1), randpt(2)-size(bg,1)/2];
    cropamt = abs([(top<=1)*(top-1), (bottom>=mat_size)*(bottom-mat_size),
(left<=1)*(left-1), (right>=mat_size)*(right-mat_size)]);

    bgog = bg;
    bg = bg(cropamt(1)+1:end-cropamt(2), cropamt(3)+1:end-cropamt(4));

    top = top+cropamt(1);
    bottom = bottom-cropamt(2);
    left = left+cropamt(3);
    right = right-cropamt(4);

    temp = blackim(top:bottom-1, left+1:right);
    if size(temp,1)~=size(bg,1)
        bg = vertcat(bg,false(1, size(bg,2)));
    end
    if size(temp,2)~=size(bg,2)
        bg = horzcat(bg,false(size(bg,1),1));
    end

    blackim(top:bottom-1, left+1:right) = blackim(top:bottom-1, left+1:right)
+ bg;

    edges = edges+1;

else
    blackim(top:bottom-1, left:right-1) = blackim(top:bottom-1, left:right-1)
+ bg;
end

i=i+1;
ptlist(i,:) = randpt;

filled_p = sum(sum(sum(blackim)))/mat_size^2;
waitbar(filled_p/void_p)

end

close(f)

end

imshow(blackim);
D_p=blackim; %location of non-energetic portion
D_m=~blackim; %location of energetic portion
pause(2)
close all

filestring = sprintf('percolation_AR%i_voidp%i_%i',AR,round(void_p*100),run_num); %
automated file naming

end

%% Thermophysical property setup

% We will assume, for simplicity, that each grid point is the midpoint
% of thermite particle aggregates which are homogenously premixed.

% Temperatures with increase via diffusion and chemical reaction which are
% accounted for at the temperature of igniton (~900K Al/CuO) (~2500K Flame
Temperature for Al/PVDF).

```

```

% Characteristic length and time (Coupled to ensure solution converges)
delta = gr*10^(-6); % characteristic distance(m)
tau = (gr^2/100)*10^(-6); % characteristic time (s), reducing this helps reduce
solution error
h = 10; % heat transfer # (W/(m^2*K) (Convection) (Air)

% Time steps
fprintf('\nTime setup');
fprintf('\n0.25-0.5 ms recommended, takes ~1-2.5 hrs with step size of 50ns\n')
steps_T = uint16(input('Simulation time (ms): ')/(tau*1000)); %time steps (total of
0.5ms)
fprintf('Number of steps: %i\n',steps_T)
user_confirm = 'n';
% If time steps seems a bit extreme, it will double check to make sure the user knows
this is gonna suck.
while steps_T>12500 && user_confirm == 'n'
    user_confirm = input('Are you sure? This will take some time... (y/n): ','s');
    if user_confirm~='y'
        steps_T = uint16(input('Simulation time (ms): ')/(tau*1000)); %time steps
(total of 0.5ms)
        fprintf('Number of steps: %i\n',steps_T)
    end
end

% Matrix initializing at zero
T = zeros(length(x),length(y),steps_T); %Grid Point Temperatures
P = zeros(length(x),length(y)); %External Input Power
rho_cp = zeros(length(x),length(y),steps_T); %Diffusivity Values (Map)
k_c = zeros(length(x),length(y),steps_T); %Thermal Conductivity values (Map)

% Rho*cp % Materials: Cu-3.46x10^6, Ti-2.43x10^6, C-1.6x10^6,
PVDF-2.49x10^6, Viton-1.9x10^6(J/m^3K)
R1 =830850;%10^6; % rho*cp unburnt region (J/m^3K)
R2 =830850;%10^6; % rho*cp burnt region (J/m^3K)
R3 = 1006068;%10^6; % rho*cp of "dead" regions, non energetic
(J/m^3K), should be ~R1, air~1200 J/m^3K

% Thermal conductivity (SI) % Materials: Cu-385, Ti-20,C-25-5000,PVDF-0.2, Viton-
0.2 W/(m*K)
k1 = 65.5; % thermal conductivity of unburnt region W/(m*K)
k2 = 65.5; % thermal conductivity burnt region W/(m*K)
k3 = 4.3; % thermal conductivity of air for the "dead" region is
0.026 W/(m*K), copper is 385, CNF is 2000, glass is 1

% Mapping of rho_cp and k
rho_cp(:, :,1)=R1.*D_m+R3.*D_p; %Actual conductivity mapping from sum of logical
mapping
k_c(:, :,1)=k1.*D_m+k3.*D_p; %Actual thermal conductivity mapping from sum of
logical mapping

t_us = tau*10^6; %time in us
time_T = t_us*steps_T; %total time (us)

% 3000, 2800, 900

T_c=input('Characteristic Temperture (K)?: ');
T_f=input('Flame Temperature (K)?: ');
T_ig=input('Ignition Temperature (K)?: ');
T_a = input('Ambient Temperature (K)?: ');
bc_calcs = input('Calculate boundary heat losses? (y/n): ','s');

T(:, :,1)=T_a; %Intital Temperatures all at room temp.

xdim = [1 size(T,2)];
ydim = [1 size(T,1)];

% Implicit modeling setup
A = spalloc(prod(dim),prod(dim),5*prod(dim)); % The 'A' matrix
b = zeros(prod(dim),1); % current temperature in vector form

```

```

chi = zeros(prod(dim),1);      % future temperature in vector form
q = zeros(dim);              % heat input matrix in vector form
b_conv = zeros(dim);         % convection matrix

% convection maps
mask_border = false(dim);
mask_border(1,:) = true;
mask_border(dim(1),:) = true;
mask_border(:,1) = true;
mask_border(:,dim(2)) = true;
mask_corner = false(dim);
mask_corner(1,1) = true;
mask_corner(dim(1),1) = true;
mask_corner(1,dim(2)) = true;
mask_corner(dim(1),dim(2)) = true;

% Chemistry setup
c_steps=600; % characteristic number of time steps allotted for chemistry to reach
flame temperature (linear) (temperature rises occur between T_ig and T_f with equal T
rise amounts which are fractions of the Temperature difference from ignition). (Ideal
time (t_us*c_steps) should be between 30-50 us)

% Video setup
imstep = input('Image spacing (1 default, 25 works pretty well): ');
if isempty(imstep)~=0
    imstep = 1;
end

% Boolean initializing
c2 = false(size(T,1),size(T,2)); % Initialize logical variable to have no
chemistry
c2dummy = true(size(T,1),size(T,2)); % Initialize memory logic as true since no
value has been above the flame temperature yet
c4=true(size(T,1),size(T,2));

%% Looping
%-----
%Heterogeniety Conductivity distribution (If needed)
%pd = makedist('Uniform','Lower',-0.9,'Upper',0.9); %Distribution of values (Uniform)
%pd=makedist('Normal',0,S); %Distribution of values (Gaussian)
%r=random(pd,[length(x),length(y),1]); %established random white noise factor at every
boundary
%-----
Q=input('"Microwave" Heating? ON(1), OFF (0): ');
tic
f=waitbar(0,'Loading'); %wait bar

%parameters for power input gradient as a function of position
%   e=1;
%   for v=1:length(x)
%
%       D_m1(v,:)=exp(-((v-1)*(gr*10^(-6)))/e)*D_m(v,:);
%   end

for k=1:steps_T-1 %loop for time

    waitbar(double(k)/double(steps_T-1),f,sprintf('Loading... Frame %i/%i',k,steps_T-
1)) %update wait bar

    % External Input Power (Edge)

    if T(8:11,2:gridsize/gr,1:k)<1.5*T_ig %if the ignition temperature has not been
yet reach along this edge
        P(8:11,2:gridsize/gr) = 5; %input power at along an edge
        %P=2*D_m1; %input power originating at the particles
    else

```

```

        P(8:11,2:gridsize/gr) = 0;           %otherwise the input power input is zero
(turns off)
        % P=0*D_m1;

end

%External Input Power (Spot)
if Q==1

    %Spot One
    if T(10:20,45:55,1:k)<1.5*T_ig
        P(10:20,45:55)=0.80;
    else
        P(10:20,45:55)=0;
    end

end

% Thermal Diffusivity Determination and Logic
% establish the diffusivities at k>1 values which may change depending the
% temperature logic

if k>1 %Starting from the second time step

    if T(:, :, 1:k-1)<T_f                    % if the temperature at any grid
point has not reached the flame temperature at any of the previous time steps, make
the next diffusivity map the same as the first

        rho_cp(:, :, k)=rho_cp(:, :, 1);
        k_c(:, :, k)=k_c(:, :, 1);

    else                                     % if the temperature of at least
one of the grid points has reached the flame temperature, replace the grid point
diffusivity with that of the "burned" material

        T_logic=logical(T(:, :, k-1)>T_f);   % create a logic matrix for the
previous Temperature map to create next diffusivity map
        D_r=R2.*T_logic-rho_cp(:, :, k-1).*T_logic; % replacement matrix (Takes away
previous value thermal diffusivity at "burned" point and replaces with new value)
        rho_cp(:, :, k)=rho_cp(:, :, k-1)+D_r; % Creates new diffusivity map
from previous map by replacing values which satisfy the logic

        k_r=k2.*T_logic-k_c(:, :, k-1).*T_logic; % Same for thermal conductivity
        k_c(:, :, k)=k_c(:, :, k-1)+k_r;      % Same for thermal conductivity

    end

end

% Constants for implicit
beta = tau./(rho_cp(:, :, k)*delta^2);

% Thermal Conductivity Averaging
% Effective thermal conductivity values at the grid boundaries of a step
% function conductivity mapping

% ^ y, i
% |
% |---> x, j

% Movsum function performs calculations on the inside, but replaces
% edge points with NaN (which is corrected later).
k_phx = (2*movprod(k_c(:, :, k), [0 1], 2, 'Endpoints', 'fill')./movsum(k_c(:, :, k), [0
1], 2, 'Endpoints', 'fill')); % +x
k_mhx = (2*movprod(k_c(:, :, k), [1 0], 2, 'Endpoints', 'fill')./movsum(k_c(:, :, k), [1
0], 2, 'Endpoints', 'fill')); % -x
k_phy = (2*movprod(k_c(:, :, k), [0 1], 1, 'Endpoints', 'fill')./movsum(k_c(:, :, k), [0
1], 1, 'Endpoints', 'fill')); % +y
k_mhy = (2*movprod(k_c(:, :, k), [1 0], 1, 'Endpoints', 'fill')./movsum(k_c(:, :, k), [1
0], 1, 'Endpoints', 'fill')); % -y

```

```

% Setting up k_xp k_xm k_yp k_ym
k_xp = (k_phx + k_mhx)/2; % effective thermal conductivity, k_xp definition
k_xm = (k_phx - k_mhx)/2; % effective thermal conductivity, k_xm definition
k_yp = (k_phy + k_mhy)/2; % effective thermal conductivity, k_yp definition
k_ym = (k_phy - k_mhy)/2; % effective thermal conductivity, k_ym definition

% Calculating omega, 1+2.*beta.*(k_xp+k_yp)
omega = 1+2.*beta.*(k_xp+k_yp);
% Calculating epsilon, beta.*(k_yp+k_ym)
epsilon = beta.*(k_xp+k_xm);
% Calculating lambda, beta.*(k_ym-k_yp)
lambda = beta.*(k_xm-k_xp);
% Calculating gamma, beta.*(k_xm-k_xp)
gamma = beta.*(k_ym-k_yp);
% Calculating phi, beta.*(k_xp+k_xm)
phi = beta.*(k_yp+k_ym);

% Boundary condition variables
if bc_calcs == 'y'

    theta = 1 + beta.*(2*k_xp + h*delta + k_mhy); % top boundary
    theta1 = 1 + beta.*(2*k_yp + h*delta + k_mhx); % right boundary
    theta2 = 1 + beta.*(2*k_yp + h*delta + k_phx); % left boundary
    theta3 = 1 + beta.*(2*k_xp + h*delta + k_phy); % bottom boundary

    theta4 = 1 + beta.*(k_mhy + 2*h*delta + k_mhx); % NE corner
    theta5 = 1 + beta.*(k_phy + 2*h*delta + k_mhx); % SE corner
    theta6 = 1 + beta.*(k_phy + 2*h*delta + k_phx); % SW corner
    theta7 = 1 + beta.*(k_mhy + 2*h*delta + k_phx); % NW corner

    eta = beta.*k_mhy;
    eta1 = beta.*k_mhx;
    eta2 = beta.*k_phx;
    eta3 = beta.*k_phy;

end

% Setting up A matrix
for m = 1:prod(dim)

    if (m-dim(1))<=0 % left boundary
        if bc_calcs == 'y'
            if m == 1
                A(m,m) = theta6(m); % bottom left (physical) corner
                A(m,m+1) = -eta3(m); % right
                A(m,m+dim(1)) = -eta2(m); % spaced right
            elseif m == dim(1)
                A(m,m) = theta7(m); % top left (physical) corner
                A(m,m-1) = -eta(m); % left
                A(m,m+dim(1)) = -eta2(m); % spaced right
            else
                A(m,m) = theta2(m); % left border
                A(m,m-1) = gamma(m); % left
                A(m,m+1) = -phi(m); % right
                A(m,m+dim(1)) = -eta2(m); % spaced right
            end
        else
            A(m,m) = 1;
        end
    end

    elseif mod(m,dim(1)) == 1 % bottom physical boundary
        if bc_calcs == 'y'
            if prod(dim)-m+1 == dim(1)
                A(m,m) = theta5(m); % bottom right (physical) corner
                A(m,m+1) = -eta3(m); % right
                A(m,m-dim(1)) = -eta1(m); % spaced left
            else
                A(m,m) = theta3(m); % bottom physical border
                A(m,m+1) = -eta3(m); % right
                A(m,m-dim(1)) = lambda(m); % spaced left
            end
        end
    end
end

```

```

        A(m,m+dim(1)) = -epsilon(m);    % spaced right
    end
else
    A(m,m) = 1;
end

elseif mod(m,dim(1)) == 0            % top physical boundary
    if bc_calcs == 'y'
        if m == prod(dim)
            A(m,m) = theta4(m);        % top right (physical) corner
            A(m,m-1) = -eta(m);        % left
            A(m,m-dim(1)) = -etal(m);  % spaced left
        else
            A(m,m) = theta(m);         % bottom row
            A(m,m-1) = -eta(m);        % left
            A(m,m-dim(1)) = lambda(m); % spaced left
            A(m,m+dim(1)) = -epsilon(m); % spaced right
        end
    else
        A(m,m) = 1;
    end

elseif (prod(dim)-m)<dim(1) && mod(m,dim(1)) ~= 0 % right boundary
    if bc_calcs == 'y'
        A(m,m) = thetal(m);           % center
        A(m,m+1) = -phi(m);           % right
        A(m,m-1) = gamma(m);          % left
        A(m,m-dim(1)) = -etal(m);     % spaced left
    else
        A(m,m) = 1;
    end

else
    A(m,m) = omega(m);                % interior
    A(m,m-1) = gamma(m);              % gamma
    A(m,m+1) = -phi(m);               % -phi
    A(m,m-dim(1)) = lambda(m);        % gamma
    A(m,m+dim(1)) = -epsilon(m);      % phi
end

% Heat Transfer and Chemical Energy Generation
%----- LOGIC HANDLING -----%
% Ignition bool, c1
c1 = T(:, :, k) > T_ig;                % Logical matrix that determines whether
or not a point is above ignition point.

% Flame temperature and chemistry bool, c2
if k~=1                                % if the time step is after the first time
step
    c2 = (T(:, :, k-1) < T_f) & c2dummy; % Logical operation that identifies
whether or not a point has ever been above the flame temperature
    c2dummy = c2;                       % Logical memory variable that was
introduced to speed up calculations
end

% Diffusivity bool, c3
c3 = D_m(:, :) == 1;                   % Logical matrix that checks the value of the
thermal diffusivity.

% Chemistry timing bool, c4
if k > c_steps+1                        % if the total time step has
surpassed the number of chemistry steps
    c4 = (T(:, :, k) > T_ig) & (T(:, :, k-c_steps) < T_ig); % Logical operation to see if
the temperature of a particular node is currently above the ignition temperature and
if it was also not above of the igiton temperature c_steps previously
end
%----- END LOGIC HANDLING -----%

% Convection terms

```

```

    if bc_calcs == 'y'
        b_conv = (mask_border+mask_corner).*beta*T_a*h*delta;
    end

    % Setting up q matrix
    q = P + ((T_f-T_ig)/c_steps).*c1.*c2.*c3.*c4; %total energy input includes
diffusion, outside power input and implicit chemistry

    % Temperature calculation
    b = reshape(T(:,:,k)+q+b_conv,[prod(dim),1]); % current temperature matrix +
volumetric energy in vector form
    chi = A\b; % next time step temperature
    T(:,:,k+1) = reshape(chi,[dim(1) dim(2)]); % formatted to fit your screen

end

close(f);
toc
%-----

%% Save data
filestring = fullfile(savepath,filestring);
% adding directory from user selection
save(sprintf('%s.mat',filestring));
S(1) = load('train');
sound(S(1).y,S(1).Fs);

%% Make video

y=0:(200/gr); %establishes positional coordinates based on the chosen grid size
x=0:(200/gr);

ax1 = gca;

v=VideoWriter(sprintf('%s.mp4',filestring),'MPEG-4');
v.FrameRate = 150;
v.Quality=100;
open(v);

xpos_lab1 = 300;
ypos_lab1 = 385;
%scale_len = 20;

for t=2:imstep:steps_T

    %T_s1=transpose(T(:,:,t));

    %contour features
    contourf(x*gr,y*gr,T(:,:,t)',T_a-50:50:T_c,'edgecolor','none');
    %imagesc(x*gr,y*gr,T(:,:,t)')
    xlabel('x-position (um)','fontweight','bold','fontsize',14)
    ylabel('y-position (um)','fontweight','bold','fontsize',14)
    colormap(jet(T_c-T_a));
    %colormap(temp_map)
    p=colorbar;
    p.Label.String='Temperature (K)';
    caxis([300 T_c])

    % If users want to see the wires, uncomment this section
    % if Y == 3
    %     hold on
    %     whiteIm = image(imresize(cat(3,ones(dim),ones(dim),ones(dim)),2));
    %     set(whiteIm, 'AlphaData', 0.6*imresize(blackim,2));
    %     ylim([0 200])
    %     xlim([0 200])
    %     hold off
    % end

    %contour text
    txt1=['time= ' num2str(t_us*(t-1),'%.2f') 'us'];

```

```

t1=text(120,185,txt1,'Color','white');
t1.FontSize = 14;

txt3=['pixel size= ' num2str(gr) 'um'];
t3=text(120,175,txt3,'Color','white');
t3.FontSize = 14;

% txt4=['porosity= ' num2str(void_p*100) '%'];
% t4=text(120,165,txt4,'Color','white');
% t4.FontSize = 14;

%getframe(gcf);
writeVideo(v,getframe(gcf));

end

close(v)
close all

S(1) = load('train');
sound(S(1).y,S(1).Fs);

%% Single image show
% If users want to see a single image at a time just to check or make
% figures, uncomment this section

% img = input('Enter image to display: ');
%
% y=0:(200/gr); %establishes positional coordinates based on the chosen grid size
% x=0:(200/gr);
%
% ax1 = gca;
%
%
% xpos_labl = 300;
% ypos_labl = 385;
% %scale_len = 20;
%
% T_s1=transpose(T(:,:,img));
%
% %contour features
% ax1 = contourf(x*gr,y*gr,T_s1,'edgecolor','none');
% xlabel('x-position (um)','fontweight','bold','fontsize',14)
% ylabel('y-position (um)','fontweight','bold','fontsize',14)
% colormap(jet);
% p=colorbar;
% p.Label.String='Temperature (K)';
% caxis([300 T_c])
%
% % if Y == 3
% % hold on
% % whiteIm = image(imresize(cat(3,ones(dim),ones(dim),ones(dim)),2));
% % set(whiteIm, 'AlphaData', 0.6*imresize(blackim',2));
% % ylim([0 200])
% % xlim([0 200])
% % hold off
% % end
%
% %contour text
% txt1=['time= ' num2str(t_us*(t-1),'%.2f') 'us'];
% t1=text(120,185,txt1,'Color','white');
% t1.FontSize = 14;
%
% txt3=['pixel size= ' num2str(gr) 'um'];
% t3=text(120,175,txt3,'Color','white');
% t3.FontSize = 14;
%
% txt4=['porosity= ' num2str(void_p*100) '%'];
% t4=text(120,165,txt4,'Color','white');
% t4.FontSize = 14;

```

List of References

- (1) Turns, S. R. *An Introduction to Combustion Concepts and Applications*, 3rd ed.; McGraw-Hill, 2012.
- (2) Oh, J.; Yoh, J. J. Critical Changes in the Ignition and Combustion Characteristics of Aged Titanium-Based Initiators. *Combust. Flame* **2020**, *221*, 74–85. <https://doi.org/10.1016/j.combustflame.2020.07.037>.
- (3) Army, D. of the. *Military Explosives*; 1984.
- (4) Shukla, M. K.; Boddu, V. M.; Steevens, Jeffery A. Damavarapu, R.; Leszczynski, J. *Energetic Materials: From Cradle to Grave*; 2017.
- (5) Chowdhury, S.; Sullivan, K.; Piekiet, N.; Zhou, L.; Zachariah, M. R. Diffusive vs Explosive Reaction at the Nanoscale. *J. Phys. Chem.* **2010**, *114*, 9191–9195. <https://doi.org/10.1021/jp906613p>.
- (6) Ma, X.; Li, Y.; Hussain, I.; Shen, R.; Yang, G.; Zhang, K. Core–Shell Structured Nanoenergetic Materials: Preparation and Fundamental Properties. *Adv. Mater.* **2020**, *2001291*, 1–31. <https://doi.org/10.1002/adma.202001291>.
- (7) Cohen, N. S.; Fleming, R. W.; Derr, R. L. Role of Binders in Solid Propellant Combustion. *AIAA J.* **1974**, *12* (2), 212–218. <https://doi.org/10.2514/3.49195>.
- (8) Pang, W. Q.; De Luca, L. T.; Wang, K.; Fu, X. L.; Li, J. Q.; Xu, H. X.; Fan, X. Z.; Li, H. *Performance of Composite Solid Propellant Containing Nanosized Metal Particles*; Elsevier Inc., 2018. <https://doi.org/10.1016/B978-0-12-813908-0.00007-1>.
- (9) Mason, B. P.; Roland, C. M. Solid Propellants. *Rubber Chem. Technol.* **2019**, *92* (1), 1–24. <https://doi.org/10.5254/rct.19.80456>.
- (10) Huang, S.; Hong, S.; Su, Y.; Jiang, Y.; Fukushima, S.; Gill, T. M.; Yilmaz, N. E. D.; Tiwari, S.; Nomura, K. ichi; Kalia, R. K.; et al. Enhancing Combustion Performance of Nano-Al/PVDF Composites with β -PVDF. *Combust. Flame* **2020**, *219*, 467–477. <https://doi.org/10.1016/j.combustflame.2020.06.011>.
- (11) Hendel, F. J. *Review of Solid Propleants for Space Exploration*; Pasadena, CA, 1965.
- (12) Zhou, W.; DeLisio, J. B.; Wang, X.; Egan, G. C.; Zachariah, M. R. Evaluating Free vs Bound Oxygen on Ignition of Nano-Aluminum Based Energetics Leads to a Critical Reaction Rate Criterion. *J. Appl. Phys.* **2015**, *118* (11), 114303. <https://doi.org/10.1063/1.4930889>.
- (13) Wang, X.; Zhou, W.; Delisio, J. B.; Egan, G. C.; Zachariah, M. R. Doped δ -Bismuth Oxides to Investigate Oxygen Ion Transport as a Metric for Condensed Phase Thermite Ignition. *Phys. Chem. Chem. Phys.* **2017**, *19* (20), 12749–12758. <https://doi.org/10.1039/c6cp08532f>.
- (14) Shevchenko, A. A.; Dolgoborodov, A. Y.; Kirilenko, V. G.; Brazhnikov, M. A. Detonation Velocity of Mechanically Activated Mixtures of Ammonium Perchlorate and Aluminum. *Combust. Explos. Shock Waves* **2017**, *53* (4), 461–470. <https://doi.org/10.1134/S0010508217040104>.
- (15) Hobosyan, M.; Lyshevski, S. E.; Martirosyan, K. S. *Integrated Micropropulsion Systems With Nanoenergetic Propellants*; Elsevier Inc., 2018. <https://doi.org/10.1016/B978-0-12-813908-0.00011-3>.
- (16) Ruesch, M. D.; Powell, M. S.; Satija, A.; Ruesch, J. P.; Vuppuluri, V. S.; Lucht, R. P.; Son, S. F. Burning Rate and Flame Structure of Cocrystals of CL-20 and a Polycrystalline Composite Crystal of HMX/AP. *Combust. Flame* **2020**, *219*, 129–135. <https://doi.org/10.1016/j.combustflame.2020.04.009>.
- (17) Kincaid, J. F. Chemistry, Solid Propellants and History. *J. Chem. Educ.* **1982**, *59* (10), 834–836. <https://doi.org/10.1021/ed059p834>.
- (18) Kabra, S.; Gharde, S.; Gore, P. M.; Jain, S.; Khire, V. H.; Kandasubramanian, B. Recent Trends in Nanothermites: Fabrication, Characteristics and Applications. *Nano Express* **2020**, *1* (3), 032001. <https://doi.org/10.1088/2632-959x/abbce7>.
- (19) Yang, W.; Hu, R.; Zheng, L.; Yan, G.; Yan, W. Fabrication and Investigation of 3D-Printed Gun Propellants. *Mater. Des.* **2020**, *192*, 108761. <https://doi.org/10.1016/j.matdes.2020.108761>.
- (20) Muravyev, N. V.; Monogarov, K. A.; Schaller, U.; Fomenkov, I. V.; Pivkina, A. N. Progress in

- Additive Manufacturing of Energetic Materials: Creating the Reactive Microstructures with High Potential of Applications. *Propellants, Explos. Pyrotech.* **2019**, *44* (8), 941–969. <https://doi.org/10.1002/prop.201900060>.
- (21) Anniyappan, M.; Talawar, M. B.; Sinha, R. K.; Murthy, K. P. S. Review on Advanced Energetic Materials for Insensitive Munition Formulations. *Combust. Explos. Shock Waves* **2020**, *56* (5), 495–519. <https://doi.org/10.1134/S0010508220050019>.
 - (22) Oommen, C.; Jain, S. R. Ammonium Nitrate: A Promising Rocket Propellant Oxidizer. *J. Hazard. Mater.* **1999**, *67* (3), 253–281.
 - (23) Wu, C.; Sullivan, K.; Chowdhury, S.; Jian, G.; Zhou, L.; Zachariah, M. R. Encapsulation of Perchlorate Salts within Metal Oxides for Application as Nanoenergetic Oxidizers. *Adv. Funct. Mater.* **2012**, *22* (1), 78–85. <https://doi.org/10.1002/adfm.201100479>.
 - (24) Shen, R.; Ye, Y.; Wang, C.; Ru, C.; Dai, J. *Chemical Propulsion of Microthrusters*; Elsevier Inc., 2018. <https://doi.org/10.1016/B978-0-12-813908-0.00010-1>.
 - (25) Wang, H.; Jian, G.; Egan, G. C.; Zachariah, M. R. Assembly and Reactive Properties of Al/CuO Based Nanothermite Microparticles. *Combust. Flame* **2014**, *161* (8), 2203–2208. <https://doi.org/10.1016/j.combustflame.2014.02.003>.
 - (26) Hu, Y.; Tao, B.; Hao, D.; Fan, R.; Xia, D.; Lin, K.; Pang, A.; Yang, Y. Fabrication and Mechanistic Study of AP/NAI/PTFE Spherical Encapsulated Energetic Materials with Enhanced Combustion Performance. *Chem. Eng. Sci.* **2020**, *222*, 115701. <https://doi.org/10.1016/j.ces.2020.115701>.
 - (27) Zachariah, M. R. NanoEnergetics: Hype, Reality and Future. *Propellants, Explos. Pyrotech.* **2013**, *38* (1), 7. <https://doi.org/10.1002/prop.201380131>.
 - (28) Bao, G.; Abe, R. Y.; Akutsu, Y. Bond Dissociation Energy and Thermal Stability of Energetic Materials. *J. Therm. Anal. Calorim.* **2020**, 1–7. <https://doi.org/10.1007/s10973-020-10273-1>.
 - (29) Anderson, D. L. Chemical Composition of the Mantle. In *Theory of the Earth*; 1989; pp 147–175.
 - (30) Haynes, W. M.; Lide, D. R.; Bruno, T. J. Abundance of Elements in the Earth's Crust and in the Sea. In *CRC Handbook of Chemistry and Physics*; pp 14–17.
 - (31) Rossi, C. Two Decades of Research on Nano-Energetic Materials. *Propellants, Explos. Pyrotech.* **2014**, *39* (3), 323–327. <https://doi.org/10.1002/prop.201480151>.
 - (32) Chen, W.; Hase, W. L.; Schlegel, H. B. Ab Initio MO Calculations of the Thermochemistry of BX, AlX, OBX and OAlX (X=O, F, Cl). In *Gas Phase Metal Reactions*; Elsevier B.V., 1992; pp 179–187.
 - (33) Osborne, D. T.; Pantoya, M. L. Effect of Al Particle Size on the Thermal Degradation of Al/Teflon Mixtures. *Combust. Sci. Technol.* **2007**, *179* (8), 1467–1480. <https://doi.org/10.1080/00102200601182333>.
 - (34) Piekiet, N. W.; Zhou, L.; Sullivan, K. T.; Chowdhury, S.; Egan, G. C.; Zachariah, M. R. Initiation and Reaction in Al/Bi₂O₃ Nanothermites: Evidence for the Predominance of Condensed Phase Chemistry. *Combust. Sci. Technol.* **2014**, *186* (9), 1209–1224. <https://doi.org/10.1080/00102202.2014.908858>.
 - (35) Glavier, L.; Taton, G.; Ducéré, J.; Baijot, V.; Pinon, S.; Calais, T.; Estève, A.; Rouhani, M. D.; Rossi, C. Nanoenergetics as Pressure Generator for Nontoxic Impact Primers: Comparison of Al/Bi₂O₃, Al/CuO, Al/MoO₃ Nanothermites and Al/PTFE. *Combust. Flame* **2015**, *162* (5), 1813–1820. <https://doi.org/10.1016/j.combustflame.2014.12.002>.
 - (36) Zarko, V. E. *The Prospects of Using Nanoenergetic Matrials in Solid Rocket Propulsion*; Elsevier Inc., 2019. <https://doi.org/10.1016/B978-0-12-813908-0.00001-0>.
 - (37) Young, G.; Wang, H.; Zachariah, M. R. Application of Nano-Aluminum/Nitrocellulose Mesoparticles in Composite Solid Rocket Propellants. *Propellants, Explos. Pyrotech.* **2015**, *40* (3), 413–418. <https://doi.org/10.1002/prop.201500020>.
 - (38) Vellaisamy, U.; Biswas, S. Effect of Metal Additives on Neutralization and Characteristics of AP/HTPB Solid Propellants. *Combust. Flame* **2020**, *221*, 326–337. <https://doi.org/10.1016/j.combustflame.2020.08.006>.
 - (39) Galfetti, L.; De Luca, L. T.; Severini, F.; Meda, L.; Marra, G.; Marchetti, M.; Regi, M.; Bellucci, S. Nanoparticles for Solid Rocket Propulsion. *J. Phys. Condens. Matter* **2006**, *18*, S1991–S2005. <https://doi.org/10.1088/0953-8984/18/33/S15>.

- (40) Jacob, R. J.; Wei, B.; Zachariah, M. R. Quantifying the Enhanced Combustion Characteristics of Electro spray Assembled Aluminum Mesoparticles. *Combust. Flame* **2016**, *167*, 472–480. <https://doi.org/10.1016/j.combustflame.2015.09.032>.
- (41) Wang, H.; Jacob, R. J.; Delisio, J. B.; Zachariah, M. R. Assembly and Encapsulation of Aluminum NP's within AP/NC Matrix and Their Reactive Properties. *Combust. Flame* **2017**, *180*, 175–183. <https://doi.org/10.1016/j.combustflame.2017.02.036>.
- (42) Yuan, J.; Liu, J.; Zhou, Y.; Zhang, Y.; Cen, K. Thermal Decomposition and Combustion Characteristics of Al/AP/HTPB Propellant. *J. Therm. Anal. Calorim.* **2020**, 1–10. <https://doi.org/10.1007/s10973-020-09297-4>.
- (43) Valluri, S. K.; Schoenitz, M.; Dreizin, E. Fluorine-Containing Oxidizers for Metal Fuels in Energetic Formulations. *Def. Technol.* **2019**, *15* (1), 1–22. <https://doi.org/10.1016/j.dt.2018.06.001>.
- (44) Esposito, P. H.; Leroux, C.; Heresanu, V.; Neisius, T.; Madigou, V.; Denoyel, R.; Coulet, M. V. Influence of Texture and Microstructure on the Reactivity of Aluminum Powders. *Materialia* **2020**, *14*, 100880. <https://doi.org/10.1016/j.mtla.2020.100880>.
- (45) Chakraborty, P.; Zachariah, M. R. Do Nanoenergetic Particles Remain Nano-Sized during Combustion? *Combust. Flame* **2014**, *161* (5), 1408–1416. <https://doi.org/10.1016/j.combustflame.2013.10.017>.
- (46) Trunov, M. A.; Schoenitz, M.; Dreizin, E. L. Effect of Polymorphic Phase Transformations in Alumina Layer on Ignition of Aluminium Particles. *Combust. Theory Model.* **2006**, *10* (4), 603–623. <https://doi.org/10.1080/13647830600578506>.
- (47) Trunov, M. A.; Schoenitz, M.; Zhu, X.; Dreizin, E. L. Effect of Polymorphic Phase Transformations in Al₂O₃ Film on Oxidation Kinetics of Aluminum Powders. *Combust. Flame* **2005**, *140*, 310–318. <https://doi.org/10.1016/j.combustflame.2004.10.010>.
- (48) Wang, H.; Julien, B.; Kline, D. J.; Alibay, Z.; Rehwoldt, M. C.; Rossi, C.; Zachariah, M. R. Probing the Reaction Zone of Nanolaminates at $\sim\mu\text{s}$ Time and $\sim\mu\text{m}$ Spatial Resolution. *J. Phys. Chem. C* **2020**, *124* (25), 13679–13687. <https://doi.org/10.1021/acs.jpcc.0c01647>.
- (49) Dreizin, E. *Reactive Materials with Burn Rate Adjusted by Initiation Method*; 2020.
- (50) Valluri, S. K.; Schoenitz, M.; Dreizin, E. Preparation and Characterization of Silicon-Metal Fluoride Reactive Composites. *Nanomaterials* **2020**, *10*, 2367.
- (51) Salvagnac, L.; Assie-Souleille, S.; Rossi, C. Layered Al/CuO Thin Films for Tunable Ignition and Actuators. *Nanomaterials* **2020**, *10* (10), 2009. <https://doi.org/10.3390/nano10102009>.
- (52) Egan, G. C.; Zachariah, M. R. Commentary on the Heat Transfer Mechanisms Controlling Propagation in Nanothermites. *Combust. Flame* **2015**, *162* (7), 2959–2961. <https://doi.org/10.1016/j.combustflame.2015.04.013>.
- (53) Jian, G.; Chowdhury, S.; Sullivan, K.; Zachariah, M. R. Nanothermite Reactions: Is Gas Phase Oxygen Generation from the Oxygen Carrier an Essential Prerequisite to Ignition? *Combust. Flame* **2013**, *160* (2), 432–437. <https://doi.org/10.1016/j.combustflame.2012.09.009>.
- (54) Comet, M.; Martin, C.; Schnell, F.; Spitzer, D. Energetic Nanoparticles and Nanomaterials for Future Defense Applications. *Hum. Factors Mech. Eng. Def. Saf.* **2019**, *3* (1), 1–6.
- (55) Ghildiyal, P.; Ke, X.; Biswas, P.; Nava, G.; Schwan, J.; Xu, F.; Kline, D. J.; Wang, H.; Mangolini, L.; Zachariah, M. R. Silicon Nanoparticles for the Reactivity and Energetic Density Enhancement of Energetic-Biocidal Mesoparticle Composites. *ACS Appl. Mater. Interfaces* **2021**, *13*, 458–467. <https://doi.org/10.1021/acsami.0c17159>.
- (56) Apperson, S. J.; Bezmelnitsyn, A. V.; Thiruvengadathan, R.; Gangopadhyay, K.; Gangopadhyay, S.; Balas, W. A.; Anderson, P. E.; Nicolich, S. M. Characterization of Nanothermite Material for Solid-Fuel Microthruster Applications. *J. Propuls. Power* **2009**, *25* (5), 1086–1091. <https://doi.org/10.2514/1.43206>.
- (57) Sullivan, K. T.; Piekielek, N. W.; Wu, C.; Chowdhury, S.; Kelly, S. T.; Hufnagel, T. C.; Fezzaa, K.; Zachariah, M. R. Reactive Sintering: An Important Component in the Combustion of Nanocomposite Thermites. *Combust. Flame* **2012**, *159* (1), 2–15. <https://doi.org/10.1016/j.combustflame.2011.07.015>.
- (58) Wang, X.; Wu, T.; Zachariah, M. R. Doped Perovskites To Evaluate the Relationship between Fuel–Oxidizer Thermite Ignition and Bond Energy, Electronegativity, and Oxygen Vacancy. *J. Phys. Chem. C* **2017**, *121* (1), 147–152. <https://doi.org/10.1021/acs.jpcc.6b10571>.

- (59) Dai, J.; Wang, F.; Ru, C.; Xu, J.; Wang, C.; Zhang, W.; Ye, Y.; Shen, R. Ammonium Perchlorate as an Effective Additive for Enhancing the Combustion and Propulsion Performance of Al/CuO Nanothermites. *J. Phys. Chem. C* **2018**, *122* (18), 10240–10247. <https://doi.org/10.1021/acs.jpcc.8b01514>.
- (60) Young, G.; Wilson, D. P.; Kessler, M.; DeLisio, J. B.; Zachariah, M. R. Ignition and Combustion Characteristics of Al/RDX/NC Nanostructured Microparticles. *Combust. Sci. Technol.* **2020**, 1–17. <https://doi.org/10.1080/00102202.2020.1733541>.
- (61) Firmansyah, D. A.; Sullivan, K.; Lee, K.-S.; Kim, Y. H.; Zahaf, R.; Zachariah, M. R.; Lee, D. Microstructural Behavior of the Alumina Shell and Aluminum Core Before and After Melting of Aluminum Nanoparticles. *J. Phys. Chem. C* **2012**, *116* (1), 404–411. <https://doi.org/10.1021/jp2095483>.
- (62) Gao, J.; Yan, J.; Zhao, B.; Zhang, Z.; Yu, Q. In Situ Observation of Temperature-Dependent Atomistic and Mesoscale Oxidation Mechanisms of Aluminum Nanoparticles. *Nano Res.* **2020**, *13* (1), 183–187. <https://doi.org/10.1007/s12274-019-2593-3>.
- (63) Huang, C.; Jian, G.; Delisio, J. B.; Wang, H.; Zachariah, M. R. Electro spray Deposition of Energetic Polymer Nanocomposites with High Mass Particle Loadings : A Prelude to 3D Printing of Rocket Motors. *Adv. Eng. Mater.* **2014**, *17* (1), 95–101. <https://doi.org/10.1002/adem.201400151>.
- (64) Egan, G. C.; Sullivan, K. T.; Lagrange, T.; Reed, B. W.; Zachariah, M. R. In Situ Imaging of Ultra-Fast Loss of Nanostructure in Nanoparticle Aggregates. *J. Appl. Phys.* **2014**, *115*, 084903. <https://doi.org/10.1063/1.4867116>.
- (65) Levitas, V. I. Burn Time of Aluminum Nanoparticles: Strong Effect of the Heating Rate and Melt-Dispersion Mechanism. *Combust. Flame* **2009**, *156* (2), 543–546. <https://doi.org/10.1016/j.combustflame.2008.11.006>.
- (66) Howard, S. M. Ellingham Diagrams. *SD School of Mines and Technology*. 2006. <https://doi.org/10.1149/1.2404111>.
- (67) Delisio, J. B.; Hu, X.; Wu, T.; Egan, G. C.; Young, G.; Zachariah, M. R. Probing the Reaction Mechanism of Aluminum/Poly(Vinylidene Fluoride) Composites. *J. Phys. Chem. B* **2016**, *120* (24), 5534–5542. <https://doi.org/10.1021/acs.jpcc.6b01100>.
- (68) Koch, E. C. Metal-Fluorocarbon-Pyrolants: III. Development and Application of Magnesium/Teflon/Viton (MTV). *Propellants, Explos. Pyrotech.* **2002**, *27* (5), 262–266. [https://doi.org/10.1002/1521-4087\(200211\)27:5<262::AID-PREP262>3.0.CO;2-8](https://doi.org/10.1002/1521-4087(200211)27:5<262::AID-PREP262>3.0.CO;2-8).
- (69) de Barros, L.; Pinheiro, A. P. M.; Câmara, J. da E.; Iha, K. Qualification of Magnesium/Teflon/Viton Pyrotechnic Composition Used in Rocket Motors Ignition System. *J. Aerosp. Technol. Manag.* **2016**, *8* (2), 130–136. <https://doi.org/10.5028/jatm.v8i2.596>.
- (70) Wang, H.; Kline, D. J.; Rehwoldt, M.; Wu, T.; Zhao, W.; Wang, X.; Zachariah, M. R. Architecture Can Significantly Alter the Energy Release Rate from Nanocomposite Energetics. *ACS Appl. Polym. Mater.* **2019**, *1* (5), 982–989. <https://doi.org/10.1021/acsapm.9b00016>.
- (71) Wu, J.; Liu, Q.; Feng, B.; Wu, S.; Zhang, S.; Gao, Z.; Yin, Q.; Li, Y.; Xiao, L.; Huang, J. A Comparative Study on the Mechanical and Reactive Behavior of Three Fluorine-Containing Thermites. *RSC Adv.* **2020**, *10* (10), 5533–5539. <https://doi.org/10.1039/d0ra00044b>.
- (72) Rehwoldt, M. C.; Wang, H.; Kline, D. J.; Wu, T.; Eckman, N.; Wang, P.; Agrawal, N. R.; Zachariah, M. R. Ignition and Combustion Analysis of Direct Write Fabricated Aluminum/Metal Oxide/PVDF Films. *Combust. Flame* **2020**, *211*. <https://doi.org/10.1016/j.combustflame.2019.08.023>.
- (73) Hoffman, D. M. Dynamic Mechanical Signatures of Viton A and Plastic Bonded Explosives Based on This Polymer. *Polym. Eng. Sci.* **2003**, *43* (1), 139–156. <https://doi.org/10.1002/pen.10012>.
- (74) Yan, Q. L.; Zeman, S.; Elbeih, A. Thermal Behavior and Decomposition Kinetics of Viton A Bonded Explosives Containing Attractive Cyclic Nitramines. *Thermochim. Acta* **2013**, *562*, 56–64. <https://doi.org/10.1016/j.tca.2013.03.041>.
- (75) Zhang, J.; Hooper, J. P.; Zhang, J.; Shreeve, J. M. Well-Balanced Energetic Cocrystals of H5IO6/HIO3 Achieved by a Small Acid-Base Gap. *Chem. Eng. J.* **2021**, *405*, 126623. <https://doi.org/10.1016/j.cej.2020.126623>.
- (76) Li, Y.; Li, B.; Zhang, D.; Xie, L. External Electric Field Induced Structural Transformation

- and Decreased Sensitivity of CL-20/EPDM Composites. *Chem. Phys. Lett.* **2020**, *757*, 137875. <https://doi.org/10.1016/j.cplett.2020.137875>.
- (77) Kline, D. J.; Alibay, Z.; Rehwoldt, M. C.; Idrogo-Lam, A.; Hamilton, S. G.; Biswas, P.; Xu, F.; Zachariah, M. R. Experimental Observation of the Heat Transfer Mechanisms That Drive Propagation in Additively Manufactured Energetic Materials. *Combust. Flame* **2020**, *215*, 417–424. <https://doi.org/10.1016/j.combustflame.2020.01.020>.
- (78) Rogachev, A. S.; Baras, F. Models of SHS: An Overview. *Int. J. Self-Propagating High-Temperature Synth.* **2007**, *16* (3), 141–153. <https://doi.org/10.3103/s1061386207030077>.
- (79) Mukasyan, A. S.; Rogachev, A. S. Discrete Reaction Waves: Gasless Combustion of Solid Powder Mixtures. *Prog. Energy Combust. Sci.* **2008**, *34* (3), 377–416. <https://doi.org/10.1016/j.peccs.2007.09.002>.
- (80) Barani, Z.; Mohammadzadeh, A.; Geremew, A.; Huang, C.-Y.; Coleman, D.; Mangolini, L.; Kargar, F.; Balandin, A. A. Thermal Properties of the Binary-Filler Hybrid Composites with Graphene and Copper Nanoparticles. *Adv. Funct. Mater.* **2020**, *30* (8), 1904008. <https://doi.org/10.1002/adfm.201904008>.
- (81) Brotman, S.; Rouhani, M. D.; Rossi, C.; Estève, A. A Condensed Phase Model of the Initial Al/CuO Reaction Stage to Interpret Experimental Findings. *J. Appl. Phys.* **2019**, *125* (3), 035102. <https://doi.org/10.1063/1.5063285>.
- (82) Roy, S.; Sen, O.; Rai, N. K.; Moon, M.; Welle, E.; Molek, C.; Choi, K. K.; Udaykumar, H. S. Structure–Property–Performance Linkages for Heterogenous Energetic Materials through Multi-Scale Modeling. *Multiscale Multidiscip. Model. Exp. Des.* **2020**. <https://doi.org/10.1007/s41939-020-00075-1>.
- (83) Collard, D. N.; McClain, M. S.; Rahman, N. A.; Dorcy, N. H.; Meyer, T. R.; Son, S. F. Dynamic X-Ray Imaging of Additively Manufactured Reactive Components in Solid Propellants. *J. Propuls. Power* **2020**, 1–7. <https://doi.org/10.2514/1.B38128>.
- (84) Zhong, L.; Mao, Y.; Zhou, X.; Zheng, D.; Guo, C.; Wang, R.; Zhang, X.; Gao, B.; Wang, D. 3D Printing of Hollow Fiber Nanothermites with Cavity-Mediated Self-Accelerating Combustion. *J. Appl. Phys.* **2021**, *129*, 105105. <https://doi.org/10.1063/5.0039604>.
- (85) Nie, H.; Pisharath, S.; Hng, H. H. Combustion of Fluoropolymer Coated Al and Al–Mg Alloy Powders. *Combust. Flame* **2020**, *220*, 394–406. <https://doi.org/10.1016/j.combustflame.2020.07.016>.
- (86) Smith, D. K.; Unruh, D. K.; Wu, C. C.; Pantoya, M. L. Replacing the Al₂O₃ Shell on Al Particles with an Oxidizing Salt, Aluminum Iodate Hexahydrate. Part I: Reactivity. *J. Phys. Chem. C* **2017**, *121* (41), 23184–23191. <https://doi.org/10.1021/acs.jpcc.7b05803>.
- (87) Bodnár, E.; Grifoll, J.; Rosell-Llompart, J. Polymer Solution Electrospaying: A Tool for Engineering Particles and Films with Controlled Morphology. *J. Aerosol Sci.* **2018**, *125*, 93–118. <https://doi.org/10.1016/j.jaerosci.2018.04.012>.
- (88) He, W.; Lyu, J. Y.; Tang, D. Y.; He, G. Q.; Liu, P. J.; Yan, Q. L. Control the Combustion Behavior of Solid Propellants by Using Core-Shell Al-Based Composites. *Combust. Flame* **2020**, *221*, 441–452. <https://doi.org/10.1016/j.combustflame.2020.07.006>.
- (89) Lee, H.; Kim, J. H.; Kang, S.; Deshmukh, P. R.; Sohn, Y.; Hyun, H. S.; Shin, W. G. Ignition of Nickel Coated Aluminum Agglomerates Using Shock Tube. *Combust. Flame* **2020**, *221*, 160–169. <https://doi.org/10.1016/j.combustflame.2020.07.021>.
- (90) Wang, H.; Jian, G.; Yan, S.; Delisio, J. B.; Huang, C.; Zachariah, M. R. Electrospay Formation of Gelled Nano-Aluminum Microspheres with Superior Reactivity. *ACS Appl. Mater. Interfaces* **2013**, *5* (15), 6797–6801.
- (91) Wang, H.; Rehwoldt, M. C.; Wang, X.; Yang, Y.; Zachariah, M. R. On the Promotion of High Temperature AP Decomposition with Silica Mesoparticles. *Combust. Flame* **2019**, *200*, 296–302. <https://doi.org/10.1016/j.combustflame.2018.11.021>.
- (92) Song, B.; Yang, Y.; Rabbani, M.; Yang, T. T.; He, K.; Hu, X.; Yuan, Y.; Ghildiyal, P.; Dravid, V. P.; Zachariah, M. R.; et al. In Situ Oxidation Studies of High-Entropy Alloy Nanoparticles. *ACS Nano* **2020**, 1–13. <https://doi.org/10.1021/acsnano.0c05250>.
- (93) Terry, B. C.; Gunduz, I. E.; Pfeil, M. A.; Sippel, T. R.; Son, S. F. A Mechanism for Shattering Microexplosions and Dispersive Boiling Phenomena in Aluminum–Lithium Alloy Based Solid Propellant. *Proc. Combust. Inst.* **2017**, *36* (2), 2309–2316.

- <https://doi.org/10.1016/j.proci.2016.06.099>.
- (94) Terry, B. C.; Sippel, T. R.; Pfeil, M. A.; Gunduz, I. E.; Son, S. F. Removing Hydrochloric Acid Exhaust Products from High Performance Solid Rocket Propellant Using Aluminum-Lithium Alloy. *J. Hazard. Mater.* **2016**, *317*, 259–266. <https://doi.org/10.1016/j.jhazmat.2016.05.067>.
- (95) Li, X.; Guerieri, P.; Zhou, W.; Huang, C.; Zachariah, M. R. Direct Deposit Laminate Nanocomposites with Enhanced Propellant Properties. *ACS Appl. Mater. Interfaces* **2015**, *7* (17), 9103–9109. <https://doi.org/10.1021/acsami.5b00891>.
- (96) Yan, S.; Jian, G.; Zachariah, M. R. Electrospun Nanofiber-Based Thermite Textiles and Their Reactive Properties. *ACS Appl. Mater. Interfaces* **2012**, *4* (12), 6432–6435.
- (97) Elder, B.; Neupane, R.; Tokita, E.; Ghosh, U.; Hales, S.; Kong, Y. L. Nanomaterial Patterning in 3D Printing. *Adv. Mater.* **2020**, *1907142*, 1–42. <https://doi.org/10.1002/adma.201907142>.
- (98) Li, X.; Zachariah, M. R. Direct Deposit of Fiber Reinforced Energetic NanoComposites. *Propellants, Explos. Pyrotech.* **2017**, *42* (9), 1079–1084. <https://doi.org/10.1002/prep.201700038>.
- (99) Kabir, S. M. F.; Mathur, K.; Seyam, A.-F. M. The Road to Improved Fiber-Reinforced 3D Printing Technology. *Technologies* **2020**, *8* (51), 1–15. <https://doi.org/10.3390/technologies8040051>.
- (100) Martins, P.; Lopes, A. C.; Lanceros-Mendez, S. Electroactive Phases of Poly(Vinylidene Fluoride): Determination, Processing and Applications. *Prog. Polym. Sci.* **2014**, *39* (4), 683–706. <https://doi.org/10.1016/j.progpolymsci.2013.07.006>.
- (101) Ligon, S. C.; Liska, R.; Stampfl, J.; Gurr, M.; Mulhaupt, R. Polymers for 3D Printing and Customized Additive Manufacturing. *Chem. Rev.* **2017**, *117* (15), 10212–10290. <https://doi.org/10.1021/acs.chemrev.7b00074>.
- (102) Golobic, A. M.; Durban, M. D.; Fisher, S. E.; Grapes, M. D.; Ortega, J. M.; Spadaccini, C. M.; Duoss, E. B.; Gash, A. E.; Sullivan, K. T. Active Mixing of Reactive Materials for 3D Printing. *Adv. Eng. Mater.* **2019**, *21* (8), 1900147. <https://doi.org/10.1002/adem.201900147>.
- (103) Sullivan, K. T.; Zhu, C.; Duoss, E. B.; Gash, A. E.; Kolesky, D. B.; Kuntz, J. D.; Lewis, J. A.; Spadaccini, C. M. Controlling Material Reactivity Using Architecture. *Adv. Mater.* **2016**, *28*, 1934–1939. <https://doi.org/10.1002/adma.201504286>.
- (104) Wainwright, E. R.; Sullivan, K. T.; Grapes, M. D. Designer Direct Ink Write 3D-Printed Thermites with Tunable Energy Release Rates. *Adv. Eng. Mater.* **2020**, *22*, 1901196. <https://doi.org/10.1002/adem.201901196>.
- (105) Singh, M.; Haring, A. P.; Tong, Y.; Cesewski, E.; Ball, E.; Jasper, R.; Davis, E. M.; Johnson, B. N. Additive Manufacturing of Mechanically Isotropic Thin Films and Membranes via Microextrusion 3D Printing of Polymer Solutions. *ACS Appl. Mater. Interfaces* **2019**, *11* (6), 6652–6661. <https://doi.org/10.1021/acsami.8b22164>.
- (106) Dickson, A. N.; Abourayana, H. M.; Dowling, D. P. 3D Printing of Fibre-Reinforced Thermoplastic Composites Using Fused Filament Fabrication — A Review. *Polymers (Basel)*. **2020**, *12* (10), 2188. <https://doi.org/https://doi.org/10.3390/polym12102188>.
- (107) Strutton, J. W.; Knott, M.; Bencomo, J. A.; Iacono, S. T.; Mates, J. E.; Alston, J. R.; McCollum, J. M. Manipulating Polymer Decomposition to Alter Burn Performance in Aluminum/PVDF Filaments. *Polym. Int.* **2020**. <https://doi.org/10.1002/pi.6129>.
- (108) Fleck, T. J.; Murray, A. K.; Gunduz, I. E.; Son, S. F.; Chiu, G. T.-C.; Rhoads, J. F. Additive Manufacturing of Multifunctional Reactive Materials. *Addit. Manuf.* **2017**, *17*, 176–182. <https://doi.org/10.1016/j.addma.2017.08.008>.
- (109) Knott, M. C.; Craig, A. W.; Shankar, R.; Morgan, S. E.; Iacono, S. T.; Mates, J. E.; McCollum, J. M. Balancing Processing Ease with Combustion Performance in Aluminum/PVDF Energetic Filaments. *J. Mater. Res.* **2020**, 1–8. <https://doi.org/10.1557/jmr.2020.221>.
- (110) Collard, D. N.; Fleck, T. J.; Rhoads, J. F.; Son, S. F. Tailoring the Reactivity of Printable Al/PVDF Filament. *Combust. Flame* **2021**, *223*, 110–117. <https://doi.org/10.1016/j.combustflame.2020.09.016>.
- (111) McClain, M. S.; Gunduz, I. E.; Son, S. F. Additive Manufacturing of Ammonium Perchlorate Composite Propellant with High Solids Loadings. *Proc. Combust. Inst.* **2019**, *37* (3), 3135–3142. <https://doi.org/10.1016/j.proci.2018.05.052>.

- (112) Wang, H.; Shen, J.; Kline, D. J.; Eckman, N.; Agrawal, N. R.; Wu, T.; Wang, P.; Zachariah, M. R. Direct Writing of a 90 Wt% Particle Loading Nanothermite. *Adv. Mater.* **2019**, *31* (23), 1–7. <https://doi.org/10.1002/adma.201806575>.
- (113) McClain, M. S.; Afriat, A.; Rhoads, J. F.; Gunduz, I. E.; Son, S. F. Development and Characterization of a Photopolymeric Binder for Additively Manufactured Composite Solid Propellant Using Vibration Assisted Printing. *Propellants, Explos. Pyrotech.* **2020**, *45*, 1–12. <https://doi.org/10.1002/prop.201900387>.
- (114) Durban, M. M.; Golobic, A. M.; Grapes, M. D.; Bukovsky, E. V.; Gash, A. E.; Sullivan, K. T. Development and Characterization of 3D Printable Thermite Component Materials. *Adv. Mater. Technol.* **2018**, *3* (12), 1800120. <https://doi.org/10.1002/admt.201800120>.
- (115) Jian, G.; Zhou, L.; Piekiet, N. W.; Zachariah, M. R. Low Effective Activation Energies for Oxygen Release from Metal Oxides: Evidence for Mass-Transfer Limits at High Heating Rates. *ChemPhysChem* **2014**, *15* (8), 1666–1672. <https://doi.org/10.1002/cphc.201301148>.
- (116) Jacob, R. J.; Kline, D. J.; Zachariah, M. R. High Speed 2-Dimensional Temperature Measurements of Nanothermite Composites: Probing Thermal vs. Gas Generation Effects. *J. Appl. Phys.* **2018**, *123* (11), 115902. <https://doi.org/10.1063/1.5021890>.
- (117) Rajak, R.; Chakravarthy, S. R.; Ganesan, S. Measurement of Admittance and Acoustic Augmentation of Burning Rate of Composite Solid Propellants Using Laser Doppler Velocimetry. *Proc. Combust. Inst.* **2020**, 1–9. <https://doi.org/10.1016/j.proci.2020.06.384>.
- (118) Shen, J.; Wang, H.; Kline, D. J.; Yang, Y.; Wang, X.; Rehwoldt, M.; Wu, T.; Holdren, S.; Zachariah, M. R. Combustion of 3D Printed 90 Wt% Loading Reinforced Nanothermite. *Combust. Flame* **2020**, *215*, 86–92. <https://doi.org/10.1016/j.combustflame.2020.01.021>.
- (119) Sarathi, P. S. In-Situ Combustion Handbook—Principles and Practices. *Energy* **1999**, 403.
- (120) Rehwoldt, M. C.; Yang, Y.; Wang, H.; Holdren, S.; Zachariah, M. R. Ignition of Nanoscale Titanium/Potassium Perchlorate Pyrotechnic Powder: Reaction Mechanism Study. *J. Phys. Chem. C* **2018**, *122* (20), 10792–10800. <https://doi.org/10.1021/acs.jpcc.8b03164>.
- (121) Wang, H.; Kline, D. J.; Rehwoldt, M.; Zachariah, M. R. Ignition and Combustion Characterization of Ca(IO₃)₂-Based Pyrotechnic Composites with B, Al, and Ti. *Propellants, Explos. Pyrotech.* **2018**, *43* (10), 977–985. <https://doi.org/10.1002/prop.201800041>.
- (122) Chen, R.; Luo, Y.; Sun, J.; Li, G. Preparation and Properties of an AP/RDX/SiO₂ Nanocomposite Energetic Material by the Sol-Gel Method. *Propellants, Explos. Pyrotech.* **2012**, *37* (4), 422–426. <https://doi.org/10.1002/prop.201000151>.
- (123) Sun, Y.; Chintersingh, K. L.; Schoenitz, M.; Dreizin, E. L. Reactive Shell Model for Boron Oxidation. *J. Phys. Chem. C* **2019**, *123* (18), 11807–11813. <https://doi.org/10.1021/acs.jpcc.9b03363>.
- (124) Wang, H.; Kline, D. J.; Zachariah, M. R. In-Operando High-Speed Microscopy and Thermometry of Reaction Propagation and Sintering in a Nanocomposite. *Nat. Commun.* **2019**, *10* (1), 8. <https://doi.org/10.1038/s41467-019-10843-4>.
- (125) Lahiner, G.; Nicollet, A.; Zapata, J.; Marín, L.; Richard, N.; Rouhani, M. D.; Rossi, C.; Estève, A. A Diffusion-Reaction Scheme for Modeling Ignition and Self-Propagating Reactions in Al/CuO Multilayered Thin Films. *J. Appl. Phys.* **2017**, *122* (15), 155105. <https://doi.org/10.1063/1.5000312>.
- (126) Gennari, S.; Maglia, F.; Anselmi-Tamburini, U.; Spinolo, G. SHS (Self-Sustained High-Temperature Synthesis) of Intermetallic Compounds: Effect of Process Parameters by Computer Simulation. *Intermetallics* **2003**, *11*, 1355–1359. [https://doi.org/10.1016/S0966-9795\(03\)00179-1](https://doi.org/10.1016/S0966-9795(03)00179-1).
- (127) Varma, A.; Rogachev, A. S.; Mukasyan, A. S.; Hwang, S. Complex Behavior of Self-Propagating Reaction Waves in Heterogeneous Media. *Proc. Natl. Acad. Sci. U. S. A.* **1998**, *95* (19), 11053–11058. <https://doi.org/10.1073/pnas.95.19.11053>.
- (128) Jian, G.; Piekiet, N. W.; Zachariah, M. R. Time-Resolved Mass Spectrometry of Nano-Al and Nano-Al/CuO Thermite under Rapid Heating: A Mechanistic Study. *J. Phys. Chem. C* **2012**, *116* (51), 26881–26887. <https://doi.org/10.1021/jp306717m>.
- (129) Zhou, L.; Piekiet, N.; Chowdhury, S.; Zachariah, M. R. Time-Resolved Mass Spectrometry of the Exothermic Reaction between Nanoaluminum and Metal Oxides: The Role of Oxygen Release. *J. Phys. Chem. C* **2010**, *114* (33), 14269–14275. <https://doi.org/10.1021/jp101146a>.

- (130) Delisio, J. B. Understanding the Relationships between Architecture, Chemistry, and Energy Release of Energetic Nanocomposites. **2017**, No. May, 194.
- (131) Ozawa, T. A New Method of Analyzing Thermogravimetric Data. *Bull. Chem. Soc. Jpn.* **1965**, 38 (11), 1881–1886. <https://doi.org/10.1246/bcsj.38.1881>.
- (132) Ozawa, T. Estimation of Activation Energy by Isoconversion Methods. *Thermochim. Acta* **1992**, 203 (C), 159–165. [https://doi.org/10.1016/0040-6031\(92\)85192-X](https://doi.org/10.1016/0040-6031(92)85192-X).
- (133) Vyazovkin, S.; Sbirrazzuoli, N. Isoconversional Kinetic Analysis of Thermally Stimulated Processes in Polymers. *Macromol. Rapid Commun.* **2006**, 27 (18), 1515–1532. <https://doi.org/10.1002/marc.200600404>.
- (134) Vyazovkin, S.; Sbirrazzuoli, N. Kinetic Methods to Study Isothermal and Nonisothermal Epoxy-Anhydride Cure. *Macromol. Chem. Phys.* **1999**, 200 (10), 2294–2303. [https://doi.org/10.1002/\(sici\)1521-3935\(19991001\)200:10<2294::aid-macp2294>3.3.co;2-m](https://doi.org/10.1002/(sici)1521-3935(19991001)200:10<2294::aid-macp2294>3.3.co;2-m).
- (135) Yi, F.; Delisio, J. B.; Zachariah, M. R.; LaVan, D. A. Nanocalorimetry-Coupled Time-of-Flight Mass Spectrometry: Identifying Evolved Species during High-Rate Thermal Measurements. *Anal. Chem.* **2015**, 87 (19), 9740–9744. <https://doi.org/10.1021/acs.analchem.5b01872>.
- (136) Dibeler, V. H.; Mohler, F. L. Dissociation of SF₆, CF₄, and SiF₄ by Electron Impact. *J. Res. Natl. Bur. Stand. (1934)*. **1948**, 40 (1), 25. <https://doi.org/10.6028/jres.040.014>.
- (137) Zhou, L.; Piekielek, N.; Chowdhury, S.; Zachariah, M. R. T-Jump/Time-of-Flight Mass Spectrometry for Time-Resolved Analysis of Energetic Materials. *Rapid Commun. Mass Spectrom.* **2009**, 23 (1), 194–202. <https://doi.org/10.1002/rcm.3815>.
- (138) Guo, H.; Sun, W.; Haas, F. M.; Farouk, T.; Dryer, F. L.; Ju, Y. Measurements of H₂O₂ in Low Temperature Dimethyl Ether Oxidation. *Proc. Combust. Inst.* **2013**, 34 (1), 573–581. <https://doi.org/10.1016/j.proci.2012.05.056>.
- (139) Crichton, E. Construction of a Molecular Beam Mass Spectrometer for In-Situ Probing of a Diamond Chemical Vapour Deposition Environment. **2007**, No. June, 161.
- (140) Horn, R.; Ihmann, K.; Ihmann, J.; Jentoft, F. C.; Geske, M.; Taha, A.; Pelzer, K.; Schlögl, R. Molecular Beam Mass Spectrometer Equipped with a Catalytic Wall Reactor for in Situ Studies in High Temperature Catalysis Research. *Rev. Sci. Instrum.* **2006**, 77 (5), 054102. <https://doi.org/10.1063/1.2200872>.
- (141) Stearns, C. A.; Kohl, F. J.; Fryburg, G. C.; Miller, R. A. NASA Technical Memorandum. **1977**, 73720 (July), 57.
- (142) Jankunas, J.; Osterwalder, A. Cold and Controlled Molecular Beams: Production and Applications. *Annu. Rev. Phys. Chem.* **2015**, 66 (1), 241–262. <https://doi.org/10.1146/annurev-physchem-040214-121307>.
- (143) Hansen, N.; Cool, T. A.; Westmoreland, P. R.; Kohse-Höinghaus, K. Recent Contributions of Flame-Sampling Molecular-Beam Mass Spectrometry to a Fundamental Understanding of Combustion Chemistry. *Prog. Energy Combust. Sci.* **2009**, 35 (2), 168–191. <https://doi.org/10.1016/j.pecs.2008.10.001>.
- (144) Zhu, C. G.; Wang, H. Z.; Min, L. Ignition Temperature of Magnesium Powder and Pyrotechnic Composition. *J. Energ. Mater.* **2014**, 32 (3), 219–226. <https://doi.org/10.1080/07370652.2013.812162>.
- (145) Berger, B.; Charsley, E. L.; Rooney, J. J.; Warrington, S. B. Quantitative Studies on the Zirconium - Potassium Perchlorate - Nitrocellulose Pyrotechnic System Using Differential Scanning Calorimetry and Chemical Analysis. *Thermochim. Acta* **1995**, 255 (C), 227–239. [https://doi.org/10.1016/0040-6031\(94\)02182-N](https://doi.org/10.1016/0040-6031(94)02182-N).
- (146) Prakash, A.; McCormick, A. V.; Zachariah, M. R. Synthesis and Reactivity of a Super-Reactive Metastable Intermolecular Composite Formulation of Al/KMnO₄. *Adv. Mater.* **2005**, 17 (7), 900–903. <https://doi.org/10.1002/adma.200400853>.
- (147) Zong, Y.; Jacob, R. J.; Li, S.; Zachariah, M. R. Size Resolved High Temperature Oxidation Kinetics of Nano-Sized Titanium and Zirconium Particles. *J. Phys. Chem. A* **2015**, 119 (24), 6171–6178. <https://doi.org/10.1021/acs.jpca.5b02590>.
- (148) Zhou, W.; DeLisio, J. B.; Wang, X.; Zachariah, M. R. Reaction Mechanisms of Potassium Oxysalts Based Energetic Composites. *Combust. Flame* **2017**, 177, 1–9. <https://doi.org/10.1016/j.combustflame.2016.05.024>.

- (149) Berger, B. Parameters Influencing the Pyrotechnic Reaction. *Propellants, Explos. Pyrotech.* **2005**, *30* (1), 27–35. <https://doi.org/10.1002/prop.200400082>.
- (150) Maharrey, S. P.; Erikson, W. W.; Highley, A. M.; Wiese-smith, D.; Kay, J. Ignition of THKP and TKP Pyrotechnic Powders : Incorporating Reactive Chemical Processes into Predictive Models. *Sandia Rep.* **2014**, No. March, 21.
- (151) Wu, T.; Sybing, A.; Wang, X.; Zachariah, M. R. Aerosol Synthesis of Phase Pure Iodine/Iodic Biocide Microparticles. *J. Mater. Res.* **2017**, *32* (4), 890–896. <https://doi.org/10.1557/jmr.2017.6>.
- (152) Sullivan, K. T.; Chiou, W. A.; Fiore, R.; Zachariah, M. R. In Situ Microscopy of Rapidly Heated Nano-Al and Nano- Al/ WO₃ Thermites. *Appl. Phys. Lett.* **2010**, *97* (13), 1–4. <https://doi.org/10.1063/1.3490752>.
- (153) Saha, N. C.; Tompkins, H. G. Titanium Nitride Oxidation Chemistry: An x-Ray Photoelectron Spectroscopy Study. *J. Appl. Phys.* **1992**, *72* (7), 3072–3079. <https://doi.org/10.1063/1.351465>.
- (154) Rtimi, S.; Baghriche, O.; Sanjines, R.; Pulgarin, C.; Bensimon, M.; Kiwi, J. TiON and TiON-Ag Sputtered Surfaces Leading to Bacterial Inactivation under Indoor Actinic Light. *J. Photochem. Photobiol. A Chem.* **2013**, *256*, 52–63. <https://doi.org/10.1016/j.jphotochem.2013.02.005>.
- (155) Jiang, N.; Zhang, H. J.; Bao, S. N.; Shen, Y. G.; Zhou, Z. F. XPS Study for Reactively Sputtered Titanium Nitride Thin Films Deposited under Different Substrate Bias. *Phys. B Condens. Matter* **2004**, *352* (1–4), 118–126. <https://doi.org/10.1016/j.physb.2004.07.001>.
- (156) Lee, J. S.; Hsu, C. K. The DSC Studies on the Phase Transition, Decomposition and Melting of Potassium Perchlorate with Additives. *Thermochim. Acta* **2001**, *367–368*, 367–370. [https://doi.org/10.1016/S0040-6031\(00\)00683-3](https://doi.org/10.1016/S0040-6031(00)00683-3).
- (157) Rudloff, W. K.; Freeman, E. S. The Catalytic Effect of Metal Oxides on Thermal-Decomposition Reactions. I. The Mechanism of the Molten-Phase Thermal Decomposition of Potassium Chlorate and of Potassium Chlorate in Mixtures with Potassium Chloride and Potassium Perchlorate. *J. Phys. Chem.* **1969**, *73* (5), 1209–1215. <https://doi.org/10.1021/j100725a006>.
- (158) Lee, J. S.; Hsu, C. K.; Jaw, K. S. The Thermal Properties of KClO₄ with Different Particle Size. *Thermochim. Acta* **2001**, *367–368*, 381–385. [https://doi.org/10.1016/S0040-6031\(00\)00691-2](https://doi.org/10.1016/S0040-6031(00)00691-2).
- (159) Ronning, C.; Feldermann, H.; Merk, R.; Hofsäss, H.; Reinke, P. Carbon Nitride Deposited Using Energetic Species: A Review on XPS Studies. *Phys. Rev. B - Condens. Matter Mater. Phys.* **1998**, *58* (4), 2207–2215. <https://doi.org/10.1103/PhysRevB.58.2207>.
- (160) Collins, L. W. The Catalytic Decomposition of Potassium Perchlorate. *Inorganica Chim. Acta* **1980**, *39* (C), 53–56. [https://doi.org/10.1016/S0020-1693\(00\)93633-8](https://doi.org/10.1016/S0020-1693(00)93633-8).
- (161) Muravyev, N. V.; Monogarov, K. A.; Zhigach, A. N.; Kuskov, M. L.; Fomenkov, I. V.; Pivkina, A. N. Exploring Enhanced Reactivity of Nanosized Titanium toward Oxidation. *Combust. Flame* **2018**, *191*, 109–115. <https://doi.org/10.1016/j.combustflame.2018.01.011>.
- (162) Rudloff, W. K.; Freeman, E. S. The Catalytic Effect of Metal Oxides on Thermal Decomposition Reactions. II. The Catalytic Effect of Metal Oxides on the Thermal Decomposition of Potassium Chlorate and Potassium Perchlorate as Detected by Thermal Analysis Methods. *J. Phys. Chem.* **1970**, *74* (18), 3317–3324. <https://doi.org/10.1021/j100712a002>.
- (163) Chandru, R. A.; Balasubramanian, N.; Oommen, C.; Raghunandan, B. N. Additive Manufacturing of Solid Rocket Propellant Grains. *J. Propuls. Power* **2018**, *34* (4), 1090–1093. <https://doi.org/10.2514/1.B36734>.
- (164) Meeks, K. A.; Clark, B. R.; Cano, J. E.; Aplett, C. A.; Pantoya, M. L. Effects of Rheological Properties on Reactivity of Energetic Thin Films. *Combust. Flame* **2015**, *162* (9), 3288–3293. <https://doi.org/10.1016/j.combustflame.2015.05.018>.
- (165) Ruz-nuglo, F. D.; Groven, L. J. 3-D Printing and Development of Fluoropolymer Based Reactive Inks. *Adv. Eng. Mater.* **2018**, *20* (2), 8. <https://doi.org/10.1002/adem.201700390>.
- (166) Hu, X.; Delisio, J. B.; Li, X.; Zhou, W.; Zachariah, M. R. Direct Deposit of Highly Reactive Bi (IO₃)₃ - Polyvinylidene Fluoride Biocidal Energetic Composite and Its Reactive Properties. *Adv. Eng. Mater.* **2017**, *19* (1), 9. <https://doi.org/10.1002/adem.201500532>.

- (167) Padhye, R.; Aquino, A. J. A.; Tunega, D.; Pantoya, M. L. Fluorination of an Alumina Surface: Modeling Aluminum – Fluorine Reaction Mechanisms. *ACS Appl. Mater. Interfaces* **2017**, *9* (28), 24290–24297. <https://doi.org/10.1021/acsami.7b05372>.
- (168) Sullivan, K.; Zachariah, M. R. Simultaneous Pressure and Optical Measurements of Nanoaluminum Thermites: Investigating the Reaction Mechanism. *J. Propuls. Power* **2010**, *26* (3), 6. <https://doi.org/10.2514/1.45834>.
- (169) McCollum, J.; Morey, A. M.; Iacono, S. T. Morphological and Combustion Study of Interface Effects in Aluminum-Poly(Vinylidene Fluoride) Composites. *Mater. Des.* **2017**, *134*, 64–70. <https://doi.org/10.1016/j.matdes.2017.08.028>.
- (170) Murray, A. K.; Novotny, W. A.; Fleck, T. J.; Gunduz, I. E.; Son, S. F.; Chiu, G. T.-C.; Rhoads, J. F. Selectively-Deposited Energetic Materials: A Feasibility Study of the Piezoelectric Inkjet Printing of Nanothermites. *Addit. Manuf.* **2018**, *22*, 69–74. <https://doi.org/10.1016/j.addma.2018.05.003>.
- (171) Heijden, A. E. D. . Van Der. Developments and Challenges in the Manufacturing, Characterization and Scale-up of Energetic Nanomaterials – A Review. *Chem. Eng. J.* **2018**, *350*, 939–948. <https://doi.org/10.1016/j.cej.2018.06.051>.
- (172) Irtyugo, L. A.; Belousova, N. V.; Denisov, V. M.; Denisova, L. T.; Kirik, S. D.; Chumilina, L. G. High-Temperature Heat Capacity of Bismuth Oxide and Bismuth-Zinc Double Oxide with the Sillenite Structure. *J. Sib. Fed. Univ.* **2012**, *2* (5), 125–130.
- (173) Berezovskaya, Y.; Budurov, S.; Spasov, T. Specific Heats of FCC Solid Solutions of the Bi₂O₃-Y₂O₃ System. *Cryst. Res. Technol.* **1987**, *22* (11), 1415–1419.
- (174) Song, J.; Guo, T.; Ding, W.; Yao, M.; Bei, F.; Zhang, X.; Huang, J.; Fang, X. Study on Thermal Behavior and Kinetics of Al/MnO₂ Poly(Vinylidene Fluorine) Energetic Nanocomposite Assembled by Electrospray. *RSC Adv.* **2019**, *9* (44), 25266–25273. <https://doi.org/10.1039/c9ra04425f>.
- (175) Lyu, J. Y.; Chen, S.; He, W.; Zhang, X. X.; Tang, D. yun; Liu, P. J.; Yan, Q. L. Fabrication of High-Performance Graphene Oxide Doped PVDF/CuO/Al Nanocomposites via Electrospinning. *Chem. Eng. J.* **2019**, *368* (November 2018), 129–137. <https://doi.org/10.1016/j.cej.2019.02.170>.
- (176) Sidebottom, M. A.; Sidebottom, M. A. Ultralow Wear Fluoropolymer Metal-Oxide Composites: Nanomechanics & Tribochemistry. **2018**.
- (177) Sengwa, R. J.; Dhatarwal, P.; Choudhary, S. A Comparative Study of Different Metal Oxide Nanoparticles Dispersed PVDF/PEO Blend Matrix-Based Advanced Multifunctional Nanodielectrics for Flexible Electronic Devices. *Mater. Today Commun.* **2020**, *25* (May), 101380. <https://doi.org/10.1016/j.mtcomm.2020.101380>.
- (178) Dutta, B.; Kar, E.; Bose, N.; Mukherjee, S. Significant Enhancement of the Electroactive β -Phase of PVDF by Incorporating Hydrothermally Synthesized Copper Oxide Nanoparticles. *RSC Adv.* **2015**, *5* (127), 105422–405434. <https://doi.org/10.1039/c5ra21903e>.
- (179) Crouse, C. A. Fluorinated Polymers as Oxidizers for Energetic Composites. *ACS Symp. Ser.* **2012**, *1106*, 127–140. <https://doi.org/10.1021/bk-2012-1106.ch009>.
- (180) Wang, H.; Rehwoldt, M.; Kline, D. J. D. J.; Wu, T.; Wang, P.; Zachariah, M. R. M. R. M. R. Comparison Study of the Ignition and Combustion Characteristics of Directly-Written Al/PVDF, Al/Viton and Al/THV Composites. *Combust. Flame* **2019**, *201*, 181–186. <https://doi.org/10.1016/j.combustflame.2018.12.031>.
- (181) Madorsky, S. I.; Hart, V. E.; Straus, S.; Sedlak, V. A. Thermal Degradation of Tetrafluoroethylene and Hydrofluoroethylene Polymers in a Vacuum. *J. Res. Natl. Bur. Stand. (1934)*. **1953**, *51* (6), 327. <https://doi.org/10.6028/jres.051.036>.
- (182) Strutton, J. W.; Knott, M.; Bencomo, J. A.; Iacono, S. T.; Mates, J. E.; Alston, J. R.; McCollum, J. M. Manipulating Polymer Decomposition to Alter Burn Performance in Aluminium/Poly(Vinylidene Fluoride) Filaments. *Polym. Int.* **2020**, No. July. <https://doi.org/10.1002/pi.6129>.
- (183) Tunega, D.; Pantoya, M. L.; Nieman, R.; Lischka, H.; Aquino, A. J. A. Reaction Mechanism for Fluorination Reactions with Hydroxylated Alumina Sites: Pathways Promoting Aluminum Combustion Reaction Mechanism for Fluorination Reactions with Hydroxylated Alumina Sites : Pathways Promoting Aluminum Combustion. *J. Chem. Phys.* **2021**, No. 154, 104308.

- <https://doi.org/10.1063/5.0040189>.
- (184) *Handbook of Fluoropolymer Science and Technology*; Smith, D. W. J., Iacono, S. T., Iyer, S. S., Eds.; John Wiley & Sons, Inc., 2014.
- (185) Rehwoldt, M. C.; Wang, H.; Kline, D. J.; Wu, T.; Eckman, N.; Wang, P.; Agrawal, N. R.; Zachariah, M. R. Ignition and Combustion Analysis of Direct Write Fabricated Aluminum/Metal Oxide/PVDF Films. *Combust. Flame* **2020**, *211*, 260–269. <https://doi.org/10.1016/j.combustflame.2019.08.023>.
- (186) Zarko, V. E.; Knyazeva, A. G. Determination of Kinetic Parameters of Exothermic Condensed Phase Reaction Using the Energetic Material Ignition Delay Data. *Combust. Flame* **2020**, *221*, 453–461. <https://doi.org/10.1016/j.combustflame.2020.08.022>.
- (187) Lonfei, J.; Jingling, W.; Shuman, X. Mechanisms of Pyrolysis of Fluoropolymers. *J. Anal. Appl. Pyrolysis* **1986**, *10*, 99–106.
- (188) Li, X.; Huang, C.; Yang, H.; Li, Y.; Cheng, Y. Thermal Reaction Properties of Aluminum/Copper (II) Oxide/Poly(Vinylidene Fluoride) Nanocomposite. *J. Therm. Anal. Calorim.* **2016**, *124* (2), 899–907. <https://doi.org/10.1007/s10973-015-5194-8>.
- (189) *CRC Handbook of Chemistry and Physics*; Lide, D. R., Ed.; CRC Press: Boca Raton, FL, 2005. <https://doi.org/10.1201/b17118-11>.
- (190) *Thermodynamic Data-Base for Metal Fluorides*; 2001.
- (191) Mansour, S. A. A. Thermoanalytical Investigations of Decomposition Course of Copper Oxysalts - I. Basic Copper Carbonate. *J. Therm. Anal.* **1994**, *42* (6), 1251–1263. <https://doi.org/10.1007/BF02546934>.
- (192) Cheng, S. C.; Vachon, R. I. The Prediction of the Thermal Conductivity of Two and Three Phase Solid Heterogeneous Mixtures. *Int. J. Heat Mass Transf.* **1969**, *12* (3), 249–264. [https://doi.org/10.1016/0017-9310\(69\)90009-X](https://doi.org/10.1016/0017-9310(69)90009-X).
- (193) Maiti, S. N.; Ghosh, K. Thermal Characteristics of Silver Powder-filled Polypropylene Composites. *J. Appl. Polym. Sci.* **1994**, *52* (8), 1091–1103. <https://doi.org/10.1002/app.1994.070520810>.
- (194) Kargar, F.; Barani, Z.; Salgado, R.; Debnath, B.; Lewis, J. S.; Aytan, E.; Lake, R. K.; Balandin, A. A. Thermal Percolation Threshold and Thermal Properties of Composites with High Loading of Graphene and Boron Nitride Fillers. *ACS Appl. Mater. Interfaces* **2018**, *10* (43), 37555–37565. <https://doi.org/10.1021/acsami.8b16616>.
- (195) Yuan, J.; Yao, S.; Li, W.; Sylvestre, A.; Bai, J. Anisotropic Percolation of SiC-carbon Nanotube Hybrids: A New Route toward Thermally Conductive High-k Polymer Composites. *J. Phys. Chem. C* **2017**, *121*, 12063–12070. <https://doi.org/10.1021/acs.jpcc.7b03372>.
- (196) Smith, D. K.; Cano, J.; Pantoya, M. L. Thermal and Combustion Properties of Energetic Thin Films with Carbon Nanotubes. *J. Thermophys. Heat Transf.* **2017**, *31* (3), 1–5. <https://doi.org/10.2514/1.T5009>.
- (197) Pal, R. On the Lewis-Nielsen Model for Thermal/Electrical Conductivity of Composites. *Compos. Part A Appl. Sci. Manuf.* **2008**, *39* (5), 718–726. <https://doi.org/10.1016/j.compositesa.2008.02.008>.
- (198) Pietrak, K.; Wiśniewski, T. A Review of Models for Effective Thermal Conductivity of Composite Materials. *J. Power Technol.* **2015**, *95* (1), 14–24.
- (199) Nielsen, L. E. The Thermal and Electrical Conductivity of Two-Phase Systems. *Ind. Eng. Chem. Fundam.* **1974**, *13* (1), 17–20. <https://doi.org/10.1021/i160049a004>.
- (200) Dang, Z.; Yuan, J.; Yao, S.; Liao, R. Flexible Nanodielectric Materials with High Permittivity for Power Energy Storage. *Adv. Mater.* **2013**, *25*, 6334–6365. <https://doi.org/10.1002/adma.201301752>.
- (201) Wanasinghe, D.; Aslani, F.; Ma, G.; Habibi, D. Review of Polymer Composites with Diverse Nanofillers for Electromagnetic Interference Shielding. *Nanomaterials* **2020**, *10*, 1–46.
- (202) Du, C.; Li, M.; Cao, M.; Feng, S.; Guo, H. Enhanced Thermal and Mechanical Properties of Polyvinylidene Fluoride Composites with Magnetic Oriented Carbon Nanotube. *Carbon N. Y.* **2018**, *126*, 197–207.
- (203) Lawless, Z. D.; Hobbs, M. L.; Kaneshige, M. J. Thermal Conductivity of Energetic Materials. *J. Energ. Mater.* **2020**, *38* (2), 214–239. <https://doi.org/10.1080/07370652.2019.1679285>.
- (204) Meeks, K.; Smith, D. K.; Clark, B.; Pantoya, M. L. Percolation of a Metallic Binder in Energy

- Generating Composites. *J. Mater. Chem. A* **2017**, *5* (15), 7200–7209.
<https://doi.org/10.1039/c7ta00689f>.
- (205) Agarwal, S.; Khan, M. M. K.; Gupta, R. K. Thermal Conductivity of Polymer Nanocomposites Made with Carbon Nanofibers. *Polym. Eng. Sci.* **2008**, *48* (12), 2475–2481.
- (206) Zheng, R.; Gao, J.; Wang, J.; Feng, S. P.; Ohtani, H.; Wang, J.; Chen, G. Thermal Percolation in Stable Graphite Suspensions. *Nano Lett.* **2012**, *12* (1), 188–192.
<https://doi.org/10.1021/nl203276y>.
- (207) Mukasyan, A. S.; Shuck, C. E. Kinetics of SHS Reactions: A Review. *Int. J. Self-Propagating High-Temperature Synth.* **2017**, *26* (3), 145–165. <https://doi.org/10.3103/S1061386217030049>.
- (208) Song, M. S.; Ran, M. W.; Kong, Y. Y. In Situ Fabrication of ZrC Powder Obtained by Self-Propagating High-Temperature Synthesis from Al-Zr-C Elemental Powders. *Int. J. Refract. Met. Hard Mater.* **2011**, *29* (3), 392–396. <https://doi.org/10.1016/j.ijrmhm.2011.01.013>.
- (209) Isert, S.; Lane, C. D.; Gunduz, I. E.; Son, S. F. Tailoring Burning Rates Using Reactive Wires in Composite Solid Rocket Propellants. *Proc. Combust. Inst.* **2017**, *36* (2), 2283–2290.
<https://doi.org/10.1016/j.proci.2016.06.141>.
- (210) Wang, H.; Delisio, J. B.; Holdren, S.; Wu, T.; Yang, Y.; Hu, J.; Zachariah, M. R. Mesoporous Silica Spheres Incorporated Aluminum/Poly(Vinylidene Fluoride) for Enhanced Burning Propellants. *Adv. Eng. Mater.* **2018**, *20* (2), 1700547. <https://doi.org/10.1002/adem.201700547>.
- (211) An, T.; Qu, W.; Yang, Y.; Zhao, F.; Yan, Q. *Preparation, Characterization, and Application of Superthermites in Solid Propellants*; Elsevier Inc., 2019. <https://doi.org/10.1016/B978-0-12-813908-0.00004-6>.
- (212) Goroshin, S.; Lee, J. H. S.; Shoshin, Y. Effect of the Discrete Nature of Heat Sources on Flame Propagation in Particulate Suspensions. In *Twenty-Seventh Symposium (International) on Combustion/The Combustion Institute*; 1998; pp 743–749.
- (213) Varma, A.; Mukasyan, A. S.; Hwang, S. Dynamics of Self-Propagating Reactions in Heterogeneous Media: Experiments and Model. *Chem. Eng. Sci.* **2001**, *56* (4), 1459–1466.
[https://doi.org/10.1016/S0009-2509\(00\)00371-7](https://doi.org/10.1016/S0009-2509(00)00371-7).
- (214) Bacciochini, A.; Radulescu, M. I.; Yandouzi, M.; Maines, G.; Lee, J. J.; Jodoin, B. Reactive Structural Materials Consolidated by Cold Spray: Al-CuO Thermite. *Surf. Coatings Technol.* **2013**, *226*, 60–67. <https://doi.org/10.1016/j.surfcoat.2013.03.036>.
- (215) Ervin, V. J.; Klett, J. W.; Mundt, C. M. Estimation of the Thermal Conductivity of Composites. *J. Mater. Sci.* **1999**, *34*, 3545–3553.
- (216) Merzhanov, A. G. The Theory of Stable Homogeneous Combustion of Condensed Substances. *Combust. Flame* **1969**, *13* (2), 143–156. [https://doi.org/10.1016/0010-2180\(69\)90045-5](https://doi.org/10.1016/0010-2180(69)90045-5).
- (217) Beck, J. M.; Volpert, V. A. Nonlinear Dynamics in a Simple Model of Solid Flame Microstructure. *Phys. D Nonlinear Phenom.* **2003**, *182*, 86–102.
[https://doi.org/10.1016/S0167-2789\(03\)00119-2](https://doi.org/10.1016/S0167-2789(03)00119-2).
- (218) Smolyakov, V. K. “Roughness” of the Gasless Combustion Front. *Combust. Explos. Shock Waves* **2001**, *37* (3), 274–284. <https://doi.org/10.1023/A:1017519821870>.
- (219) Chakraborty, N.; Swaminathan, N. Influence of the Damköhler Number on Turbulence-Scalar Interaction in Premixed Flames. I. Physical Insight. *Phys. Fluids* **2007**, *19* (4), 045103.
<https://doi.org/10.1063/1.2714070>.
- (220) Oberlack, M.; Arlitt, R.; Peter, N. On Stochastic Damkohler Number Variations in a Homogeneous Flow Reactor. *Combust. Theory Model.* **2000**, *4* (4), 495–509.
<https://doi.org/10.1088/1364-7830/4/4/307>.
- (221) Rogachev, A. S. Microheterogeneous Mechanism of Gasless Combustion. *Combust. Explos. Shock Waves* **2003**, *39* (2), 150–158. <https://doi.org/10.1023/A:1022956915794>.
- (222) Grinchuk, P. S. Combustion of Heterogeneous Systems with a Stochastic Spatial Structure near the Propagation Limits. *J. Eng. Phys. Thermophys.* **2013**, *86* (4), 875–887.
<https://doi.org/10.1007/s10891-013-0907-y>.
- (223) Tang, F. D.; Higgins, A. J.; Goroshin, S. Effect of Discreteness on Heterogeneous Flames: Propagation Limits in Regular and Random Particle Arrays. *Combust. Theory Model.* **2009**, *13* (2), 319–341. <https://doi.org/10.1080/13647830802632184>.
- (224) Becker; Kaus. Two-Dimensional Heat Equation with FD. In *Numerical Modeling of Earth Systems*; 2016; pp 1–9.

- (225) Niragire, L. 2D Numerical Heat Inverse Model for Diffusivity Coefficients in Cartesian Coordinates, 2013.
- (226) Hwang, S.; Mukasyan, A. S.; Varma, A. Mechanisms of Combustion Wave Propagation in Heterogeneous Reaction Systems. *Combust. Flame* **1998**, *115* (3), 354–363. [https://doi.org/10.1016/S0010-2180\(98\)00016-9](https://doi.org/10.1016/S0010-2180(98)00016-9).
- (227) Mukasyan, A. S.; Rogachev, A. S.; Varma, A. Mechanisms of Reaction Wave Propagation during Combustion Synthesis of Advanced Materials. *Chem. Eng. Sci.* **1999**, *54* (15–16), 3357–3367. [https://doi.org/10.1016/S0009-2509\(98\)00457-6](https://doi.org/10.1016/S0009-2509(98)00457-6).
- (228) Zhou, W.; Zuo, J.; Ren, W. Thermal Conductivity and Dielectric Properties of Al/PVDF Composites. *Compos. Part A* **2012**, *43* (4), 658–664. <https://doi.org/10.1016/j.compositesa.2011.11.024>.
- (229) Bama, G. K.; Devi, P. I.; Ramachandran, K. Structural and Thermal Properties of PVDF/PVA Blends. *J. Mater. Res.* **2009**, *44*, 1302–1307. <https://doi.org/10.1007/s10853-009-3271-8>.
- (230) Delisio, J. B.; Wang, X.; Wu, T.; Egan, G. C.; Jacob, R. J.; Zachariah, M. R. Investigating the Oxidation Mechanism of Tantalum Nanoparticles at High Heating Rates. *J. Appl. Phys.* **2017**, *122* (24), 245901. <https://doi.org/10.1063/1.4995574>.
- (231) Chen, Y.; Guildenbecher, D. R.; Hoffmeister, K. N. G.; Cooper, M. A.; Stauffacher, H. L.; Oliver, M. S.; Washburn, E. B. Study of Aluminum Particle Combustion in Solid Propellant Plumes Using Digital In-Line Holography and Imaging Pyrometry. *Combust. Flame* **2017**, *182*, 225–237. <https://doi.org/10.1016/j.combustflame.2017.04.016>.
- (232) Barkley, S. J.; Kindem, D. K.; Zhu, K.; Michael, J. B.; Sippel, T. Dynamic Control of Composite Solid Propellant Flame Spread Through Microwave Eddy Current Heating of Propellant-Embedded Antennas. *AIAA SciTech Forum* **2019**, No. January, 1–8. <https://doi.org/10.2514/6.2019-1239>.
- (233) Sippel, T. Pulsed Microwave Plasma Instrumentation for Investigation of Plasma-Tuned Multiphase Combustion. *Air Force Res. Lab.* **2018**, No. AFRL-AFOSR-VA-TR-2018-0413, 1–32.
- (234) Katz, J. D. Microwave Sintering of Ceramics. *Annu. Rev. Mater. Sci.* **1992**, *22*, 153–170.
- (235) Leonelli, C.; Veronesi, P.; Denti, L.; Gatto, A.; Iuliano, L. Microwave Assisted Sintering of Green Metal Parts. *J. Mater. Process. Technol.* **2008**, *205* (1–3), 489–496. <https://doi.org/10.1016/j.jmatprotec.2007.11.263>.
- (236) Roy, R.; Agrawal, D.; Cheng, J.; Gedevarishvili, S. Full Sintering of Powdered-Metal Bodies in a Microwave Field. *Nature* **1999**, *399*, 668–670.
- (237) Batanov, G. M.; Bereghetskaya, N. K.; Kopiev, V. A.; Kossyi, I. A.; Magunov, A. N.; Shcherbakov, V. A.; Sachkova, N. V. Pulse Ignition of Heterogeneous Condensed Systems by a Set of Surface Sparks Generated by a Microwave Beam. *Dokl. Phys.* **2006**, *51* (4), 180–185. <https://doi.org/10.1134/S1028335806040057>.
- (238) Horikoshi, S.; Serpone, N. *Microwaves in Nanoparticle Synthesis: Fundamentals and Applications*; Wiley-VCH, 2013.
- (239) Hasue, K.; Tanabe, M.; Watanabe, N.; Nakahara, S.; Okada, F. Initiation of Some Energetic Materials by Microwave Heating. *Propellants, Explos. Pyrotech.* **1990**, *15*, 181–186.
- (240) Horikoshi, S.; Schiffmann, R. F.; Fukushima, J.; Serpone, N. *Microwave Chemical and Materials Processing: A Tutorial*, 1st ed.; Springer, 2018.
- (241) Kaur, R.; Newborough, M.; Probert, S. D. Multi-Purpose Mathematical Model for Electromagnetic-Heating Processes. *Appl. Energy* **1993**, *44* (4), 337–386.
- (242) Crane, C. A.; Pantoya, M. L.; Weeks, B. L.; Saed, M. The Effects of Particle Size on Microwave Heating of Metal and Metal Oxide Powders. *Powder Technol.* **2014**, *256*, 113–117. <https://doi.org/10.1016/j.powtec.2014.02.008>.
- (243) Ignatenko, M.; Tanaka, M.; Sato, M. Absorption of Microwave Energy by a Spherical Nonmagnetic Metal Particle. *Jpn. J. Appl. Phys.* **2009**, *48*, 067001. <https://doi.org/10.1143/JJAP.48.067001>.
- (244) Porch, A.; Slocombe, D.; Edwards, P. P. Microwave Absorption in Powders of Small Conducting Particles for Heating Applications. *Phys. Chem. Chem. Phys.* **2013**, *15* (8), 2757–2763. <https://doi.org/10.1039/c2cp43310a>.
- (245) Yoshikawa, N.; Ishizuka, E.; Taniguchi, S. Heating of Metal Particles in a Single-Mode

- Microwave Applicator. *Mater. Trans.* **2006**, *47* (3), 898–902.
- (246) Meir, Y.; Jerby, E. Thermite Powder Ignition by Localized Microwaves. *Combust. Flame* **2012**, *159* (7), 2474–2479. <https://doi.org/10.1016/j.combustflame.2012.02.015>.
- (247) Crane, C. A.; Pantoya, M. L.; Weeks, B. L. Investigating the Trade-Offs of Microwave Susceptors in Energetic Composites: Microwave Heating versus Combustion Performance. *J. Appl. Phys.* **2014**, *115* (10), 104106. <https://doi.org/10.1063/1.4868337>.
- (248) Kim, T.; Lee, J.; Lee, K.-H. Microwave Heating of Carbon-Based Solid Materials. *Carbon Lett.* **2014**, *15* (1), 15–24. <https://doi.org/10.5714/CL.2014.15.1.015>.
- (249) Chandrasekaran, S.; Basak, T.; Srinivasan, R. Microwave Heating Characteristics of Graphite Based Powder Mixtures. *Int. Commun. Heat Mass Transf.* **2013**, *48*, 22–27. <https://doi.org/10.1016/j.icheatmasstransfer.2013.09.008>.
- (250) Bohren, C. F.; Huffman, D. R. *Absorption and Scattering of Light by Small Particles*; Wiley, 1998.
- (251) Biswas, P.; Mulholland, G. W.; Rehwoldt, M. C.; Kline, D. J.; Zachariah, M. R. Microwave Absorption by Small Dielectric and Semi-Conductor Coated Metal Particles. *J. Quant. Spectrosc. Radiat. Transf.* **2020**, *247*, 106938. <https://doi.org/10.1016/j.jqsrt.2020.106938>.
- (252) Swinehart, D. F. The Beer-Lambert Law. *J. Chem. Educ.* **1962**, *39* (7), 333–335. <https://doi.org/10.1021/ed039p333>.
- (253) Kitchen, H. J.; Vallance, S. R.; Kennedy, J. L.; Tapia-ruiz, N.; Carassiti, L.; Harrison, A.; Whittaker, A. G.; Drysdale, T. D.; Kingman, S. W.; Gregory, D. H. Modern Microwave Methods in Solid-State Inorganic Materials Chemistry: From Fundamentals to Manufacturing. *Chem. Rev.* **2014**, *114* (2), 1170–1206. <https://doi.org/10.1021/cr4002353>.
- (254) Rankinen, J. L. Microwave Characterization of Thin Film Titania, The Pennsylvania State University, 2005.
- (255) Gong, C.; Zhang, J.; Yan, C.; Cheng, X.; Zhang, J.; Yu, L.; Jin, Z.; Zhang, Z. Synthesis and Microwave Electromagnetic Properties of Nanosized Titanium Nitride. *J. Mater. Chem.* **2012**, *22* (8), 3370–3376. <https://doi.org/10.1039/c1jm13509k>.
- (256) Noor, F.; Vorozhtsov, A.; Lerner, M.; Wen, D. Exothermic Characteristics of Aluminum Based Nanomaterials. *Powder Technol.* **2015**, *282*, 19–24. <https://doi.org/10.1016/j.powtec.2014.12.058>.
- (257) Sharma, R. K.; Kaneriya, R.; Patel, S.; Bindal, A.; Pargaien, K. C. Microwave Integrated Circuits Fabrication on Alumina Substrate Using Pattern up Direct Electroless Nickel and Immersion Au Plating and Study of Its Properties. *Microelectron. Eng.* **2013**, *108*, 45–49. <https://doi.org/10.1016/j.mee.2013.02.061>.
- (258) Zimmerman, D. T.; Cardellino, J. D.; Cravener, K. T.; Feather, K. R.; Miskovsky, N. M.; Weisel, G. J. Microwave Absorption in Percolating Metal- Insulator Composites. *Appl. Phys. Lett.* **2008**, *93* (21), 214103. <https://doi.org/10.1063/1.3036900>.
- (259) Larring, Y.; Pishahang, M.; Tolchard, J.; Lind, A. M.; Sunding, M. F.; Stensrød, R. E.; Jacobs, M.; Snijkers, F.; Kolk, T. Van Der; Albertsen, K. Fabrication Process Parameters Significantly Affect the Perovskite Oxygen Carriers Materials (OCM) Performance in Chemical Looping with Oxygen Uncoupling (CLOU). *J. Therm. Anal. Calorim.* **2020**, *140* (2), 577–589. <https://doi.org/10.1007/s10973-019-08860-y>.
- (260) Sarshar, Z.; Kleitz, F.; Kaliaguine, S. Novel Oxygen Carriers for Chemical Looping Combustion : La_{1-x}Ce_xBO₃ (B =Co,Mn) Perovskites Synthesized by Reactive Grinding and Nanocasting. *Energy Environ. Sci.* **2011**, *4* (10), 4258–4269. <https://doi.org/10.1039/c1ee01716k>.
- (261) Huang, Y.-H.; Dass, R. I.; Xing, Z.-L.; Goodenough, J. B. Double Perovskites as Anode Materials for Solid-Oxide Fuel Cells. *Science* (80-.). **2006**, *312*, 254–258.
- (262) Laguna-bercero, M. A.; Kilner, J. A.; Skinner, S. J. Performance and Characterization of (La, Sr)MnO₃/YSZ and La_{0.6}Sr_{0.4}Co_{0.2}Fe_{0.8}O₃ Electrodes for Solid Oxide Electrolysis Cells. *Chem. Mater.* **2010**, *22*, 1134–1141. <https://doi.org/10.1021/cm902425k>.
- (263) Schiestel, T.; Kilgus, M.; Peter, S.; Caspary, K. J.; Wang, H.; Caro, J. Hollow Fibre Perovskite Membranes for Oxygen Separation. *J. Memb. Sci.* **2005**, *258*, 1–4. <https://doi.org/10.1016/j.memsci.2005.03.035>.
- (264) Dai, X. P.; Wu, Q.; Li, R. J.; Yu, C. C.; Hao, Z. P. Hydrogen Production from a Combination

- of the Water-Gas Shift and Redox Cycle Process of Methane Partial Oxidation via Lattice Oxygen over LaFeO₃ Perovskite Catalyst. *J. Phys. Chem. B* **2006**, *110* (51), 25856–25862. <https://doi.org/10.1021/jp0654664>.
- (265) Liu, L.; Taylor, D. D.; Rodriguez, E. E.; Zachariah, M. R. Influence of Transition Metal Electronegativity on the Oxygen Storage Capacity of Perovskite Oxides. *Chem. Commun.* **2016**, *52*, 10369–10372. <https://doi.org/10.1039/c6cc01997h>.
- (266) Wang, Z. L.; Yin, J. S.; Jiang, Y. D. EELS Analysis of Cation Valence States and Oxygen Vacancies in Magnetic Oxides. *Micron* **2000**, *31* (5), 571–580. [https://doi.org/10.1016/S0968-4328\(99\)00139-0](https://doi.org/10.1016/S0968-4328(99)00139-0).
- (267) Unocic, K. A.; Shin, D.; Unocic, R. R.; Allard, L. F. NiAl Oxidation Reaction Processes Studied In Situ Using MEMS-Based Closed-Cell Gas Reaction Transmission Electron Microscopy. *Oxid. Met.* **2017**, *88*, 495–508. <https://doi.org/10.1007/s11085-016-9676-2>.
- (268) Pivkina, A.; Ulyanova, P.; Frolov, Y. Nanomaterials for Heterogeneous Combustion. *Propellants, Explos. Pyrotech.* **2004**, *29* (1), 39–48. <https://doi.org/10.1002/prop.200400025>.
- (269) Wang, H.; Delisio, J. B.; Jian, G.; Zhou, W.; Zachariah, M. R. Electro spray Formation and Combustion Characteristics of Iodine-Containing Al/CuO Nanothermite Microparticles. *Combust. Flame* **2015**, *162* (7), 2823–2829. <https://doi.org/10.1016/j.combustflame.2015.04.005>.
- (270) Zhao, W.; Wang, X.; Wang, H.; Wu, T.; Kline, D. J.; Rehwoldt, M.; Ren, H.; Zachariah, M. R.; Holdren, S.; Rehwoldt, M.; et al. Titanium Enhanced Ignition and Combustion of Al/I₂O₅ Mesoparticle Composites. *Combust. Flame* **2020**, *212*, 245–251. <https://doi.org/10.1016/j.combustflame.2019.04.049>.
- (271) Shancita, I.; Miller, K. K.; Silverstein, P. D.; Kalman, J.; Pantoya, M. L. Synthesis of Metal Iodates from an Energetic Salt. *R. Soc. Chem.* **2020**, *10*, 14403–14409. <https://doi.org/10.1039/d0ra02250k>.
- (272) Kim, S. H.; Liu, B. Y. H.; Zachariah, M. R. Synthesis of Nanoporous Metal Oxide Particles by a New Inorganic Matrix Spray Pyrolysis Method. *Chem. Mater.* **2002**, *14* (7), 2889–2899. <https://doi.org/10.1021/cm010957g>.
- (273) Mora, J. F. de la M.; Navascues, J.; Fernandez, F.; Rosell-Llompart. Generation of Submicron Monodisperse Aerosols in ElectroSprays. *J. Aerosol Sci.* **1990**, *21* (2), 673–676.
- (274) Choi, S.; Kim, Y. Analysis of Pyrolysis Products of Poly(Vinylidene Fluoride-Co-Hexafluoropropylene) by Pyrolysis-Gas Chromatography/Mass Spectrometry. *J. Fluor. Chem.* **2014**, *165*, 33–38.
- (275) Gronert, S. An Alternative Interpretation of the C-H Bond Strengths of Alkanes. *J. Org. Chem.* **2006**, *71*, 1209–1219. <https://doi.org/10.1021/jo052363t>.
- (276) Mikhailenko, S. N.; Naumenko, O. V.; Nikitin, A. V.; Vasilenko, I. A.; Liu, A. W.; Song, K. F.; Ni, H. Y.; Hu, S. M. Absorption Spectrum of Deuterated Water Vapor Enriched by ¹⁸O between 6000 and 9200cm⁻¹. *J. Quant. Spectrosc. Radiat. Transf.* **2012**, *113* (9), 653–669. <https://doi.org/10.1016/j.jqsrt.2012.02.009>.
- (277) Lavrov, B. P.; Umrikhin, I. S. Optimal Values of Rovibronic Energy Levels for Triplet Electronic States of Molecular Deuterium. *J. Phys. B At. Mol. Opt. Phys.* **2008**, *41* (10). <https://doi.org/10.1088/0953-4075/41/10/105103>.
- (278) Chahrour, O.; Cobice, D.; Malone, J. Stable Isotope Labelling Methods in Mass Spectrometry-Based Quantitative Proteomics. *J. Pharm. Biomed. Anal.* **2015**, *113*, 2–20. <https://doi.org/10.1016/j.jpba.2015.04.013>.
- (279) Zou, X.; Wang, N.; Liao, L.; Chu, Q.; Shi, B. Prediction of Nano/Micro Aluminum Particles Ignition in Oxygen Atmosphere. *Fuel* **2020**, *266* (November 2019), 116952. <https://doi.org/10.1016/j.fuel.2019.116952>.
- (280) Nguyen, L.; Hashimoto, T.; Zakharov, D. N.; Stach, E. A.; Rooney, A. P.; Berkels, B.; Thompson, G. E.; Haigh, S. J.; Burnett, T. L. Atomic-Scale Insights into the Oxidation of Aluminum. *ACS Appl. Mater. Interfaces* **2018**, *10* (3), 2230–2235. <https://doi.org/10.1021/acsami.7b17224>.
- (281) Wainwright, E. R.; Dean, S. W.; De Lucia, F. C.; Weihs, T. P.; Gottfried, J. L. Effect of Sample Morphology on the Spectral and Spatiotemporal Characteristics of Laser-Induced Plasmas from Aluminum. *Appl. Phys. A Mater. Sci. Process.* **2020**, *126* (2).

- <https://doi.org/10.1007/s00339-019-3201-9>.
- (282) Boreskov, G. K. The Catalysis of Isotopic Exchange in Molecular Oxygen. In *Advances in Catalysis*; 1964; p 351.
- (283) Yamamoto, D.; Kuroda, M.; Tachibana, S.; Sakamoto, N.; Yurimoto, H. Oxygen Isotopic Exchange between Amorphous Silicate and Water Vapor and Its Implications for Oxygen Isotopic Evolution in the Early Solar System. *Astrophys. J.* **2018**, *865* (2), 98. <https://doi.org/10.3847/1538-4357/aadcee>.
- (284) Delisio, J. B.; Mayo, D. H.; Guerieri, P. M.; Decarlo, S.; Ives, R.; Bowen, K.; Eichhorn, B. W.; Zachariah, M. R. Oxidation and Decomposition Mechanisms of Air Sensitive Aluminum Clusters at High Heating Rates. *Chem. Phys. Lett.* **2016**, *661*, 168–172. <https://doi.org/10.1016/j.cplett.2016.08.065>.
- (285) Langtangen, H. P.; Linge, S. *Finite Difference Methods for Diffusion Processes*; 2016.
- (286) Recktenwald, G. W. *Finite-Difference Approximations to the Heat Equation*; 2011.
- (287) Wesseling, P. Von Neumann Stability Conditions for the Convection-Diffusion Equation. *IMA J. Numer. Anal.* **1996**, 583–598.
- (288) Mahadevan, R.; Lee, D.; Sakurai, H.; Zachariah, M. R. Measurement of Condensed-Phase Reaction Kinetics in the Aerosol Phase Using Single Particle Mass Spectrometry. *J. Phys. Chem. A* **2002**, *106* (46), 11083–11092. <https://doi.org/10.1021/jp025784c>.
- (289) Lee, D.; Park, K.; Zachariah, M. R. Determination of the Size Distribution of Polydisperse Nanoparticles with Single-Particle Mass Spectrometry: The Role of Ion Kinetic Energy. *Aerosol Sci. Technol.* **2005**, *39* (2), 162–169. <https://doi.org/10.1080/027868290904537>.
- (290) Kline, D. J.; Rehwoldt, M. C.; Wang, H.; Eckman, N. E.; Zachariah, M. R. Why Does Adding a Poor Thermal Conductor Increase Propagation Rate in Solid Propellants? *Appl. Phys. Lett.* **2019**, *115* (11), 114101. <https://doi.org/10.1063/1.5113612>.